Simplified Equivalent Modelling of Electromagnetic Emissions from Printed Circuit Boards

Xin Tong, BSc

Thesis submitted to the University of Nottingham
for the degree of Doctor of Philosophy

May, 2010

Abstract

Characterization of electromagnetic emissions from printed circuit boards (PCBs) is an important issue in electromagnetic compatibility (EMC) design and analysis of modern electronic systems. This thesis is focused on the development of a novel modelling and characterization methodology for predicting the electromagnetic emissions from PCBs in both free space and closed environment. The basic idea of this work is to model the actual PCB radiating source with a dipole-based equivalence found from near-field scanning.

A fully automatic near-field scanning system and scanning methodology are developed that provide reliable and sufficient data for the construction of equivalent emission models of PCB structures. The model of PCB emissions is developed that uses an array of equivalent dipoles deduced from magnetic near-field scans. Guidelines are proposed for setting the modelling configuration and parameters. The modelling accuracy can be improved by either improving the measurement efforts or using the mathematical regularization technique. An optimization procedure based on genetic algorithms is developed which addresses the optimal configuration of the model.

For applications in closed environments, the equivalent model is extended to account for the interactions between the PCB and the enclosure. The extension comprises a dielectric layer and a ground plane which explicitly represent the necessary electromagnetic passive properties of a PCB. This is referred to as the dipole-dielectric-conducting plane (DDC) model and provides a completely general representation which can be incorporated into electromagnetic simulation or analysis tools.

The modelling and characterization methodology provides a useful tool for efficient analysis of issues related to EMC design of systems with PCBs as regards predicting electromagnetic emissions in both free space and closed environment. The proposed method has significant advantages in tackling realistic problems because the equivalent models greatly reduce the computational costs and do no rely on the knowledge of detailed PCB structure.

Published Papers

- X. Tong, D. W. P. Thomas, A. Nothofer, P. Sewell, and C. Christoplous, “Modelling electromagnetic emissions from printed circuit boards in closed environments using equivalent dipoles”, accepted for publication on *IEEE Trans. Electromagn. Compat.*
- X. Tong, D. W. P. Thomas, K. Biwojno, A. Nothofer, P. Sewell, and C. Christoplous, “Modelling electromagnetic emissions from PCBs in free space using equivalent dipoles”, in *Proc. 39th European Microwave Conference*, pp. 280-283, Rome, Sep. 2009.
- X. Tong, D. W. P. Thomas, A. Nothofer, P. Sewell, and C. Christoplous, “A genetic algorithm based method for modelling equivalent emission sources of printed circuits from near-field measurements”, *Asia-Pacific Symposium on EMC* 2010, Beijing, Apr. 2010.
- X. Tong, D. W. P. Thomas, A. Nothofer, P. Sewell, and C. Christoplous, “Optimized equivalent dipole model of PCB emissions based on genetic algorithms”, submitted to *EMC Europe* 2010.
- D. W. P. Thomas, K. Biwojno, X. Tong, A. Nothofer, P. Sewell and C. Christopoulos, “PCB electromagnetic emissions prediction from equivalent magnetic dipoles found from near field scans,” *XXIX URSI General Assembly*, EB.5(125), Chicago, USA, 7-16 Aug. 2008.
- D. W. P. Thomas, K. Biwojno, X. Tong, A. Nothofer, P. Sewell and C. Christopoulos, “Measurement and simulation of the near-field emissions from microstrip lines,” in *Proc. EMC Europe* 2008, pp. 1-6, Sep. 2008.

Acknowledgements

I would like to express my sincere gratitude to my supervisors, Dr. David W. P. Thomas, Dr. Angela Nothofer and Prof. Christos Chirstopoulos for their invaluable guidance and assistance during my PhD study. I learned all aspects of doing research, presenting and publishing my work from my supervisors.

I would like to thank Dr. Xavier Ngu, who shared his years of experience in EMC instrumentation with me, Dr. John Paul, who provided very useful guidance in TLM simulation, and Dr. Konrad Biwojno, with whom I had helpful conversations related to my research. I would like to appreciate Dr. Ana Vukovic, Prof. Phil Sewell and Prof. Trevor Benson for their teaching in my classes. Thanks also go to the technicians in the ground floor workshop, particularly Mr. Kevin Last and Mr. Paul Moss, who provided technical support for my experimental work.

I would like to acknowledge the University of Nottingham for the opportunity provided to undertake my doctorate programme within the world class GGIEMR group by bestowing upon me the prestigious Tower Innovation Scholarship and EPSRC studentship.

Finally, I would like to express my deepest gratitude to my mother for her never ending love and encouragement.

Contents

CHAPTER 4
EQUIVALENT DIPOLE MODEL BASED ON GENETIC ALGORITHMS..................... 144

CHAPTER 5
EQUIVALENT DIPOLE MODELLING IN CLOSED ENVIRONMENTS 175

CHAPTER 6
CONCLUSIONS AND FUTURE WORK 203

Acronyms

CEM	Computational Electromagnetics
DDC	Dipole-Dielectric-Conducting plane
DUT	Device Under Test
E field	Electric field
EMC	Electromagnetic Compatibility
EMI	Electromagnetic Interference
FDTD	Finite Difference Time Domain
FEM	Finite Element Method
GA	Genetic Algorithm
GCV	Generalized Cross Validation
GPIB	General Purpose Interface Bus
GTEM	Gigahertz TEM cell
PCB	Printed Circuit Board
HF	High Frequency
H field	Magnetic field
IC	Integrated Circuit
MoM	Method of Moment
MSE	Mean Squared Error
OATS	Open Area Test Site
PEC	Perfectly Electrically Conducting
PEEC	Partial Element Equivalent Circuit
RF	Radio Frequency
SA	Spectrum Analyzer
TDR	Time Domain Reflectometer
TEM	Transverse Electromagnetic Mode
TLM	Transmission Line Matrix
UTD	Uniform Theory of Diffraction
VNA	Vector Network Analyzer

List of Figures

Chapter 1

Chapter 2

Chapter 3

Chapter 4

Chapter 5

Chapter 6

Appendices

List of Tables

Chapter 1

Chapter 2

Chapter 3

Chapter 4

Chapter 5

Appendix A

CHAPTER ONE

INTRODUCTION

1.1 Background

Significant advances have been made in recent years in developing circuits driven by fast clocks thus increasing dramatically processing speeds. Industry has now passed another threshold whereby clock rates of a few GHz are available in the market. Considering even a few harmonics of the clock rate, this takes designs well into the microwave region. In the microwave region printed circuit boards (PCBs) have dimensions of the order of several wavelengths and become efficient radiators of electromagnetic energy. Electromagnetic field driven issues make circuit geometry as well as network connectivity important for PCBs which are electrically large (compared to wavelength). The increase in clock speed in combination with the driving down of device switching voltage levels is making emissions and susceptibility critical issues in modern systems. This has gained significant attentions in the electronic industry. For example, the European Standard EN-55022 specified the limits of electromagnetic emissions of information technology equipment [1]. Another product standard EN-55011 specified the limits for industrial, scientific and medical radio frequency equipment [2]. Therefore it is becoming critically important to include electromagnetic compatibility (EMC) very early in the design phase of high speed systems.

EMC is primarily concerned with the emission of electromagnetic fields from devices and the susceptibility of a device to an external electromagnetic field [3]. It is of course possible, through detailed 3D electromagnetic simulation, to accurately reproduce the electromagnetic fields around a PCB. But this requires unrealistically large computing power and excessive simulation run times, as modern PCBs are becoming increasingly more complex. Circuit solvers alone can not account fully for the complexity of propagation of fast transients in PCBs. Full field-based tools, although accurate and well developed for the solution of microwave circuits, cannot deal efficiently with the complexity of modern designs. In addition, EMC issues are frequently concerned with harmonic frequencies outside the operating frequency and beyond the range for which device characteristics are accurately quantified. The complexity of modern systems would also make it difficult for design engineers to evaluate the results. Moreover, electronics manufacturers sometimes wish to perform EMC tests of their circuits without revealing the confidential designs. For these reasons, the provision of efficient CAD analysis tools and concepts to help in the interpretation and quantification of the EMC of one or more PCBs in their operating environment would be a timely addition to modern advanced engineering design.

It is the objective of this work to simplify the problem of electromagnetic emissions from PCBs as much as possible and to provide design engineers with a simple coherent measure of the performance of a PCB. This means the formulation of simple and general emission equivalents of complex PCBs, which can easily be incorporated into full-field electromagnetic models for the purpose of assessing EMC of PCBs either in free space or in their operating environment (e.g. inside a conducting cabinet with apertures). The basic idea behind the work is to develop and evaluate a technique where the electromagnetic emissions and coupling of a PCB are characterized by an array of infinitesimal electric and/or magnetic dipoles as shown in Fig. 1.1, which is referred to as an equivalent dipole model. The fundamental problem is to determine the parameters of the dipoles, including the number, layout, orientation, moment, etc. In this work, the model parameters are extracted from near-field scanning of the PCB.

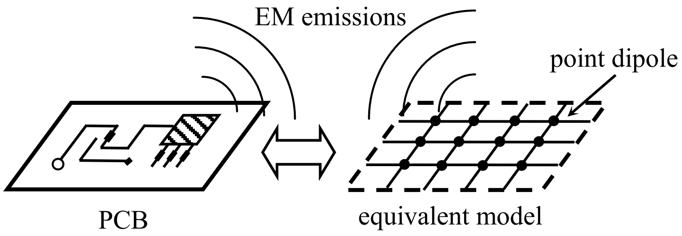

Fig. 1.1 Basic idea of the equivalent dipole model

Near-field based techniques have been widely used in EMC studies because of the high accuracy and reliability [4]. Generally, near-field scanning provides information on electromagnetic fields in the vicinity of integrated circuits (ICs) or PCBs resulting from current distributions. With appropriate model extraction and simulation tools near-field scanning can be used to predict radiated electromagnetic emissions. In early work the measured near-field data are directly transformed to the far field using modal expansions [5]-[9]. These techniques are very useful in antenna designs. But the usefulness in modelling PCBs is limited due to the lack of an appropriate representation for the radiating sources. Another important idea is to deduce equivalent sources from the scanning measurements. The radiated fields can then be calculated directly from the equivalent sources. Sarkar first explored this idea and proposed an equivalent magnetic current approach [10] and an equivalent electric current approach [11]. This idea was then followed by some authors and different equivalent modelling techniques have been reported [12]-[18]. These approaches, although successful in deducing the radiated fields from isolated PCBs, do not provide accurate results when the PCB is close to other structures like neighboring PCBs or enclosures [19]. Moreover, in most approaches only the radiated fields in a certain spatial range can be predicted depending on the geometry of the near-field scans. This would make these approaches difficult for system level EMC analysis. One possible reason is that only the characteristics of the radiating elements are extracted from near-field scans, but essential features of PCBs, such as ground planes, diffraction effects, and PCB body dampening the field, are not included. In this research work, an equivalent dipole model which is able to predict the electromagnetic emissions both in the whole free space and in closed environments is presented.

The outcome of this research work includes both modelling and measurement techniques. On the modelling side, a simple and efficient emission model is presented, which can be "plugged" into standard electromagnetic field solvers to rapidly prototype a system design for emission and internal electromagnetic field strengths. This also means that realistic problems can be tackled at a reasonable computational cost. On the measurement side, a near-field scanning system is built and its corresponding measurement methodology is established. It is a useful addition to the experimental facilities of an EMC laboratory which can be used for EMC measurements and product tests.

This chapter is focused on the fundamental theory and literature review of characterization of PCB emissions. In Section 1.2, generic characteristics of a radiating system are briefly discussed. Then the theory of electromagnetic emissions of PCBs is reviewed in Section 1.3. The widely used measurement and modelling techniques for characterizing PCB emissions are reviewed in Section 1.4 and Section 1.5. Then in Section 1.6 and Section 1.7 near-field measurement and near-field based modelling algorithms are reviewed in detail. Finally in Section 1.8 the research work presented in this thesis is outlined.

1.2 Radiating Systems

Electromagnetic emissions are produced by time varying currents and voltages. Before the investigation of PCBs, it is necessary to discuss the generic characteristics of electromagnetic emissions from a radiating system. Here is considered the simplest radiating system – an elementary current (point dipole).

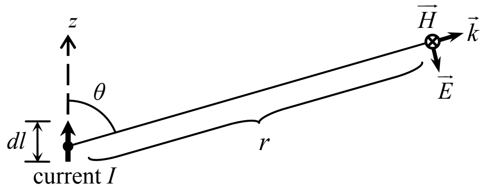

Fig. 1.2 A z-directed electric point dipole

For a *z*-directed electric point dipole located with current *I* and length *dl* at the origin of the coordinate system, as shown in Fig. 1.2, the vector potential can be expressed as [20, Chapter 3]:

$$\vec{A}\left(\vec{r}\right)=\frac{\mu_0}{4\pi}\int_V \frac{\vec{J}\left(\vec{r}\,'\right)e^{-jk\left|\vec{r}-\vec{r}\,'\right|}}{\left|\vec{r}-\vec{r}\,'\right|}dV=\frac{\mu_0 Idl}{4\pi}\frac{e^{-jkr}}{r}\vec{z_0} \tag{1.1}$$

where *k* is the free space wave number $k=2\pi/\lambda$, λ is the wavelength, $\vec{r}$ and *r* are the vector and scalar distance from the radiator.

From $\vec{H}=\frac{1}{\mu_0}\nabla\times\vec{A}$ and $\vec{E}=\frac{1}{j\omega\varepsilon_0}\nabla\times\vec{H}$, each component of the electromagnetic field can be obtained in spherical coordinates as:

$$
\begin{aligned}
E_\theta &= -Idl\frac{k^2e^{-jkr}}{4\pi}Z_0\sin\theta\left[\frac{1}{jkr}+\frac{1}{(jkr)^2}+\frac{1}{(jkr)^3}\right] \\
E_r &= -Idl\frac{k^2e^{-jkr}}{4\pi}Z_0 2\cos\theta\left[\frac{1}{(jkr)^2}+\frac{1}{(jkr)^3}\right] \\
H_\varphi &= -Idl\frac{k^2e^{-jkr}}{4\pi}\sin\theta\left[\frac{1}{jkr}+\frac{1}{(jkr)^2}\right] \\
E_\varphi &= H_r = H_\theta = 0
\end{aligned}
\tag{1.2}
$$

where $Z_0 = \sqrt{\mu_0 / \varepsilon_0} \approx 377\Omega$ is the free space wave impedance.

It can be seen that the radiated field changes with the distance from the source. Considering an actual radiator with the largest dimension *D*, it is commonly defined that emissions transit through three regions, namely the reactive near field ($r < 0.62\sqrt{D^3/\lambda}$), radiating near field ($0.62\sqrt{D^3/\lambda} < r < 2D^2/\lambda$) and far field ($r > 2D^2/\lambda$) from the nearest to the farthest [20, Chapter 4], as shown in Fig. 1.3. In fact the boundaries between the regions are only vaguely defined and changes between them are gradual. To enable mathematical simplifying approximations, a rough definition is that the near field is the region within a radius $r \ll \lambda$, while the far field is the region for which $r \gg \lambda$. Difference of electromagnetic fields in the near and far field is related to the energy transport and wave impedance.

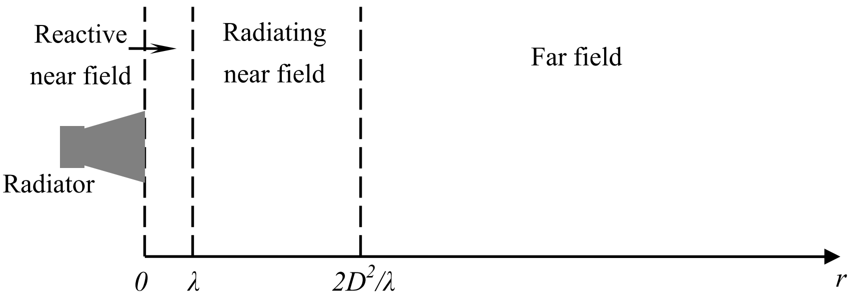

Fig. 1.3 Definition of near and far field regions

The power and energy associated with electromagnetic fields can be described by the power density which is defined by the complex Poynting vector. For the infinitesimal electric dipole, the power density is

$$\begin{aligned}\overrightarrow{W} &= \frac{1}{2}\left(\overrightarrow{E}\times\overrightarrow{H}^{*}\right) = \frac{1}{2}\left(\hat{a}_r E_r + \hat{a}_\theta E_\theta\right)\times\left(\hat{a}_\varphi H_\varphi^{*}\right) \\ &= \frac{1}{2}\left(\hat{a}_r E_\theta H_\varphi^{*} - \hat{a}_\theta E_r H_\varphi^{*}\right) \\ &= \hat{a}_r W_r - \hat{a}_\theta W_\theta\end{aligned} \tag{1.3a}$$

whose radial and transverse components W_r and W_θ are given by

$$\begin{aligned}W_r &= \frac{Z_0}{8}\left|\frac{Idl}{\lambda}\right|^2 \frac{\sin^2\theta}{r^2}\left[1 - j\frac{1}{(kr)^3}\right] \\ W_\theta &= jZ_0 \frac{k|Idl|^2\cos\theta\sin\theta}{16\pi^2 r^3}\left[1 + j\frac{1}{(kr)^2}\right]\end{aligned} \tag{1.3b}$$

The power density is a complex number. The real part naturally represents the radiated power, and the imaginary part represents the reactive power stored in the electromagnetic fields. It is clear from (1.3b) that in the near field ($(kr \ll 1)$) the reactive (imaginary) power density is dominant, suggesting that the energy is stored in the near field. However, in the far field ($r \to \infty$) the reactive power diminishes and vanishes. The power density only has a radial component therefore all the energy radiates away. The variation of reactive and radiated power as a function of distance (θ=45°) is shown in Fig. 1.4.

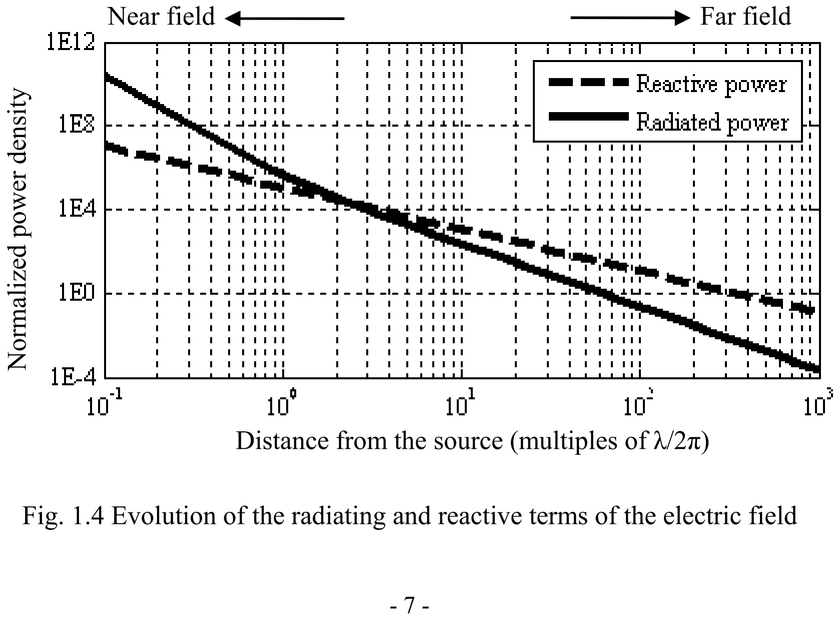

Fig. 1.4 Evolution of the radiating and reactive terms of the electric field

The wave impedance *Z*, which is the ratio of the electric and magnetic field, also depends on the distance from the source. In the far field $\left(r \gg \lambda\right)$ only the radiating term (1/*r* term) of the field is significant so the electric and magnetic field is related by the free space wave impedance as

$$Z\big|_{r\gg\lambda} = \frac{E_\theta}{H_\varphi}\big|_{r\gg\lambda} = Z_0 \tag{1.4}$$

But in the near field, the wave impedance varies widely and depends on the characteristics of the source. For the electric point dipole discussed above, the near-field wave impedance can be expressed as:

$$Z = \frac{E_\theta}{H_\varphi} = Z_0 \frac{1 - j\dfrac{1}{\left(kr\right)^3}}{1 + j\dfrac{1}{\left(kr\right)^2}} \tag{1.5}$$

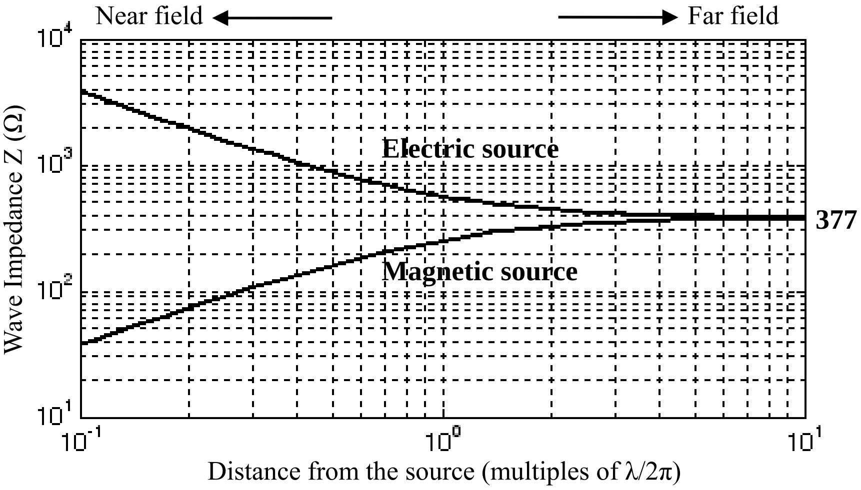

Fig. 1.5 Variation of the wave impedance of an electric source and a magnetic source

Very near to the electric dipole, the wave impedance is very high (when *r*→0, *Z*→∞), showing a predominantly electric field in the near field. But it is the converse situation for a pure magnetic source which produces predominantly magnetic field and displays very low wave impedance in the near field. The variation of the wave impedance of a pure electric and magnetic source as a function of distance is shown in Fig. 1.5. In the near field the characteristics of the source are reflected in the electromagnetic wave properties. But in the far field there is nothing in the field properties to identify the characteristics of its source.

1.3 Electromagnetic Emissions of PCBs

Conducted and radiated emissions

Electric circuits on PCBs, which can produce electromagnetic emissions, are composed of ICs, associated active and passive components, connecting traces, power, control and signal lines as well as I/O ports and attached cables. The emissions are caused by functional activities of active components and by the flow of time varying currents. With regard to EMC, electronic systems have to work in an electromagnetically polluted environment where wires and PCB traces act as receiving antennas and emissions are captured and translated into voltages and currents which are superimposed on intended system signals. Received emissions may cause system failures. Thus emissions from electronic equipment have to be compliant with the limits defined in national and international EMC standards.

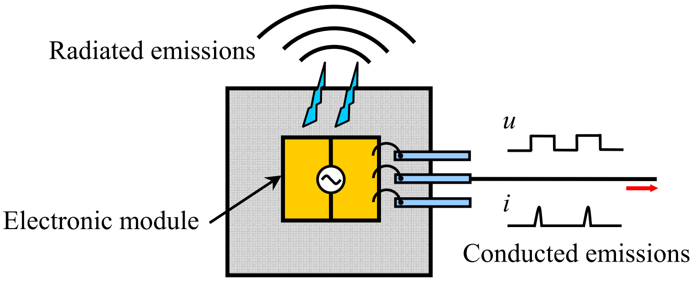

Fig. 1.6 Conducted and radiated emissions of an electronic system

In EMC matters, electromagnetic emissions are divided into two groups – conducted and radiated [21, Chapter 1], as shown in Fig. 1.6. Conducted emissions consist of unwanted signals superimposed on system signals which are described by voltages and currents. Radiated emissions consist of electromagnetic fields surrounding the electronic equipment. Actually the distinction between the two groups of emissions is not clear, since radiated electromagnetic emissions exist in conjunction with voltage and current variations, and vice versa. The conducted and radiated emissions are considered separately because of different measurement methods adopted in evaluating low frequency and high frequency emissions [22]. Low frequency emissions (usually below 30 MHz) are easily evaluated by measuring the voltages and currents while over 30 MHz radiated emissions are normally evaluated by using receiving antennas to measure fields.

Common mode and differential mode

Based on the generation mechanism, electromagnetic emissions are classified in terms of common mode and differential mode [23, Chapter 2]. Examples of the two types of emissions are illustrated in Fig. 1.7(a) and (b). Common-mode emissions are caused by unwanted voltage drops, appearing in the systems with cables and conductors used as the forward path of the signals, and with the reference (ground) plane, which serves as the return path. The voltage drops may be related to the voltage difference between the reference plane (local ground) and module or equipment ground. The attached cables and conductors, working as rod antennas, mostly radiate high frequency common-mode emissions with a dominant electric component. Differential model emissions are generated by current loops inside the circuits on PCBs which have the characteristics of differential-mode signals in the systems with forward and return conductors. The current loop can be considered as a small loop antenna that creates in its close vicinity an electromagnetic field with a dominant magnetic component. The radiated field intensities depend on the frequency and loop area.

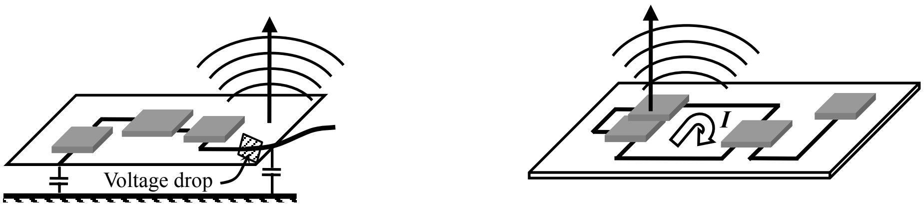

a) Generation of common mode emissions b) Generation of differential mode emissions

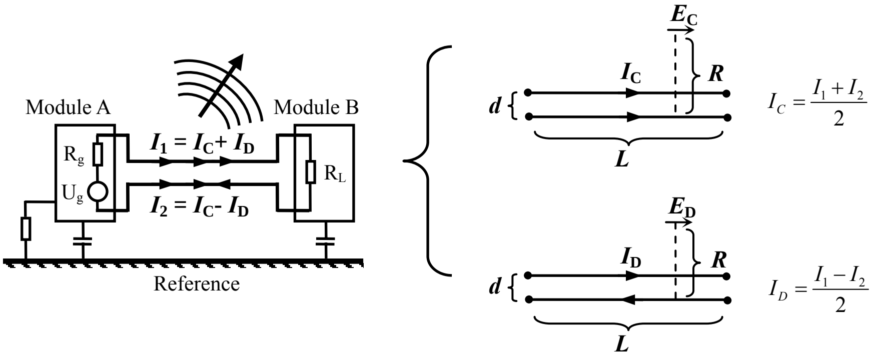

c) Decomposition of total currents into common and differential mode components for estimation

Fig. 1.7 Common and differential mode emissions

C. Paul proposed estimation formulae for the maximum common mode and differential mode emissions [24]. In his approach, the currents I_1 and I_2 on two wires are decomposed into common- and differential-mode current components I_C and I_D, as illustrated in Fig. 1.7(c). By applying Kirchhoff's current law, the maximum electric field intensities are predicted for electrically small current wires. Suppose the wire length is L (cm), wire separation is d (cm), the frequency is f (MHz), and the observation point is R (m) from the first wire, for common mode currents I_C (mA):

$$E_{C_{\max}} = 1.257 \times 10^{-6} \frac{I_C f L}{R} \text{ in V/m} \tag{1.6}$$

For differential mode currents I_D (mA):

$$E_{D_{\max}} = 1.316 \times 10^{-14} \frac{I_D f^2 L d}{R} \text{ in V/m} \tag{1.7}$$

It can be seen that the emissions for differential mode currents vary as the loop area Ld, and as the square of the frequency. The common mode current emissions depend only on the line length *L* and vary directly with frequency. This estimation is widely recognized in PCB designs and, based on this, some empirical design rules are commonly employed for reducing the emissions of PCBs [23]. The most important rules include:

- Avoid using higher voltage or current than necessary.
- Avoid using faster circuit devices than necessary.
- Use short connections at all levels.
- Avoid large HF-current loops by using decoupling capacitors, multiple voltage planes.
- Use proper grounding, shielding and filtering.

These rules provide effective guidelines for design engineers, but cannot give a quantitative evaluation of the EMC performance of a product. Measurement at PCB or system level is necessary to ensure compliance with EMC standards.

1.4 Measurement Methods of PCB Emissions

The measurement of conducted or radiated emissions from PCBs, under controlled conditions, can yield useful information about the potential and severity of RF emissions in an application. In order to ensure consistent test procedures and comparable results, the International Electrotechnical Commission (IEC) proposed as the standard five measurement methods of emission of ICs in the IEC-61967 series standards [25]-[30], and measurement methods of information technology equipment in EN 55022 [1]. In addition, in EN 61000-4 series standards the generic EMC test techniques are proposed, some of which can be applied to PCB emissions, such as the GTEM cell method [31] and reverberation chamber method [32]. These methods are widely approved and used in product tests and designs. Basic characteristics of the methods are summarized in Table 1.1.

TABLE 1.1 Basic characteristics of measurement methods of PCB emissions

Standard & Method	Measurement	Frequency	Speed	Accuracy	Complexity
IEC-61967-2 TEM cell	Radiated emissions	150kHz – 1GHz *	Fast	Medium	Low
IEC-61967-3 Surface scan	Radiated emissions	10MHz – 1GHz **	Slow	High	High
IEC-61967-4 Direct coupling	Conducted CM and DM emissions	150kHz – 1GHz	Medium	Medium	Medium
IEC-61967-5 Faraday cage	Conducted CM emissions	150kHz – 1GHz	Medium	Medium	Medium
IEC-61967-6 Magnetic probe	Conducted CM and DM emissions	150kHz – 1GHz	Medium	Medium	Low
EN-55022 Radiation pattern	Radiated emissions	>30 MHz	Medium	Low	High
EN-61000-4-21 Reverb chamber	Radiated emissions	>LUF ***	Medium	Medium	High

* Extended beyond 1 GHz with a GTEM cell, limited by the GTEM characteristics

** Extended beyond 1 GHz depending on the probe characteristics

*** The lowest usable frequency (LUF) depends on the chamber's characteristics

1.4.1 TEM Cell Method

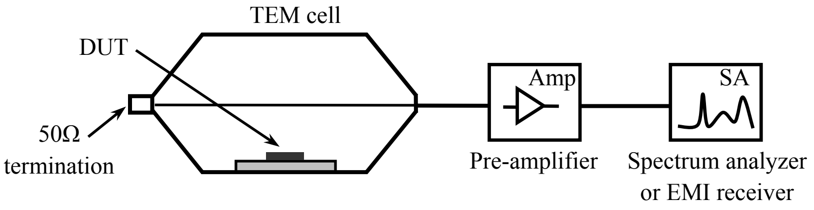

Fig. 1.8 TEM cell method for measuring radiated emissions

The radiation level of a device under test (DUT) can be measured inside a transverse electromagnetic mode (TEM) cell, as shown in Fig. 1.8. The applicable frequency range of a TEM cell is 150 kHz to 1 GHz, and can be extended beyond 1 GHz with a GTEM (Giga Hertz TEM) cell [26], [31]. The DUT is mounted on a test board that is clamped to a mating port cut in the top or bottom of the TEM cell. The DUT faces the interior of the cell while the support circuitry is maintained outside the cell. The RF voltage appearing at the input of the connected spectrum analyzer or receiver is related to the electromagnetic potential of the DUT. The DUT is tested in at least two orientations to capture the total emission.

1.4.2 Surface Scan Method

The radiated electromagnetic emissions of a DUT can be measured by spatially scanning a probe over near-field surfaces (roughly at the distance from radiating source of less than 1/6 of the wavelength [27]). An illustrative test setup is shown in Fig. 1.9. Because of the required precision and the large amount of data, the probe is scanned by a computer-controlled automatic positioning system to achieve accurate and repeatable data. The probe outputs are then converted to a 2D field map showing the field strength distribution. A variety of probes can be used to perform the surface scan including electric field probes, magnetic field probes, and combined electromagnetic field probes. The measurement result of the surface scan method provides not only the electromagnetic fields from the DUT but also the relative strength of the sources. It has been reported that the TEM cell measurement can be predicted from surface scans [33].

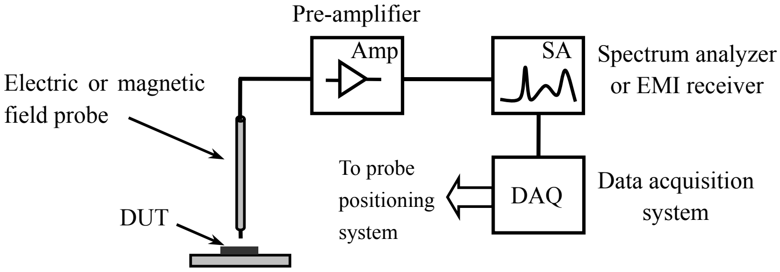

Fig. 1.9 Surface scan method for measuring radiated emissions

1.4.3 Radiation Pattern Measurement Method

The radiation pattern of a DUT can be measured in the far field using a receiving antenna. A typical measurement configuration is shown in Fig. 1.10. The standard test procedure defined in EN-55022 [1] requires that measurement to be performed in an open-area test site (OATS), or alternatively a semi-anechoic chamber. The DUT and the receiving antenna must be separated by 10m, or 3m in case of high ambient noise level. A balanced dipole is used as the receiving antenna below 1 GHz, and a log-periodical antenna or a horn antenna should be used for tests above 1 GHz. The DUT is mounted on a turntable and rotated through 360° to find the maximum emission direction. The receiving antenna is scanned in height from 1 to 4m to find the maximum level. The DUT-to-antenna azimuth and polarization are varied through 360° during the measurement to record the radiation pattern of the DUT.

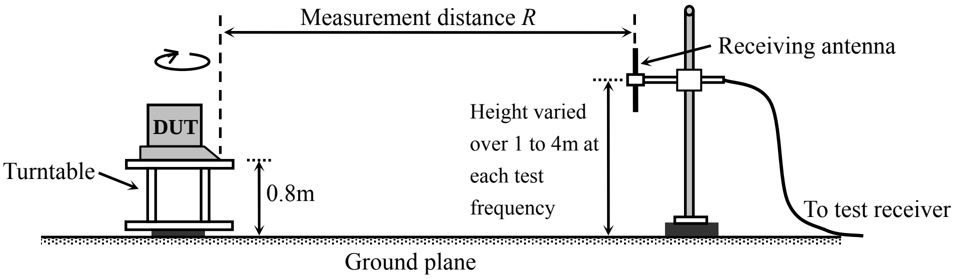

Fig. 1.10 Radiation pattern measurement method for radiated emissions

1.4.4 Reverberation Chamber Method

The emission tests using a reverberation chamber are used to measure the total radiated power of a DUT. A reverberation chamber is an electrically large, highly conductive overmoded enclosed cavity equipped with one or more metallic tuners/stirrers whose dimensions are a significant fraction of the chamber dimensions. The mechanical tuners/stirrers can “stir” the multi-mode field in the chamber to achieve a statistically uniform and statistically isotropic electromagnetic environment.

A typical setup of emission measurement in a reverberation chamber is illustrated in Fig. 1.11 [32]. The DUT should be at least $\lambda/4$ from the chamber walls. The stirrers are rotated very slowly compared to the sweep time of the EMI receiver in order to obtain a sufficient number of samples. Signals at the receiving antenna are recorded to measure either the maximum received power or averaged received power during a cycle period of the stirrers. The recorded signals are then converted to the total radiated power and the free space field strength. The reverberation chamber method is able to measure the total field on all sides of a DUT without multiple test positions and orientations.

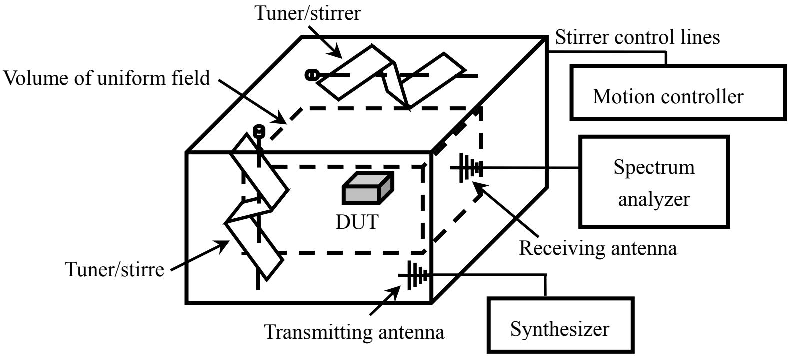

Fig. 1.11 Reverberation chamber method for radiated emissions

1.4.5 Direct Coupling Method

The 1/150Ω direct coupling method is designated to determine the conducted emissions from power and signal ports of a small electronic module especially an IC. RF currents developed across a standardized load is measured to allow indirect estimation of the emission level. A variety of the standardized load configurations is proposed in IEC-61967-4 [28], depending on the type of the supply pins. Fig. 1.12 shows the simplified configuration of the 1Ω method for measuring the sum current in the common ground path. The variable RF component of the current on the supply lines is dominant and reflects the activity of the whole module in respect to the generation of the electromagnetic disturbances. Thus, spectral characteristics of the supply current of the electronic module as well as the selected parameters of its waveform, defined in the time domain, can be easily correlated to the emission level. This method requires that the DUT be mounted on a standard EMC test board.

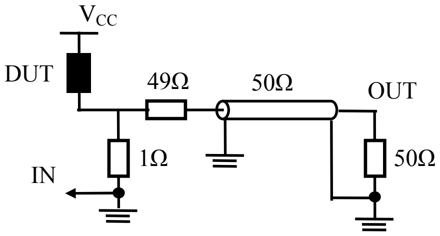

Fig. 1.12 1Ω direct coupling method for measuring conducted emissions

1.4.6 Magnetic Probe Method

The magnetic probe method can be used to indirectly determine the conducted electromagnetic emissions from a port of an electronic module by means of non-contact current measurement [29]. The simplified test setup is shown in Fig. 1.13. A magnetic probe is used to measure the magnetic field associated with a connected PCB trace, and the RF currents inside the circuit are then calculated. The preferred test configuration is with the DUT mounted on a standard EMC test board to maximize repeatability and minimize probe coupling to other circuits.

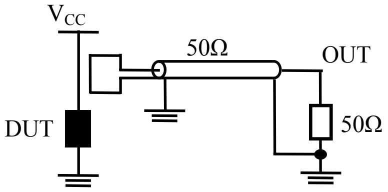

Fig. 1.13 Magnetic probe method for measuring conducted emissions

1.4.7 Workbench Faraday Cage (WBFC) Method

The WBFC method can be used to measure the conducted electromagnetic emissions at defined common-mode points in order to estimate emissions of an electronic module. The simplified test setup is shown in Fig. 1.14. The Faraday cage is typically a metallic box of 500x300x150 mm [30], equipped with adequate connectors, filters and matching elements. The DUT can be mounted on either a standard EMC test board or an application board. With all input, output, and power connections to the test board filtered and connected to common-mode chokes, RF voltage at the selected port is measured across the used common-mode impedance.

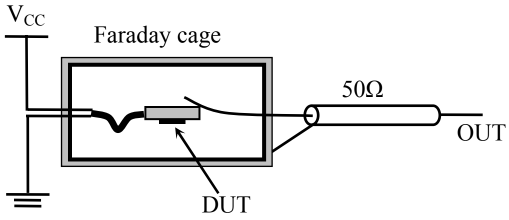

Fig. 1.14 Workbench Faraday cage method for measuring conducted emissions

1.5 Modelling Methods of PCB Emissions

As post-layout modifications of PCB designs are difficult and expensive, it is widely held that the most cost-effective means of complying with limits on emissions and susceptibility is to consider EMC from the earliest stage in the design process. Modelling methods of PCB emissions are therefore useful because they can predict the EMC performance of electronic products early in the design phase.

1.5.1 Full Field Modelling

Full field modelling involves modelling the detailed structure of PCBs by discretizing the space in terms of grid or mesh and solving Maxwell equations in free space, dielectrics, and conductors utilizing numerical methods. In principle, the physical geometry of all the elements, including conductors, dielectrics, excitations, loads, etc, is modelled, taking into consideration material properties and frequency. The models are then solved with computational electromagnetics (CEM) methods. CEM methods have been well established and developed over the past decades for numerically solving the Maxwell equations in integral or differential forms. Popular integral equation solvers [34] include the method of moments (MoM), boundary element method (BEM), and partial element equivalent circuit (PEEC) method. Differential equation solvers [34] include the finite-difference time-domain (FDTD), finite element method (FEM), and transmission line matrix (TLM). Tools to implement CEM methods are available from software vendors, such as MoM based FEKO [35], IE3D [36], and Concept-II [37], FDTD based EMA3D [38], FEM based HFSS [39], TLM based RegSolve [40], and hybrid methods based CST [41]. Effectiveness of full field modelling for a particular problem largely depends on the CEM method employed by the tool. Generally, integral equation solvers are well suited for relatively large, resonant structures. FEM is good at solving relatively complex geometries with many irregularly shaped dielectric regions at low frequencies. The time domain methods FDTD and TLM are usually the best choice for broadband modelling and complex materials.

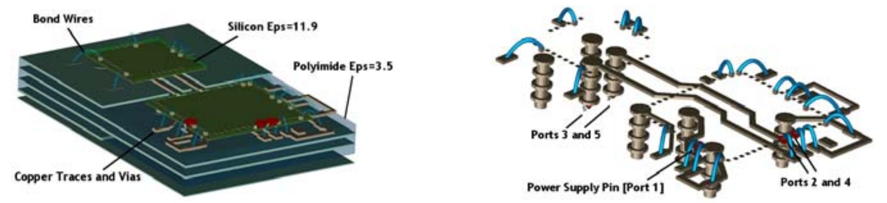

a) Model structure and material properties b) Definition of excitations and loads

Fig. 1.15 Full field model of a multilayer PCB in CST environment [42]

An example of full field modelling taken from CST website [42] is shown in Fig. 1.15 where the detailed structure and material properties are modelled to simulate a multilayer PCB. Full field modelling naturally provides accurate quantitative predictions of electromagnetic emissions. In order to facilitate the modelling, several software vendors have packaged full field modelling software with software that automatically extracts PCB geometry data from automated board layout tools [43]. However, in practice the computer speed and memory required to solve directly any but the simplest systems soon become excessive. Furthermore, the level of detail required for such tools tends not to be known at early stages of the design process.

1.5.2 Design Rule Checking

Design rule checking attempts to distil the experience of an EMC expert into a set of empirical rules. EMC rule checking software reads board layout information from automated board layout tools (such as Allegro, Protel, Board Station, etc.) and checks if certain EMC design guidelines have been adhered to. This method does not usually attempt to predict the quantitative electromagnetic behavior of the system, but instead is intended to give a goodness factor of the design. EMC rule checkers can help board designers to locate potential problems with their designs and they can also help experienced EMC engineers to quickly identify problems that would otherwise be hard to spot. Important PCB design rule checkers include EMIStream [44], EMSAT [45], and Zuken CR-5000 Lightning EMC [46].

A significant advantage of rule checkers is that they do not require the user to have expertise in electromagnetic modelling. However, the rules, whilst improving EMC, do not allow any quantitative prediction of the improvement to be obtained. Moreover, although many EMC design rules are available in the literature, the rules and their impact on EMC can vary significantly from one design to another.

1.5.3 Intermediate Level Modelling

With intermediate level modelling, EMC is determined by a set of “generic design parameters” which influence the path of unwanted energy into or out of an electronic system [47]. These models generally develop quantitative formulae as a function of the simplest design parameters based on the basic electromagnetic theory. The formulae can be computed in seconds and give a good estimate of PCB emissions. Intermediate level modelling has been successfully applied to address some practical EMC problems of PCBs, including shielding effectiveness [48], PCB emissions through an aperture [49], and coupling effects inside an enclosure [50]. For example [49], in order to estimate the peak emissions of a PCB inside an enclosure, the coupling of PCB to waveguide modes in the enclosure is modelled with transmission line theory, leading to an analytical formula which only depends on the frequency, positions and physical size of the PCB, aperture and enclosure.

Compared to full field modelling, this method is computationally much more efficient. Compared to EMC rule checking, this method is able to give a quantitative estimate, and is usually more accurate because it is based on basic electromagnetic theory. However, every intermediate level model is designated to address a specific problem thus the application range can not be extended until more models dealing with a wider range of problems have been developed.

1.5.4 Equivalent Modelling

In order to implement quantitatively accurate but fast simulations of electromagnetic emissions from PCBs, equivalent modelling methods are developed. The complex structure of PCBs is partly or fully modelled with equivalent representations which are normally computationally simple. Electromagnetic emissions are then obtained by computing from the equivalence. To the author’s knowledge, equivalent modelling can be broadly divided into two categories which are based on analytical methods and measurements, respectively.

In analytical methods based modelling, the complex PCB structure is modelled with relatively simple equivalence based on having identical or similar characteristics as obtained from electromagnetic theory. A range of successful applications have been developed. The frequently used formulae for estimating common-mode and differential-mode radiated emissions (1.6) and (1.7) are based on the analytical fields of an equivalent Hertzian dipole or infinitesimal current element [24]. If the conductor lengths are electrically small in terms of wavelength, this model is a good equivalence. Another interesting example is the modelling of power buses and power planes with cavities modes. This idea has been explored by some authors [51]-[52] and a powerful simulator HISES [53] was developed to implement the models. Techniques of equivalently modelling PCB traces with thin wires [54], modelling substrates with impedance sheets [55], and modelling ground planes with equivalent circuits [56] were also reported. These models, when incorporated into full field solvers, significantly reduce computational costs while retaining good simulation accuracy. However, analytical methods based equivalent modelling still requires knowledge of the circuit structure of PCBs.

In measurement based equivalent methods, the equivalent representation for a PCB is derived from measurement data. Therefore measurements must be performed in advance of modelling, but once the model or sub-model is built it is able to predict the emissions without reference to the detailed PCB structure. Most equivalent models are derived from near-field measurements as the characters of the radiating source are only reflected in the near field. Near field based modelling is the technique used in this thesis, and literature review on this issue will be presented in detail in Section 1.6 and Section 1.7.

1.6 Near-field Measurement

Near-field measurement is a popular technique for characterizing the operation of a device under test (DUT) also its radiated emissions. Generally, the magnitude and/or phase information of the near field over a surface above or surrounding a DUT is obtained from the output of a measuring probe. Sometimes the term “near-field measurement” includes not only the measurement part, but also the associated numerical post-processing methods, especially in antenna studies [4]. For the purpose of clarity, near-field measurement in this research work refers to the measurement part only.

Why near-field measurement?

The electromagnetic emissions can be measured in either a near-field or far-field range with appropriate implementation. Compared to far-field measurement, near-field measurement has advantages in accuracy, reliability, costs and application range [57]. First, the DUT and probe are coupled in close proximity so there are fewer uncertain factors (weather, scattering, electromagnetic interference, etc.) between them. The probe-DUT interactions can be sufficiently considered to provide a more accurate measurement. Second, near-field measurement is less dependent on test conditions, making it a highly feasible technique. It can be conducted in normal lab environments rather than an OATS or an anechoic chamber as required for far-field measurement. Third, according to a survey of Nearfield Systems Inc. [58], a far-field compact range would typically cost 3-4 times more than a planar near-field range capable of testing the same DUT, due to the value of the real estate required (OATS) or the large chamber size required and cost of the compact range reflectors (anechoic chamber). Finally but most importantly, far-field measurement can be regarded as a direct measurement of radiation patterns [59], but is unable to provide information on the radiating source. On the other hand, near-field measurement can be used not only to obtain the electromagnetic fields from a DUT [5]-[9], but also to provide emission tests and source diagnostics in EMC studies of PCBs and ICs [60]-[61]. For example, it was used to estimate the current distribution on a microstrip transmission line of a PCB [16] and to detect and locate the fault in high-frequency chips [62]. The near-field to far-field transformation has also been extensively studied since the plane-wave expansion method with probe correction proposed by Kerns in 1963 [6].

Several successful methods have been developed such as Fast Fourier Transformation (FFT) [7]-[9] and equivalent source methods [10]-[15]. These activities greatly enhance the application and popularity of near-field measurement.

Depending on the applications, near-field measurement can be divided into antenna near-field measurement and EMI/EMC near-field measurement. Antenna near-field measurement focuses on the determination of antenna far-field patterns from the near field. Measurements are performed in the radiating near-field range (typically $3\lambda \sim 5\lambda$) to characterize the radiating energy of the antenna and the fields are then expanded in terms of plane wave to calculate the far field from an FFT transformation. On the other hand, the main focus of the EMI/EMC near-field measurement is on the determination of real or equivalent radiating sources distributed in a DUT. Accordingly, it is performed in the highly reactive region (typically $<\lambda/6$) to enable relative spatial diagnostics of the radiating sources from the mapped pattern of probe signals. The measurement part of this research work is of the category of the EMI/EMC near-field measurement, as the measured data are used to develop equivalent emission models of PCBs.

Setups of near-field measurement

There have been two different near-field measurement setups. The first one uses a planar array of probes terminated with 50 Ω loads [63], and the other uses a single probe controlled by a precise positioning system and scanning over a surface [64], as shown in Fig. 1.16. As in the former case the presence of a large amount of probes induces first order disturbances to the measured field, the second probe setup, specifically named near-field scanning, is more widely used. The typical scanning surfaces can be planar, cylindrical and spherical, as shown in Fig. 1.17. Table 1.2 compares the basic features of the three scanning geometries. Generally, planar near-field scanning is easy to be implemented and its hardware and software requirements are relatively simple, leading to high feasibility and reliability. But the scanned planar fields only represent the DUT's radiation properties in a half space without repeating the measurements. On the other hand, cylindrical and spherical scanning characterizes the radiations in a wider range, but the basic requirements and costs are higher and it is sometimes not easy to operate. For example, rotating a DUT powered by a coaxial cable is difficult and may bring cable induced errors into the measurement.

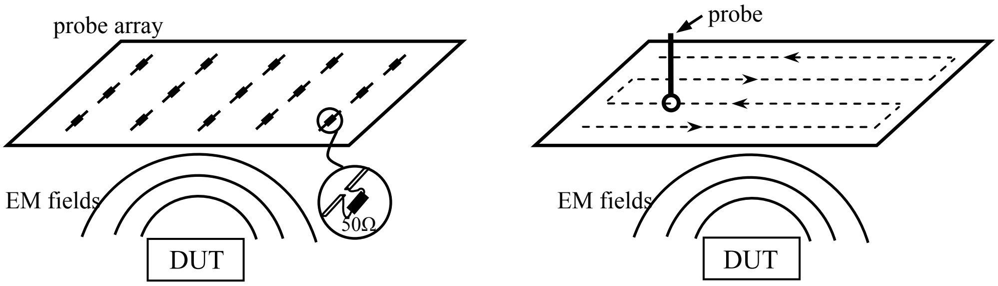

a) measurement with a probe array b) measurement with a single scanning probe

Fig. 1.16 Probe setups in near-field measurement

TABLE 1.2 Comparisons between near-field scanning geometries

Characteristics	Scanning geometry		
	Planar	Cylindrical	Spherical
Moving objects	Probe (scanning)	Probe (scanning) DUT (rotating)	Probe (rotating) DUT (rotating)
Sampling motion control	Easy	Medium	Difficult
Sampling time	Short	Medium	Long
Calibration	Easy	Medium	Difficult
Far field transformation	Easy	Medium	Difficult
Range of represented DUT radiation properties	Half space ($0^o<\theta<90^o$)	Open-ended cylinder	Whole space
Main applicable DUTs	Low-directivity radiators	Sector-beam radiators	Any radiator

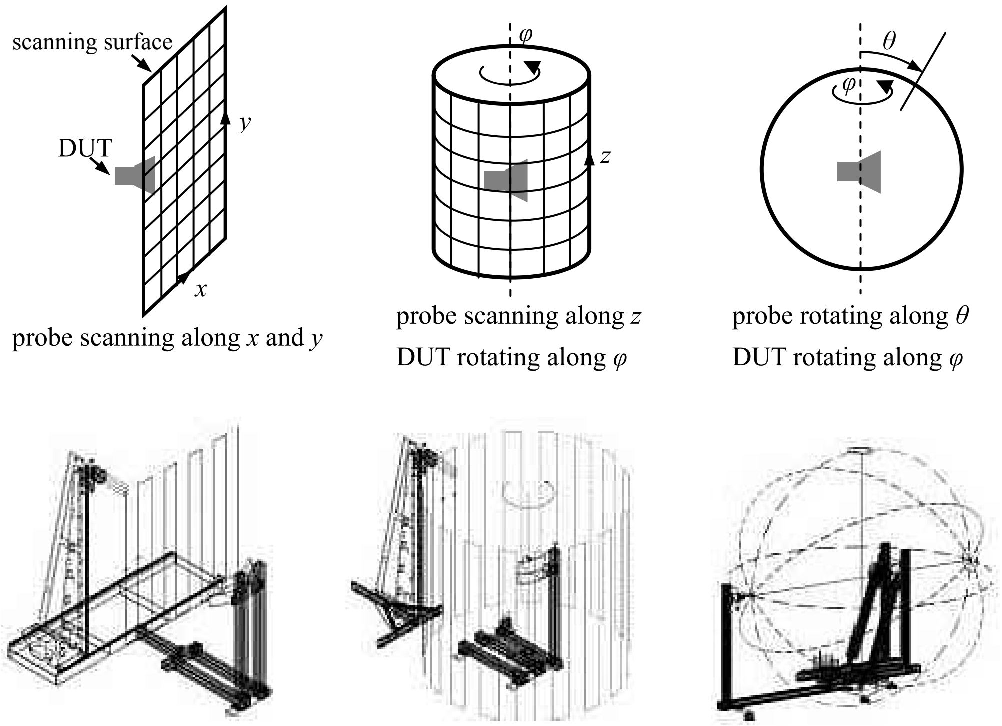

a) Planar b) Cylindrical c) Spherical

Fig. 1.17 Geometry of scanning surfaces: planar, cylindrical and spherical

1st row: schematic of scanning surfaces; 2nd row: typical setups

Important topics in near-field measurement

The choice of probe is a critical factor in near-field scanning as the probe is the direct detector of the field. Based on a lot of practice, open-ended waveguides, loop antennas and monopole antennas [65] are proven to have good performance and have been widely used in appropriate near-field measurements. Fig. 1.18 illustrates the typical configuration and primarily measured field component of these probes.

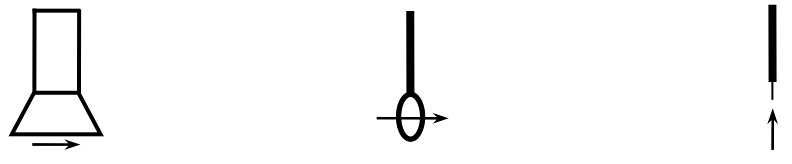

a) Open-ended waveguide
Measuring E-field component parallel to the horn

b) Loop antenna
Measuring H-field component perpendicular to the loop

c) Monopole antenna
Measuring E-field component aligned with the monopole

Fig. 1.18 Commonly used near-field probes

An ideal near-field probe should measure a single component of either the electric or magnetic field at a point, with the output of the probe proportional to the field component. But there are potentially several limiting factors to the measurement of near fields. The first important point is that the probe may respond to more than one field component. The significance of this response depends on the probe's polarization characteristics. Thus the applicable frequency range of a probe must be found and correction to the measured field can be applied if necessary. The second problem is that, in the near field the radiator and the probe are closely coupled and may interact with each other. Thus the measured near field may be disturbed by the presence of the probe [66]. Third, in the near field the ratio of the electric and magnetic field components varies widely and does not in general correspond to that in free space. The second and third problems mentioned above require careful calibrations, and sometimes compensations as well, made to the probe to extract the actual field being measured. Under certain conditions, some probes, such as small balanced loop and termination matched short monopole, have been proven to be very close to the ideal case [67]. However, calibration and compensation of probes are important topics in near-field measurement.

The first rigorous and complete solution to the probe correction problem was Kerns' plane wave analysis for an arbitrary measuring antenna in 1963 [6]. Leach and Paris reported the technique of probe-compensated near-field measurement in terms of plane wave and cylindrical wave expansions by using the Lorentz reciprocity theorem [7]. This technique was then extended to the spherical systems [8]. Later on A. Newell proposed the error analysis techniques for near-field measurement [68]. More recently a probe self-compensation method was described that the correction coefficients of a probe were determined by measuring the probe with an "identical" probe [69]. W. Joseph and L. Martens specifically studied the probe disturbance effects [66]. J. Shi *et. al.* also proposed a probe correction technique based on a plane wave calibration [70]. Based on a lot of experience, in IEC-61967-3 a calibration method is suggested using a reference field from a standardized microstrip line [27].

1.7 Modelling Electromagnetic Emissions Based on Near-field Measurement

Near field measurement provides information on the radiation characteristics of a DUT. Different algorithms of modelling electromagnetic emissions based on near-field measurement have been reported in the literature, which can be broadly divided into direct near-field to far-field transformation and modelling the real or equivalent source.

The earliest works are direct near-field to far-field transformation based on modal expansion methods. The fields radiated by a DUT are expanded in terms of planar (Kerns, 1963 [6]), cylindrical (Leach and Paris, 1973 [7]), or spherical (Wacker, 1975 [8], and Jensen, 1975 [9]) wave functions in order to obtain the far field, and the measured near-field data are used to determine the coefficients of the wave functions. Fig. 1.19(a) shows the modal expansion based on planar near fields. These methods are normally focused on the radiation patterns of antennas, but characterization of the radiating source is not of concern. Accordingly, near-field measurements are usually performed in the radiating near field (3λ~5λ). The main drawback of modal expansion is the assumption of zero fields outside the measurement region thus the far field is only accurate within a particular angular sector depending on the near-field measurement size.

The idea of equivalent magnetic or electric currents for representing the fields was first explored by Sarkar, *et. al.* in the 1990s [10]-[11]. In their method, an aperture antenna is

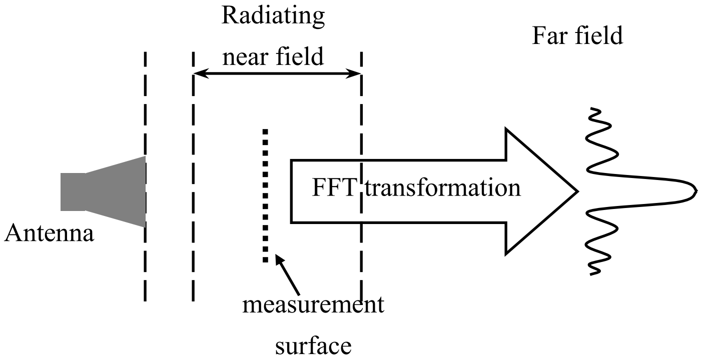

a) Modal expansion method

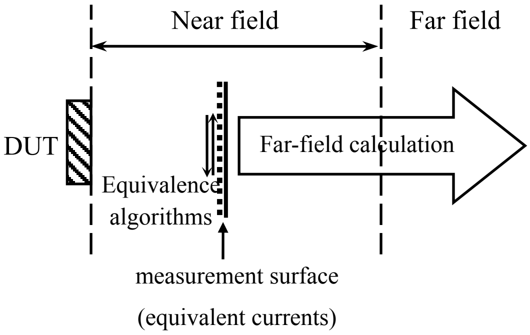

b) Equivalent currents on the scanning surface

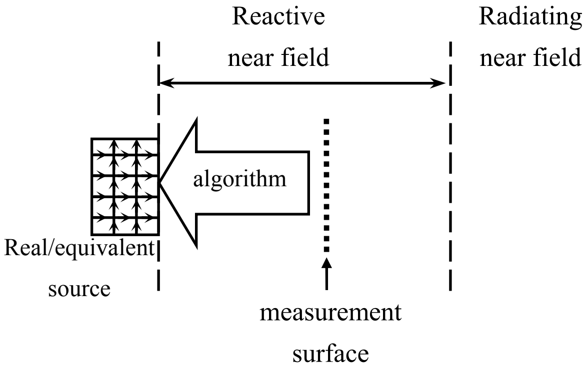

c) Real/equivalent source bound to the DUT

Fig. 1.19 Modelling electromagnetic emissions based on near-field measurement

replaced by equivalent magnetic or electric currents over a fictitious plane on the near-field scanning surface, as illustrated in Fig. 1.19(b). An electric field integral equation is developed to relate the near fields to equivalent currents, and the conjugate gradient method is used to solve the far field. With these methods, the correct far field in front of the antenna can be produced regardless of the geometry of the near-field measurement. However, the equivalent currents are placed in the aperture in front of the antenna so these methods do not apply to emissions in the other half space behind the antenna. In practice sometimes it is necessary to simulate the field in the whole space rather than only in the half space where near-field measurement is taken, especially when considering the interactions between PCBs and an enclosure.

An alternative idea is to identify the real or equivalent sources bound to the actual DUT surface in order to locate the radiating source, as illustrated in Fig. 1.19(c). As the near-field data must fully reflect the characteristics of the source, scans are performed in very close proximity of the DUT (normally in the highly reactive near field). After the real or equivalent sources are identified, the near and far fields can be then calculated either analytically or numerically. Laurin, *et. al.* proposed a method of using a uniform wire-mesh composed of equivalent piecewise sinusoidal dipoles derived from the coupling to the measurement probe. This approach was initially focused on small printed antennas [12] and then extended to high-speed digital PCBs [13]. The uniform theory of diffraction (UTD) was introduced to account for the edge diffractions thus fields in the whole space could be calculated. However, the UTD has a limited application range such that the size of a scatterer must be large relative to the wavelength. In another interesting approach proposed by Reguè, *et. al.* [14], a DUT is equivalently modelled with a number of dipoles surrounding the DUT found from global optimization algorithms. This method accurately predicts the fields from a DUT, but in order to build the models near-field scans must be performed surrounding the DUT. This requires a complex cylindrical or spherical scanning system. A computationally efficient and planar scans based approach was presented by Gilarbet, *et. al.* [15] which worked well for predicting electromagnetic fields up to a few wavelengths. Alternatively, Chen, *et. al.* proposed a method for estimating the real current distribution on a PCB from near-field measurement and FDTD formulae [16]. However, detailed structure and design of the PCB must be known in advance which is normally difficult for confidential reasons. Although most methods require both amplitude and phase information of the near field, modelling using amplitude-only data was studied by Yaccarino, *et. al* [17] and Las-Heras, *et. al.*, [18] based on phase retrieval technique and direct optimization, respectively. But in both methods, very heavy computations are required to avoid local convergence of the algorithms due to the lack of phase information.

The currently available equivalent modelling methods, although successful in deducing the radiated fields from isolated PCBs, do not provide accurate results when the PCB is close to other structures or in closed environments [19]. Moreover, in most methods only the radiated fields in a certain spatial range can be predicted. Therefore the potential to develop a methodology for system level EMC simulations is limited.

1.8 Organization of the Thesis

In this thesis, simplified modelling methods of PCB emission sources using equivalent dipoles are presented. With these models, radiated emissions from PCBs, either in free space or closed environments, can be accurately computed at a reasonable computational cost and without reference to the detailed PCB structure. The equivalent dipoles are derived from near-field scanning. Solution to inverse problems and global optimization by genetic algorithms are used to link the equivalent dipoles and the near fields.

Chapter 2 is focused on the development of a near-field scanning system and measurement methodology. Hardware and software development for the automatic system, including a number of mechanical and electrical components, is described. The measurement methodology of using a vector network analyzer and a spectrum analyzer is presented. For the most important component in the near-field scanning system – near-field probes, the construction, characterization and calibration are presented. Validating measurements and error analysis are presented to demonstrate the reliability of the scanning system to provide near-field information of PCBs.

In Chapter 3, the equivalent modelling method in free space is presented. The fundamental problem is the efficient configuration of the equivalent model to represent the electromagnetic characteristics of general PCBs. In this chapter, the equivalent sources are identified from the solution to inverse problems. It is demonstrated that efficient numerical techniques, namely regularization, are essential for the accuracy and stability of inverse problem solutions. As the equivalent dipoles are derived from near-field scanning, the dependence of the model on scanning parameters is discussed.

In Chapter 4, an alternative source identification method is proposed which searches for equivalent sources using global optimization method based on genetic algorithms. Different schemes are developed to implement the genetic algorithm optimization. With this method, the optimal number and layout of the equivalent dipoles can be determined.

In Chapter 5, the equivalent modelling method is extended to applications in closed environments. To the author’s knowledge, there have been very few reports on equivalent modelling for PCBs inside an enclosure. In order to build the equivalent model, the interactions between PCBs and enclosure are characterized. Based on these results, approximations and extensions are made to the free space equivalent model, and a dipole-dielectric-conducting plane model is developed. This general model is able to predict electromagnetic emissions in both free space and closed environment.

Finally in Chapter 6, conclusions of this research work are presented and possible future research is discussed.

References

[1] *Information technology equipment - Radio disturbance characteristics - Limits and methods of measurement*, EN 55022:2006+A1, 2007.

[2] *Industrial, scientific and medical (ISM) radio-frequency Equipment - Electromagnetic disturbance characteristics - Limits and methods of measurement*, EN 55011:2007, 2007.

[3] C. Christopoulos, *Principles and Techniques of Electromagnetic Compatibility*, 2nd edition, CRC Press, 2007.

[4] A. D. Yaghjian, "An overview of near-field antenna measurement," *IEEE Trans. Antennas Propagat.*, vol. AP-34, no. 1, pp. 30-45, Jan. 1986.

[5] J. Brown and E. V. Jull, "The prediction of aerial radiation patterns for near-field measurements," in *Proc. Inst. Elec. Eng.*, vol. 108B, pp. 635-644, Nov. 1961.

[6] D. M. Kerns, "Analytical techniques for the correction of near-field antenna measurements made with an arbitrary but known measuring antenna," in *Abstracts of URSI-IRE Meeting*, Washington, DC, pp. 6-7, Apr.-May 1963.

[7] W. M. Leach, Jr. and D. T. Paris, "Probe-compensated near-field measurements on a cylinder," *IEEE Trans. Antennas Propagat.*, vol. AP-21, pp. 435-445, July 1973.

[8] P. F. Wacker, "Non-planar near-field measurements: spherical scanning," NBSJR 75-809, Jun. 1975

[9] F. Jensen, “On the probe compensation for near-field measurements on a sphere,” *AEU*, vol. 29, pp. 305-308, Jul.-Aug. 1975.

[10] P. Petre and T. K. Sarkar, “Planar near-field to far-field transformation using an equivalent magnetic current approach,” *IEEE Trans. Antennas Propagat.*, vol. 40, no. 11, pp. 1348-1356, Nov. 1992.

[11] T. K. Sarkar and A. Taaghol, “Near-field to near/far-field transformation for arbitrary near-Field geometry utilizing an equivalent electric current and MoM”, *IEEE Trans. Antennas Propagat.*, vol. 47, no. 3, pp. 566-573, Mar. 1999.

[12] J. J. Laurin, J. F. Zürcher, and F. E. Gardiol, “Near-field diagnostics of small printed antennas using the equivalent magnetic current approach,” *IEEE Trans. Antennas Propagat.*, vol. 49, no. 5, pp. 814-828, May 2001.

[13] P. A. Barrière, J. J. Laurin, and Y. Goussard, “Mapping of equivalent currents on high speed digital PCBs based on near-field measurements”, *IEEE Trans. Electromagn. Compat.*, vol. 51, no. 3, pp. 649-658, Aug. 2009.

[14] J. R. Reguè, M. Ribo, J. M. Garrell, and A. Martin, “A genetic algorithm based method for source identification and far-field radiated emissions prediction from near-field measurements for PCB characterization,” *IEEE Trans. Electromagn. Compat.*, vol. 43, no. 4, pp. 520–530, Nov. 2001.

[15] Y. Vives-Gilabert, C. Arcambal, A. Louis, F. de Daran, P. Eudeline, and B. Mazari, “Modelling magnetic radiations of electronic circuits using near-field scanning method,” *IEEE Trans. Electromagn. Compat.*, vol. 49, no. 2, pp. 391-400, 2007.

[16] Q. Chen, S Kato, and K Sawaya, “Estimation of current distribution on multilayer printed circuit board by near-field measurement”, *IEEE Trans. Electromagn. Compat.*, vol. 50, no. 2, pp. 399-405, May 2008.

[17] R. G. Yaccarino and Y. R. Samii, “Phase-less bi-polar planar near-field measurements and

diagnostics of array antennas," *IEEE Trans. Antennas Propagat.*, vol. 47, pp. 574–583, Mar. 1999.

[18] F. Las-Heras and T. K. Sarkar, "A direct optimization approach for source reconstruction and NF-FF transformation using amplitude-only data," *IEEE Trans. Antennas Propagat.*, vol. 50, no. 4, pp. 500-510, Apr. 2002.

[19] J. Shi, "Near-field measurement and analysis procedures for characterizing electromagnetic interference," Ph.D. dissertation, Dept. Elect. Eng., Univ. Missouri-Rolla, Rolla, MO, 2005.

[20] C. A. Balanis, *Antenna Theory - Analysis and Design*, 3rd edition, New York: Wiley, 2005.

[21] T. Williams, *EMC for Product Designers*, 4th edition, Elsevier, 2007.

[22] *Electromagnetic compatibility - Generic standards - Emission standard for residential, commercial and light-industrial environments*, EN 61000-6-3:2007, 2007.

[23] M. I. Montrose, *EMC and the Printed Circuit Board – Design, Theory, and Layout Made Simple*, New York: IEEE Press, 1998.

[24] C. R. Paul, "A comparison of the contributions of common-mode and differential-mode currents in radiated emissions", *IEEE Trans. Electromagn. Compat.*, vol. 31, no. 2, pp. 189-193, May 1989.

[25] *Integrated circuits - Measurement of electromagnetic emissions, 150 kHz to 1 GHz - Part 1: General conditions and definitions*, IEC 61967-1:2002, 2002.

[26] *Integrated circuits - Measurement of electromagnetic emissions, 150 kHz to 1 GHz - Part 2: Measurement of radiated emissions - TEM cell and wideband TEM cell method*, IEC 61967-2:2005, 205.

[27] *Integrated circuits - Measurement of electromagnetic emissions, 150 kHz to 1 GHz - Part 3: Measurement of radiated emissions - Surface scan method*, IEC 61967-3:2005, 2005.

[28] *Integrated circuits - Measurement of electromagnetic emissions, 150 kHz to 1 GHz - Part 4: Measurement of conducted emissions - 1Ω/150Ω direct coupling method*, IEC 61967-4:2005,

2005.

[29] *Integrated circuits - Measurement of electromagnetic emissions, 150 kHz to 1 GHz - Part 5: Measurement of conducted emissions - Workbench faraday cage method*, IEC 61967-5:2003, 2003.

[30] *Integrated circuits - Measurement of electromagnetic emissions, 150 kHz to 1 GHz - Part 6: Measurement of conducted emissions - Magnetic probe method*, IEC 61967-6:2002+A1:2008, 2008.

[31] *Electromagnetic compatibility - Testing and measurement techniques - Emission and immunity testing in transverse electromagnetic (TEM) waveguides*, EN 61000-4-20:2003, 2003.

[32] *Electromagnetic compatibility - Testing and measurement techniques – Reverberation chamber test methods*, EN 61000-4-21:2003, 2003.

[33] H. Weng, D. G. Beetner, and R. E. DuBroff, “Predicting TEM cell measurements from near field scan data,” in *2006 IEEE International Symposium on EMC*, pp. 560-564, 2006.

[34] T. Hubing, “Survey of numerical electromagnetic modelling techniques,” University of Missouri Rolla, EMC Lab., Report TR91-1-001.3, 1991.

[35] (2010) FEKO homepage. [Online]. Available: http://www.feko.info

[36] (2010) IE3D homepage. [Online]. Available: http://www.zeland.com/ie3d.htm

[37] (2010) Concept - II homepage. [Online]. Available: http://www.tet.tu-harburg.de/concept/index.en.html

[38] (2010) EMA3D homepage. [Online]. Available: http://www.electromagneticapplications.com/software/ema3d.htm

[39] (2010) Ansoft HFSS homepage. [Online]. Available: http://www.ansoft.com/products/hf/hfss/

[40] J. Paul, “A 3D time-domain TLM electromagnetic field solver: the regSolve manual,” GGIEMR, University of Nottingham, 2008.

[41] CST Microwave Studio, CST Computer Simulation Technology, Darmstadt, Germany.

[42] (2010) Transient simulation of a system in package. [online]. Available: http://www.cst.com/Content/Applications/Article/Transient+Simulation+of+a+System-in-Package+(SiP)

[43] D. Edgar, PCB radiated emissions linked with enclosure, Ansoft online tutorial, [Online]. Available: http://www.ansoft.co.uk/emi/pdf/PCBRadiatedEmissionsLinkedWithEnclosure.pdf

[44] (2010) NEC EMIStream homepage. [Online]. Available: http://www.nec-nis.co.jp/emistream/

[45] (2010) EMSAT homepage. [Online]. Available: http://www.mossbayeda.com/emsat.html

[46] (2010) Zuken CR-5000 Lighting EMC homepage. [Online]. Available: http://www.zuken.com/products/cr-5000.aspx

[47] "Intermediate level modelling tools for EMC design", University of Nottingham and York, EPSRC report GR/L-89723 & GR/L-89716, 2000.

[48] M. P. Robinson, T. M. Benson, C. Christopoulos, J. F. Dawson, M. D. Ganley, A. C. Marvin, S. J. Porter, and D. W. P. Thomas, "Analytical formulation for the shielding effectiveness of enclosures with apertures", *IEEE Trans. Electromagn. Compat.*, vol. 40, no. 3, pp. 240-248, Aug. 1998.

[49] J. F Dawson, T. Konefal, C Christopoulos, D. W. P. Thomas, A Denton, A. C. Marvin, S. J. Porter, T. M. Benson, and M. P. Robinson, "Intermediate level tools for emissions and immunity: enclosure contents to aperture coupling," in *IEEE Int. Conf. on EMC, Montreal 2001*, pp. 189-194, 2001.

[50] T. Konefal, J.F. Dawson, A. Denton, T.M. Benson, C. Christopoulos, A.C. Marvin, S.J. Porter, and D.W.P. Thomas, "Electromagnetic coupling between wires inside a rectangular cavity using multiple mode analogous transmission line circuit theory," *IEEE Trans. Electromagn. Compat.*, vol. 43, no. 3, pp. 273-281, Aug. 2001.

[51] M. Leone, "The radiation of a rectangular power-bus structure at multiple cavity-mode resonances," *IEEE Trans. Electromagn. Compat.*, vol. 45, no. 3, pp. 486-492, Aug. 2003.

[52] H. W. Shim, and T. H. Hubing, “A closed-form expression for estimating radiated emissions from the power planes in a populated printed circuit board,” *IEEE Trans. Electromagn. Compat.*, vol. 48, no. 1, pp. 74-81, Feb. 2006.

[53] O. Wada *et. al.*, “High-speed simulation of PCB emission and immunity with frequency-domain IC/LSI source models”, in *Proceedings of the 2003 IEEE International Symposium on Electromagnetic Compatibility*, vol. 1, pp 4-9, 2003.

[54] C. Labarre., P. Petit, F. Costa, and C. Gautier, “Printed circuit board model using the thin-wire method to compute conducted EMI in power electronics systems,” *Eur. Phys. J*, AP 3, pp. 169-I81, Apr. 1998.

[55] A. McCowen and B.G. Salman, “Efficient modelling of finite-size ungrounded PCBs with a full wave 3D moment-method analysis,” *Electronics Letters*, vol. 35, no. 17, pp. 1410-1412, Aug. 1999.

[56] K.J. Scott, “An equivalent circuit model for arbitrarily-shaped metallization areas on printed circuit boards”, in *Proc. 7th IEE Int. Conf. on EMC*, York, pp. 42-49, 1990.

[57] D. Slater, *Near-Field Antenna Measurements*. Norwood, MA: Artech House, 1991.

[58] A comparison of near-field and far-field measurement systems (NSI near-field vs far-field). Nearfield Systems Inc. technical report.

[59] C. A. Balanis, *Antenna Theory: Analysis and Design*. New York: Wiley, 2005.

[60] D. W. P. Thomas, K. Biwojno, X. Tong, A. Nothofer, P. Sewell, and C. Christopoulos, “Measurement and simulation of the near-field emissions from microstrip lines,” in *Proc. EMC Europe* 2008, pp 1-6, Sep. 2008.

[61] K. Sugawara, C. P. Chen, Z. Ma, T. Anada, and D. W. P. Thomas, “Non-contacting electric and magnetic field probe for measuring EM fields on microwave planar circuits,” in *Proc. Asia-Pacific Microwave Conference* 2007, pp 1441-1444.

[62] A. Tankielun, U. Keller, E. Sicard, P. Kralicek, and B. Vrignon, “Electromagnetic near-field

scanning for microelectronic test chip investigation," *IEEE EMC Society Newsletter*, Oct. 2006.

[63] P. Petre and T. Sakar, "Planar near-field to far-field transformation using an array of dipole probes," *IEEE Trans. Antennas Propagat.*, vol. 42 , no. 4, pp. 1348-1356, Apr. 1994.

[64] D. Baudry, C. Arcambal, A. Louis, B. Mazari, and P. Eudeline, "Applications of the Near-Field Techniques in EMC Investigations," *IEEE Trans. Electromagn. Compat.*, vol. 49, no. 3, pp. 485-493, Aug. 2007.

[65] *IEEE standard methods for measuring electromagnetic field strength of sinusoidal continuous waves, 30 Hz to 30 GHz*, IEEE Std. 291-1, 1991, IEEE New York, 1991.

[66] W. Joseph and L. Martens, "The influence of the measurement probe on the evaluation of electromagnetic fields," *IEEE Trans. Electromagn. Compat.*, vol. 43, no. 2, pp. 339-349, May 2003.

[67] M. Kanda, "Standard probes for electromagnetic field measurements," *IEEE Trans. Antennas Propagat.*, vol. AP-41, no. 10, pp. 1349-1364, Oct. 1993.

[68] A. Newell, "Error analysis techniques for planar near-field measurements," *IEEE Trans. Antennas Propagat.*, vol. AP-36, no. 6, pp. 754-768, Jun. 1988.

[69] G. Masters, "Probe-correction coefficient derived from near-field measurements," in *Proc. Antenna Measurement Techniques Association Conference* 1991, pp. 1-8, Oct. 1991.

[70] J. Shi, M. Cracraft, K. Slattery, M. Yamuguchi, and R. DuBroff, "Calibration and compensation of near-field scan measurements," *IEEE Trans. Electromagn. Compat.*, vol. 47, no. 3, pp. 642-650, Aug. 2005.

CHAPTER TWO

Near-field Measurement

2.1 Introduction

Near-field measurement is a popular technique for characterizing radiated emissions from a device under test (DUT). Generally the magnitude and/or phase information of the near field over a surface above or surrounding a DUT is obtained from the output of a measuring probe. Sometimes the term “near-field measurement” includes not only the measurement part, but also the associated numerical post-processing methods, especially in antenna studies [1], [2]. For the purpose of clarity, near-field measurement in this research work refers to the measurement part only.

Collecting near-field information is the first step in this research work for characterizing the electromagnetic emissions from printed circuit boards (PCBs). The objective of the measurement part is to develop and validate a reliable near-field scanning system. The reliability of the experimental characterization also affects the accuracy of the emission models built from near-field data. As PCBs are the main DUTs which are relatively thin and can be regarded as a two-dimensional structure, a planar scanning system is developed so that scans can be performed in planes parallel to the PCB. These planes cover the effective radiating area in close proximity of a PCB therefore sufficient information of the radiation properties can be collected from the scans.

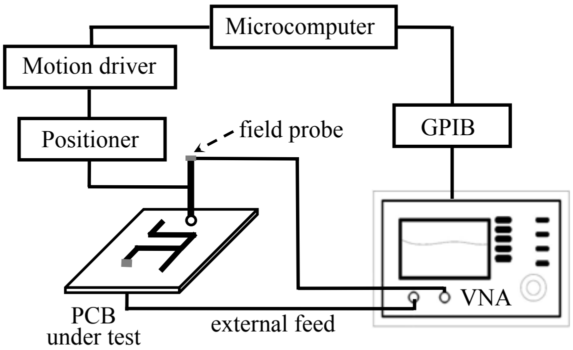

a) schematic of the system

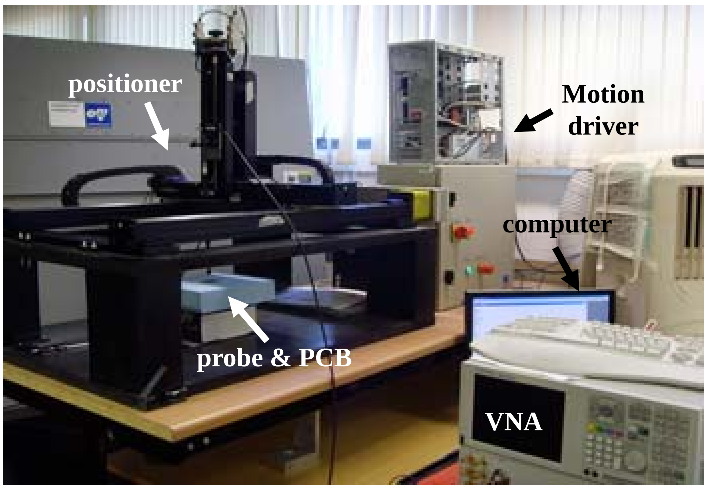

b) hardware implementation

Fig. 2.1 Near-field scanning system using a VNA

TABLE 2.1 Basic specifications of the scanning system

Scanning volume			Best scanning resolution	Maximum load capacity
Horizontal 1	Horizontal 2	Vertical		
900 mm	700 mm	300 mm	10μm	30 lb

The schematic and the photograph of the near-field scanning system developed in this work at the George Green Institute for Electromagnetic Research (GGIEMR) are shown in Fig. 2.1(a) and (b). The basic specifications of the system are listed in TABLE 2.1. The system consists of a positioning subsystem, near-field probes, measurement equipment, a controlling computer and interconnection devices. In the positioning subsystem three programmable motors precisely drive a load carriage moving along three slides in *x*, *y*, and *z* directions in order to locate the loaded object. The near-field probe is loaded on the 3D positioner and scans over a measurement plane. The measurement equipment, typically a vector network analyzer (VNA) or a spectrum analyzer (SA) for frequency domain measurements, is used to measure the probe output for both magnitude and phase information. Automatic scanning software was developed to control the *xyz*-positioner through a motion driver to move the probe step by step on the scan surface in the near field of the PCB. It also controls the sampling and data acquisition at each scanning step through a GPIB (General Purpose Interface Bus) interface connected to the measurement equipment. The near-field data are automatically pre-processed and stored in an Excel file. In the following sections of this chapter, the development of each component of the near-field scanning system is presented, as well as the validation of the system.

For the measurement equipment, the VNA and SA based measurement methodology of obtaining both magnitude and phase information of the probe output is presented in Section 2.2.

For the positioning subsystem, the mechanical hardware components, including programmable motors, stepper drives, slides and load carriages, were commercially bought and then assembled and wired at GGIEMR. The specifications of the mechanical components are detailed in Appendix A. The controlling software for the positioning system was developed at GGIEMR as a part of this work, including positioning, sampling and automation as well as the inter-connection and inter-communication with other components in the whole system. This will be discussed in Section 2.3.

For the near-field probes, both commercial probes and handmade probes were used in this work. The construction of near-field probes is discussed in Section 2.4, and characterization of the probe performance is investigated in Section 2.5. Based on the characterization results of the probes, calibration methods of near-field measurements, which are used to covert the direct probe outputs to absolute field values, are presented in Section 2.6

The near-field results of a test board and a practical PCB measured on the system are presented in Section 2.7 for validating the system performance. Finally errors associated with the measurement are discussed in Section 2.8.

2.2 Measurement Equipment and Methodology

2.2.1 Measurement with a Vector Network Analyzer

Both magnitude and phase are to be measured from the output of near-field probes. As the VNA (HP E8362B in this system) is able to directly measure the ratio of two complex signals in both magnitude and phase, it is chosen to be the primary measurement equipment. For PCBs powered by external RF signals, port 1 of the VNA acts as the feeding source and is connected to the RF input of the PCB. The radiated field is measured by a movable near-field probe on the scanning plane. The received signal from the probe is fed to port 2 of the VNA, where it is recorded as an S_{21} measurement. After a calibration to remove the cable effects, the S_{21} measurement represents the ratio of the signal received by the probe V_o (induced by the radiated field) and the signal injected to the PCB V_i.

$$S_{21} = \frac{V_o}{V_i} \tag{2.1}$$

The S_{21} measurement is a complex number containing both magnitude and phase information. Thus, once the near-field probe is calibrated, the absolute field can be calculated from the S_{21} measurement.

For most practical PCBs which are self-powered, an appropriate reference is needed to obtain the phase information. Based on the VNA, a dual probe measurement is developed with the VNA working in the external source mode, as shown in Fig. 2.2. The internal source of the VNA is disabled, and the source – receiver – reference jumpers are removed from the front panel to cut off the internal relationship of the signals, as shown in Fig. 2.3. This allows the VNA to read the absolute value of signals fed to each receiver, as well as to compare the ratio between them. Then a measuring probe moves in the scanning plane and the output V_o is fed to receiver A, while the reference probe is kept fixed and the signal V_{ref} is fed to receiver R1. Thus output A represents the field magnitude and output A/R1 gives the phase information.

$$|A|=|V_o|; \quad \text{Phase}(A/R1)=\text{Phase}(V_o/V_{ref}) \tag{2.2}$$

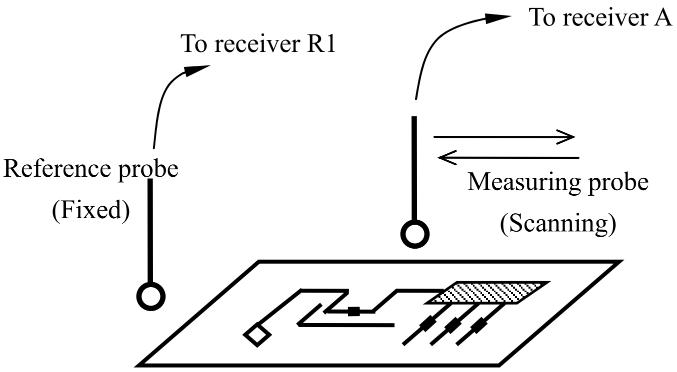

Fig. 2.2 Setup for measuring a self-powered PCB based on a VNA

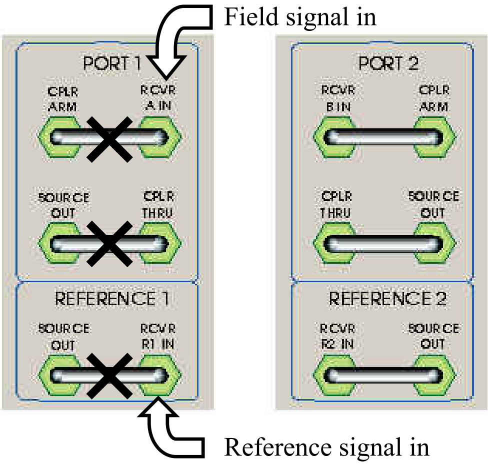

Field signal in

Reference signal in

Fig. 2.3 Front panel settings for external source mode of the VNA

As the input to receiver A and R1 are not the pre-defined measurement signals of the VNA, some requirements for the signals must be met to allow a correct measurement [3]. First, the typical maximum and minimum input levels of the two receivers are 0 dBm and -80 dBm, respectively. Second, to allow a correct phase lock, the amplitude difference between the two signals should be no larger than 30 dB. Therefore theoretically this technique offers a maximum measurable range of 60 dB. The method of using the external source mode of a VNA is the most convenient way to obtain the phase information as phase is directly included in the complex readings. However, it should be noted that not every VNA has an option of external source mode and sometimes the available equipment is for magnitude only. In this case, an alternative method of phase measurement by using a spectrum analyzer and a power combiner was developed.

2.2.2 Measurement with a Spectrum Analyzer

A spectrum analyzer (SA) is a magnitude-only receiver. The measurement of near-field magnitude can be finished simply by feeding the output of the probe to the spectrum analyzer. However, phase information can not be obtained directly. A possible way to obtain the phase information of a signal with a spectrum analyzer is to make use of a power combiner with an output which is the vector combination of two complex signals – the signal being measured and the reference. Fig. 2.4 explains the signal combination of a power combiner, also known as a 0º hybrid coupler.

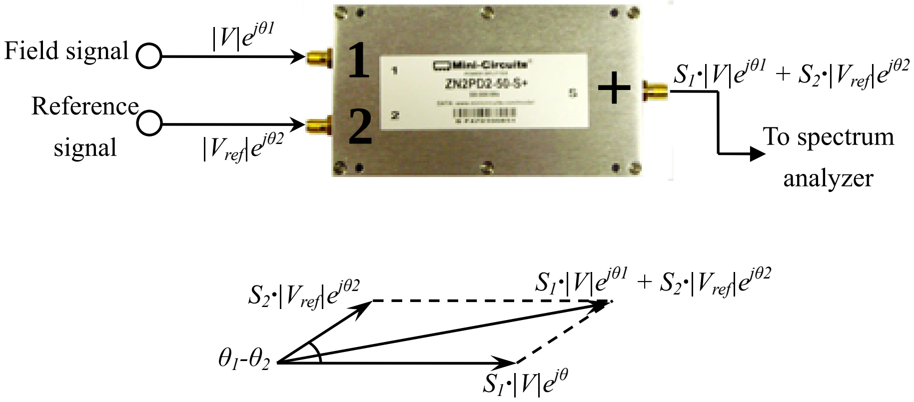

Fig. 2.4 Signal combination of a power combiner (0º hybrid coupler)

With the field signal $|V|e^{j\theta 1}$ and reference signal $|V_{ref}|e^{j\theta 2}$ fed to the input port 1 and 2 respectively, the magnitude of the output can be expressed as:

$$\begin{aligned} |V_{sum}| &= \left|S_1 \cdot |V| e^{j\theta_1} + S_2 \cdot |V_{ref}| e^{j\theta_2}\right| \\ &= \sqrt{|S_1|^2 \cdot |V|^2 + |S_2|^2 \cdot |V_{ref}|^2 + 2|S_1| \cdot |S_2| \cdot |V| \cdot |V_{ref}| \cdot \cos(\theta_1 - \theta_2)} \end{aligned} \tag{2.3}$$

where S_1 and S_2 are the transmission coefficients from port 1 and port 2 to the sum port, respectively. The reference probe is kept fixed so the magnitude of the reference signal $|V_{ref}|$ is a constant and the value can be measured. The quantity to be determined is the phase of the field signal against the reference signal θ_1-θ_2. This is done by performing the scans three times at the same sampling points over the same surface.

In the first scan, the magnitude of the field signal $|V|$ at every sampling point of the scanning surface is measured by feeding the signal directly to the spectrum analyzer.

In the second scan, the field signal $|V|e^{j\theta 1}$ and reference signal $|V_{ref}|e^{j\theta 2}$ are fed to the input port

1 and 2 of the power combiner, and the combined signal $|V_{sum}|$ is recorded with the spectrum analyzer. From (2.3) the following expression for the phase can be derived:

$$\cos(\theta_1-\theta_2)=\frac{|V_{sum}|^2-|S_1|^2\cdot|V|^2-|S_2|^2\cdot|V_{ref}|^2}{2|S_1|\cdot|S_2|\cdot|V|\cdot|V_{ref}|} \tag{2.4}$$

$$|\theta_1-\theta_2|=\arccos\left(\frac{|V_{sum}|^2-|S_1|^2\cdot|V|^2-|S_2|^2\cdot|V_{ref}|^2}{2|S_1|\cdot|S_2|\cdot|V|\cdot|V_{ref}|}\right) \tag{2.5}$$

Although all the quantities on the right hand side of (2.4) have been known or measured, it is impossible to determine the sign of the relative phase θ_1-θ_2 from this formula alone, because the value range of arccosine is only from 0º to 180º. Therefore a third scan is needed to obtain the complete phase information.

In the third scan, a cable with a certain length, acting as a phase shifter, is inserted between the reference probe and port 2 of the power combiner. Port 1 is still fed with the field signal $|V|e^{j\theta 1}$ and the combined signal $|V'_{sum}|$ is measured with the spectrum analyzer. The inserted cable introduces a known phase shift $\Delta\theta$ therefore, similarly to (2.5), the relative phase θ_1-θ_2-$\Delta\theta$ can be derived as

$$|\theta_1-\theta_2-\Delta\theta|=\arccos\left(\frac{|V'_{sum}|^2-|S_1|^2\cdot|V|^2-|S_2|^2\cdot|V_{ref}|^2}{2|S_1|\cdot|S_2|\cdot|V|\cdot|V_{ref}|}\right) \tag{2.6}$$

Finally from (2.5) and (2.6) the phase of the field signal against the reference θ_1-θ_2 can be extracted in the range of [0º, 360º). There is still a 2π ambiguity here as for the VNA method but if the field is expressed in terms of complex numbers, e.g. $H=|H|\cdot e^{j\theta}$, phase information from 0 to 360º is sufficient.

Compared to the measurement method based on a VNA, this alternative method is less convenient as it requires three scans over the same surface. This is not only time-consuming but also increases the possibility of bringing more random errors. However, it is still a reliable technique. Fig. 2.5 compares the results of the same measurement made with the two different methods, showing the amplitude part in mV and phase part in degrees of the direct probe output (the phase is normalized to the same reference). The two methods have a good agreement in terms of both peak magnitude and distribution. The root mean square disagreement is approximately 5.7% for amplitude and 3.8° for phase.

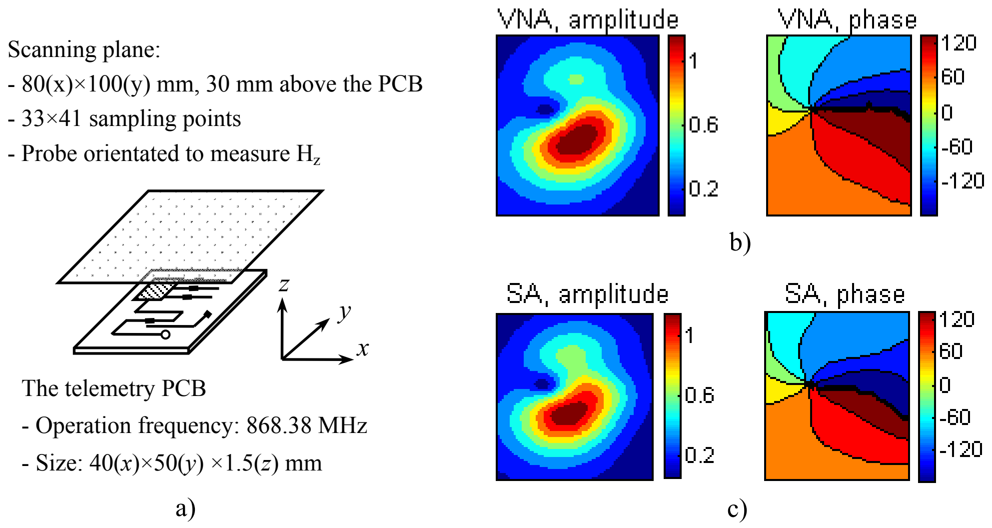

Fig. 2.5 Direct probe output of H field measurements using VNA and SA based methods

a) measurement setup; b) results based on the VNA; c) results based on the SA

2.3 Automatic Motion and Sampling Control

The development of controlling software for the near-field scanning system is discussed here. The fundamental problems are precise motion and sampling control, and system automation.

Near-field scanning is sensitive to the sampling position as the spatial distribution of near fields can have large spatial gradients. Errors caused by imprecise sampling positions have been studied by several authors, and techniques to compensate this error have also been developed in [4], [5], based on matrix equation iteration and Taylor expansion, respectively. However, it is always better to avoid any predictable errors in the measurement phase rather than to correct them in post-processing.

Motion control

The precision of motion depends on the performance of the positioning subsystem (the positioner and its motion algorithms). Roughly speaking, the positioner consists of a carriage arm, three slide tracks, three programmable motors and servo panels. The motors drive the carriage arm, where the probe is mounted, moving along the slide tracks in *x*, *y*, *z* directions. The unloaded motors have a very precise mechanical resolution of 10μm, but this does not mean that the carriage arm has the same resolution because of a number of factors, e.g. mechanical transmission, load capacity. In order to approach the best resolution of 10μm, the point-to-point motion control algorithm [6] of piecewise velocity profile $v(t)$ given by (2.7) is applied for every step movement, which considers the tradeoff between speed and stability.

$$v(t)=\begin{cases} 0.5v_f\left(1-\cos\left(\pi t/T\right)\right), & \left(0<t\le T\right) \\ v_f, & \left(T<t\le T_d\right) \\ 0.5v_f\left(1-\cos\left(\pi\left(t-T_d-T\right)/T\right)\right), & \left(T_d<t\le T_d+T\right) \end{cases} \tag{2.7}$$

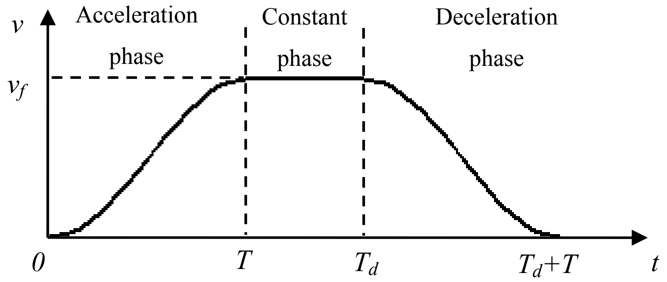

Fig. 2.6 Velocity profile in the motion algorithm

where t is the movement time and v_f is the steady velocity which must be less than the maximum one depending on the load capacity of the motor found from the manufacturer's specifications [7]. In relatively instable phases (acceleration and deceleration), the cosine-like gradual velocity profile is produced as shown in Fig. 2.6. In this system $T=T_d/2$ is used for the non-constant phases. The acceleration/deceleration $a(t)$ and displacement D within a step are then

$$a(t)=\frac{dv(t)}{dt}=\begin{cases}0.5v_f\cdot\sin\left(\pi t/T\right)\cdot\pi/T, & \left(0<t\le T\right)\\ 0, & \left(T<t\le T_d\right)\\ 0.5v_f\cdot\sin\left(\pi\left(t-T_d-T\right)/T\right)\cdot\pi/T, & \left(T_d<t\le T_d+T\right)\end{cases} \tag{2.8a}$$

$$D=\int_0^{T_d+T}v(t)\,dt=v_fT_d \tag{2.8b}$$

D and T_d are user-specified according to the requirements of the scans, and v_f is determined from (2.8b).

The validity of the motion algorithm was tested by continuously moving the carriage arm 1,000 steps with randomly generated displacements and orientations at different steps. With a vernier calliper of a minimum measurable level 0.1 mm, no obvious difference could be detected between the actual and expected accumulated position change. This confirms that the resolution of the whole positioning subsystem is close to the possibly best of 10μm by using the motion control algorithm.

Sampling control

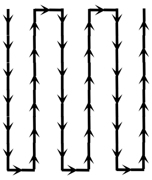

Fig. 2.7 A possible movement route for planar scanning

For planar scanning, the S-shaped route as shown in Fig. 2.7 is the easiest one to implement.

Multiple readings of the receiver are taken at each sampling point to reduce the random error, and the Chauvenet criterion [8] is applied to eliminate the spurious readings and the average is recorded. According to the Chauvenet criterion, in an independently measured data set, x_i is spurious if it satisfies:

$$\left|x_i - \overline{x}\right| > w_n \cdot \sigma \tag{2.9a}$$

where $\overline{x}$ is the average of the data set, w_n is a coefficient depending on the number of data listed in Table 2.2, and σ is the standard deviation of the data set given by

$$\sigma = \sqrt{\frac{\sum_{i=1}^{n}\left(x_i - \overline{x}\right)^2}{n-1}} \tag{2.9b}$$

TABLE 2.2 Chauvenet coefficients

Number of readings N	3	4	5	6	7	8	9	10	15	20	50	100
w_n	1.38	1.54	1.65	1.73	1.80	1.87	1.91	1.96	2.13	2.24	2.57	2.81

System automation

Fig. 2.8 shows the hardware connection of the automatic system and Fig. 2.9 shows the flowchart of scanning steps. A central controlling software was developed (in VC++ environment) to communicate with the positioning subsystem using the serial port protocol via RS232 cables, and the receiving equipment via the GPIB interface. The motion algorithm is encoded to motor-recognizable codes and sent to the servo panel to drive the motors. The servo also returns the feedback information of every motion step, based on which the computer controls the receiver to take readings in every correctly finished motion step. A delay between moving the probe and taking receiver readings is necessary because the receiver always has a finite sweep time. Depending on the number of readings taken at a step, the operation time of one step is normally between 5s and 10s. A 1000-step scan takes approximately 1.4~2.8h. During the long measurement period, the computer triggers an alarm in case of abnormal situations (e.g. incorrect displacement moved, mechanical problems).

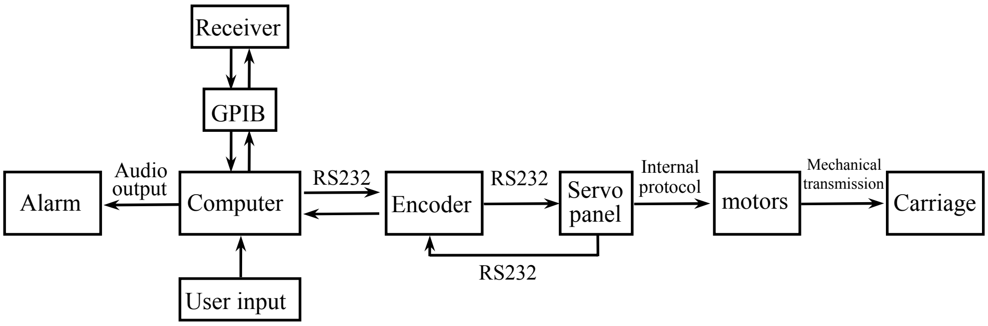

Fig. 2.8 Hardware architecture of the automatic system

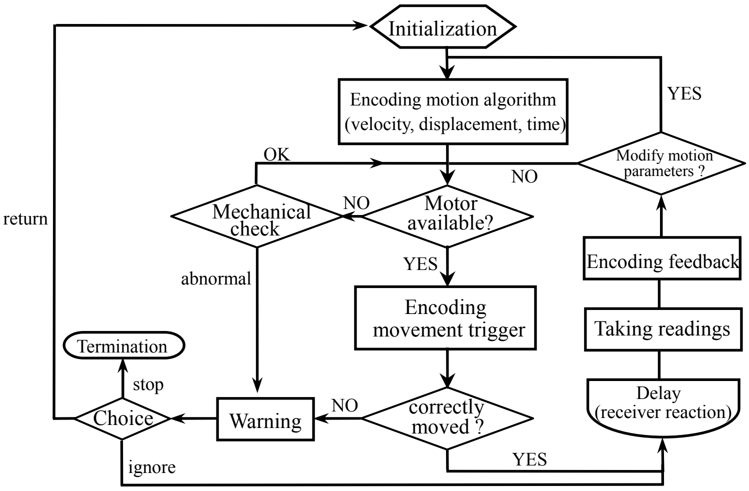

Fig. 2.9 Flowchart of implementing the scanning steps

The controlling software was developed as a part of this work. Fig. 2.10 shows the screenshots of the software during a measurement. Based on this software, near-field scanning on the system at GGIEMR is implemented as the following steps:

a) Search the available receiving equipment in the GPIB network and establish communications with the receiver.

b) Set parameters of the receiver, including frequency span, sweep parameters and port parameters. Then the self-calibration routine of the receiver is performed.

c) Define the parameters of the near-field measurement. Measurements are performed at discrete frequency points.

d) Define the scanning plane by setting the movement route of the probe and sampling rate.

e) Start the scan and monitor the process from the interface.

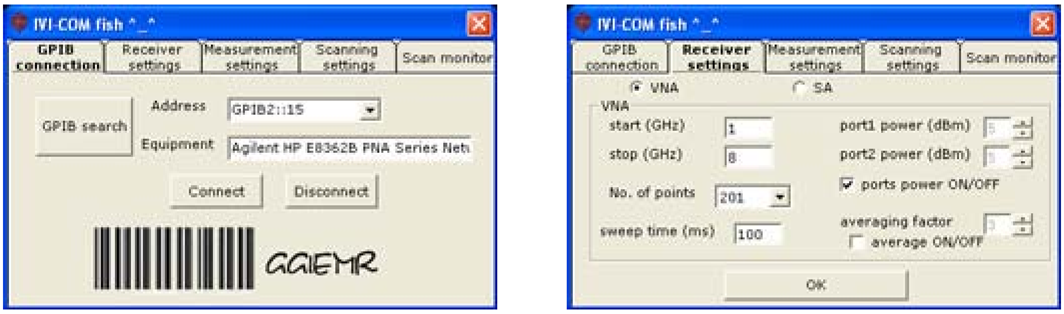

Address GPIB2::15

Equipment Agilent HP E8362B PNA Series Netw

● VNA ○ SA

VNA

start (GHz) 1

stop (GHz) 8

No. of points 201

sweep time (ms) 100

port1 power (dBm) 5

port2 power (dBm) 5

☑ ports power ON/OFF

averaging factor 3

☐ average ON/OFF

a) Search equipment in the GPIB network and establish communication

b) Set all parameters of the VNA or SA required for near-field scanning

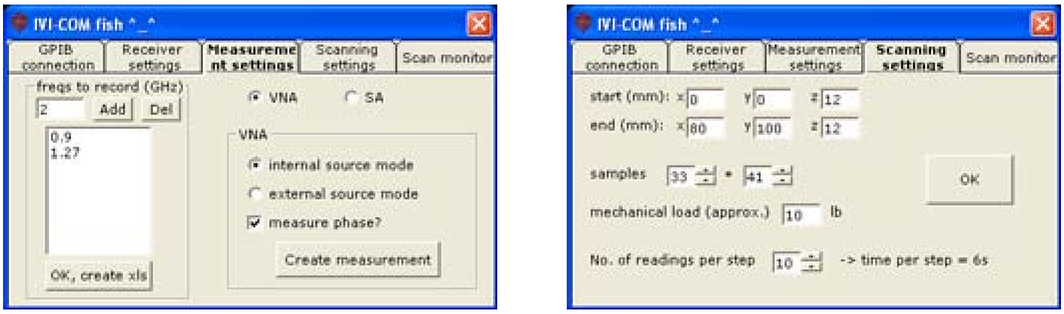

freqs to record (GHz) 2

0.9
1.27

● VNA ○ SA

VNA

● internal source mode

○ external source mode

☑ measure phase?

start (mm): x 0 Y 0 Z 12

end (mm): x 80 Y 100 Z 12

samples 33 * 41

mechanical load (approx.) 10 lb

No. of readings per step 10 -> time per step = 6s

c) Set the measurements to be performed

d) Scanning motion settings

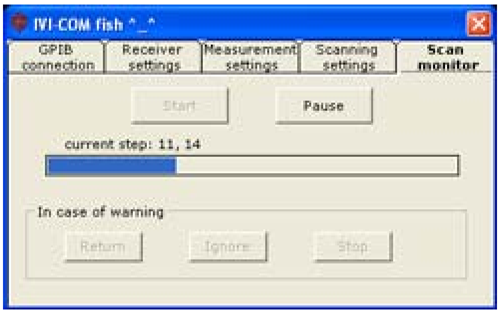

current step: 11, 14

e) Scan monitor interface

Fig. 2.10 Screen shots of the controlling software

2.4 Construction of Near-Field Probes

Near-field probes are the tools for spatially quantifying the emissions from a radiator. They respond in a certain manner to the near fields and can be connected to a VNA or SA for a frequency domain display. An ideal probe should pick only one out of the three orthogonal components of the electric or magnetic field. Small loop construction and rod construction [9]-[11] are normally used for H-field and E-field probes because they have the maximum directivity along a certain axis.

Both H probes and E probes are constructed using semi-rigid coaxial cables as shown in Fig. 2.11. An H probe contains a single turn, shorted loop inside a balanced E-field shield, as shown in Fig. 2.11(a). It is constructed by taking a single piece of a 50Ω, semi-rigid coaxial cable from the connector and turning it into a loop which picks the H field component perpendicular to the loop aperture. When the end of the coaxial cable meets the shaft of the probe, both the inner and outer conductors are soldered to the outer conductor at the shaft. Thus a single, shorted turn is formed. A gap is then cut at the high point of the loop which creates a balanced E-field shield. The three orthogonal H field components, H_x, H_y, and H_z, are measured by rotating the probe to align the loop to the wanted directions.

E probe 1, as shown in Fig. 2.11(b), is designed to measure the vertical component E_z assuming that the EUT is in the horizontal plane (*xy* plane). It is made of a single piece of a 50Ω, semi-rigid coaxial cable with a short inner conductor exposed at the tip which serves as a monopole antenna to pick up E field component along it. As there is no loop structure to carry current, the unit has a high rejection to the H field.

E probe 2, as shown in Fig. 2.11(c), is designed to measure the tangential components E_x and E_y. It is a balanced wire dipole composed of two 50Ω semi-rigid coaxial cables and a 180°

hybrid coupler. The outer conductors of the two cables are soldered together, and identically long inner conductors are exposed and bent by 90º to form a wire dipole. The exposed wire dipole picks up the tangential E-field component, but parasitic responses to the tangential E-field component also take place due to the probe's feed cables. Therefore the outputs of the two cables are fed to the input ports of a 180º hybrid coupler to balance the response of the probe. If the separation of the two wires is much less than the wavelength of the field being measured, the parasitic responses of the two cables can be assumed to be identical. Then the difference signal at the output of the 180º hybrid corresponds to the desired coupling to the tangential E-field component.

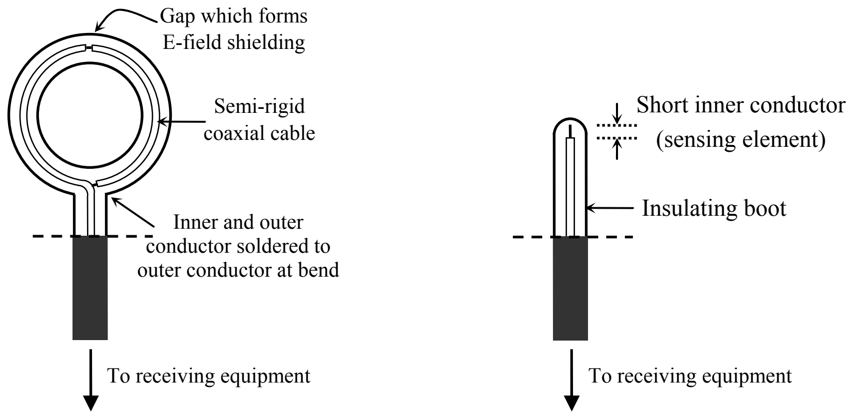

a) H probe with loop structure b) E probe with rod structure

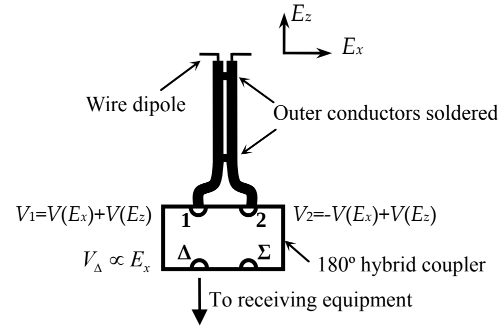

c) E probe with balanced wire dipole

Fig. 2.11 Construction of H and E probes

The built probes are shown in Fig. 2.12 as well as their dimensions.

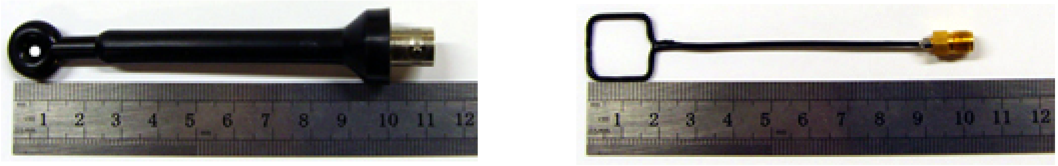

a) H probe 1, circular loop structure

b) H probe 2, square loop structure

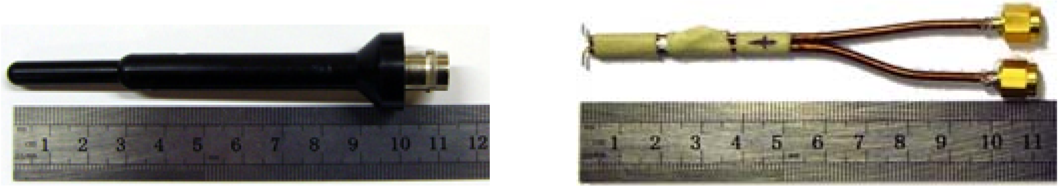

c) E probe 1, rod structure

d) E probe 2, balanced dipole structure

Fig. 2.12 Probes used in the near-field scanning system

2.5 Characterization of Near-Field Probes

For ideal probes, the voltage output V_i has a linear relationship with the field component E_i or H_i being measured at a point. This can be expressed as

$$V_i = C \cdot E_i \quad \text{or} \quad V_i = C \cdot H_i \quad (i = x, y, z) \tag{2.9}$$

where C is defined as the conversion factor. But for practical probes there are potentially several limiting factors. First, practically it is impossible to measure the field at a point but only within a certain integration area. Second, practical probes may respond to more than one field component. Furthermore, the presence of the probe will introduce a disturbance to the original field being measured due to the currents induced on it. Considering that the ratio of E/H in the near field varies widely, the multiple response and disturbance factors are normally not constant.

The following factors are considered to characterize the probes: spatial resolution, sensitivity, H/E rejection and disturbance to the field. The results presented below are for H probe 1 with a circular loop but the characterization methods apply to the E probe as well.

2.5.1 Spatial Resolution and Sensitivity

The spatial resolution corresponds to the limit distance of separation of field variations. The sensitivity corresponds to the level of the received voltage due to a given field. The two parameters are closely related with the dimensions of the probe as the received voltage is proportional to the weighted integration of the field in the effective area of the probe. The spatial resolution and sensitivity of the probes should be considered in the design phase.

To characterize them, simulations were performed on a full field solver Concept-II 9.4 [12] which is based on the Method of Moment (MoM). Essential parts of the probe, including the coaxial cable, termination, gap, and soldering joint, were modelled as shown in Fig. 2.13. The size of each element was determined according to the specifications in Fig. 2.12 (a) except the loop diameter *d* being a variable. The cylindrical coaxial cable was discretized as a hexagonal structure, with an outer conductor, dielectric material and inner wire from outside to inside. At the end of the probe, a 50 Ω terminator was lumped between the inner wire and the outer conductor to simulate the connection to the receiver.

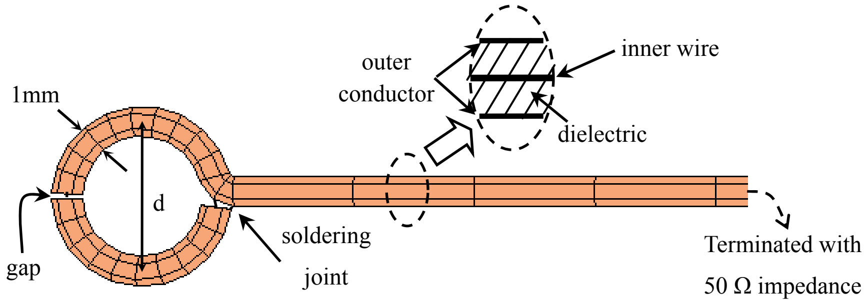

Fig. 2.13 Model of H probe 1

To study the spatial resolution, a special radiating setup was implemented consisting of two z-directed magnetic dipoles separated by 2.5mm. This setup allows a very sharp variation in the near-field H_z along a line vertically above the dipoles. The real field has a local minimum between two peaks. Then the probes with different diameters were modelled to "measure" H_z along this line and the output voltage was recorded. The criterion for good spatial resolution is that the probe must detect the local minimum. The results for probes with a loop diameter 1mm, 5mm, 10mm and 20mm are shown in Fig. 2.14. For the 1mm one, the outer conductor of the loop was not included. The 20mm probe presents a flat response between the two peaks as it is not able to detect the minimum. For the other probes, the local minimum can be detected but the difference between the maximum and minimum decreases with the increase in probe diameters. This shows that the spatial resolution is a descending function of the probe dimension. Moreover, 10mm is almost the largest probe size for an acceptable measurement of the 2.5mm gap, implying that the minimum meaningful resolution of a loop probe should be roughly not smaller than *d*/4.

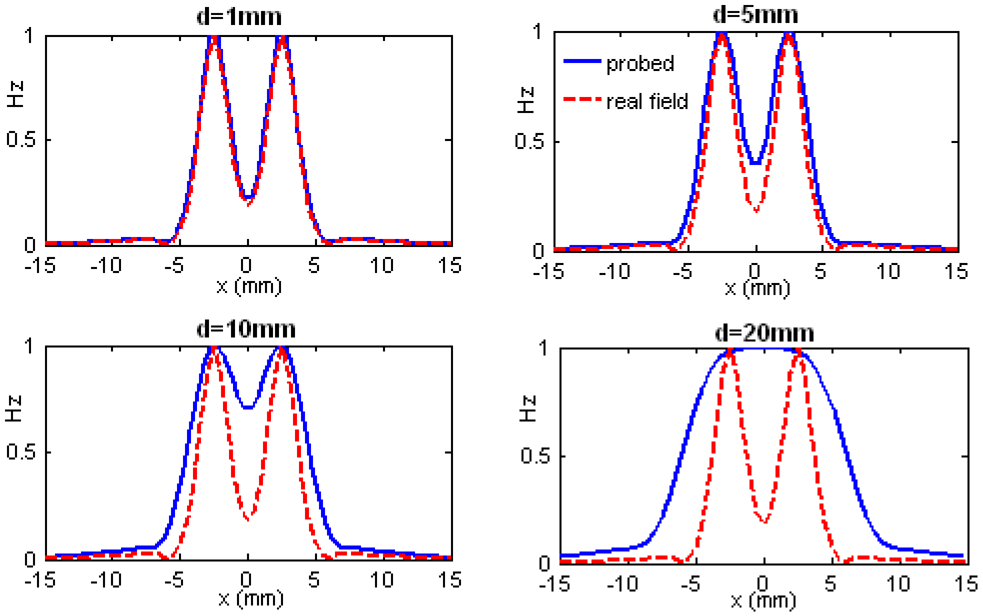

Fig. 2.14 Normalized probe outputs and real field above two magnetic dipoles for different probe diameters

Sensitivity was then studied by illuminating different sized probes with a plane wave. The same H field was incident across the loops and the outputs were recorded and presented in Fig. 2.15. Due to the fact that the probe has a disturbance effect to the field and also secondarily responds to the E field, no analytical expressions can be derived to relate the received voltage and the probe dimension. However, the results show that a rise of the probe dimension greatly enhances the sensitivity. The received power of the 10mm diameter probe is almost 15 dB greater than the 1mm one.

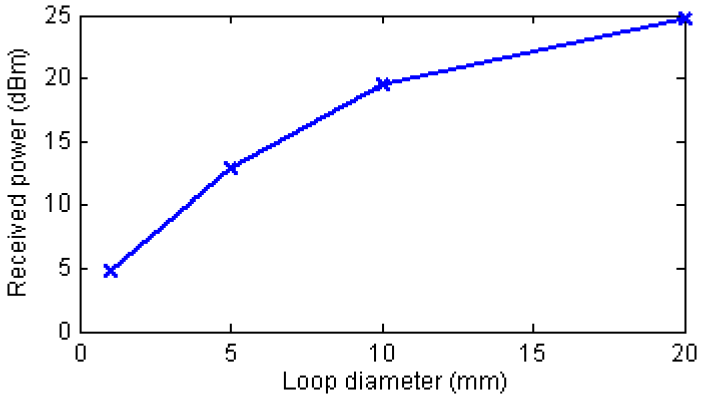

Fig. 2.15 Output of probes with different dimensions illuminated by the same plane wave

The dimension of probes is a trade-off between sensitivity and spatial resolution. The smaller the probe, the more accurately it can locate signals but the less sensitive it will be. In addition, smaller probes generally introduce less distortion to the measured field [13]. Therefore a smaller probe is preferred for EMI measurement as long as the signal level is measurable enough at the receiving equipment. A pre-amplifier can be used to increase the sensitivity of the probe if necessary.

2.5.2 H/E Rejection

Practical H probes may respond to more than one H-field components as well as the E-field components, because the loop structure and the shaft can also behave like an electric monopole. A simulation to study the field selectivity was first carried out by modelling H probe 1 illuminated with a plane wave at 1 GHz, as shown in Fig. 2.16. The polarization angle *θ*, which was the angle between the H component and the loop orientation and also the angle between the E component and the shaft, was a variable from 0º to 90º. The E component and H component of the plane wave could then be expressed as:

$$\begin{aligned} \vec{H} &= H_0 \cos(\theta) e^{-jkz} \overline{a_x} + H_0 \sin(\theta) e^{-jkz} \overline{a_y} \\ \vec{E} &= E_0 \sin(\theta) e^{-jkz} \overline{a_x} + E_0 \cos(\theta) e^{-jkz} \overline{a_y} \end{aligned} \tag{2.10}$$

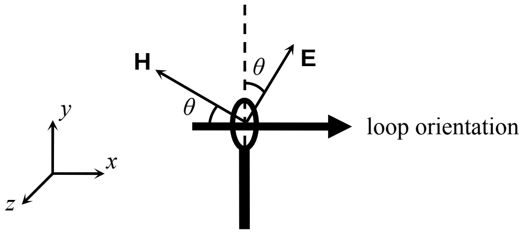

Fig. 2. 16 H probe illuminated with a plane wave with polarization angle *θ*

The normalized probe outputs for different *θ* are plotted in Fig. 2.17 and compared with cos(*θ*). The probe outputs are strongly correlated with the cosine curve. This indicates that small loop probes primarily respond to the H field component perpendicular to the loop aperture and the E field component parallel to the shaft. The response to other field components (H-field components parallel to the loop and E-field components perpendicular to the shaft) is negligible.

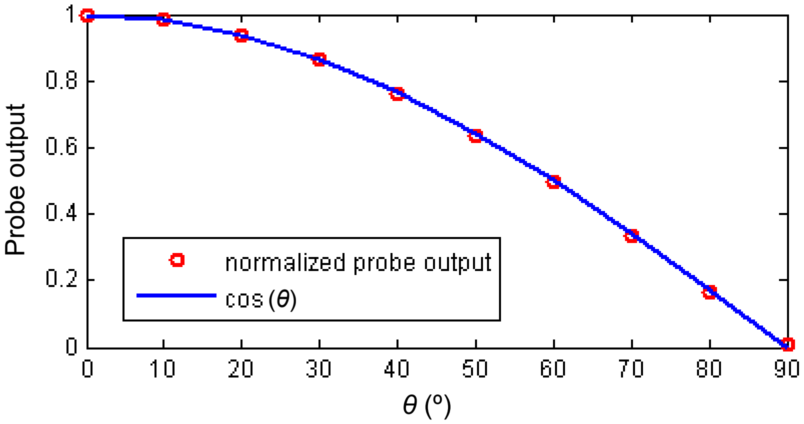

Fig. 2. 17 Normalized probe outputs for different polarization angle *θ* of the plane wave

Therefore the conversion relationship for H-field probes in (2.9) becomes:

$$V = V_H + V_E = C_H \cdot H + C_E \cdot E \tag{2.11}$$

where C_H and C_E are the conversion factors of probe response to the H field and E field respectively. Next the E-field rejection ability of the probe is characterized and the relative contribution of C_H and C_E is established. As this characteristic depends on not only the probe structure but also the intrinsic capacitance and manufacture uncertainties, the most appropriate way to establish this is to carry out experimental tests. These tests will also indicate the frequency range over which the H-field probe is applicable. The H/E rejection tests can be done in a GTEM (Giga Hertz Transverse Electromagnetic) cell.

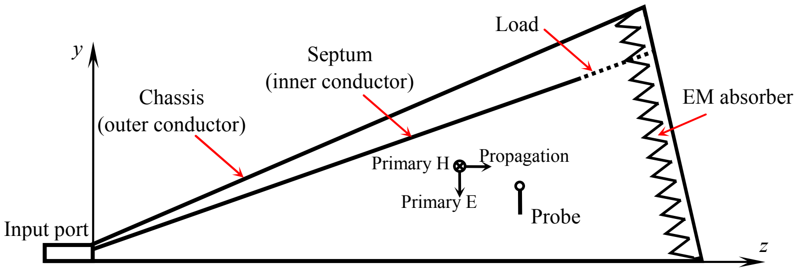

Fig. 2.18 E-field rejection test of H probe 1 with the GTEM cell

Fig. 2.18 shows the test setup. The GTEM cell is a one-port TEM waveguide with the upper frequency limit extended to the GHz range. It is designed to generate a TEM wave between the septum and bottom ground where the primary field components of the electric and magnetic fields (E_y and H_x) are much greater than the secondary cross-polar components (E_x, E_z, H_y and H_z) across any transverse cross-section. According to the EMC standard EN 61000-4-20 [14] (GTEM cell as measurement facility for emission and immunity tests), the field in the GTEM cell can be approximated to a TEM wave only in a “uniform area” at each frequency where both secondary electric field components are at least 6 dB less than the primary component over at least 75% of the measured points. If this requirement is fulfilled, the primary electric field and magnetic field in the uniform area has the relationship of

$$\frac{E}{H}=\eta_0, \qquad \eta_0=377\pm 50\ \ \Omega \tag{2.12}$$

The probe was placed vertically in the GTEM cell to pickup the transverse vertical E field and/or the transverse horizontal H field. By orienting the loop aperture of the probe into two perpendicular directions the relative E-field and H-field coupling can be found. The test strategy, as depicted in Fig. 2.19, is then

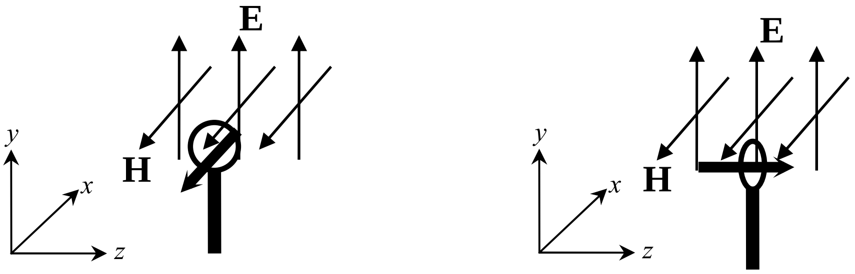

a) Aperture perpendicular to H

b) Aperture parallel to H

Fig. 2.19 Loop orientations in E-field rejection test

1) Let the loop aperture be perpendicular to primary H field component so the H component can fully couple to the loop (Fig. 2.19 a). In this case, the probe will respond to both E and H primary field component. The probe output is the contribution of the two parts and recorded as $V = V_H + V_E$.

2) Rotate the probe by 90° so that the primary H field component is parallel to the loop aperture (Fig. 2.19 b). In this case the probe should only be sensitive to the unwanted vertical primary E field component, and a secondary H field component. The probe output is $V = V_E + \Delta$.

3) The relative sensitivity of the H-field probe can then be calculated. The H/E rejection

ability can be evaluated by a rejection factor R defined as

$$R = \frac{V_H}{V_E} = \frac{C_H H}{C_E E} = \frac{C_H}{C_H \eta_0} \tag{2.12}$$

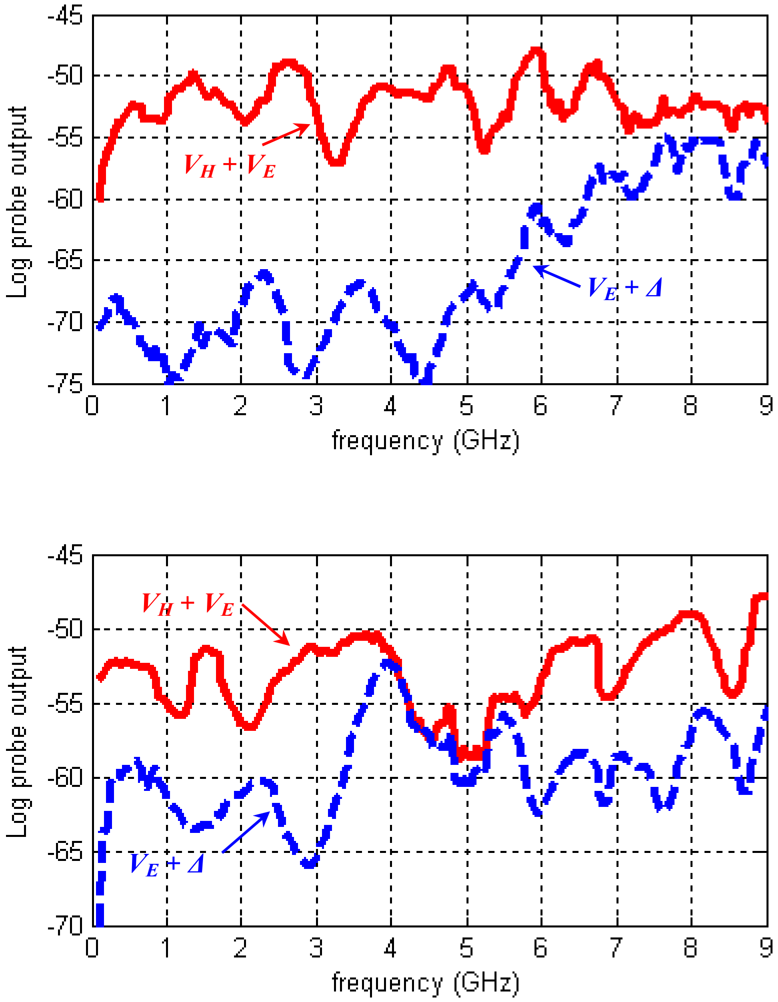

Fig. 2.20 H/E rejection ability of the two H-field probes

a) H probe 1;   b) H probe 2

Tests were performed for the two H-field probes and the results are presented in Fig. 2.20. Different excitation powers were applied to the GTEM cell for the two probes to keep both outputs in a measurable range. The rejection factor R can be represented by the difference of the two curves if the secondary H field component is negligible. Generally H probe 1 (circular loop) has better E-field rejection than H probe 2 (square loop). H probe 1 highly rejects the E field with $R \geq 15$ dB from 0.5 GHz to 5 GHz (except a local minimum at around 3.2 GHz where $R \approx 13$ dB). Above 5 GHz the test shows the rejection R gradually reduces to about 3 dB. One possible reason is that the GTEM cell does not have "uniform areas" at those higher frequencies so that the secondary H field components become comparable to the primary component thus the minor response Δ is no longer negligible. The other possible reason is that the E-field rejection of the probe indeed reduces at higher frequencies. However, H probe 1 definitely has an application range at least from 0.5 GHz to 5 GHz. For H probe 2, the application range is from 0.1 GHz up to 8 GHz (R = 5~15 dB) except for a window between 3.5 GHz and 6 GHz where the probe appears to have a resonance with very low H-field response.

Based on the E-field rejection tests, different probe output – field value conversion methods should be applied to the probes with different E-field rejection ability, because the probe output is a combination of an H-field response and an E-field response

$$V = C_H \cdot H + C_E \cdot E = \left(C_H + \eta C_E\right) \cdot H \tag{2.13}$$

It should be noted that in the near field the ratio η of the vertical E field and the horizontal H field can vary widely and will generally not correspond to the free space η_0. If $C_H \gg \eta_0 C_E$ ($R \geq 15$ dB), the variation of η does not have a significant effect on the total value of $C_H + \eta C_E$ so the probe output V and the measured field H still retain a linear relationship. The probe can be sufficiently calibrated by finding out the total conversion factor $C_T = C_H + \eta C_E$. If $C_H > \eta_0 C_E$ but not $C_H \gg \eta_0 C_E$ (R = 5~15 dB), using the total conversion factor C_T is still acceptable but the error increases. An alternative conversion is to find out both C_H and C_E, and compensate the contribution of the E field from the total probe output. If C_H is comparable to $\eta_0 C_E$ ($R < 5$ dB), generally the probe is not suitable for performing H-field measurements at this frequency. The determination of conversion factors C_T, C_H and C_E is discussed in Section 2.6.

2.5.3 Probe Disturbance to Field

Once the probe is present in the near field being measured, it introduces disturbances to the original field. This disturbance effect can be expressed as:

$$H = H_0 - \Delta H = H_0 \left(1 - \rho\right) \tag{2.14}$$

where H_0 and H are the original and disturbed magnetic field at the sampling point, and ρ is defined as the disturbance factor $\rho = \left(H_0 - H\right) / H_0$. Considering the disturbance effect, the measuring probe responds to the affected field H instead of the original field H_0. Thus the probe response formula (2.9) becomes:

$$V_i = C \cdot H_i = C \cdot H_{0i} \left(1 - \rho\right) \tag{2.15}$$

The conversion factor found from a calibration is actually $C \cdot (1 - \rho)$. Therefore, even though the conversion factor has been determined, the conversion to absolute field intensities is not 100% correct unless the disturbance factor ρ is a constant between the calibration environment and other measurement environments. But actually the disturbance factor depends on a number of factors thus inevitably introducing an error into the near-field measurement.

According to [13], the disturbance factor ρ is a function of the probe size and scanning height. In our studies it is found that ρ also slightly depends on the field distribution even in the same scanning height where the field intensities are of the same order. In order to evaluate the disturbance effect, simulations for near fields with the presence of the probe (H probe 1) were performed. The disturbance factor ρ is characterized as a function of the scanning position, frequency and field distribution, and the error introduced to the final near-field results is estimated statistically.

Simulation setup

The simulations were performed with the MoM based solver Concept II 9.4. The simulation setup included a test board and the H probe 1, as shown in Fig. 2.21(a). The probe model was the same as in Section 2.5.1 for spatial resolution simulations. The test board had a 40mm ×2mm microstrip located in the center of an 80mm × 50 mm × 1.5 mm grounded FR4 substrate, with 1V RF excitation at one end and a 50 Ω load at the other end. The center of the board was defined as the origin of the coordinate system. The side view Fig. 2.21(b) shows the geometrical relationship between the probe and the microstrip board. The loop of the probe was orientated to measure H_x at different heights.

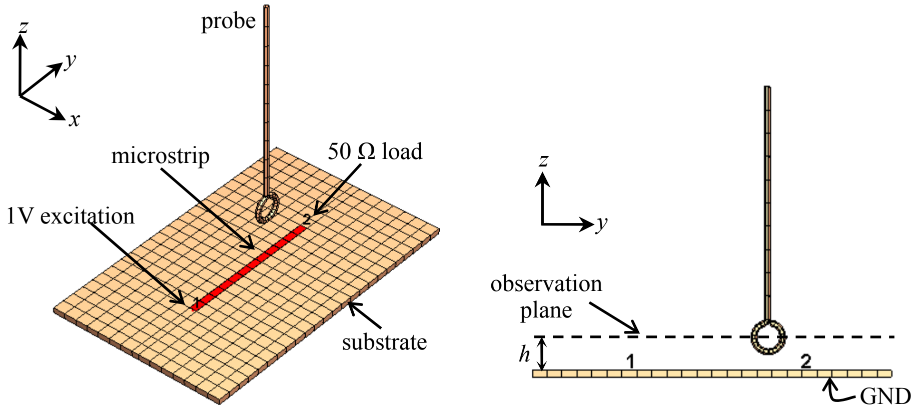

a) Simulation setup

b) Side view

Fig. 2.21 Simulation model for probe disturbance effect on near-field measurement

The general disturbance effect

The x-directed magnetic field H_x in a plane, which had the same size as the board (80 mm × 50 mm) and was *h*=15mm above the board, was first simulated without the presence of the probe and recorded as H_{0x}. Then simulation for the same field was then performed with the presence of the probe and recorded as H_x. The probe was located to measure H_x at (-5 mm, 12.5 mm , 15 mm).The disturbance factor was found from the two field values at the point of the center of the loop, as shown in Fig. 2.22. Without the probe the field shows good symmetry, but the presence of the probe obviously distorts the field. At the center of the loop, H_x is smaller than H_{0x} by 9.2%. Generally the disturbed field at the measurement point is always smaller than the original one. This is reasonable and can be explained from the Lentz's law in classical electromagnetics - an induced current is always in such a direction as to oppose the motion or change causing it.

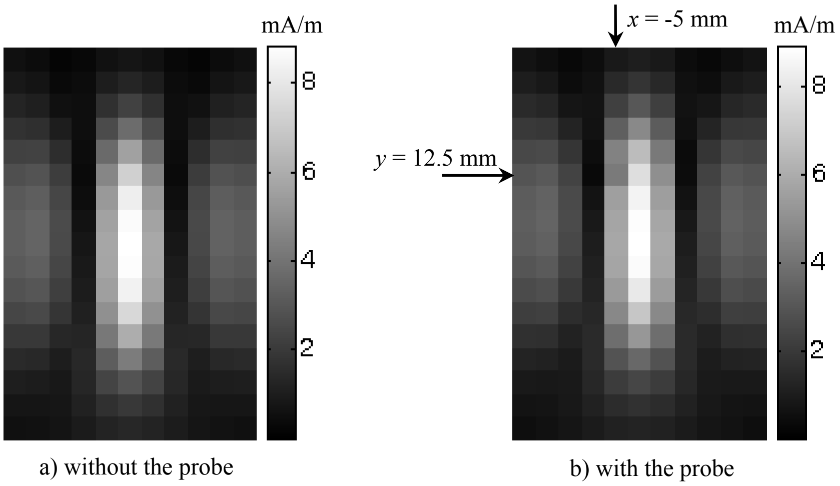

a) without the probe b) with the probe

Fig. 2.22 Difference of the x-directed magnetic near field due to the probe disturbance

Dependence on the scanning height

The dependence on the scanning height was studied by simulating the H_x component at (0, 0, h) with different scanning height h up to 2λ. Our region of interest – the reactive near field was included in this range. Fig. 2.23 shows the disturbance factor ρ against the observation height h at two frequencies, 1 GHz and 3 GHz for illustration. The observation height h is normalized against the wavelength λ. The results indicate that the disturbance effect decreases with the observation height in the near field and tends to be a constant in the far field. In the reactive near field, the disturbance factor decreases from 9.5% to 5.5% and from 10% to 6%

at 1 GHz and 3 GHz, respectively. Theoretically, the closer to the source the more likely is the reactive energy to be the dominant which is stored in the field rather than radiating outward, thus the near field is more affected by an object inserted in the energy storage space. Therefore greater disturbance effects appear at closer scanning heights. But when the observation height goes beyond the reactive near-field boundary λ, the radiating energy dominates and the wave impedance tends to be a constant η_0=377Ω. So the disturbance factor is independent of the observation distance in the far field.

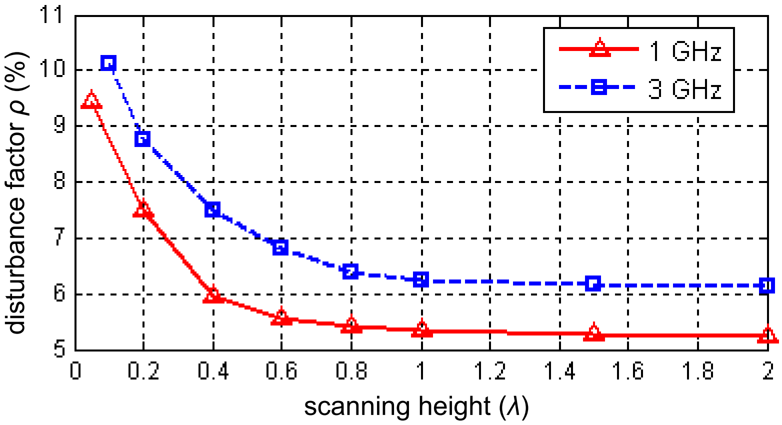

Fig. 2.23 Probe disturbance factor as a function of the scanning height

Dependence on frequency

The dependence on frequency was studied by comparing the disturbance factor ρ at a distance of 2λ for each frequency from 0.5 GHz to 3 GHz. At this distance the wave impedance for every frequency is approximately equal to the free space one 377 Ω, making frequency the only significant factor affecting the disturbance effect. The simulation result in Fig. 2.24 shows that the disturbance factor increases with frequency. In [13] it is pointed out that larger probes introduce greater disturbance. The frequency dependence is consistent with this result. Probe of larger dimension, not only physically larger but also relative to the wavelength, introduces greater disturbance to the measured field. For H probe 1 with a loop diameter 10mm, the ratio to the wavelength is 1/30 at 1 GHz and becomes “larger” (1/10 to the wavelength) at 3 GHz. However, the disturbance factor is within a relatively small level (< 6.5 %) because the probe is still “small” even at 3 GHz.

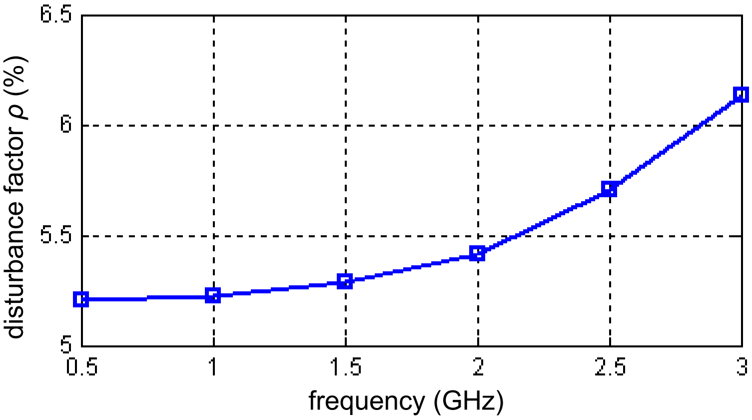

Fig. 2.24 Probe disturbance factor as a function of the frequency

Dependence on the field distribution

Unlike the far field where the wave is uniform, the field distribution in the near field varies widely, as well as the wave impedance. The disturbance of the probe, which is an effect of interaction with both E and H field, therefore also has a variation in the near field even though the observation is from the same distance. This dependence was studied by statistical analysis of the disturbance factors ρ at different sampling points in several planes. In every simulation for a specific sampling point, the probe was modelled at the due position. Simulations were performed on two planes, one with an observation height h=0.1λ well in the reactive near field and the other h=λ was on the boundary of the reactive near field. The planes had the same size (80 × 50 mm) with the board so as to cover the most interested area in EMI measurements. As there is an “error spectrum” over the whole plane, a reasonable estimate is the standard deviation of all the sampling points which describes how the individual points differ from the average. Results at 1 GHz are shown in TABLE 2.3. The standard deviation at a closer distance is greater than at a higher distance because the field tends to be uniform as it approaches the far field.

TABLE 2.3 Statistics of the probe disturbance factor depending on the field distribution

plane	sampling points	max (ρ)	min (ρ)	average (ρ)	standard deviation
h=0.1λ	17 × 11 =187	11.3 %	7.1 %	8.8 %	1.1 %
h=λ	17 × 11 =187	5.8 %	5.0 %	5.3 %	0.2 %

Error due to the disturbance effect

It has been demonstrated that the disturbance factor ρ depends on the spacing from the source, probe size relative to the wavelength and the field distribution. The difference of ρ in the measurement and calibration means that an error will be caused when the probe output voltages are converted into field intensities using (2.13).

An approximate error budget can be estimated based on the studies above with the microstrip board if we assume that it represents a typical situation. According to the dependence on the scanning height, if both calibration and measurement are performed in the reactive near field ($h \leq \lambda$) the maximum error is approximately 4%. In EMI scans very often the observation height is limited to $\lambda/4$ (75mm at 1 GHz), leading to a typical systematic error of $\varepsilon \approx 2\%$. Also considering the dependence on the field distribution over the same plane, a typical value at h=0.1λ is σ=1.1%. Because of the 3σ criterion and the classical central limit theorem [15], the total error due to the probe disturbance is given by

$$\varepsilon_{disturbance} = \sqrt{3\sigma^2 + \varepsilon^2} \approx 3\% \qquad (2.16)$$

2.6 Calibration of Near-Field Probes

The voltage outputs of a probe over a scanning plane are converted to absolute field values from a probe calibration. Calibration is essential to quantify the electromagnetic emissions; otherwise we can only obtain the normalized patterns. The conversion factors could be influenced by several factors, e.g. uncertainty of manufacture, irregular geometries and imperfect materials. Therefore analytical formulae of the probe's antenna factor are not reliable so an experiment based method is used. Basically, the conversion factors are determined by illuminating the probe being calibrated with a known reference field and comparing the probe output with the reference field. The reference radiation source should be simple enough to allow accurate analytical or numerical solutions for its electromagnetic fields, for example, monopoles, dipoles and microstrip antennas, or commercial calibrated radiators. The routine of conversion factor determination is then:

1) Analytical or numerical solution for the reference radiator to obtain the near-field values $[H_i]$ and $[E_i]$ ($i = x, y$ or z depending on measurements) at a number of near-field points.

2) Near-field measurement over the reference radiator to obtain the probe output $[V_i]$ in one target orientation at the same sampling points as the reference.

3) Calculation of the conversion factors depending on the H/E rejection factor.

The procedure is detailed below taking the results at 1 GHz as an example.

The reference radiation source was a calibrated whip antenna (generically manufactured, no individual calibration) whose structural and electrical characteristics were given in the datasheet. The near fields were obtained using the Method of Moment (MoM) simulation [12] by fine-tuning the model parameters based on the datasheet. Tangential H-field component H_x and vertical E-field component E_z at 21×21 sampling points in a 50×50 mm plane which was 10 mm above the tip of the whip were simulated as the reference field, as shown in Fig. 2.25.

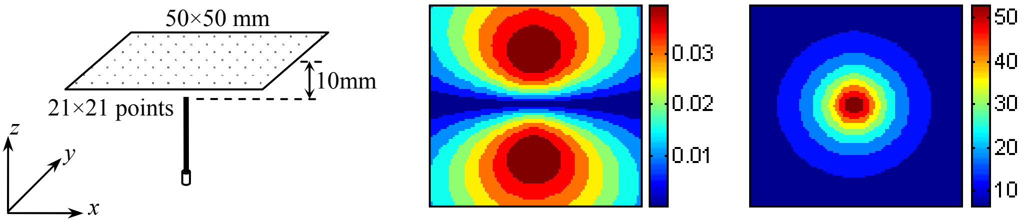

a) setup b) H_x (A/m) c) E_z (V/m)

Fig. 2.25 Reference fields from the whip antenna

Then a near-field scan was performed to obtain the received voltage of the probe V_x at the same sampling points as the reference fields, by placing the loop of the probe in the x orientation. Fig. 2.26 presents the distribution of V_x using H probe 1 and 2. The larger probe – H probe 2 – has greater sensitivity thus the output level is higher. But the spatial resolution of both probes is enough at this scanning spacing as profile of the field is detected by both probes.

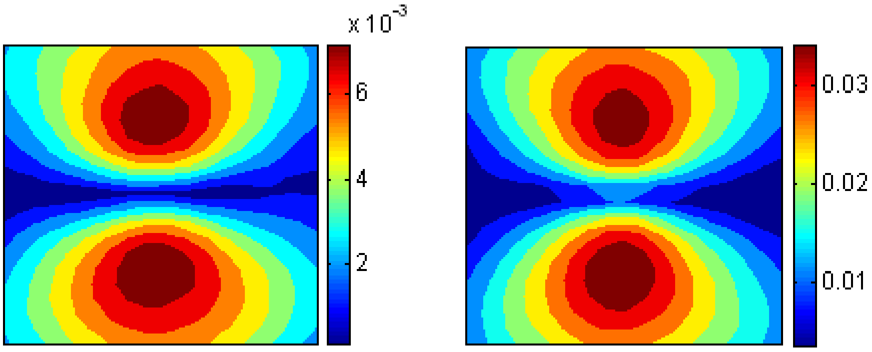

a) V_x of probe 1 (V) b) V_x of probe 2 (V)

Fig. 2.26 Received voltage of the two H-field probes over the reference field

The V_x distribution of H probe 1, of which the E-field rejection ability is very high, agrees well with the H_x distribution of the reference field. On the other hand, the V_x distribution of H probe 2, of which the E-field rejection ability is relatively low, almost agrees with H_x but it has considerable output voltages around the center where H_x is actually nearly 0. This is because E_z has peak value in the center of the scanning plane and the output around the center is primarily the response to E_z.

Following the discussion after (2.13), when the probe highly rejects the E fields (in this case H probe 1), V_x and H_x simply have linear relationship as

$$V_x = C_T \cdot H_x \quad if \quad C_H \gg \eta_0 C_E \tag{2.17}$$

The conversion factor C_T can be found in three different ways.

1) by comparing the maximum values in the two data sets

$$C_T = \max\left(\left[V_x\right]\right) / \max\left(\left[H_x\right]\right) \tag{2.18}$$

2) by taking an integration over the whole scanning plane and comparing the spatial sum.

$$C_T = \frac{\int V_x dxdy}{\int H_x dxdy} = \frac{\sum\left[V_x\right]}{\sum\left[H_x\right]} \tag{2.19}$$

3) by comparing V_x and H_x at N points and taking the average.

$$C_T = \left(\sum_{i=1}^{N} \frac{Vx_i}{Hx_i}\right) / N \tag{2.20}$$

The second and third calculations are believed to be more reliable because the calculated conversion factor represents an average of the variation in η. However, the results given by the three calculations for this specific case were very close, 0.173, 0.181, 0.182 respectively. Then in every near-field scan the voltage outputs of the probe V_i in Volts can be converted to absolute field intensities H_i in A/m by $H_i = V_i / C_T$ (i can be any component).

When $C_H > \eta_0 C_E$ but not $C_H \gg \eta_0 C_E$, in this case for probe 2, the response to the E field has a more significant contribution to the probe output.

$$V_x = C_H \cdot H_x + C_E \cdot E_z \quad \text{if} \quad C_H > \eta_0 C_E \quad \text{but not} \quad C_H \gg \eta_0 C_E \tag{2.21}$$

An alternative calibration to finding out the total conversion factor C_T is to calibrate C_H and C_E. In measurements the orthogonal E-field component $E_\perp$ can be measured to compensate the H probe outputs. The H-field component can then be extracted by $H_i = \left(V_i - C_E E_\perp\right)/C_H$. C_H and C_E are determined by solving linear equations with N pairs of known H_x and E_z as:

$$\begin{bmatrix} Hx_i & Ez_i \end{bmatrix}_{N\times 2} \cdot \begin{bmatrix} C_H \\ C_E \end{bmatrix} = \begin{bmatrix} V_x \end{bmatrix}_{N\times 1} \tag{2.22}$$

Normally more than 2 sampling points are used thus the least square method is applied to solve the equations. For H probe 2 the conversion factors were $C_H = 0.84$ and $C_E = 3.31\times10^{-4}$. Based on this calibration, the E-field rejection factor R in (2.12) is calculated as 8.3 dB which is close to the GTEM cell test result in Fig. 2.22b (7 dB).

Errors in the conversion factors found from the calibration come from the probe's polarization properties and the variation of wave impedance. A practical probe, as a receiving antenna, can not respond to only a single field component. The calibrations discussed above are meant to convert the probe output to a single component being measured, and the very minor effects of other field components are not taken into account. However, the variation of wave impedance means that the minor effects are not identical thus the conversion relationship to the component being measured is not a constant at different positions. The conversion factors found from the calibration actually reflect the average of the conversion relationship. At every sampling point, the real conversion factor may slightly differ from the average and thus produces an error spectrum.

In order to estimate an error bound, the conversion factors were calculated with several randomly chosen subsets from the reference fields ($[H_x]_i$ and $[E_z]_i$) and probe outputs ($[V_x]_i$)

on surfaces at different height. The relative standard deviation of the calculated conversion factors [C_i] describes how the measured conversion factors differ from the real value, so it can be used as an indicator of its error as

$$\sigma = \sqrt{\sum_{i=1}^{N} \frac{\left(C_i - \overline{C}\right)^2}{N-1}} / \overline{C} \tag{2.23}$$

where $\overline{C}$ is the average of the calculated conversion factors (C can be C_T, C_H and C_E). The error estimation for probe 1 and probe 2 are listed in TABLE 2.4.

TABLE 2.4 Error of the conversion factors

	N	$\max\left[\left(C_i - \overline{C}\right)/\overline{C}\right]$	$\min\left[\left(C_i - \overline{C}\right)/\overline{C}\right]$	$\sigma(C_T)$ or $\max\left[\sigma(C_H), \sigma(C_E)\right]$
Probe 1	50	6%	-4%	3%
Probe 2	50	9%	-7%	5%

2.7 Measurement Results of PCBs

2.7.1 Validation with a Test Board

Validating measurements were performed with a test microstip board. It is an 80 × 50 × 1.5 mm FR4 board with a 40 × 2 mm microstrip in the center of one side and a ground plane on the other side, as shown in Fig. 2. 27. The microstrip is fed with a 1 V excitation via a 50 Ω coaxial cable at one end and terminated with a 50 Ω load at the other end. The simple structure allows accurate full field simulations for the board for verification purposes.

Near-field probes were scanned over the whole surface of this PCB (80mm×50mm) at the height of 11.5 mm above, with 33×21 sampling points. This scanning surface is well in the reactive near field at the sample frequency 1 GHz. The voltage outputs of the probe were then converted to the absolute field intensities using the calibrated conversion factors. Both H-probes 1 and 2 were used in the measurement for comparison purposes.

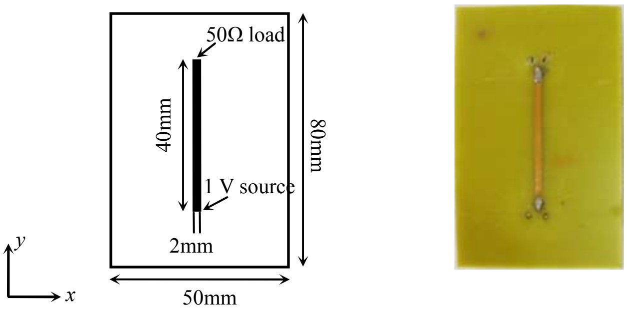

a) schematic b) photograph (top view)

Fig. 2.27 The test microstrip board used for validating measurement

To verify experimental measurements computer simulations were carried out with two independent numerical methods of different nature namely, time-domain transmission line modelling (TLM) as a well establish technique in electromagnetic field modelling [16] and the MoM and integral equations incorporated in Concept-II 9.4 code [12]. Fig. 2.28 presents the simulation setup of the metal trace placed above a grounded FR4 material, as well as the model of the excitation and termination.

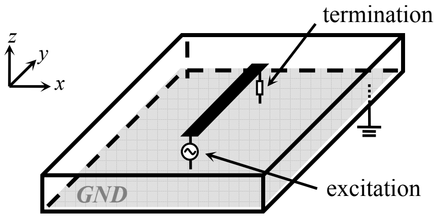

Fig. 2.28 Simulation setup for the test board

In both TLM and Concept-II models the metal strip was assumed to be a zero-thickness perfect electric conductor (PEC) plate and the FR4 material was approximated by a dielectric slab of permittivity ε_r = 4.6. In the case of TLM one end of the strip was excited by a z-directed voltage source of resistance R_S = 50 Ω and the opposite end was terminated by a load resistance, R_L =50 Ω. The source function had a sinusoid dependence of 1 V amplitude at the required frequency and the computational area was descretized with symmetrical condensed nodes of ΔL = 0.5 mm. For the MoM based solver Concept-II, non-uniform meshes were employed with doubly finer meshes for the microstrip than substrate. The excitation was a 1 V voltage source with 50 Ω internal resistance and the load was a 50 Ω lumped load. Measurements and simulations for the three orthogonal H-field components, H_x, H_y and H_z, are presented in Fig. 2.29.

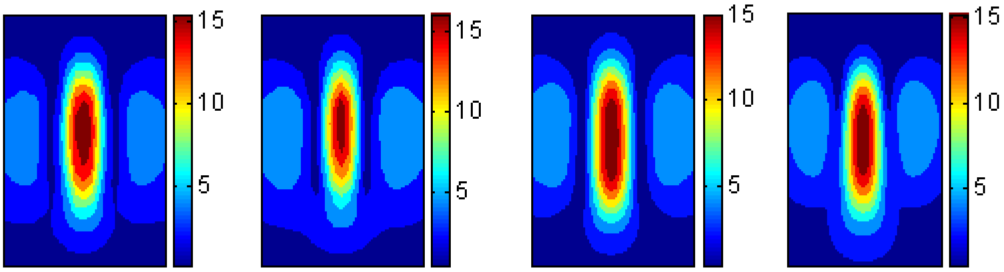

Measurement H-probe 1 | Measurement H-probe 2 | Simulation MoM | Simulation TLM

a) H_x component

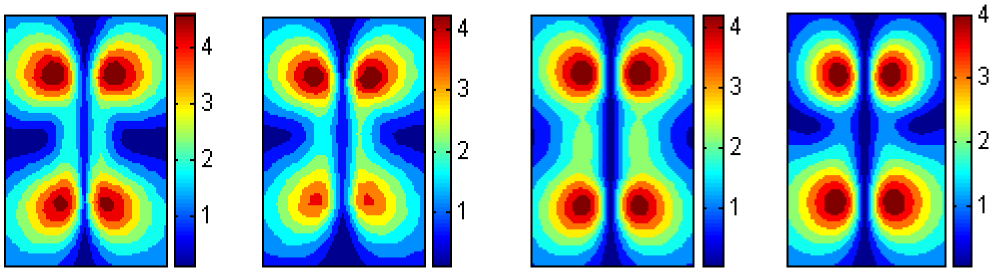

Measurement H-probe 1 | Measurement H-probe 2 | Simulation MoM | Simulation TLM

b) H_y component

Fig. 2.29 Tangential magnetic near field obtained from measurement and simulation

The maximum emission level and field distribution are the main interests in EMC studies. There is a slight difference between the measurement results obtained with the two probes. The first reason is that the two probes have different spatial resolution. Smaller probes are more sensitive to the details of the spatial variation of the field. Secondly, the probe-related errors depend on the probe's intrinsic characteristics and thus are different for the two probes. However, the field distributions obtained by both probes have a good agreement with simulations. By applying the conversion factors the measured field amplitudes also agree well with simulations. The maximum amplitudes of the measured and simulated fields are summarized in TABLE 2.5.

TABLE 2.5 Maximum amplitudes of the measured and simulated magnetic field (mA/m)

Field component	H-Probe 1	H-Probe 2	MoM	TLM
H_x	17.5	18.2	16.8	17.1
H_y	4.8	4.4	4.5	4.2

More detailed comparisons can be made by observing from a number of cuts through the scanning plane. The observation lines are defined to include the point of the maximum amplitude, as marked in Fig. 2.27. H_x is observed along the line y = 40 mm and H_y along x =15 mm. The comparisons are presented in Fig. 2.30. Close agreement can be found not only at the maximum point but also across the whole horizon. The difference to the MoM simulated field is approximately less than 5% and 10% at most points for H probe 1 and H probe 2 respectively.

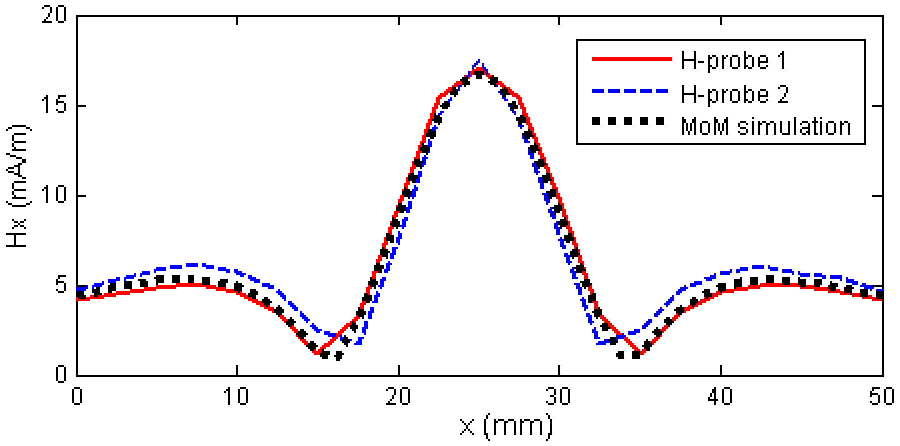

a) H_x along the line y=40mm

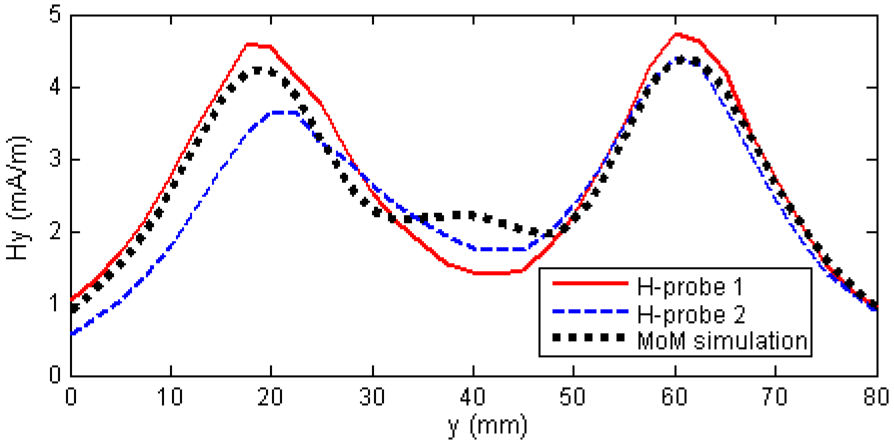

b) Hy along the line x=15mm

Fig. 2.30 Detailed H-field amplitudes along the observation lines

Although EMC studies mainly care about field amplitude, phase information, as the second nature of a field, provides the complete characterization for the radiation properties of the DUT. It is important for source characterization and far-field mapping. The phase measurements of H field in the same plane as the amplitude measurements are presented in Fig. 2.31. All phase maps are normalized to the same reference. A general agreement with simulations can be observed. However, the phase error is greater where the field amplitude is weaker. This is because the phase information is obtained by synchronizing the field signal with a constant reference signal, so the phase at weaker fields is more sensitive to measurement noise.

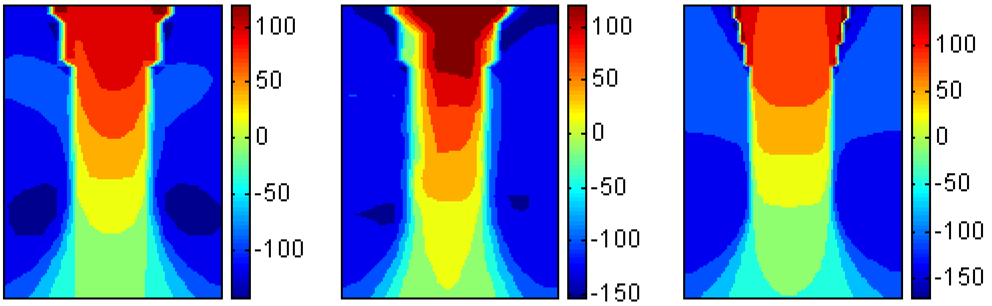

Measurement
H-probe 1

Measurement
H-probe 2

Simulation
MoM

a) H_x component

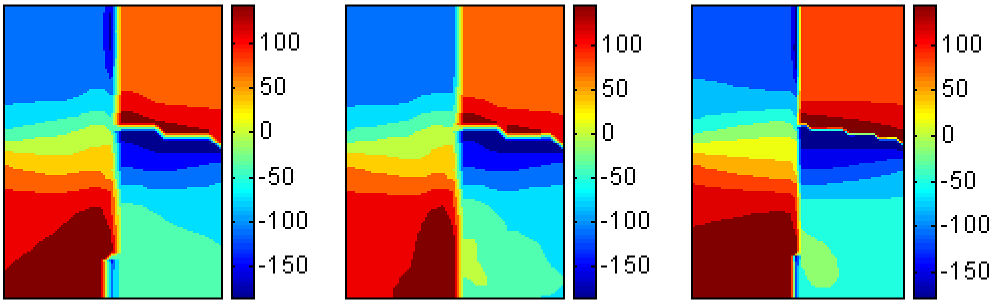

Measurement
H-probe 1

Measurement
H-probe 2

Simulation
MoM

b) H_y component

Fig. 2.31 Phase information of the magnetic field

Finally, measurement results of electric field at 1 GHz are presented in Fig. 2.32. Measurements were performed over the whole surface of the test board (80mm×50mm) at the height of 10 mm above, with 33×21 sampling points. The tangential components E_x and E_y were measured using E probe 2 (balanced wire dipole), while the normal component E_z was measured using E probe 1 (rod probe). Measurement results are compared with MoM simulations. It can be seen that the interference to electric field measurement is more significant than that to magnetic field measurement, as indicated by the slightly distorted field patterns which are theoretically symmetrical. This may be due to the naturally lower sensitivity of electric field probes, either rod type or wire dipole type. However, the general profiles of the maps agree and the maximum field amplitudes are very close to that of simulations.

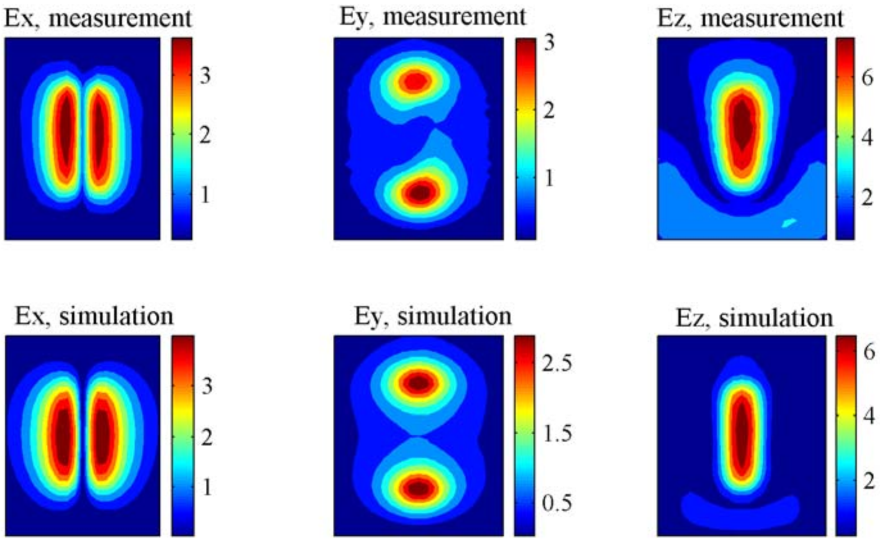

Fig. 2.32 Electric near field of the test board at 1 GHz

Validation studies with the test board confirm that reliable amplitude and phase information of magnetic near-fields can be obtained with the scanning system architecture as well as the measurement and calibration methodology.

2.7.2 Fast Clock Digital PCB

In order to assess the accuracy of near-field scans for estimation the emissions from PCBs, a digital circuit, as shown in Fig. 2.33, was fabricated on an 80×50×1.5 mm FR4 substrate, representing a more complex and practical situation. The two-layer PCB has a ground plane on one side as a voltage reference and circuit components on the other side. The RF components include an oscillator of a fundamental frequency 32 MHz (item 2 in Fig. 2.33(a)) and two logic processors for a single FET bus switch (item 3 and 4). The 3.3V DC power is generated by an onboard voltage regulator (item 1). Some bypass components, such as decoupling capacitors, were used where appropriate according to the manufacturer's guidelines. The function of the circuit is to generate fast clock signals whose logic is controlled by the two logic processors. As the interest is to investigate the unintentional EM emissions, a fixed logic is applied. The tracks sketched in red in Fig. 2.32(a) are those carrying clock signals.

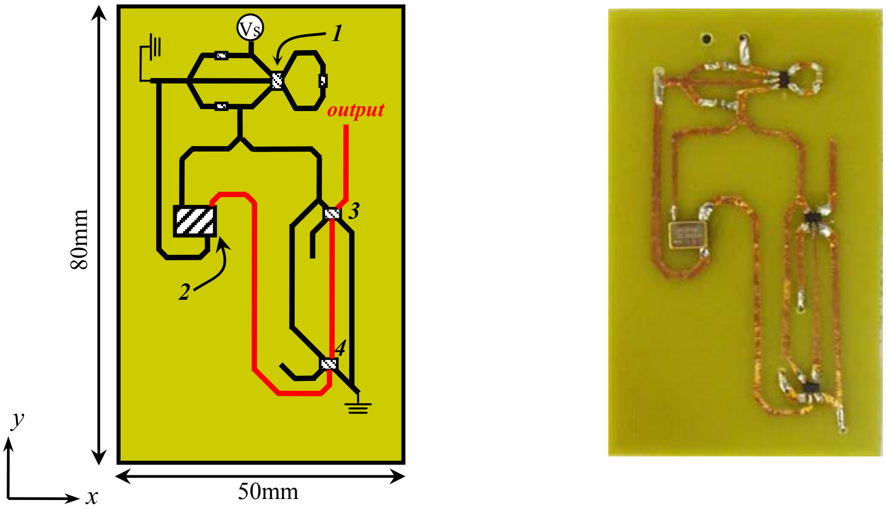

a) Schematic b) Photograph

Fig. 2.33 Top view of the digital circuit of fast clock

TABLE 2.6 Parameters of the near-field scans for the digital circuit

Frequency (MHz)	$N \times 32$ ($N = 1,2,3\ldots$)
Scanning plane height (mm)	8 (above the PCB plane)
Scanning plane size (mm)	120 × 75
Scanning resolution (mm)	2.5
Sampling points	49 × 31
Scanned field components	H_x, H_y, H_z

In order to diagnose the radiation sources and characterize the emissions, planar magnetic near-field scans were performed at the harmonics of the clock. TABLE 2.6 summarizes the detailed parameters of the scans. The following set of plots in Fig. 2.34 shows the first four harmonics of the circuit measured with near-field scanning for magnetic field distributions across the PCB. The dash-lined inner border indicates the area of the PCB. The total magnetic fields in the last row of the plots are calculated from the three orthogonal components (H_x, H_y and H_z are complex numbers to include both amplitude and phase) by

$$H_{total} = \left| \sqrt{H_x^2 + H_y^2 + H_z^2} \right| \tag{2.24}$$

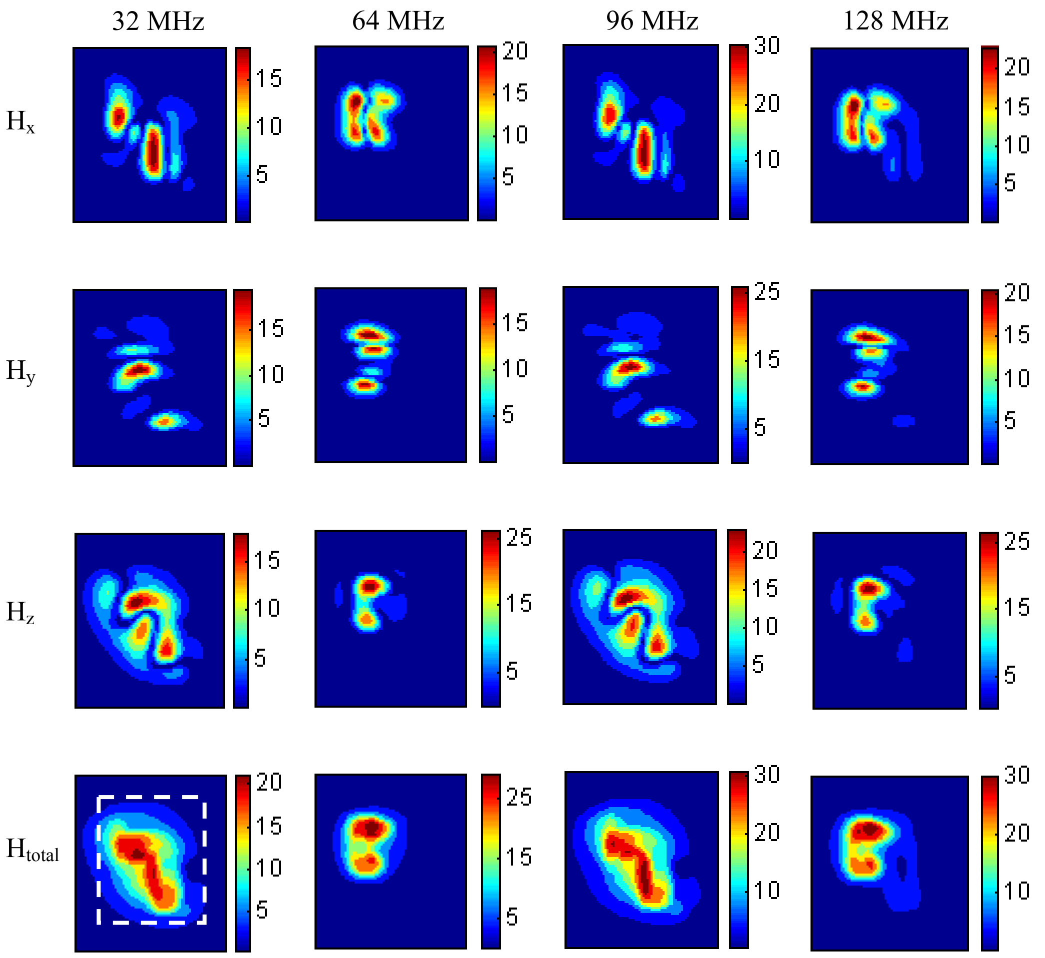

Fig. 2.34 Magnetic field over the digital circuit at the first four harmonics

It can be seen that higher harmonics repeat the patterns shown in the first two harmonics. Odd harmonics are associated with a particular region of dominant fields while even harmonics dominate in another region. At odd harmonics, hot spots in the field map are located near the oscillator and along the tracks carrying clock signals, indicating that both the oscillator and the clock signal tracks significantly contribute to the radiated field. On the other hand, at even harmonics strong fields can be observed only around the oscillator, thus the oscillator is the only significant radiation source. In addition, at all harmonics the logic processors and the voltage regulator are not significant sources of EM emissions compared to the oscillator and tracks.

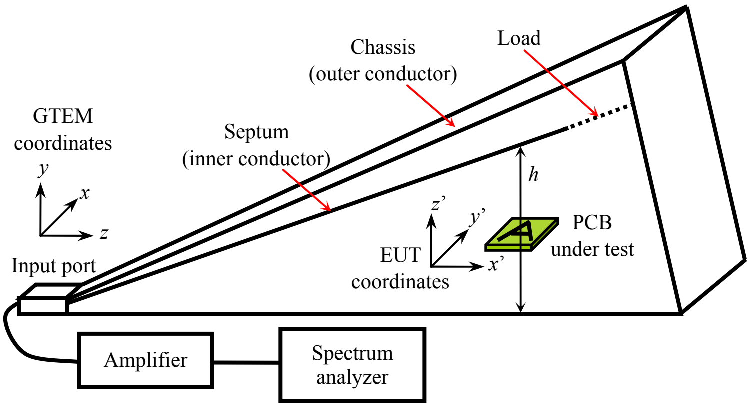

a) configuration of emission test with a GTEM cell

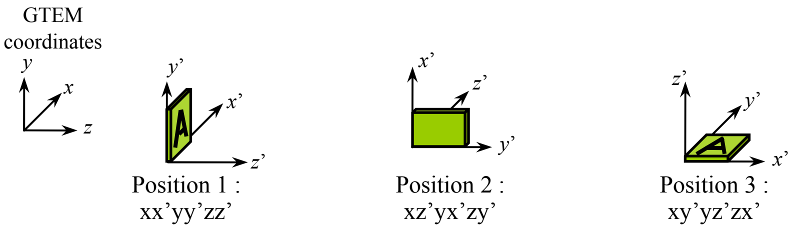

b) three positions of the PCB in the GTEM emission test

Fig. 2.35 Emission tests with a GTEM cell for the digital circuit

The maximum emission level measured with near-field scanning is compared with the GTEM cell measurement which is a widely used technique for emission test. According to the standard of emission test with a GTEM cell [14], a three-position measurement procedure was carried out, as shown in Fig. 2.35. The definition of the GTEM cell coordinates was to align the *z*-axis in the direction of propagation, the *y*-axis parallel to the E field (vertical) and *x*-axis parallel to the H field. A local coordinate system (*x*', *y*', *z*') was assigned to the PCB under test. The centre of the PCB was placed at (*x*=0, *y*, *z*) with *x*=0 in the middle of the septum. Position 1 aligned *x*' with *x*, *y*' with *y* and *z*' with *z*. Position 2 was obtained by rotating the PCB by 90º twice to align *x*' with *y*, *y*' with *z*, and *z*' with *x*. Position 3 was obtained by two further 90º rotations to align *x*' with *z*, *y*' with *x* and *z*' with *y*. The received voltages in the three orientations were recorded as V_{p1}, V_{p2} and V_{p3}. The total radiated power due to the PCB is then given by:

$$P_0 = \frac{\eta_0}{3\pi} \cdot \frac{k_0^2}{e_{0_y}^2 Z_c} \cdot \left(V_{p1}^2 + V_{p2}^2 + V_{p3}^2 \right) \quad \text{in W} \tag{2.25}$$

where

V_{p1}, V_{p2}, V_{p3} are the voltage measurements from three EUT positions, in V;

$k_0 = 2\pi/\lambda$ is the wave number in /m;

$\eta_0 = 377\Omega$ is the free space wave impedance, in Ω;

Z_c is the characteristic impedance of the TEM waveguide (typically 50 Ω), in Ω;

e_{0y} is the field factor: the normalized primary component of the electric field of the TEM mode at the EUT location, in $\sqrt{\Omega}/m$. It was determined experimentally from a measurement of E_y (in V/m) using the E-field probe at the location of the PCB centre in the empty cell excited by a known power P_i (in W):

$$e_{0_y} = E_y / \sqrt{P_i} \tag{2.26}$$

The maximum emission level of the PCB in the free space is then given by

$$E_{\max} = g_{\max} \cdot \sqrt{\frac{3\eta_0}{4\pi} P_0} \tag{2.27}$$

where g_{max} is the geometry factor determined by the height-scan of the receiving antenna, in /m.

Obviously $E_{\max} \propto \sqrt{P_0}$. For comparison purposes only, $\sqrt{P_0}$ measured with the GTEM cell was directly normalized to the maximum emission level obtained from near-field scanning in dB scale. This was done by taking the average difference between the GTEM cell values and near-field scanning values at each harmonic and adding this average to the GTEM cell values. Two GTEM cell tests were carried out where the PCB was placed at different septum-to-floor height, *h*=75cm and *h*=60cm, respectively. Measurements were done up to the 11th harmonic (352 MHz) limited by the measurable level of the receiver. The comparison is presented in Fig. 2.36. Near-field scans and GTEM cell tests show consistent results for the emission level as summarized in TABLE 2.7.

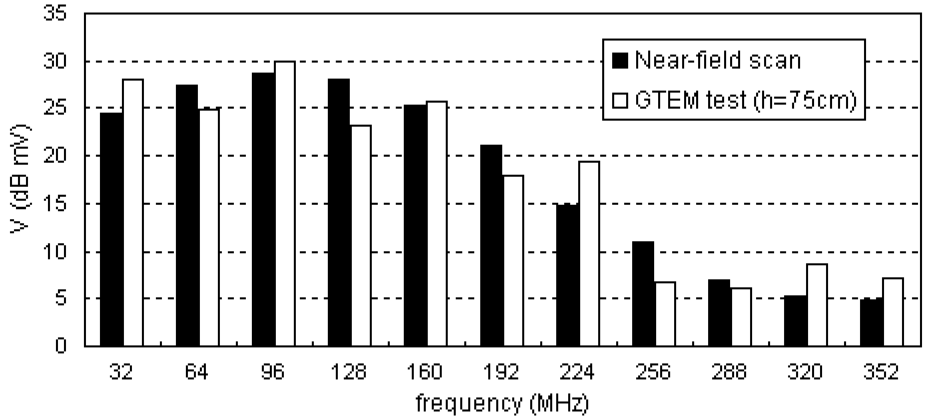

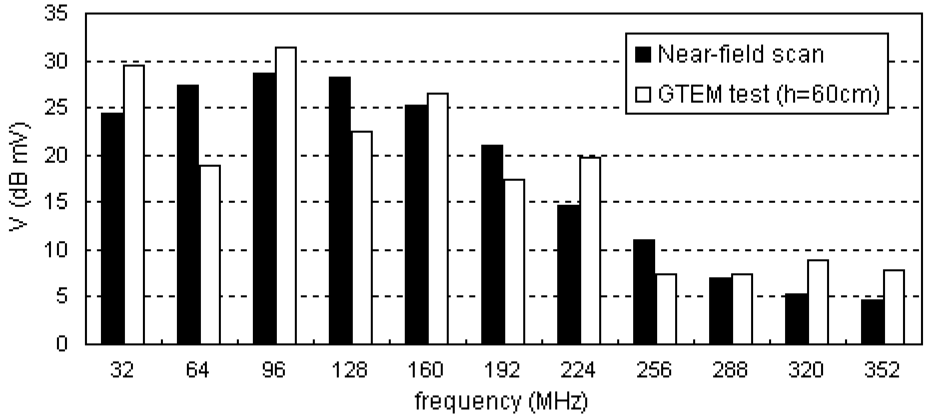

Fig. 2.36 Normalized comparison of GTEM cell tests and near-field scans for the emission level of the digital circuit

TABLE 2.7 Comparison between near-field scanning and GTEM test for the digital PCB

	Average of absolute difference at each harmonic	Standard deviation of difference at each harmonic	Correlation coefficient
Near-field scans vs GTEM tests (h=75cm)	2.81 dB	3.31 dB	87 %
Near-field scan vs GTEM test (h=60cm)	3.82 dB	4.57 dB	79 %

2.8 Error Analysis

The electromagnetic properties of a PCB are characterized by collecting the near-field data. The data will be then used to build electromagnetic models for the PCB. Thus, it is necessary to estimate the uncertainties in the measurement. All significant error sources are first identified and itemized for our specific near-field scanning system, and a typical value of all errors is then estimated based on simulation, measurement tests or statistical analysis where appropriate.

2.8.1 Identification of Error Sources

Near-field scanning includes a number of mechanical and electrical system components and a series of operational procedures. Many factors could possibly affect the measurement, each being an error source as summarized in TABLE 2.8. Depending on the source component, the error can be broadly divided into three categories, related to the probe, receiver and test conditions, respectively.

Each error is assumed independent thus is treated separately. Very often an error depends on the position of the sampling point and produces an error spectrum. In this case the average error over the sampling surface is taken as the typical value. The error estimation below is for near-field scanning with H probe 1 and the VNA HP E8632B.

TABLE 2.8 Error sources in near-field measurement

Category	Source
Probe	Probe positioning
	Antenna parameters
	Response to the variation of E/H
	Disturbance effect to the field
Receiver	Dynamic range
	Receiver imperfections
	Mismatch / joint
	Receiver random errors
Test conditions	Room scattering
	Leakage and crosstalk

2.8.2 Errors Related to the Probe

The 3D positioner can achieve a resolution close to 10 μm which is much less than RF wavelengths, so the movement of probe positioning is approximately error free. However, the DUT, more specifically the PCB under test, is manually aligned to be parallel with the scanning plane using a spirit level accurate to 1mm/m. This leads to a relative positioning errors. A rough analysis for this error is shown in Fig. 2.37 where the setup is simplified to a 2D structure. A randomly defined current $I(l)$ distributes along the PCB from 0 to L and the spacing between the scanning plane and the correctly aligned PCB is h. r and r' are the distance from a current segment to an scanning point when the PCB is correctly aligned or has a slope bias.

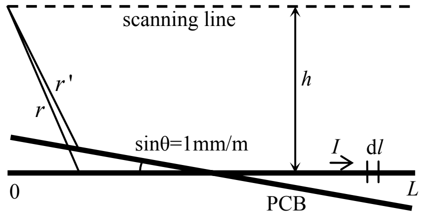

Fig. 2.37 Analysis of errors due to the relative alignment of probe and PCB

Field intensities at all the scanning points are numerically evaluated with the MoM when the PCB is flat or oblique, and recorded as H_i and $H_i^{'}$. The error is then given by

$$\varepsilon_{\text{probe}}^{\text{positioning}}{}_i = \left|\left(H_i^{'} - H_i\right) / H_i\right| \tag{2.28}$$

The average error along the scanning line is then evaluated by taking into account 20 randomly distributed currents *I*(*l*). The error is characterized as a function of the scanning height *h* and PCB size *L*, as shown in Fig. 2.38. It can be seen that the small equipment uncertainty 1mm/m can lead to 0.2 dB error in near-field scans when the scanning height is small and the PCB is large. Considering the typical case, the scanning height is normally beyond 10mm because of the dimension of the probe itself. For a PCB of a dimension around 100mm, a typical error estimate $\varepsilon_{\text{probe}}^{\text{positioning}} = 0.05\text{dB}$ is reasonable.

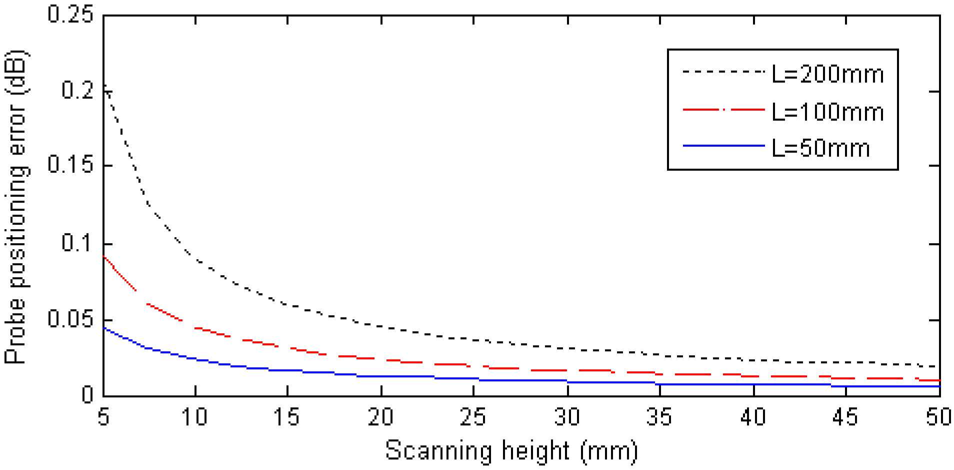

Fig. 2.38 Probe positioning error as a function of scanning height and PCB size

The errors due to the probe antenna parameters and response to the variation of wave impedance have been studied in Section 2.6 and indicated by the standard deviation of the conversion factors. The typical value in dB scale is $\sigma_{\text{probe}}^{\text{conversion}} = 0.13\text{dB}$. The probe disturbance error is indicated by the typical error bound in Section 2.5.3 as $\varepsilon_{\text{probe}}^{\text{disturbance}} = 0.13\text{dB}$

2.8.3 Errors Related to the Receiver

Dynamic range is the difference between the receiver's maximum input power and the minimum measurable power (noise floor). For a measurement to be valid, input signals must be within these boundaries. It is important if large variations in signal amplitude are to be measured. The dynamic range is defined experimentally. As the receiver input damage level is 15 dBm, to protect the instrument the upper limit is not tested and assumed to be 0 dBm. The lower limit is tested by decreasing the available signal level fed to the PCB so as to decrease the probe output from 0 dBm downward. When the phase readings begin to fluctuate by more than 5 º - 10º the lower level is indicated [17]. For this specific case it is -80 dBm so the dynamic range is 80 dB. Empirically the variation in near-field amplitude over a plane covering the area of a PCB is no more than 30 dB, so measurements can be performed well within the dynamic range. It is therefore possible to avoid the error due to the finite dynamic range.

A receiver has inherent systematic and random uncertainties even though measurements are performed well within its valid range. As these uncertainties are receiver dependent, the best method for estimating an error bound is to clarify the error sources and look up the receiver datasheet. For the two-port VNA the error sources include receiver imperfections, mismatch/joint and random errors.

The receiver imperfections arise from its intrinsic characteristics such as nonlinearities, synchronization and residual tracking. Impedance mismatch between the probe/DUT, receiver, connectors and cables can cause two primary problems that are the noise power lost at an interface where mismatch is present and unpredictable effects due to reflections of the noise power. These errors are the systematic components and can be significantly reduced by a measurement self-calibration routine. The datasheet provides the information of the residual (after a self-calibration) systematic errors resulting from imperfections in the calibration standards.

On the other hand, the error sources of the random components include noise, connector repeatability and interconnecting cable repeatability. The random components can be reduced by averaging several (typically N=10) readings. According to the classical central limit theorem [15], for a random variable of expectation μ and variance $\sigma^2>0$, as the sample size N increases the distribution of the sample average approaches the normal distribution with a mean μ and variance σ^2/N irrespective of the shape of the original distribution.

The total receiver uncertainty is given by

$$\varepsilon_{\text{receiver}} = \sqrt{\left(systematic + stability\right)^2 + random^2} \tag{2.29}$$

The total receiver uncertainty (after the self-calibration routine) as a function of the test port power and frequency is directly taken from the datasheet [3] and shown in Fig. 2.38. The typical error bound can be estimated from Fig. 2.39 by taking an average across the measured dynamic range as $\varepsilon_{\text{receiver}}\approx$0.25 dB.

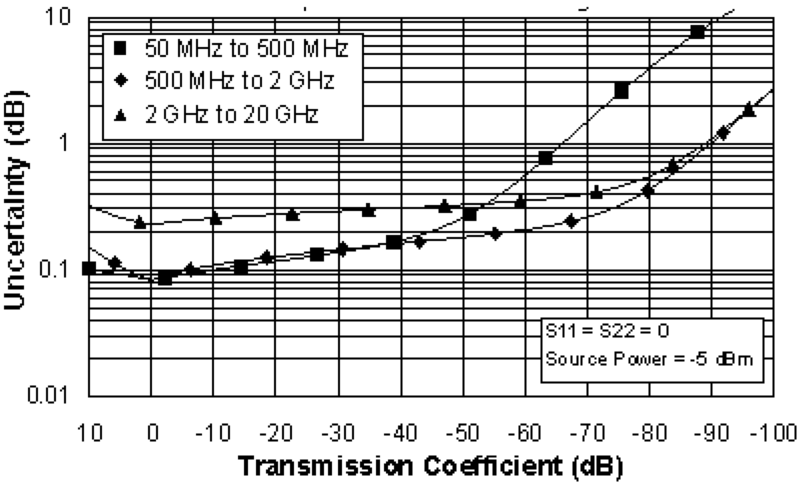

Fig. 2.39 Inherent measurement uncertainties of the VNA [3]

2.8.4 Errors Related to Test Conditions

This category includes errors due to room scattering, leakage and crosstalk. For a better mechanical stability most near-field scanning benches are constructed in the laboratory environment instead of an anechoic chamber or open area test site (OATS), thus here rises a room scattering problem. For higher accuracy scattering by fixed objects in the room is reduced by surrounding the scanning bench with wave absorbing materials during the measurement. In addition, leakage and crosstalk occur when cables on either the transmitting or receiving side radiate or receive RF energy, or when signals within the receiver's reference and measurement channels interfere.

The errors due to imperfect test conditions can be estimated from a series of experimental tests, including background measurements and cable effect measurements. Due to the limits of the measurable level it is difficult to perform reliable tests with the equipment at GGIEMR. However, the test conditions for most near-field scanning systems are consistent thus lead to similar error bound. The extensively studied test condition errors in [17] are believed to be the standard for near-field scanning techniques as $\varepsilon_{\text{scattering}}$=0.05 dB and $\varepsilon_{\text{leakage}}$=0.05 dB.

2.8.5 Combination of Errors

TABLE 2.9 Typical bound of each error source

Category	Source	Typical value (dB)
Probe	Probe positioning	0.05
	Antenna parameter	0.13
	Response to the variation of E/H	
	Disturbance effect to the field	0.13
Receiver	Dynamic range	0.00
	Receiver imperfections	0.25
	Mismatch / joint	
	Receiver random errors	
Test conditions	Room scattering	0.05
	Leakage and crosstalk	0.05

Estimates for each independent error source are summarized in TABLE 2.9. According to Lyapunov's central limit theorem [15] for independent but not necessarily identically distributed variables, the typical value of the total error bound in the near-field scanning is combined as:

$$\varepsilon_{\text{total}} = \sqrt{\sum_i 3\sigma_i^2 + \sum_j \varepsilon_j^2} = 0.35\text{dB} \tag{2.30}$$

The estimation above is for errors associated with amplitude measurement only. The phase measurement is strongly correlated with amplitude measurement. All the error sources above, either systematic or random, exert influence to both amplitude and phase information at the same time. In the near-field scanning system, there is no error source affecting amplitude or phase only. Therefore the idea of estimating the phase error from amplitude error [18] is presented in Fig. 2.40, assuming the error is due to an independent signal adding or subtracting as a vector. If the amplitude A of the measured vector has an uncertainty $\varepsilon_{\mathrm{mag}}$, the phase uncertainty is given by

$$\varepsilon_{\mathrm{phase}} = \sin^{-1}\left(\frac{\varepsilon_{\mathrm{mag}}}{A}\right) \tag{2.31}$$

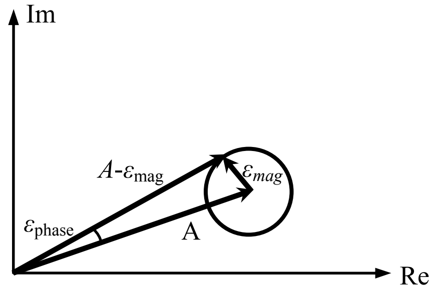

Fig. 2.40 Estimation of phase error from amplitude error

In this case a 5 degree error is predicted. It is important to note that this is only an estimate based on an assumed relation between the main signal and error signal instead of analytical or experimental analysis as for the amplitude error.

2.9 Conclusions

A mechanical and electrical system was constructed for planar near-field scanning. The hardware architecture is based on a 3D positioner which holds the probe to scan over the interested region, the receiving equipment for measurement, and some peripheral components for inter-communications. The software development, including motion control, sampling control and measurement automation, allows a fully automatic near-field scan with approximately 10 μm motion precision.

The measurement methodology consisting of a series of procedures is developed and tested.

Generally there are two methods for measuring both amplitude and phase based on the vector receiver (VNA) and amplitude-only receiver (SA) respectively. The VNA based method is the most convenient way to obtain the phase information. On the other hand, the SA based method measures phase indirectly from three scans by using a power combiner. Both methods have been tested to be reliable although the SA based one is more time-consuming. In addition, measuring phase from a single signal yields meaningless results thus a dual probe approach is used when the DUT is self-powered.

The near-field probes, either the loop H-field probe or monopole E-field probe, are designed for measuring individual field components. The electrical characteristics, such as sensitivity, spatial resolution, rejection ability to the unwanted field components, and disturbance to the measured fields, are investigated by taking H-field probe 1 as an example. Those investigations show how the probe outputs are related to the field intensities being measured. Then the conversion factors from probe outputs to field intensities are obtained by using a reference near field from a simple whip antenna.

Error analysis is then done for the near-field scanning system considering all the significant error sources. It is estimated that a typical error bound of 0.35 dB and 5° for amplitude and phase measurement. This error has an impact on the subsequent modelling and this will be discussed in Section 3.5 and 3.7.

The near fields for a simple test PCB were scanned and compared with full field simulations to validate the performance of the measurement system. Scans for a fast clock digital circuit board were carried out and compared with the GTEM cell emission tests. Reasonable agreement was obtained for the frequencies and distances of interest. The developed near-field scanning system is used to locate emission sources on PCBs and electronic systems in order to model the radiated emissions. A possible way explored in this research work is to develop equivalent models based on the measured near-field data [19]. With the scanning system, the near-field data required for building the PCB emission models can be experimentally collected with confidence.

References

[1] D. Yaghjian, "An overview of near-field antenna measurements," *IEEE Trans. Antennas Propagat.*, vol. AP-34, no. 1, pp. 30-45, Jan. 1986.

[2] D. Slater, *Near-Field Antenna Measurements*. Norwood, MA: Artech House, 1991.

[3] HP E8362B User's Guide, Hewlett-packard Co. Santa Rosa, CA, 2000.

[4] O. M. Bucci, G. Shirinzi, and G. Leone, "A compensation technique for positioning errors in planar near-field measurements", *IEEE Trans. Antennas Propagat.*, vol. AP-36, no. 8, pp. 1167-1172, 1988.

[5] L. A. Muth and R. L. Lewis, "A general technique to correct probe position errors in planar near-field measurements to arbitrary accuracy", *IEEE Trans. Antennas Propagat.*, vol. AP-38, no. 12, pp. 1925-1932, 1990.

[6] K. K. Tan, T. H. Lee and S. Huang, *Precision motion control: Design and implementation*, 2nd edition, London: Springer, 2008.

[7] *ViX 250/500IM Stepper Drivers User Guide*, Parker Hannifin Eletromechanical Division Europe, Offenburg, Germany, 2004.

[8] J. R. Taylor. *An Introduction to Error Analysis*. 2nd edition. Sausalito, California: University Science Books, 1997.

[9] *IEEE standard methods for measuring electromagnetic field strength of sinusoidal*

continuous waves, 30 Hz to 30 GHz, IEEE Std. 291-1, 1991, IEEE New York, 1991.

[10] Y. Gao and I. Wolff, "Miniature electric near-field probes for measuring 3D fields in planar microwave circuits," *IEEE Trans. Microwave Theo. Techn.*, vol. 46, no. 7, pp. 907-913, Jul. 1998.

[11] Z. Ouardirhi and J. J. Laurin, "Experimental characterization of miniature near-field probes," in *Proc. URSI General Assembly*, pp. ABP-4-1 - ABP-4-4, Aug. 2002.

[12] (2010) Concept – II 9.4 homepage. [Online]. Avaiable: http://www.tet.tu-harburg.de/concept/allgemein.en.html

[13] W. Joseph and L. Martens, "The influence of the measurement probe on the evaluation of electromagnetic fields," *IEEE Trans. Electromagn. Compat.*, vol. 43, no. 2, pp. 339-349, May 2003.

[14] *Electromagnetic compatibility - Testing and measurement techniques - Emission and immunity testing in transverse electromagnetic (TEM) waveguides*, EN 61000-4-20:2003, 2003.

[15] P. Billingsley, *Probability and Measure*, 3rd edition, New York: Wiley, 1995.

[16] C. Christopoulos, *The Transmission Line Modelling Method*, New York: IEEE press, 1995.

[17] A. Newell, "Error analysis techniques for planar near-field measurements," *IEEE Trans. Antennas Propagat.*, vol. AP-36, no. 6, pp. 754-768, Jun. 1988.

[18] J. Dunsmore, "Comparison of mixer characterization using new vector characterization techniques," in *Proc. 32nd European Microwave Conf.*, vol. 1, pp. 163-166, Sep. 2002.

[19] X. Tong, D. W. P. Thomas, A. Nothofer, P. Sewell, and C. Christopoulos, "Modelling electromagnetic emissions from printed circuit boards in closed environments using equivalent dipoles", accepted for publication on *IEEE Trans. Electromagn. Compat.*

CHAPTER THREE

Equivalent Dipole Model in Free Space

3.1 Introduction

This chapter presents the characterization of electromagnetic emissions from single layer PCBs using the equivalent dipole model derived from near-field scans. Near-field scanning systems have been widely used to characterize the electromagnetic properties of PCBs and integrated circuits. The important applications of near-field scanning include the diagnostics of emission sources [1], [2] and prediction of near/far fields [3]-[8] from the scanned near-field data in the close vicinity of the PCB. However, very often the structure of the PCB is very complex and complete information of the circuit is not available, making the determination of real current distribution and real sources difficult. Therefore it is useful to provide efficient simplified equivalent models to accurately represent the radiated emissions without knowing the exact details of the PCB.

Representation of electromagnetic emissions from near-field scanning has been studied in some previous works. The early work used modal expansion methods which take a Fourier transform of the measured near-field data to obtain the far field [3], [4]. In [5], [6], the idea of equivalent magnetic / electric currents for representing the fields is explored. In this method, an aperture antenna is replaced by equivalent magnetic / electric currents over a fictitious plane in front of the antenna. The equivalent currents are determined from the equivalence principle applied to the measured near fields. With this method, the correct far field in front of the antenna can be produced regardless of the geometry of the near-field measurement. Alternatively, other authors have attempted global optimization algorithms [7] to search for equivalent sources placed surrounding the real radiator. However, most methods are focused on the prediction of the near and far fields, and the equivalent sources are not bound to be in the proximity of the PCB. Therefore the usefulness of these approaches in EMC diagnostics for emission sources is limited. Better characterization should include not only the representation of the emissions but also the location of the emission sources as well as the presence of the PCB. Then the equivalent sources can be included in a model of an electronic system replacing the PCB and fully representing the interaction with nearby objects.

In this chapter an equivalent model is developed for simulating electromagnetic emissions from a PCB in the whole free space region around it. The basic idea is to replace the PCB with a set of equivalent dipoles which generate the same radiated fields. The method includes three major steps. Firstly, planar near-field scans are performed above the PCB using the scanning system described in Chapter 2 to acquire sufficient information for electromagnetic characterization. Secondly, the model of equivalent sources is constructed to replace the real emission sources of the PCB, the equivalent sources being identified from the scanned near-field data. Finally, numerical simulations with equivalent sources are performed to predict the near and far fields.

3.2 Basic Equivalent Model

The objective of the method is to replace the emission sources of a PCB with an array of equivalent sources that should generate field values in the best possible agreement with those of the PCB. Considering the fact that the electromagnetic emissions from PCBs are normally produced by the currents of onboard components, infinitesimal dipoles are used for the equivalent sources as an infinitesimal dipole represents the emissions from an elemental current. Also, a dipole is the simplest radiator which can be included in any electromagnetic solver or self-developed code and thus keeps the computational costs low.

For generality, the model is built without *a priori* knowledge of the PCB structure or circuit information except its overall geometrical dimensions. The PCB is segmented with rectangular mesh and each segment is replaced by an arbitrarily orientated equivalent dipole. Thus the equivalent dipoles are in a matrix array. As most printed circuits are relatively thin, the equivalent point dipoles can be placed in a planar surface in the proximity of the PCB, as shown in Fig. 3.1.

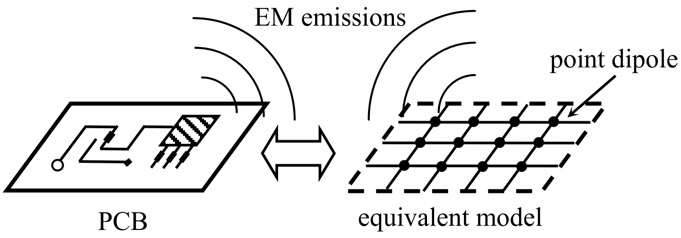

Fig. 3.1 Basic principle of the equivalent dipole model

Theoretically either electric or magnetic dipoles, or a combination of both, can be used as the equivalent sources of a PCB. Equivalent magnetic dipoles and electric dipoles are based on the equivalent representation of onboard currents by magnetic and electric currents, respectively. For free space problems, the use of magnetic dipoles with arbitrary orientations is illustrated.

The parameters of the model to be determined are the moment and orientation of each dipole.

To simplify the problem, each point dipole is decomposed into three moment components M^x, M^y and M^z. By doing this the orientation parameter θ is eliminated so it becomes a linear problem. Based on the equivalence principle, the equivalent dipoles should radiate the same field as the real PCB. Therefore, the moment (magnitude and phase) and orientation of the dipoles are determined by fitting the measured tangential magnetic field distribution in a near-field plane from a solution of the inverse problem. In Cartesian coordinates, the magnetic field H_x, H_y and H_z at (x, y, z) radiated by an infinitesimal dipole M^z at (x_0, y_0, z_0) can be expressed as (taking M^z component as an example) [9]

$$\begin{aligned}
H_x &= M^z \frac{jke^{-jkr}}{4\pi r^4}(x-x_0)(z-z_0)\left(jkr+3+\frac{3}{jkr}\right) = M^z\xi_x^z \\
H_y &= M^z \frac{jke^{-jkr}}{4\pi r^4}(y-y_0)(z-z_0)\left(jkr+3+\frac{3}{jkr}\right) = M^z\xi_y^z \\
H_z &= M^z \frac{jk^2e^{-jkr}}{4\pi r}\left[\frac{(z-z_0)^2}{r^2}\left(j+\frac{3}{kr}+\frac{3}{jk^2r^2}\right)-\left(j+\frac{1}{kr}+\frac{1}{jk^2r^2}\right)\right] \\
&= M^z\xi_z^z
\end{aligned} \tag{3.1}$$

where k is the wave number and r is the distance from the dipole to the measurement point given by:

$$r = \sqrt{(x-x_0)^2+(y-y_0)^2+(z-z_0)^2}$$

The other two components, M^x and M^y, have similar expressions with just a coordinate transformation.

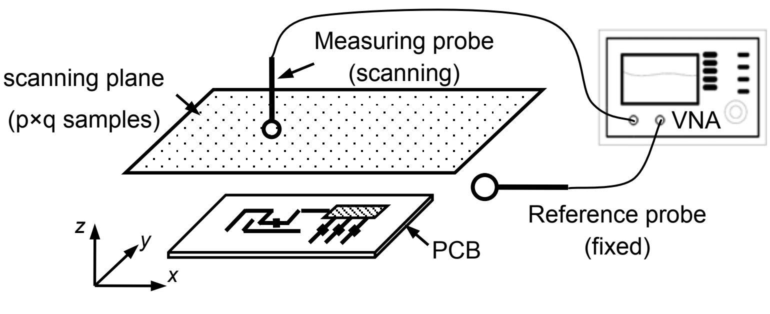

Fig. 3.2 Equivalent source identification from near-field scanning

Fig. 3.2 shows the configuration of equivalent source identification from near-field scanning. Both magnitude and phase of the tangential magnetic near field, H_x and H_y, over a plane above the PCB are measured discretely at $p \times q$ sampling points. The field at each measurement point is the total contribution of all the equivalent dipoles. Suppose there are m measurement sampling points and n dipole components, the measured tangential magnetic field in the planar array of discrete points are therefore related to the array of source magnetic dipoles by a linear matrix equation:

$$\begin{aligned} \begin{bmatrix} \xi_x^x & \xi_x^y & \xi_x^z \end{bmatrix}_{m\times n} \begin{bmatrix} M^x \\ M^y \\ M^z \end{bmatrix}_{n\times 1} &= \begin{bmatrix} H_x \end{bmatrix}_{m\times 1} \\ \begin{bmatrix} \xi_y^x & \xi_y^y & \xi_y^z \end{bmatrix}_{m\times n} \begin{bmatrix} M^x \\ M^y \\ M^z \end{bmatrix}_{n\times 1} &= \begin{bmatrix} H_y \end{bmatrix}_{m\times 1} \end{aligned} \tag{3.2}$$

where superscripts refer to the dipole components and subscripts to the measured field components.

In (3.2) the coefficients ξ_x and ξ_y, as defined in (3.1), depend on positions and frequency, thus the moment of each dipole can be found by solving the inverse problem of the linear equations in the frequency domain. To obtain a unique solution for M the total number of dipoles must not exceed the total number of measured field points ($n \leq m$). With accurate near-field measurement, the equivalent dipole sources fully characterize the radiation properties of the PCB for the half space where the near-field measurement is taken, both in the near field and far field.

3.3 Configuration of the Equivalent Dipoles

A test PCB, as shown in Fig. 3.3, is introduced and the analysis below takes this board as an example. It is an 80×50×1.5 mm board (FR4 substrate) with a 2 mm wide L-shaped microstrip track on one side and a ground plane on the other side. At one end the microstrip is powered with an external 1V RF voltage source, and at the other end it is terminated with a 50Ω load. The connection type of both ends of the board is female SMA.

In order to quantify the accuracy of the model, the mean squared error σ_{MSE} between the measured field intensities $[|H|]_{\mathrm{m}\times 1}$ and the reconstructed field intensities by the equivalent dipoles $[|H'|]_{\mathrm{m}\times 1}$ is introduced which is defined by

$$\sigma_{\mathrm{MSE}} = \frac{\left[|H'|-|H|\right]_{m\times 1}^{T}\left[|H'|-|H|\right]_{m\times 1}}{\left[|H|\right]_{m\times 1}^{T}\left[|H|\right]_{m\times 1}} \tag{3.3}$$

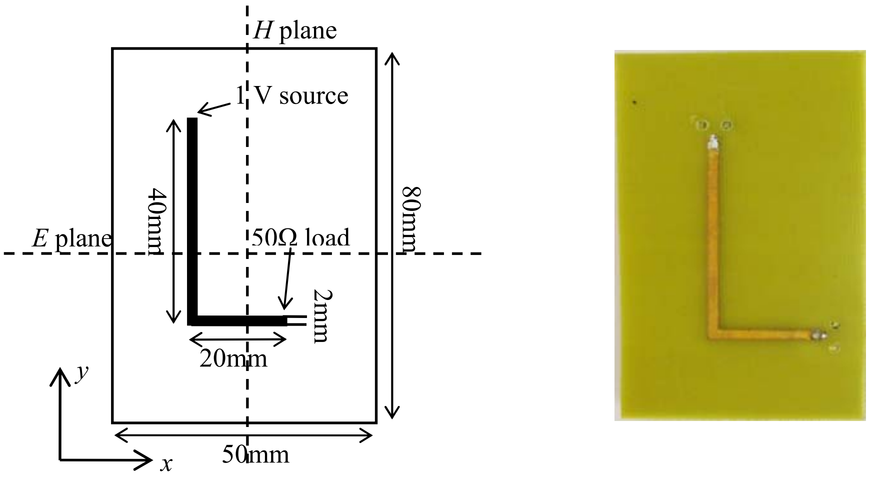

a) schematic

b) photograph

Fig. 3.3 Top view of the L-shaped microstrip test board

3.3.1 Number of Dipoles

The number of dipoles for the equivalent model (e.g. resolution of the matrix dipole array) depends on the size and complexity of the PCB. A larger number of equivalent dipoles, with a finer resolution, leads to higher accuracy but also requires more computational resources. This profile for the above test board at 1 GHz is shown in Fig. 3.4 where σ_{MSE} and CPU time of modelling with different array resolutions were investigated. Here the field data used to build the equivalent model were obtained from a full field numerical solution in a Method of Moment (MoM) based solver Concept-II 9.4 [10] thus no measurement error would affect the profile. The near-field plane was 75×120 mm with a 2.5 mm scanning resolution and 10 mm above the board.

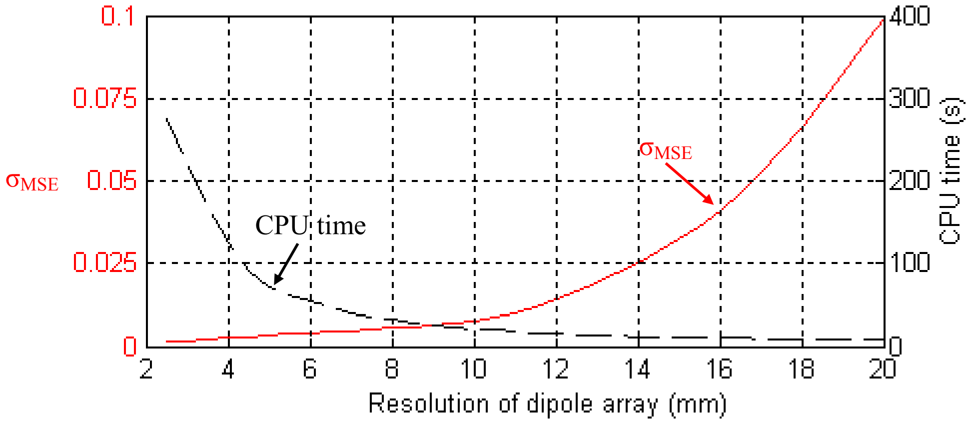

Fig. 3.4 Accuracy and computational time as a function of the dipole array resolution

It can be seen that below a critical resolution value (in this case around 10 mm), the model is able to achieve a good accuracy but the computational costs gradually increase. As minimizing the number of dipoles will significantly facilitate the subsequent modelling, a resolution near the critical value is a good tradeoff between accuracy and computational costs.

3.3.2 Simplification of the Array

The matrix array is simple to model, but may contain some redundant dipoles. On the other hand, an array found by optimization methods [11] is efficient but the long computational time and irregular position of dipoles can cause difficulties in subsequent numerical modelling where a regular mesh is normally employed. Here an efficient dipole array configuration is obtained by making some reasonable simplifications of the initial matrix array.

First, the moment of every dipole in the matrix is calculated. Then a simplification procedure is applied which involves ‘removing’ and ‘combining’, as shown in Fig. 3.5. Removing is applied if the absolute value of a dipole’s moment is very small. A removing factor is defined as s_{rem} in percent. With appropriate value of s_{rem} the dipoles with a moment < s_{rem} of the maximum dipole moment can be removed without creating a significant error and their small contribution to the total field will be compensated by other dipoles. Combining is applied if the moment of a dipole is very similar to that of the adjacent dipoles, as the contribution of these dipoles to the total field can be approximated by a single dipole placed at the centre of the original cluster dipoles. A combining factor is defined as s_{com} in percent. Therefore, adjacent dipoles whose real and imaginary parts of the moments are within s_{com} are combined. Finally, after the simplification procedure the moments of these dipoles in the reduced array are re-calculated to build the final model.

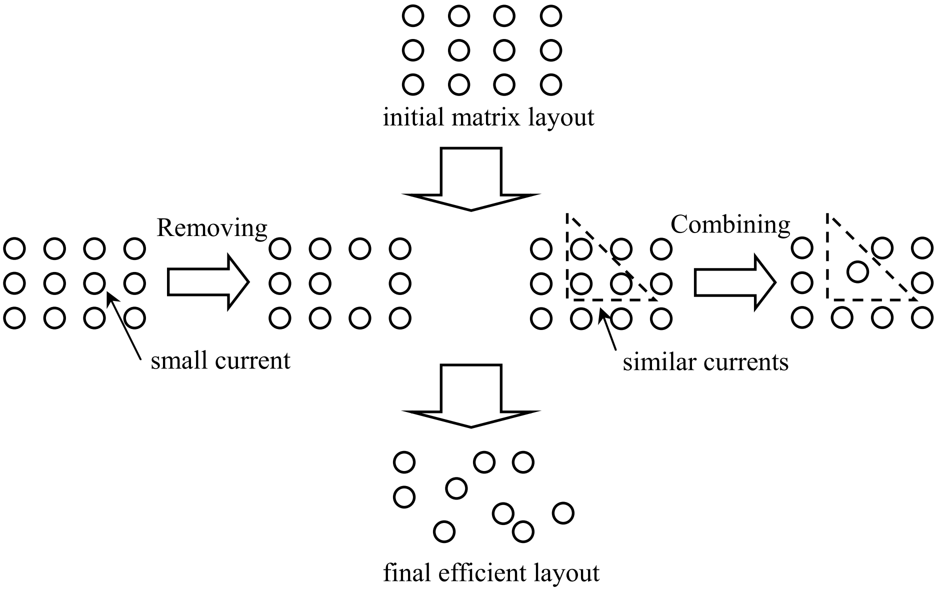

Fig. 3.5 Simplification of the equivalent dipole array

The effectiveness of the simplification procedure is shown in Fig. 3.6 taking the model of the test board as an example. A matrix array of 5 mm resolution was initially modelled.

Increasing the simplification factors can gradually reduce the number of dipoles but too much simplification leads to a significantly increased error. Also, from Fig. 3.6(b) there is a critical value for the simplification factors below which σ_{MSE} is almost a constant. Therefore considering both simplicity and accuracy, the choice of s_{rem} and s_{com} near the critical value is reasonable, e.g. s_{rem} between 10~15% and s_{com} between 10~20%. After simplification, the more efficient array normally has approximately 70% of the original number of dipoles.

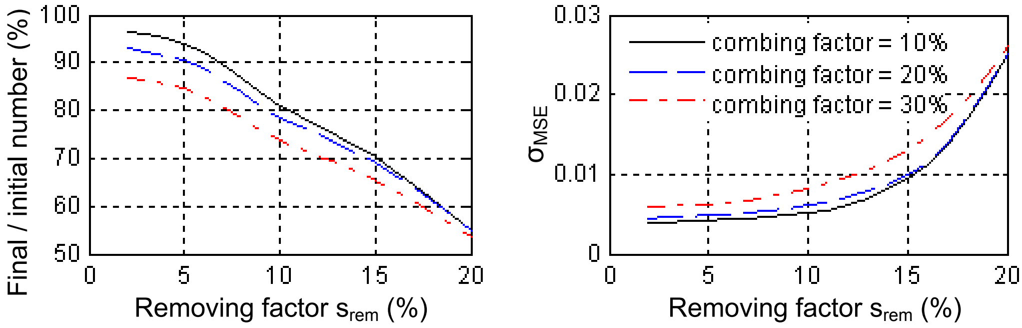

a) effects on the number of dipoles

b) effects on modelling

Fig. 3.6 Effectiveness of the simplification

3.4 Modelling the Ground Plane

When a PCB is backed by a ground plane, it causes a difficulty in the mapping of the far-field radiation in the space below the ground plane where the near field is normally too weak to be measured due to the finite dynamic range of the measurement system. Moreover, the edge effects of a finite ground plane lead to inaccuracies when the far field is calculated near the equatorial plane (plane of PCB). An interesting approach for the equivalent current method is proposed in [8] where the uniform theory of diffraction (UTD) is introduced to account for the edge effects of a ground plane, for antennas with particular configurations. However, the UTD has a limited application range requiring that the size of a scatterer must be large relative to the wavelength [12, Chapter 1].

To deal with these problems, the finite ground plane is directly included in the model to account for its diffraction effects. Considering that the circuit structure is unknown, equivalent dipoles are placed on a surface which is *h* (*h* is the thickness of the PCB) above the ground plane and over an area that is 6*h*~10*h* smaller than the PCB dimensions, and the ground plane is modelled as a perfect conducting plate of the real PCB size, as depicted in Fig. 3.7.

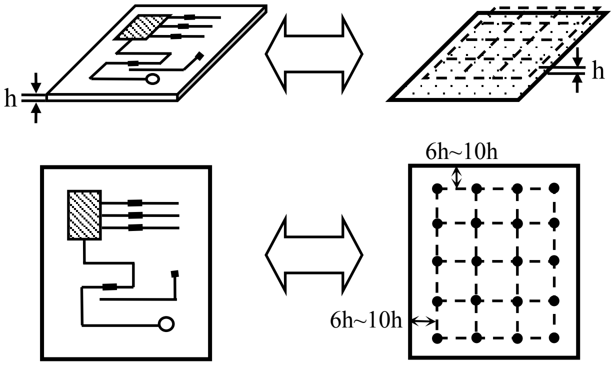

Fig. 3.7 Equivalent model for a grounded PCB: dipoles and ground

Image theory is used in the equivalent source identification. For a finite ground plane, the total field has a diffraction term besides the direct and image terms. Therefore to apply image theory the near-field scans must be performed in a region where the magnetic fields are to a good approximation the contribution of direct and image radiation, with only a negligible proportion of diffraction. The reactive near field vertically above the PCB is such a region. Fig. 3.8 shows the diffraction term and total field in a reactive near-field plane (10 mm above) from a single dipole in an arbitrary position over a ground plane. Diffractions were calculated from a MoM solution. The diffracted term is more than 9 dB smaller than the total field in the places where the dipole contributes significantly to the measured field, confirming the reactive near field is a good approximation to apply image theory. This agrees with the analytical expressions for radiations of microstrip antenna on a finite ground plane [13]. Therefore in the source identification procedure the ground plane can be assumed to be of infinite size.

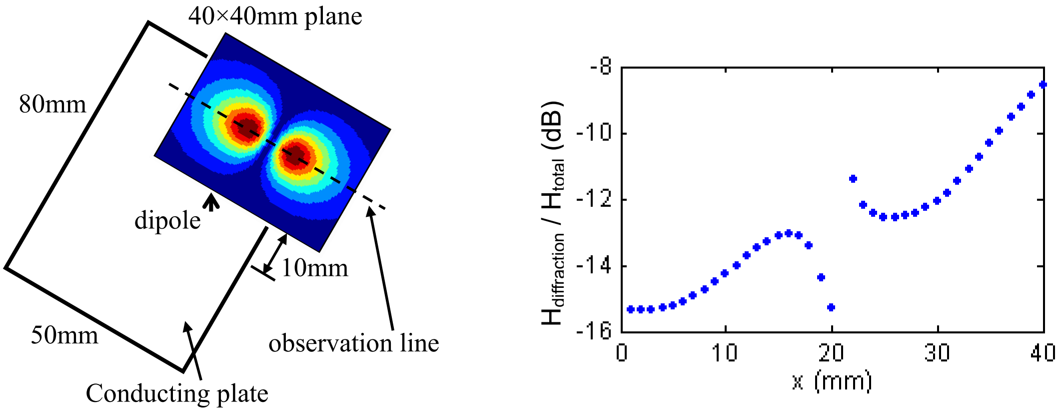

a) Position of dipole and observation plane b) $H_{diffraction}$ / H_{total} along the observation line

Fig. 3.8 The reactive near field of a dipole over a conducting plane: the diffraction term and the total field

Based on these approximations, applying image theory and assuming an infinite ground plane the equivalent dipoles can then be identified as:

$$\begin{aligned}
\begin{bmatrix}\xi_x^x & \xi_x^y & \xi_x^z\end{bmatrix}_{m\times n}\begin{bmatrix}M^x\\ M^y\\ M^z\end{bmatrix}_{n\times 1}+\begin{bmatrix}\xi'^{x}_{x} & \xi'^{y}_{x} & \xi'^{z}_{x}\end{bmatrix}_{m\times n}\begin{bmatrix}M^x\\ M^y\\ M^z\end{bmatrix}_{n\times 1}&=\begin{bmatrix}H_x\end{bmatrix}_{m\times 1}\\
\begin{bmatrix}\xi_y^x & \xi_y^y & \xi_y^z\end{bmatrix}_{m\times n}\begin{bmatrix}M^x\\ M^y\\ M^z\end{bmatrix}_{n\times 1}+\begin{bmatrix}\xi'^{x}_{y} & \xi'^{y}_{y} & \xi'^{z}_{y}\end{bmatrix}_{m\times n}\begin{bmatrix}M^x\\ M^y\\ M^z\end{bmatrix}_{n\times 1}&=\begin{bmatrix}H_y\end{bmatrix}_{m\times 1}
\end{aligned}\qquad(3.4)$$

where the superscript and subscript have the same meaning as in (3.2). The second term in (3.4) represents the contribution of the image dipoles. So far the equivalent sources have been identified and a model consisting of an array of equivalent magnetic dipoles and a finite ground plane has been built with only one plane scanned. Following this, the near and far field can be obtained by simulating the emissions from this configuration using a numerical field technique such as MoM. The diffraction caused by the finite ground plane, which makes a more significant impact near the equatorial plane and below the ground, is implicitly included in this numerical calculation procedure by computing the currents on the ground plane. Since the structure that has to be defined in the full-field model is only a perfect conducting plate, the computational cost is very low. To build the model, some information of the PCB must be known in advance, i.e. the dimension of the ground plane and the thickness of the PCB. Normally this information is readily available at the design phase or can be obtained during the near-field scanning.

It must be noted that the model is built based on the approximation that the diffraction term is negligible in the imaging configuration. It has been shown that the vertical reactive near field is a good region to satisfy this condition, but if the scans go too far beyond this region the approximation is more likely to be invalid. So only near-field data acquired in the allowed region can be used for the model, and the modelling accuracy also depends on how good the experimental scans can be made to satisfy the approximations. In addition, in the equivalent method the dipoles are not meant to represent the real current distribution but to replace the PCB as an equivalent radiation source.

3.5 Numerical Accuracy

3.5.1 Effects of Measurement Errors

The equivalent dipoles are derived from near-field measurement which is always associated with errors. In Chapter 2 the error sources of the scanning system were identified and a typical error bound 0.35 dB was predicted. The effects of measurement errors on the calculated dipoles through the numerical computation are examined here. The moments of the equivalent dipoles are numerically determined from the inverse problem of a linear equation system:

$$\xi \cdot \overline{M}e^{i\vec{\theta}} = \overline{H}e^{i\vec{\phi}} \tag{3.5}$$

where ξ is the coefficient matrix, $\overline{M}$ and $\vec{\theta}$ are vectors of the amplitude and phase of equivalent dipoles, and $\overline{H}$ and $\vec{\phi}$ are vectors of the amplitude and phase of measured magnetic fields. ξ has exact values but $\overline{H}e^{i\vec{\phi}}$ contains inevitable errors $\overline{\Delta H}$ and $\overline{\Delta\phi}$, leading to errors in the resulting dipole moments. The linear equation system then becomes:

$$\xi\cdot\left(\overline{M}e^{i\vec{\theta}}+\overline{\Delta M}e^{i\overline{\Delta\theta}}\right)=\left(\overline{H}+\overline{\Delta H}\right)e^{i\left(\vec{\phi}+\overline{\Delta\phi}\right)}=\left[\overline{H}e^{i\overline{\Delta\phi}}+\overline{\Delta H}e^{i\overline{\Delta\phi}}\right]e^{i\vec{\phi}} \tag{3.6}$$

The right-hand side can be Taylor expanded with only terms of first and second order retained.

$$\xi\cdot\left(\overline{M}e^{i\vec{\theta}}+\overline{\Delta M}e^{i\overline{\Delta\theta}}\right)=\overline{H}e^{i\vec{\phi}}+\left(\overline{\Delta H}+i\overline{H}\,\overline{\Delta\phi}+i\overline{\Delta H}\,\overline{\Delta\phi}-\overline{H}\,\overline{\Delta\phi^{2}}/2\right)e^{i\vec{\phi}} \tag{3.7}$$

From (3.5) and (3.7), the following relationship can be obtained

$$\overline{\Delta M}e^{i\overline{\Delta\theta}}=\xi^{-1}\cdot\left(\overline{\Delta H}+i\overline{H}\,\overline{\Delta\phi}+i\overline{\Delta H}\,\overline{\Delta\phi}-\overline{H}\,\overline{\Delta\phi^{2}}/2\right)e^{i\vec{\phi}} \tag{3.8}$$

$$\left\|\overline{\Delta M}e^{i\overline{\Delta\theta}}\right\|\le\left\|\xi^{-1}\right\|\cdot\left\|\left(\overline{\Delta H}+i\overline{H}\,\overline{\Delta\phi}+i\overline{\Delta H}\,\overline{\Delta\phi}-\overline{H}\,\overline{\Delta\phi^{2}}/2\right)e^{i\vec{\phi}}\right\| \tag{3.9}$$

where the operator $\left\|\bullet\right\|$ stands for the Euclidean norm [14, Chapter 2].

From (3.5), another relationship can be obtained as

$$\left\|\xi\right\|\cdot\left\|\overline{M}e^{i\vec{\theta}}\right\|\ge\left\|\overline{H}e^{i\vec{\phi}}\right\| \tag{3.10}$$

Therefore the upper bound of relative error in the equivalent dipoles due to measurement errors can be expressed by combining (3.9) and (3.10) as

$$\frac{\left\|\overline{\Delta M}e^{i\overline{\Delta\theta}}\right\|}{\left\|\overline{M}e^{i\vec{\theta}}\right\|}\le\operatorname{cond}\left(\xi\right)\cdot\frac{\left\|\left(\overline{\Delta H}+i\overline{H}\,\overline{\Delta\phi}+i\overline{\Delta H}\,\overline{\Delta\phi}-\overline{H}\,\overline{\Delta\phi^{2}}/2\right)e^{i\vec{\phi}}\right\|}{\left\|\overline{H}e^{i\vec{\phi}}\right\|} \tag{3.11}$$

where $\operatorname{cond}\left(\xi\right)=\left\|\xi^{-1}\right\|\cdot\left\|\xi\right\|$ is the condition number of matrix ξ [14, Chapter 2]. $\overline{\Delta H}$ and $i\overline{H}\,\overline{\Delta\phi}$ in the right hand side represent the dominant error terms in measured magnitude and phase, respectively. Due to the fact that the condition number of a matrix is always ≥1, small errors in measurement may be magnified in the resulting equivalent dipole array. Mathematically this situation is called an ill-conditioned equation system.

Equation (3.11) links the possibly largest modelling errors to a number of factors, including magnitude and phase error of measured data and conditioning of the inverse problem. A commonly used technique to evaluate an over-determined equation system is the least square method, e.g. seeking a solution *M* to satisfy

$$\min \left\| \xi M - H \right\|^2 \tag{3.12}$$

To examine the modelling error using the least square method, the equivalent dipoles for the test board in Fig. 3.3 were built with near-field data with intentionally added noise. Both amplitude and phase of the noise followed a normally distribution so the standard deviation corresponded to the measurement uncertainty. The phase uncertainty was calculated from the amplitude uncertainty using (2.31) as described in Section 2.8.5. The mean squared errors σ_{MSE} between the original and reconstructed near fields are presented in Fig. 3.9.

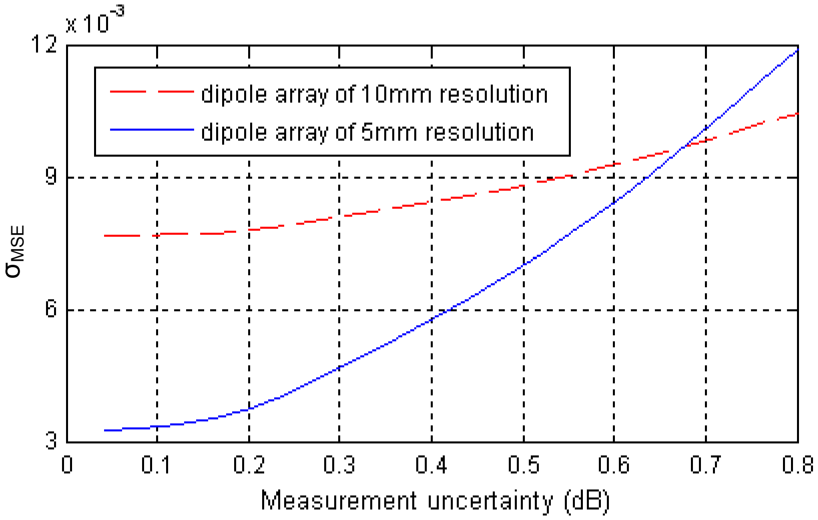

Fig. 3.9 Modelling error transmitted from measurement errors

Two dipole arrays, with a different resolution of 5mm and 10mm, were employed for the model. It can be seen that the accuracy of the inverse problem is obviously affected by measurement errors. Also, the finer the array resolution (e.g. dipoles of higher density), the effects are more sensitive. When the measurement error is greater than 0.7 dB, modelling with a finer array (5mm resolution) even leads to a greater error than a coarser one (10mm resolution). This is because the modelling error depends not only on the measurement errors but also on the condition number of the coefficient matrix ξ of the equation system according to (3.11). In this particular model, the condition number of the dipole array with 10 mm and 5 mm resolution is 64 and 7347, respectively. Therefore, a mathematical technique to reduce the dependence on measurement errors and to enhance the numerical stability would be useful.

3.5.2 Regularization

Mathematically the inverse problem associated with the equivalent dipole method is based on complex linear equations which are actually the discrete version of the Fredholm equations of the first kind [15]. Numerical tools for the analysis and solution of these equations have been extensively discussed. A useful way to deal with ill-conditioned and noisy equation systems is the regularization technique. In this work a classical regularization scheme proposed by Tikhonov [16] and the L-curve method for optimizing the regularization proposed by Hansen [15] are used. Some related mathematics are described in Appendix B.

Regularization for the inverse problem

For a linear algebraic problem $Ax = b$ where there are some deviations in *b*, the objective is to seek to single out a solution which is, in some sense, close to the desired but unknown exact solution. Given some *a priori* estimate x_0 of the solution, regularization requires one more term to minimize besides the original noisy algebraic problem which is the Euclidean norm of the difference between the computed solution x and the estimate x_0:

$$\min\left\|L\left(x-x_0\right)\right\|_2 \tag{3.13}$$

where L is an appropriately chosen matrix (typically either the identity matrix or discrete approximation to a derivative operator). The quantity in (3.13) is called the side constraint of the solution to the algebraic problem.

Then the side constraint is combined with the original algebraic problem and a regularized solution x_λ is to be determined from the solution of the combined minimum:

$$\min\left\{\left\|Ax-b\right\|_2^2+\lambda\left\|L\left(x-x_0\right)\right\|_2^2\right\} \tag{3.14}$$

where λ is the regularization parameter controlling the weight given to the minimization of the side constraint relative to the minimization of the residual norm. Therefore, the criterion of Tikhonov regularization includes the minimization of two quantities – the original least square and the side constraint which are balanced by the parameter λ. If the null spaces of A and L intersect trivially, then the regularized solution x_λ to (3.14) is unique and formally given by

$$x_\lambda=\left(A^{\mathrm{T}}A+\lambda L^{\mathrm{T}}L\right)^{-1}A^{\mathrm{T}}b \tag{3.15}$$

where A^{T} is the complex conjugate transpose of matrix A.

Determination of the regularization parameter

The next problem is the choice of the regularization parameter λ. It is discussed in [15] that too much regularization leaves out information actually available in b while too little regularization produces a solution dominated by errors. Hence, one should ideally find a regularization parameter that balances the regularization error and the perturbation error from the errors in b. This optimal regularization parameter is determined using the L-curve method.

The L-curve is a log plot of side constraint $\|L(x_\lambda-x_0)\|_2$ versus residual norm $\|Ax_\lambda-b\|_2$, as shown in Fig. 3.10. It is in fact a parametric curve with regards to λ. Mathematically it has been proven [17] that for most problems the curve has an L-shaped "corner" corresponding to the optimal λ for the balance discussed above. Once the optimal λ has been determined, the regularized solution x_λ to the linear equation system can be found from (3.15).

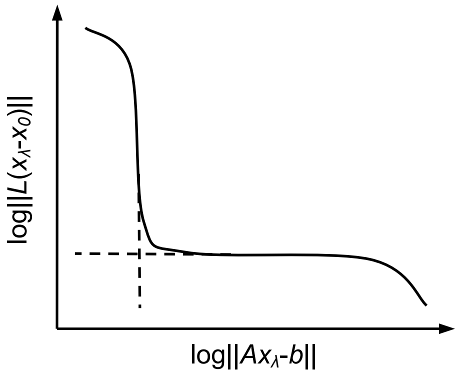

Fig. 3.10 A generic plot of the L-curve for the right-hand side consisting of errors

Although very effective, the L-curve method has a drawback that the optimal λ can not be determined directly from a closed form. Some alternative techniques have been proposed based on different principles [18]-[20]. An easy to implement one is the generalized cross-validation (GCV) scheme [20]. Its underlying principle is that if an arbitrary observation is left out and then predicted using the remaining m-1 observations, then the optimal regularization parameter minimizes the sum of squares of these prediction errors. This leads to choosing the regularization parameter as the minimizer of the following function:

$$G(\lambda)=\frac{\left\|\left(I_{\mathrm{m}}-A\left(A^{\mathrm{T}}A+\lambda L^{\mathrm{T}}L\right)^{-1}A^{\mathrm{T}}\right)b\right\|_2^2}{\left[\operatorname{trace}\left(I_{\mathrm{m}}-A\left(A^{\mathrm{T}}A+\lambda L^{\mathrm{T}}L\right)^{-1}A^{\mathrm{T}}\right)\right]^2} \tag{3.16}$$

where I_m is an $m\times m$ identity matrix and trace(X) is the trace of matrix X. Numerically this minimization is very easy to implement as $G(\lambda)$ is a explicit function of λ. Hansen has pointed out that the GCV selection often leads to an optimal λ close to that from the L-curve method.

Validation of the technique

In order to validate the regularization technique, equivalent modelling for the test board with noisy near-field data was repeated. An extreme example is first demonstrated where the intentionally added noise was as large as 1.5 dB (hence 25° for phase) following a normal distribution, and a dipole array of a resolution 10mm was modelled. Fig. 3.11 shows the determination of the optimal regularization parameter λ. With the GCV and L-curve method, the optimal λ was singled out at approximately 6×10^{-2} and 3×10^{-2} respectively which were not very different from each other. Regularization was then applied to the noised inverse problem. The original, noised and retrieved magnetic field component H_x is illustrated in Fig. 3.12. It can be seen that the field map has been seriously distorted by the 1.5 dB noise. The maximum field intensity is boosted from approximately 18 to 26 mA/m. However, after regularization for the inverse problem the integrity of the field has been retrieved and the field intensity has also been correctly represented.

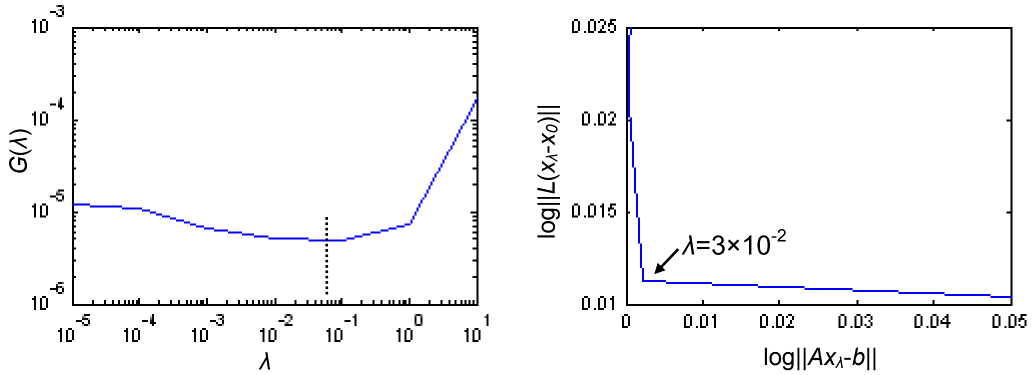

a) *G(λ)* as a function of λ　　b) corresponding L curve

Fig. 3.11 An example of determination of the optimal regularization parameter

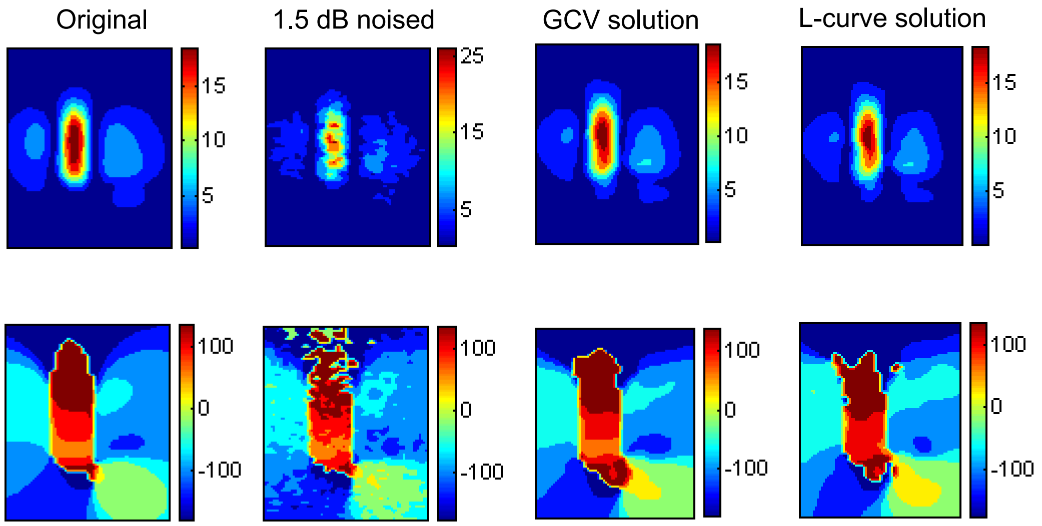

Fig. 3.12 An example of the effects of regularization for the inverse problem

1st row: $|H_x|$ in mA/m; 2nd row: phase(H_x) in °

The effectiveness of regularization is then demonstrated by comparing with the least square method. Fig. 3.13 shows the resulting mean squared error between the original field and the field reconstructed from data with different levels of error. A significant improvement can be observed for both the 5mm resolution array (worse conditioned) and the 10mm one (better conditioned), especially when the measurement error becomes considerable.

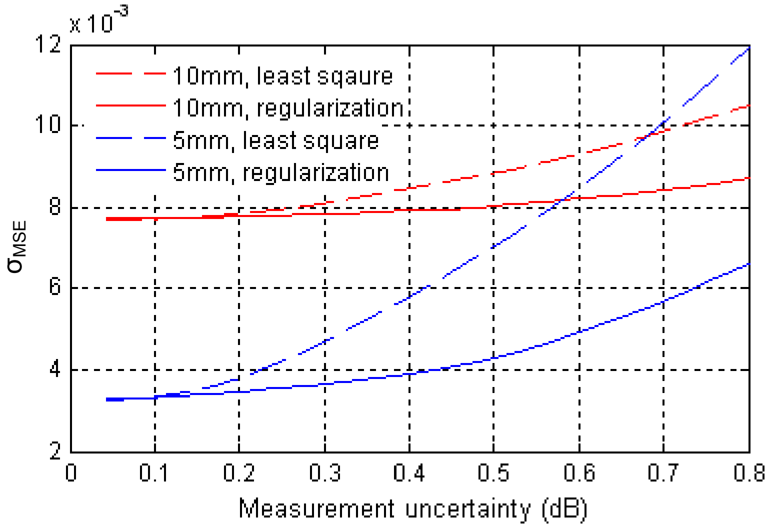

Fig. 3.13 A comparison of modelling error using the least square method and L-curve regularization method

3.6 Simulation Results

One of the main interests in EMC tests is the intensities and distributions of the radiated fields from an EUT. Results of the model and numerical techniques described in previous sections are presented here for the near- and far-field emissions from two PCBs. One is a basic test board with only a bent microstrip printed on the substrate and the other is a more complex commercial telemetry board. The former can be modelled directly in a full-field solver so the results given by the equivalent dipole simulations are compared with direct full-field simulations. The latter PCB represents a more generic situation that is not practically possible to be modelled in a full field solver. Therefore the results from this board are compared with measurements only. All full field simulations were performed with a Method of Moment (MoM) based solver Concept – II 9.4 [10].

3.6.1 Validation with a Test Board

Building the model

The simple structure of the test board with an L-shaped microstrip backed by a ground plane, as shown in Fig. 3.3, allows for an accurate full field simulation to be made for validation purposes. The frequency is arbitrarily chosen to be 1 GHz.

TABLE 3.1 Configuration of near-field measurements with the test board

frequency (GHz)	1
scanning plane height (mm)	11.5 above the PCB
scanning plane size (mm)	120 × 75
scanning resolution (mm)	2.5
sampling points	49 × 31

To obtain the equivalent model, tangential magnetic fields (H_x and H_y) were measured over a near-field plane on the near-field scanning system described in Chapter 2. Details of the measurements are listed in Table 3.1. The equivalent model consisting of an initial matrix of 8×5=40 dipoles within an area of 64×36 mm in the plane of the PCB plus a real-sized ground plane was then built. The near fields represented by the equivalent dipoles are compared with measurements in Fig. 3.14. The inner border shows the position and size of the PCB. Good agreement is observed. The patterns of the simulated fields are almost the same as the measured ones, although there are slight differences (< 0.1 dB) in the maximum magnitude.

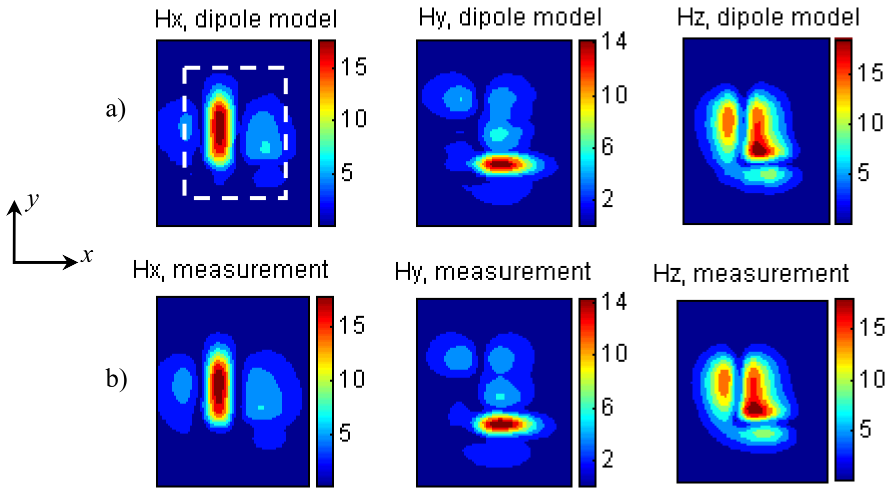

Fig. 3.14 Magnetic field in the scanning plane (field unit in mA/m)

a) Simulation based on equivalent dipole model; b) measurement

Near field prediction

With the equivalent model, it is possible to predict emissions from the PCB at any position by solving the model consisting of magnetic dipoles plus a ground plane using a numerical technique such as the MoM. First, prediction for two near-field planes on the side of the PCB is demonstrated. Fig. 3.15(a) shows the setup. The scans performed for building the model were vertically above the PCB and did not cover the two prediction planes which extended from below to above the PCB. The total E and H fields were simulated and compared with full-field simulations in Fig. 3.15(b) and Fig. 3.15(c) for the left and right side plane, respectively. Good agreement can be observed for the field distributions. Particularly, the maximum field intensities in each field map are summarized in Table 3.2. The equivalent model and full-field simulation give very close results with a difference within 0.5 dB.

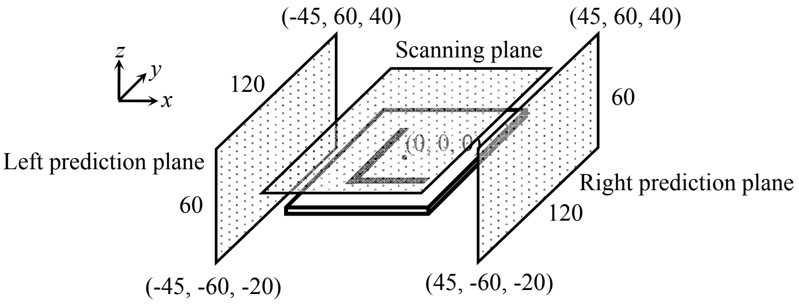

a) Schematic of the configuration

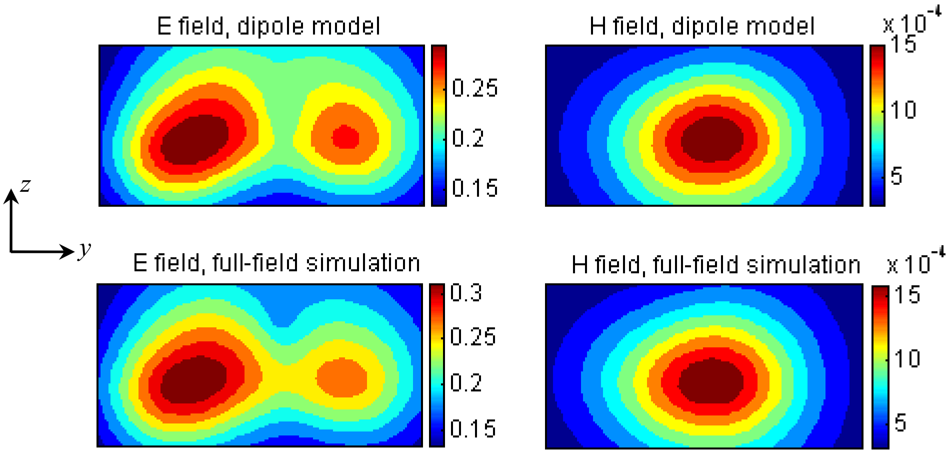

b) Fields over the left side plane

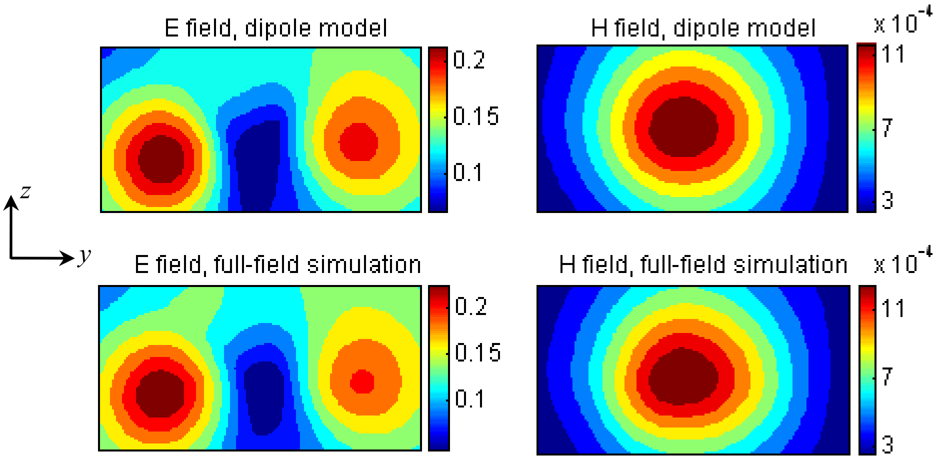

c) Fields over the right side plane

Fig. 3.15 Electromagnetic fields over the side planes (E field unit in V/m, H field unit in A/m)

TABLE 3.2 Maximum field intensities in the side planes

	Left plane E	Left plane H	Right plane E	Right plane H
Dipole model	0.317 V/m	1.66 mA/m	0.234 V/m	1.29 mA/m
Full-field simulation	0.336 V/m	1.76 mA/m	0.249 V/m	1.34 mA/m

The model was built with near-field information from only above the PCB but emissions in other regions can be also mapped correctly. Below the ground plane diffractions have a more considerable contribution to the total field. Computation for this effect has been implicitly included in the numerical solution for the model. Moreover, although the model was built from tangential magnetic near-field scans, both electric and magnetic fields can be obtained once the model is built. These results confirm that the model fully characterizes the electromagnetic properties of the PCB in the whole space with only one near-field plane scanned.

Far-field prediction

Next, the far field produced by the test board is predicted. Suppose the PCB is in the *xy* plane as shown in Fig. 3.3, the predicted far-field patterns in the *E* plane (*xz* plane or φ=0), *H* plane (*yz* plane or φ=90º) and PCB plane (*xy* plane or θ=0º) are presented in Fig. 3.16(a), (b), (c), respectively, and compared with full field simulation results. The azimuth and polar components E_θ and E_φ are shown separately. In the upper half space (-90º<θ<90º), where we have near-field information, the mapped far fields agree well with direct simulations with less than 2 dB difference. In the lower half space (90º<θ<270º, below the ground plane), the far field intensity is comparable to that above the ground, because the finite ground plane (8×5 cm) is relatively very small compared to the wavelength (30 cm). But the effects of incomplete grounding and the field diffraction are represented by the model with ±3dB accuracy.

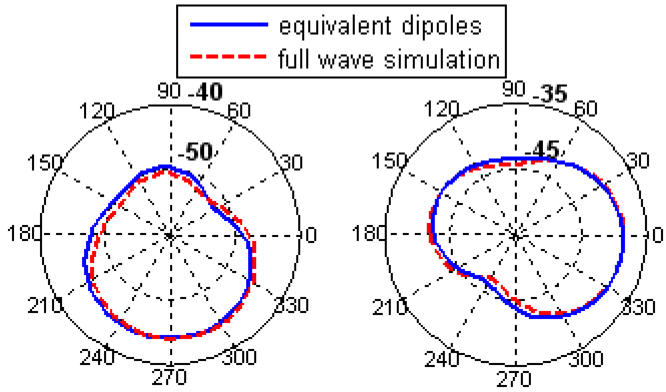

a) Far field in the *E* plane (Left: E_θ; right: E_φ)

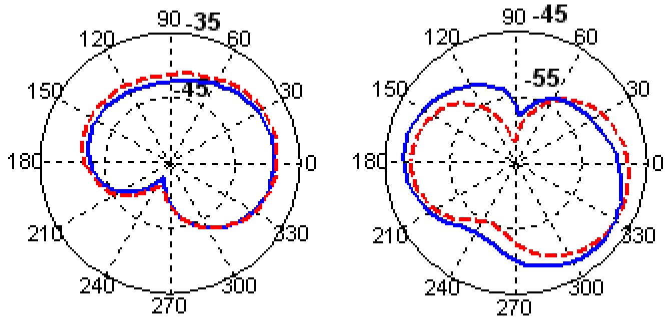

b) Far field in the *H* plane (Left: E_θ; right: E_φ)

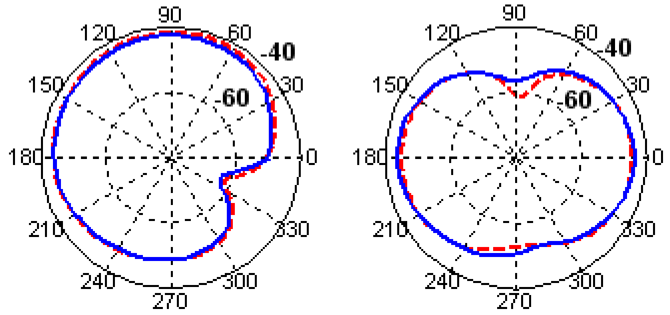

c) Far field in the PCB plane (Left: E_θ; right: E_φ)

Fig. 3.16 Electric far-field patterns of the test board (field unit in dB V)

Computational costs

An advantage of the equivalent dipole method is the computational simplicity which leads to lower computing requirements and a faster simulation run time. Information on computational costs compared with the full field simulation is summarized in Table 3.3. Nevertheless, if the PCB’s structure becomes more complex, the computational costs of the full field solver will rapidly increase, but for the equivalent dipole model they remain almost at the same level.

TABLE 3.3 Comparison of computational costs

	Memory required	Runtime	Modelling time
Equivalent dipole simulation	10 MB	1 min	5 min
Full-field simulation	200 MB	20 min	30 min

3.6.2 Application on a Telemetry PCB

The PCB and its equivalent dipole model

The equivalent dipole model is applied for a practical PCB. The board is used for radio telemetry operating at 868.38 MHz which consists of a data encoding module (manufacturer: RF Solutions, Part No.: FM-RTFQ1-868), an external meander antenna, and some bypass components, as depicted in Fig. 3.17(a) (b). Due to the complexity of the structure, it is impossible to directly model the PCB in a full field solver, so the results given by the equivalent dipole simulation are compared with measurements only.

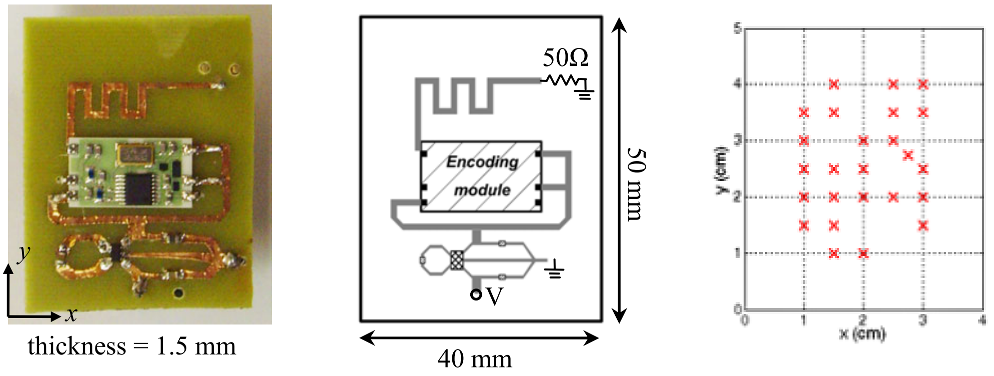

a) b) c)

Fig. 3.17 Geometry of the telemetry PCB and it equivalent dipole model (top view)

a) photo; b) schematic; c) equivalent dipole configuration

TABLE 3. 4 Configuration of near-field measurements with the telemetry PCB

frequency (MHz)	868.38
scanning plane height (mm)	12 above the PCB
scanning plane size (mm)	100 × 80
scanning resolution (mm)	2.5
sampling points	41 × 33

As with the procedure used for the first test board, tangential magnetic fields (H_x and H_y) were measured and the details are listed in Table 3.4. The equivalent magnetic dipoles were then derived with initially 7×5=35 dipoles in a matrix layout. After simplification there were 25 dipoles left and the layout is shown in Fig. 3.17(c). Fig. 3.18 compares the measured and reconstructed fields. The difference in the maximum field intensities is within 0.4 dB. Good agreement shows that the method works well for this more complex configuration.

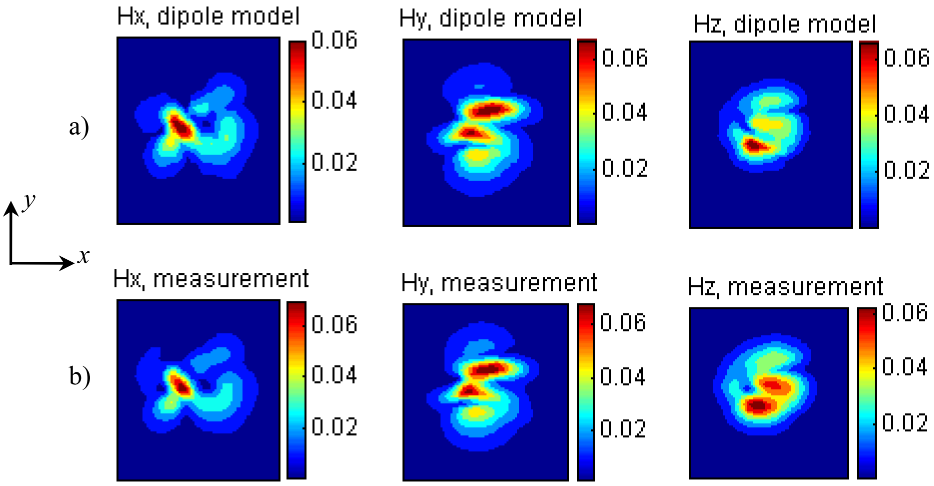

Fig. 3.18 Magnetic field in the scanning plane (field unit in A/m)

a) Simulation based on equivalent dipole model; b) measurement

Near-field prediction

The prediction is still focused on the distributions and intensities of the electromagnetic fields. Fig. 3.19 shows the magnetic near-field distribution in a 100×80 mm plane which is 30 mm above the PCB. Fig. 3.20 shows the variation of the vertical electric field component (E_z) along a vertical line which extends from the centre of the PCB upwards. Both predictions are compared with near-field measurements. Limited by the sensitivity of the probe, the measurement for E_z field variation was performed up to a height of 50mm. In the studied range, a good agreement can be obtained between the model and the measurement.

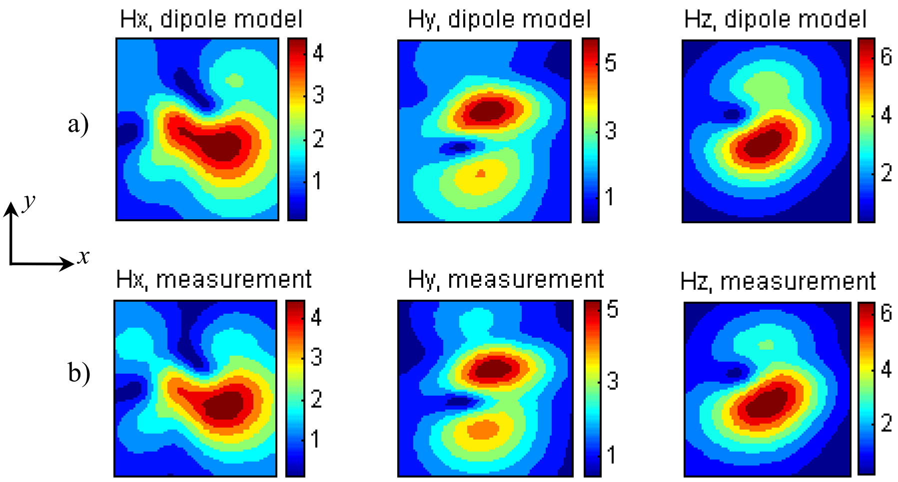

Fig. 3.19 Magnetic field at 30mm above the PCB (field unit in mA/m)

a) Simulation based on equivalent dipole model; b) measurement

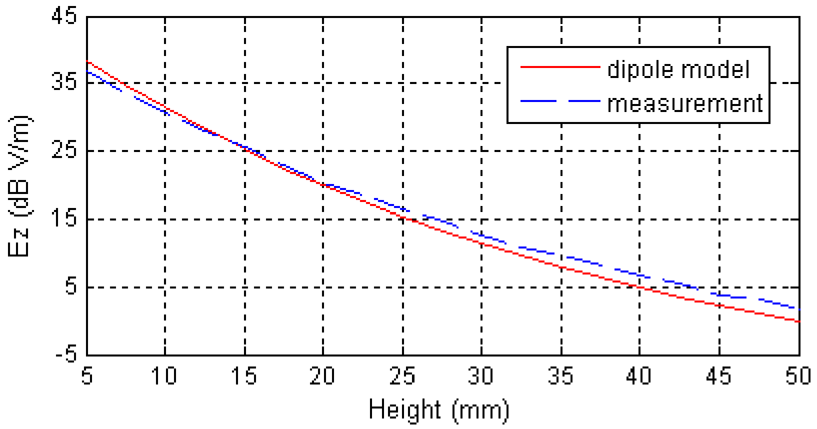

Fig. 3.20 Evolution of E_z against the observation height from the PCB (field unit in dB V/m)

Far-field prediction

Another topic of interest is the prediction of the far field. The measurements for comparison purposes were taken at 3 m distance in a semi-anechoic chamber according to the standard of generic emission test EN 55022 [21]. The PCB was mounted on a non-conductive turntable 0.8 m above the chamber floor. The fields were received with a horn antenna placed by 3 m from the PCB. The azimuth and polar far-field components E_θ and E_φ in the E plane were swept by rotating the PCB through 360º. The far-field results obtained by the prediction of the equivalent model and measurements are illustrated in Fig. 3.21. An acceptable agreement can be found with less than 3 dB difference error at most observation points. However, it should be pointed out that the tested frequency 868.38 MHz is close to the upper applicable range of the chamber (approximately 1 GHz). The imperfect propagation characteristics of the chamber were not taken into account in the test. This might be the reason for the slight shift of angle and scale appearing on the far-field patterns.

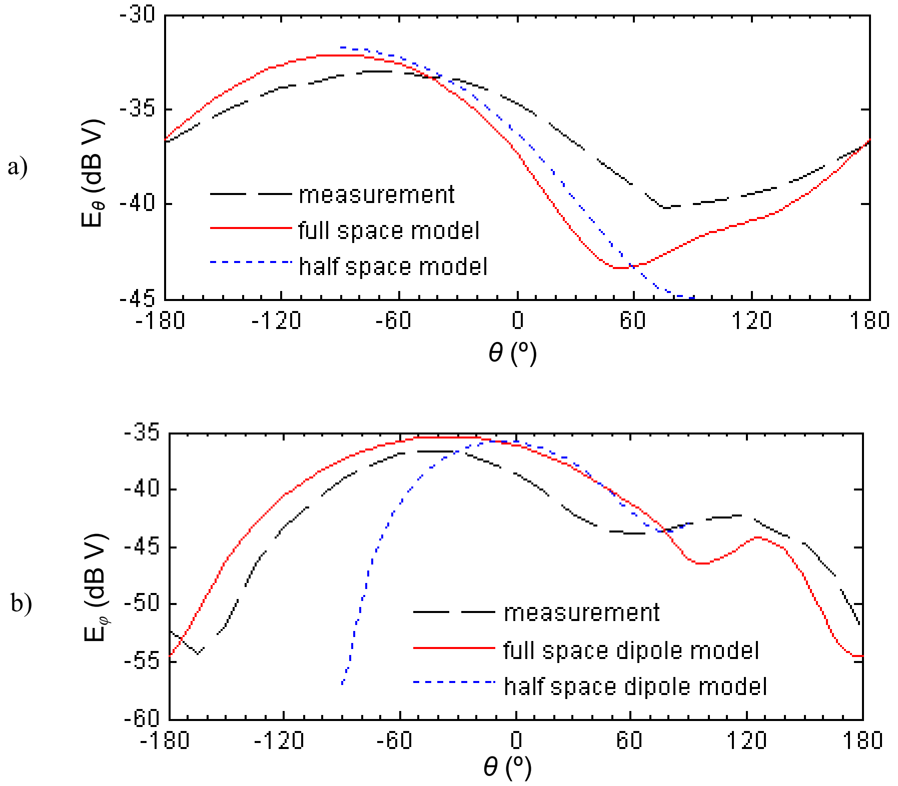

Fig. 3.21 Far-field patterns of the telemetry PCB in the E plane (field unit in dB V)

a) E_θ;   b) E_φ

As a comparison, the far field predicted by the basic equivalent model without an equivalent ground plane is also shown in the figure. As expected, the basic model without a ground plane only works in the upper half space (-90º<θ<90º) and is obviously in error when approaching the equatorial plane.

3.6.3 Discussions

The equivalent dipole model permits a good representation for the electromagnetic emissions produced by PCBs. However, for a grounded PCB the approximations made to the ground plane require that all the radiators must be mounted on the substrate of the PCB. If the PCB has an outboard radiator, for example, an external antenna mounted on the L-shaped microstrip board as depicted in Fig. 3.22(a), the techniques applied to the ground plane will not be appropriate. This is because the mechanism of interactions between outboard radiators and the ground plane is different from that of onboard radiators. Modelling the whole structure in Fig. 3.22(a) simply using a single dipole array plus a ground plane leads to unacceptably erroneous results. Fig. 3.23 shows the far-field patterns in the E plane obtained with a single dipole array for the whole PCB setup where completely erroneous results can be found. For better accuracy the outboard antenna must be regarded as another radiator additional to the PCB and modelled separately.

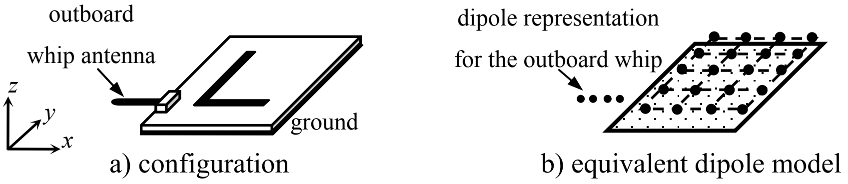

a) configuration b) equivalent dipole model

Fig. 3.22 An example of a PCB with an outboard radiator

Another representation for this configuration is shown in Fig. 3.22(b) where a dipole array and a ground plane represent the PCB main body while another four dipoles in a line represent the outboard whip antenna. The two equivalent arrays are derived separately from the simulated near-field data produced by the PCB main body and the whip antenna alone. With this model, the correct far-field patterns can be predicted which is also shown in Fig. 3.23, indicating that it is a good representation for PCBs with outboard radiators.

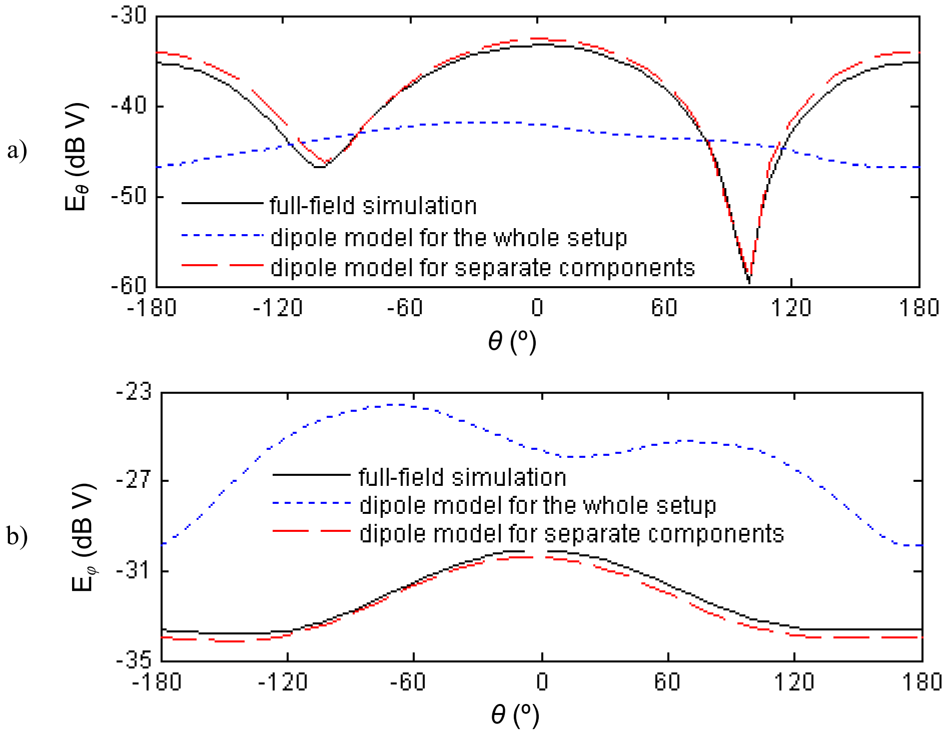

Fig. 3.23 Far-field patterns in the E plane produced by the L-shaped microstrip board with an outboard whip antenna (field unit in dB V)

a) E_θ; b) E_φ

3.7 Dependence on Near-Field Measurement

For the near-field scanning based method, the measurement parameters have noticeable effects on the accuracy of modelling and simulation. Generally the near-field information must be “sufficient” in order to fully characterize the PCB so that the equivalent model is able to represent the emissions in the whole space. The criterion of “sufficiency” is defined by studying the parameters of near-field scanning. This knowledge helps to determine the choice of measurement configuration.

Scanning resolution, scanning plane area, scanning height from the PCB and measurement errors are critical parameters in near-field sampling. For a quantitative assessment, the far-field simulation in the E plane for the basic test board was repeated using the equivalent model built from different measurement parameters, while full-field simulation for the same configuration was also carried out for a reference. Three equivalent dipole configurations were considered with an array resolution of 7.5mm, 10mm and 15mm, corresponding to 5×9=45, 4×7=28 and 3×5=15 dipoles, respectively.

The correlation coefficient γ between the far-field results given by equivalent dipole simulation and full field simulation is introduced as a measure of accuracy. The correlation coefficient is defined as:

$$\gamma = \frac{\sum_{i=1}^{N}\left(E_i - \overline{E}\right)\left(E_i' - \overline{E}'\right)}{\sqrt{\sum_{i=1}^{N}\left(E_i - \overline{E}\right)^2 \bullet \sum_{i=1}^{N}\left(E_i' - \overline{E}'\right)^2}} \tag{3.17}$$

where $\left[\overline{E}\right]$ is the result set from equivalent dipole model, $\left[\overline{E}'\right]$ is the result set from full field simulation, $\overline{E}$ and $\overline{E}'$ are the averages of $\left[\overline{E}\right]$ and $\left[\overline{E}'\right]$ respectively, and N is the number of the far-field samples.

Meanwhile, it was demonstrated in (3.11) that the condition number cond(ξ) of an equation system in the inverse problem is closely related with the numerical stability and modelling accuracy, as a larger value of cond(ξ) means higher sensitivity of the model to measurement errors. Its dependence on the measurement parameters is also investigated.

3.7.1 Scanning Resolution

According to information theory, scanning resolution, also known as sampling rate, is a key factor in acquiring sufficient near-field information. A fine enough scanning resolution guarantees the information integrity. In all the simulation examples above, a 2.5 mm resolution was used for both PCBs. This is based on the sampling criterion recommended by Joy and Paris [22] which estimates the maximum spacing between sampling points (Δs) allowed to obtain sufficient information for planar near-field scanning as

$$\Delta s = \frac{\lambda}{2\sqrt{1+\left(\lambda / d\right)^2}} \tag{3.18}$$

where λ is the wavelength and d is the separation distance between the EUT and the probe. The maximum spacing allowed for the test board and the telemetry board according to (3.18) is 5.7 mm and 6.0 mm, respectively. So the choice of 2.5 mm is reasonable.

To validate this criterion, the far field prediction for the test board was repeated with the same set of near-field data but of different resolutions, and the correlation coefficients with full field simulation are shown in Fig. 3.24. The results from near-field data of 2.5 and 5 mm resolution are close to the direct simulation result, as they are within the range of the maximum spacing allowed. But the data with a 10 mm resolution and above has obvious inaccuracies as indicated by the lower correlation. This confirms the criterion for the choice of sampling points that any space sampling less than the maximum spacing allowed in (3.18) is sufficient.

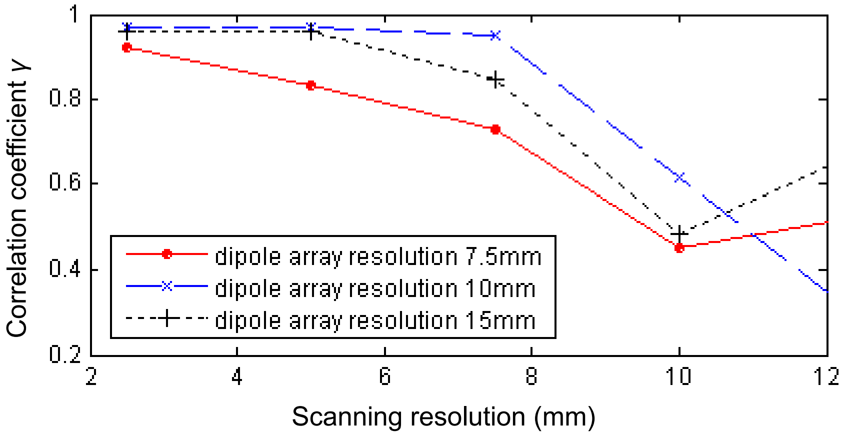

Fig. 3.24 Effects of near-field scanning resolution

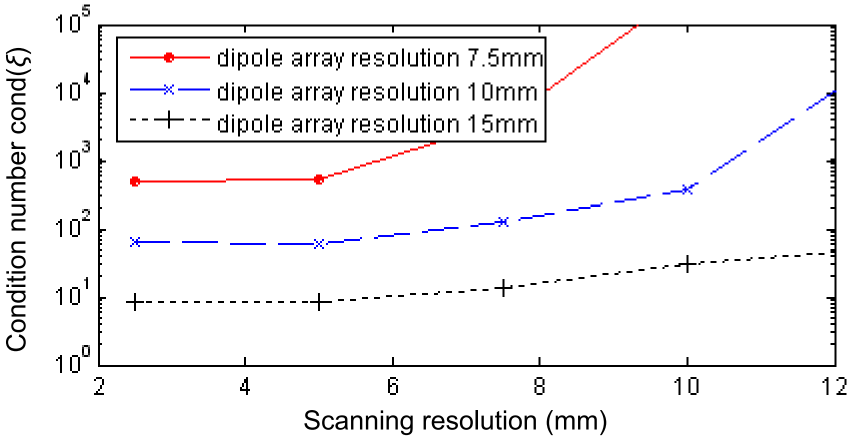

Fig. 3.25 Condition number as a function of near-field scanning resolution

Moreover, increasing the scanning resolution also significantly reduces the condition number of the inverse problem therefore enhances the stability to measurement errors, as presented in Fig. 3.25. When the scanning resolution is approximately finer than the maximum spacing allowed (5.7mm in this example), the condition number almost converges to a constant. These results imply that further refining the scanning resolution would not help enhance the accuracy, therefore, a scanning resolution near the maximum spacing allowed is sufficient for characterization of a PCB.

Interestingly, modelling with a larger number of dipoles (7.5mm dipole array resolution) yields worse results than with fewer dipoles (10mm and 15mm). This is reasonable because the condition number of the inverse problem sharply increases with the number of dipoles, as indicated in Fig. 3.25. The condition number for the 7.5mm resolution dipole array is at least 10 times and 100 times than the 10mm and 15mm one thus the model is much more instable to measurement errors. On the other hand, a fine enough resolution for the dipole array is necessary to fully represent the PCB. Therefore there is an optimal value considering the balance to the information sufficiency and numerical stability. In this particular case the 10mm resolution (hence 4×7 dipoles) is near the optimal as indicated by the strongest correlation with the full field simulation for the far-field prediction. Unfortunately, no closed-form formulae for this optimal value have been developed, and the array is determined empirically which is similar to setting the mesh size in a full field solver.

3.7.2 Scanning Plane Area

Another important topic with regard to near-field sampling is the size of the scanning plane, also known as information volume. Unlike the modal expansion methods [3], [4], the method presented here does not assume the field outside the scanning area to be zero. The equivalent sources are established by fitting to the measured near-field data. Therefore if any significant field area is not covered in the near-field scanning plane, some information will be lost and the equivalent sources established from it would have a noticeable error. It is well known that magnetic near-field maps from a PCB are dominated by the fields vertically above the board and gradually become weaker as the sampling point extends outward to the perimeter of the PCB [23], [24]. This implies that the scanning area must at least cover the area of the PCB, and could possibly extend beyond it. Ideally, the scanning plane should extend until the field on the edges of the plane reaches the minimum measurable level (noise floor) of the equipment. But in practice it is not necessary to scan so widely to collect sufficient near-field information.

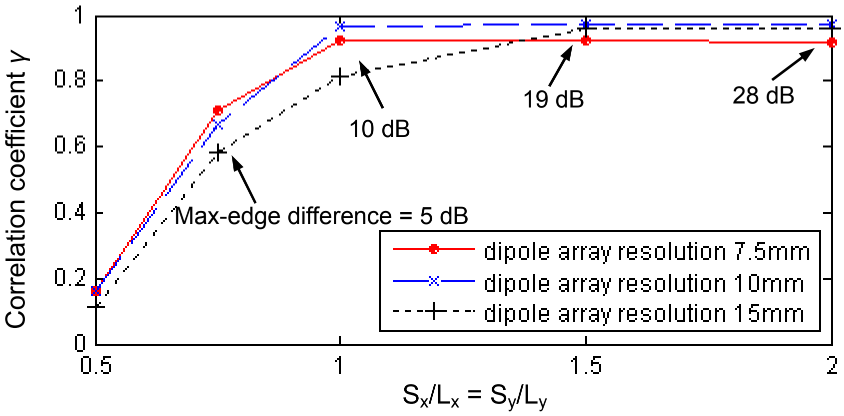

Fig. 3.26 Effects of near-field scanning area

S_x, S_y: length of the scanning plane in *x* and *y* direction, respectively

L_x, L_y: length of the PCB in x and t direction, respectively

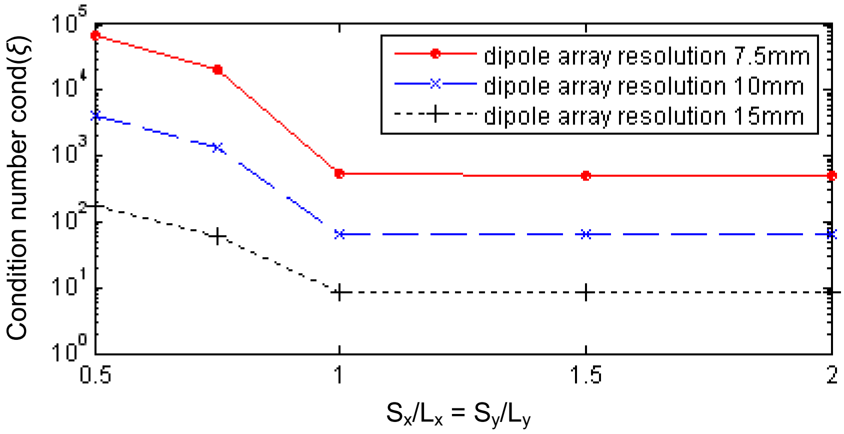

Fig. 3.27 Condition number as a function of near-field scanning area

S_x, S_y: length of the scanning plane in *x* and *y* direction, respectively

L_x, L_y: length of the PCB in x and t direction, respectively

Based on the studies in this work, a near-field plane where the maximum field on the edges is approximately 20 dB lower than the overall maximum field is required. Fig. 3.26 shows the effects of scanning area size on far field prediction for the test board. It is found that insufficient scanning information (when the maximum – edge difference is less than 10 dB) results in significant inaccuracies, but the far field is correctly predicted when the scanning plane reaches a large enough size (19 and 28 dB maximum – edge difference). Actually the plane area required to satisfy this criterion is not very large. In the case above, a 19 dB maximum – edge difference corresponds to a plane which is 1.5 times of the PCB dimension (100 × 75 mm). This result also implies that when a scanning plane is large enough, further increasing its size does not significantly improve the accuracy of the equivalent dipole method.

Fig. 3.27 shows the effects of scanning area size on the condition number. When the scanning area is large enough to cover the PCB area, the condition number decreases to a constant therefore the numerical stability is also guaranteed. Again modelling with more dipoles does not always outperform that with fewer dipoles due to the more ill-conditioned inverse problem.

3.7.3 Scanning Height

The effects of scanning height on the far-field prediction and condition number are shown in Fig. 3.28 and Fig. 3.29, respectively. Generally closer scanning distance leads to a more accurate representation of the PCB. For one thing, when the scans are performed at a higher distance the same sized scanning plane covers less information volume. In addition, the approximations made to the ground plane require the scans to be performed in the close reactive near field. The higher the scanning distance, the approximations are more likely to be invalid. Moreover, the condition number dramatically increases with the scanning distance, making the solution of the inverse problem less stable.

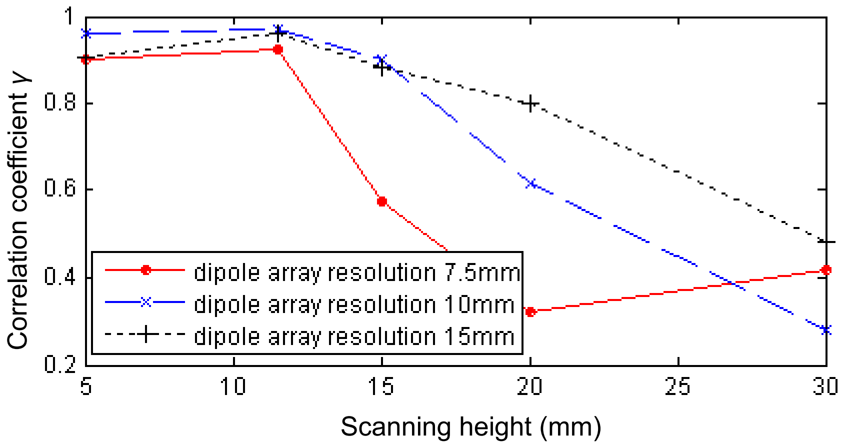

Fig. 3.28 Effects of near-field scanning height

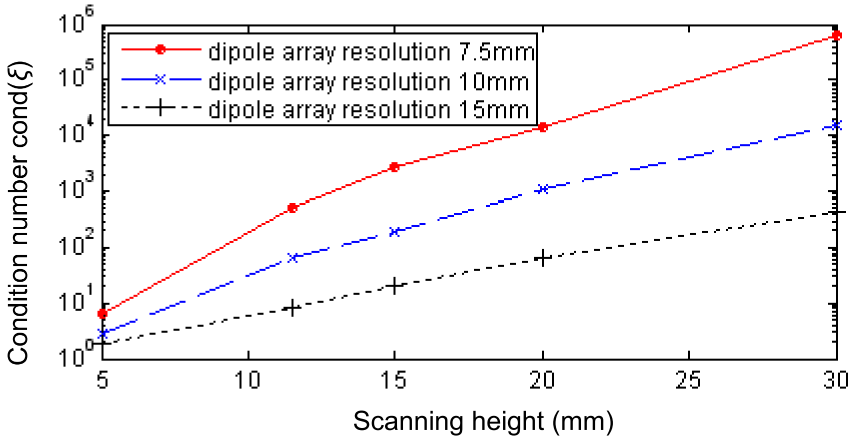

Fig. 3.29 Condition number as a function of near-field scanning height

3.7.4 Measurement Errors

To study the impact of measurement errors on predicting the emissions, the far field of the basic test board was predicted with near-field data with different levels of normally distributed noise as well as a reference with no intentionally added noise. The other parameters of the near-field data were: resolution=2.5mm, area=1.5 times of the PCB and height=11.5mm. All the settings are able to provide sufficient near-field information according to the results above.

As the noise was randomly generated, the results may differ from one time to another. Fig. 3.30 shows an example illustrating the general idea where a dipole array of 10mm resolution was used. The result from the near field data with 0.35 dB error (hence 5° for phase) makes very little difference to that from noise free data. It also has a strong correlation of 0.961 with the full field simulation result. A greater near-field error of 1 dB (hence 15° for phase) affects the far-field prediction more significantly and a maximum variation of 3 dB can be observed. But the agreement with full-field simulation is still favorable (γ=0.929). This suggests that the method has a high stability to measurement errors by means of regularization for the inverse problem. Particularly, in Chapter 2 it was predicted that there was a 0.35 dB measurement error with this near-field scanning system. The results here prove that the 0.35 dB measurement error would not significantly affect the accuracy of the equivalent dipole model.

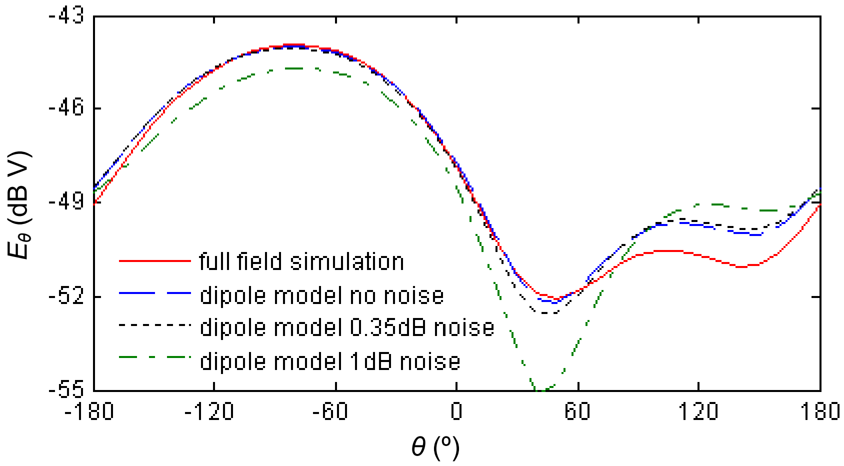

Fig. 3.30 Far-field patterns obtained from near-field data with noise

A more extensive result is presented in Fig. 3.31 showing the effects of measurement errors from 0 to 1.5 dB (hence 0° to 25° for phase). The dipole models with a resolution of 10mm and 15mm are very stable to measurement noise. When the noise is up to 1.5 dB, the resulting correlation coefficient is still above 90%. But the 7.5mm resolution dipole model is much more sensitive to measurement noise due to the very ill conditioning of the inverse problem, even though regularization was applied as for the other two models. This suggests that the regularization techniques are no longer able to retrieve the original field information when the inverse problem is too ill-conditioned and the error is too large.

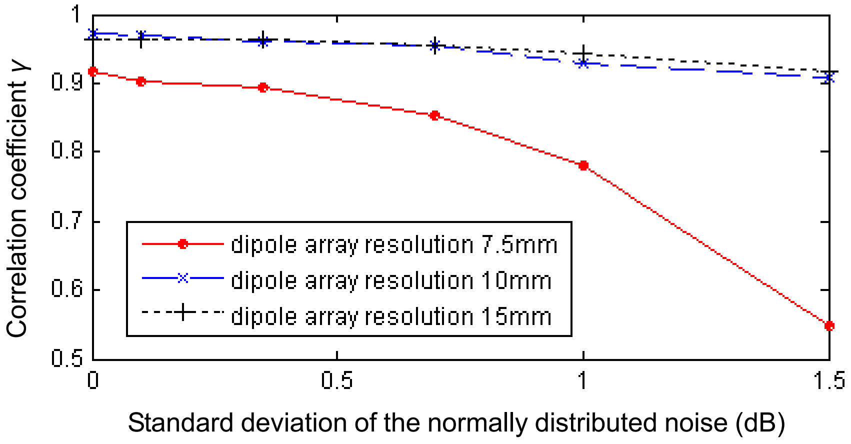

Fig. 3.31 Far-field patterns obtained from near-field data with noise

3.8 Modelling with Electric Dipoles

The model

The model discussed in previous sections uses magnetic dipoles as the equivalent sources. Theoretically either electric or magnetic dipoles can be used as the equivalent sources of a PCB. The idea of electric dipole modelling is to represent the onboard currents of a PCB with elemental electric currents. Based on the equivalence principle, it is assumed that the near fields are produced by the electric dipoles. Therefore the equivalent electric dipoles, instead of magnetic dipole, are placed in a matrix layout on the two-dimensional surface of the PCB component side.

The moments of the electric dipoles are derived from the inverse problem by fitting to the measured near field as for the magnetic dipole model. Each point dipole is decomposed in to three orthogonal components P^x, P^y and P^z. The magnetic field at (x, y, z) produced by an infinitesimal dipole P^z at (x_0, y_0, z_0) can be expressed as (taking P^z component as an example) [9]

$$\overline{H} = P^z \frac{jke^{-jkr}}{4\pi r}\left(1+\frac{1}{jkr}\right)\sin\theta\left(\cos\varphi\overline{e_y} - \sin\varphi\overline{e_x}\right)$$

$$H_x = -P^z \frac{jke^{-jkr}}{4\pi r^2}\left(1+\frac{1}{jkr}\right)\left(y-y_0\right) = P^z\xi_x^z \tag{3.19}$$

$$H_y = P^z \frac{jke^{-jkr}}{4\pi r^2}\left(1+\frac{1}{jkr}\right)\left(x-x_0\right) = P^z\xi_y^z$$

$$H_z = 0$$

It should be noted here an electric dipole only contributes to its orthogonal components of the magnetic field (e.g. P^x to H_y and H_z, P^y to H_z and H_x, P^z to H_x and H_y). Then the moments of the dipoles can be determined from the inverse problem of the following linear equations:

$$\begin{bmatrix} 0 & \xi_x^y & \xi_x^z \end{bmatrix}_{m\times n} \begin{bmatrix} P^x \\ P^y \\ P^z \end{bmatrix}_{n\times 1} = \begin{bmatrix} H_x \end{bmatrix}_{m\times 1}$$

$$\begin{bmatrix} \xi_y^x & 0 & \xi_y^z \end{bmatrix}_{m\times n} \begin{bmatrix} P^x \\ P^y \\ P^z \end{bmatrix}_{n\times 1} = \begin{bmatrix} H_y \end{bmatrix}_{m\times 1} \tag{3.20}$$

Modelling with magnetic and electric dipoles is based on the same theory thus their modelling procedure is very similar except the formulation. All the techniques and analysis for the magnetic dipole model, such as layout, simplification, regularization and dependence on measurement, also apply to the electric dipole model. When the PCB has a ground plane, the same approximated model taking into account the ground plane can be built. However, in the image theory there is a 180° difference between their polarities of electric images and magnetic images, as illustrated in Fig. 3.32. The dot indicates the position of an electric dipole and the diamond a magnetic one, while the direction of the arrow identifies the polarity.

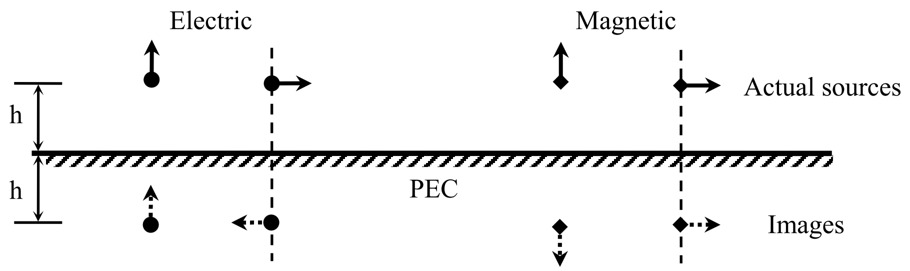

Fig. 3.32 Images of electric and magnetic dipoles near a perfect electric conductor (PEC)

Comparison with magnetic dipole model

An electric dipole model, with the same mesh size (5×7=35 dipoles) and derived with the same near-field data as for the magnetic dipole model, was established for the telemetry PCB. Prediction for emissions was repeated and compared with the magnetic dipole simulation. The first comparison is the variation of the vertical electric field component E_z from the centre of the PCB upward, as shown in Fig. 3.33. At a very small height a relatively large divergence is observed. This is because in very close range the spatial variation of field intensities is very sensitive thus any small shift of the field map would significantly change the one-point field value. At higher distance, the two models achieve a consistent result.

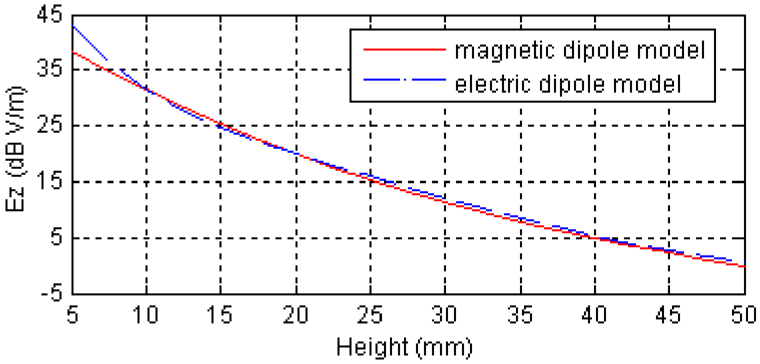

Fig. 3.33 Evolution of vertical electric field obtained from electric / magnetic dipole model

The comparison of far field in the *E* plane is shown in Fig. 3.34. It seems that the results from the magnetic dipole model agree better with measurement. But it is hard to say which model better predicts the real emissions because the far-field measurement result also contains errors.

However, results from all the three methods, either experimental or numerical, have a strong correlation with each other. The correlation coefficients between each far-field result are summarized in TABLE 3.5. These results confirm that characterization of emissions from a PCB with the electric dipole model and magnetic dipole model is generally consistent.

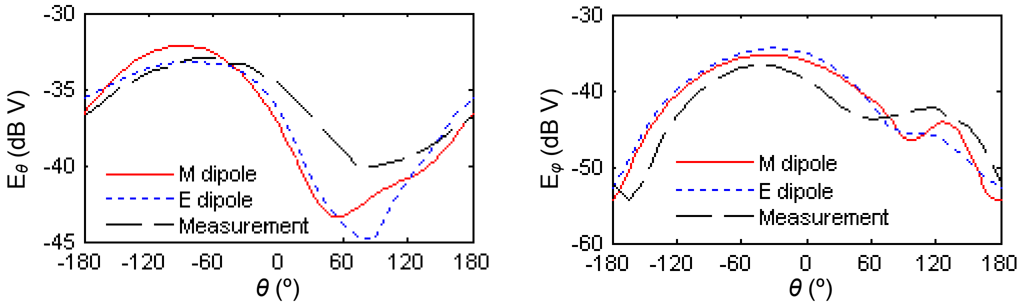

a) E_θ b) E_φ

Fig. 3.34 Far field in the *E* plane obtained from the electric / magnetic dipole model

TABLE 3.5 Correlation coefficients between far-field data obtained from electric / magnetic dipole model and measurement

	M dipole & measurement	E dipole & measurement	M dipole & E dipole
E_θ	91.6%	91.8%	96.9%
E_φ	92.3%	90.9%	98.5%

However, based on a lot of experience, the magnetic dipole model always gives a better solution than the electric one. This may be mathematically attributed to the fact that the inverse problem associated with the electric dipole model is always more ill-conditioned than that with the magnetic one, thus the solution is more instable and sensitive to noise. The condition number of the magnetic / electric dipole model for the telemetry board case is listed in TABLE 3.6. For this reason the magnetic dipole model is preferred.

TABLE 3.6 Condition number of the inverse problem for the electric / magnetic dipole model

Model \ Number of dipoles	3×5=15	4×6=24	5×7=35
Magnetic dipole model	114	805	9525
Electric dipole model	220	1647	15453

3.9 Conclusions

A method to represent radiated emissions from a PCB using an equivalent dipole model deduced from magnetic near-field scans has been described. In free space, a PCB is modelled with a set of equivalent dipoles placed on the component surface. The PCB ground plane is also included in the model based on certain approximations in order to take into account the effects of incomplete grounding and diffraction. The equivalent dipoles are identified by fitting to the measured tangential magnetic near fields.

Mathematically, regularization is applied to the inverse problem for equivalent source identification where the measured near-field data are always associated with errors. Case studies show that the regularization techniques are effective in retrieving the original data from the noisy ones thus this significantly enhances the stability to measurement errors.

There are a number of parameters, including near-field scanning parameters and dipole number and layout, affecting the modelling accuracy. The effects of near-field scanning parameters on the modelling accuracy are demonstrated, based on which the criterion of sufficiency of the near-field information and the conditioning of the inverse problem are determined. On the other hand, the number of dipoles used for the model is not only a tradeoff between computational costs and modelling accuracy, but also a tradeoff between numerical stability and information sufficiency. Unfortunately no closed form formulae have been derived for an optimum to be established. The number of dipoles and layout of the array are determined empirically.

The method was validated experimentally with a simple test board and a practical telemetry PCB. For the microstrip test board, the field prediction by the equivalent model was compared with full field simulation and good agreements were found in both near and far field. For the telemetry board the model predictions were compared with measurements and a generally reasonable agreement was obtained. Low computational cost and no requirements for detailed information on PCB circuit structure are the significant advantages of the method. It is demonstrated that the proposed techniques have the potential to characterize emissions from complex structures in realistic environments reducing computational effort significantly

Although this chapter is mainly focused on modelling with magnetic dipoles from magnetic field scans, modelling with electric dipoles is based on the same principle and consistent results for field prediction with the magnetic one are demonstrated.

References

[1] Tankielun, U. Keller, E. Sicard, P. Kralicek, and B. Vrignon, “Electromagnetic near-field scanning for microelectronic test chip investigation,” *IEEE EMC Society Newsletter*, Oct. 2006.

[2] Q. Chen, S. Kato, and K. Sawaya, “Estimation of current distribution on multilayer printed circuit board by near-field measurement”, *IEEE Trans. Electromagn. Compat.*, vol. 50, no. 2, pp. 399-405, May 2008.

[3] A. D. Yaghjian, "An overview of near-field antenna measurements," *IEEE Trans. Antennas Propagat.*, vol. AP-34, no. 1, pp. 30-45, Jan. 1986.

[4] E. Joy, W. Leach Jr., G. Rodrigue, and D. Paris, "Applications of probe-compensated near-field measurements," *IEEE Trans. Antennas Propagat.*, vol. AP-26, no. 3, pp. 379-389, May 1978.

[5] P. Petre and T. K. Sarkar, "Planar near-field to far-field transformation using an equivalent magnetic current approach," *IEEE Trans. Antennas Propagat.*, vol. 40, no. 11, pp. 1348-1356, Nov. 1992.

[6] T. Sarkar and A. Taaghol, "Near-field to near/far-field transformation for arbitrary near-field geometry utilizing an equivalent electric current and MoM," *IEEE Trans. Antennas Propagat.*, vol. 47, no. 3, pp. 566–573, Mar. 1999.

[7] J. R. Reguè, M. Ribo, J. M. Garrell, and A. Martin, "A genetic algorithm based method for source identification and far-field radiated emissions prediction from near-field measurements for PCB characterization," *IEEE Trans. Electromagn. Compat.*, vol. 43, no. 4, pp. 520–530, Nov. 2001.

[8] J. J. Laurin, J. F. Zürcher, and F. E. Gardiol, "Near-field diagnostics of small printed antennas using the equivalent magnetic current approach," *IEEE Trans. Antennas Propagat.*, vol. 49, no. 5, pp. 814-828, May 2001.

[9] C. A. Balanis, *Antenna Theory - Analysis and Design*, 3rd edition, New York: Wiley, 2005.

[10] (2010) Concept - II homepage. [Online]. Available: http://www.tet.tu-harburg.de/concept/index.en.html

[11] X. Tong, D. W. P. Thomas, A. Nothofer, P. Sewell, and C. Christopoulos, "A genetic algorithm based method for modelling equivalent sources of printed circuit boards from near-field measurements", in *Proc. Asia Pacific EMC* 2010.

[12] D. A. McNamara, *An Introduction to the Uniform Geometrical Theory of Diffraction*, Boston, MA: Artech House, 1990.

[13] S. A. Bokhari, J. R. Mosig, and F. E. Gardiol, “Radiation pattern computation of microstrip antennas on finite size ground planes”, in *IEE Proc. H* 1992, vol.139, no. 3, pp. 278-286, Jun. 1992.

[14] T. S. Shores, *Applied Linear Algebra and Matrix Analysis*, New York: Springer, 2007.

[15] P. C. Hansen, “Numerical tools for analysis and solution of Fredholm integral equations of the first kind,” *Inverse Problem* 8, pp. 849-872, 1992.

[16] A. Tikhonov and V. Arsenin, *Solutions of Ill-Posed Problems*. Washington DC: Winston, 1977.

[17] P. C. Hansen, “Analysis of discrete ill-posed problems by means of the L-curve,” *SIAM Rev.*, vol. 34, pp. 561–580, 1992.

[18] G. Golub, M. Heath, and G. Wahba, “Generalized cross-validation as a method for choosing a good ridge parameter,” *Technometrics*, vol. 21, pp. 215–223, May 1979.

[19] C. W. Groetsch, *The Theory of Tikhonov Regularization for Fredholm Equations of he First Kind,* Boston, MA: Pitman, 1984, chapter 3.

[20] V. A. Morozov, *Methods for Solving Incorrectly Posed Problems*, Berlin: Springer, 1984, section 27.

[21] *Information technology equipment - Radio disturbance characteristics - Limits and methods of measurement*, EN 55022:2006+A1, 2007.

[22] E. B. Joy and D. T. Paris, “Spatial sampling and filtering in near-field measurements,” *IEEE Trans. Antennas Propagat.*, vol. AP-20, pp. 253-261, May 1972.

[23] R. G. Kaires, “Radiated emissions from printed circuit board traces including the effect of vias, as a function of source, termination and board characteristics”, *IEEE International Symposium on EMC*, pp. 872 – 877, 1988.

[24] R. Garg, P. Bhartia, I. Bahl, and A. Ittipiboon, *Microstrip Antenna Design Handbook*. Norwood, MA: Artech House, 2001.

CHAPTER FOUR

Equivalent Dipole Model Based on Genetic Algorithms

4.1 Introduction

The issues of electromagnetic compatibility (EMC) of printed circuit boards (PCBs) include not only predicting the far fields, but also identifying the primary radiating sources. This will provide a diagnosis of the electromagnetic characteristics of the circuit components and assist the analysis of the electromagnetic emissions radiated by the PCB in the whole space including near- and far-field regions, as required in product designs. Considering that very often the real current distribution of a PCB is difficult to fully characterize due to the structural complexity and the unknown characteristics, the idea of representing a PCB with a set of equivalent currents or dipoles is therefore attractive because of its simplicity.

For most approaches [1]-[4] the equivalent source is placed in a pre-defined grid and then deduced from the measured near-field distribution. In Chapter 3, an equivalent dipole model was discussed which replaced a PCB with an array of equivalent magnetic dipoles placed in a pre-fixed grid on a 2D surface. The dipoles were determined from the solution of an inverse problem by directly fitting the scanned near-field data. The effectiveness of the method was demonstrated but there were some problems deserving of further considerations.

First, the determination of the number and layout of the dipole array was empirical rather than the optimal. The dipoles were placed in a matrix layout but this might be not the most efficient representation for the real radiating source. Considering an extreme example, if the real source to be identified is a single dipole, the matrix layout can never be the optimum unless a node of the grid happens to overlap with this dipole. Moreover, the matrix layout may lead to redundant dipoles which not only complicate subsequent modelling but also increase the condition number of the inverse problem so as to make the model less stable to measurement errors. Therefore a better representation calls for the optimal placement and number of the equivalent dipoles.

Second, both magnitude and phase information of the near field was needed to build the model, but this is sometimes a high requirement for experimental works and may be limited by lab facilities. It is reported that the phase information can be retrieved from near-field amplitude over two surfaces by an iterative algorithm [5]. However, it is interesting to directly establish the model from amplitude-only data.

In this chapter, genetic algorithms (GAs) are introduced for equivalent source identification in order to address the problems above. Genetic algorithms - the global optimization schemes based on the mechanics of natural selection and genetics - are well-known for their robust performance. The main features making GAs attractive for this application are the global type of search and the capability of solving complex problems involving a large number of parameters and nonlinear or non-differentiable functions. In this application, a PCB is represented by an array of magnetic dipoles found from a GA optimization based on near-field scans. The basic idea is to implement balanced multi-objective optimizations considering both accuracy (better fitted to the field) and efficiency (less dipoles) by properly defining the genes and the evolution process. The number and layout of dipoles used is determined from the optimization rather than a pre-defined empirical value, giving a more efficient representation of a PCB. Also, the method works with several kinds of near-field information (amplitude, amplitude and phase; any component or a combination), provided that the given information is sufficient for electromagnetic characterization.

This chapter is organized as follows. In Section 4.2, the configuration of the equivalent dipole model is presented. In Section 4.3, the theory of GAs employed in this work is briefly reviewed. Section 4.4 describes the implementation of GAs for equivalent source identification. In Section 4.5, validation with analytical fields and experimental application to a digital circuit is presented, and the dependence on near-field information is discussed.

4.2 The Equivalent Dipole Model

The electromagnetic emissions from PCBs are normally produced by the currents of onboard components, which can be modelled as an array of infinitesimal dipoles. In Chapter 3 it has been demonstrated that modelling with electric or magnetic dipoles is consistent for representing the electromagnetic characteristics. Here magnetic dipoles are used based on the representation of a radiator by equivalent magnetic currents. Considering most PCBs have relatively thin planar structure, the dipoles can be placed on a planar surface which is on the component side of the PCB. The equivalent dipoles should radiate a near and far field pattern that is as close to that of the PCB as possible. Parameters of the dipoles (number, position, orientation, moment) are determined from an optimization procedure using a genetic algorithm which minimizes the difference between the near field generated by the dipoles and the measured field, while keeping the number of dipoles as small as possible.

The expression of the magnetic field radiated by an infinitesimal magnetic dipole is needed for the source identification. For an infinitesimal dipole $\overrightarrow{M}$ in arbitrary orientation, the radiated magnetic field is given by [6]:

$$\overrightarrow{H}\left(\vec{r}\right)=\frac{k^2}{4\pi}\left[\left(1+\frac{j}{kr}-\frac{1}{\left(kr\right)^2}\right)\overrightarrow{M}-\left(1+\frac{3j}{kr}-\frac{3}{\left(kr\right)^2}\right)\frac{\left(\vec{r}\cdot\overrightarrow{M}\right)\vec{r}}{r^2}\right]\frac{e^{jkr}}{r} \tag{4.1}$$

where k is the wave number, $\vec{r}$ and r are the vector and scalar distance from the dipole to the observation point, respectively. Unlike the inverse problem for equivalent dipole identification where the spectrum of tangential field components is needed, the optimization by GA is able to make use of any combination of field components. For example, half of the sampling points can be $\overrightarrow{a_x}\mathrm{H_x}+\overrightarrow{a_y}\mathrm{H_y}$ and the other half $\overrightarrow{a_x}\mathrm{H_x}$ depending on the feasibility of measurement. The expression in (4.1) is in the vector form so any combination of field components can be derived from it. Based on the equivalence principle, the measured field at every observation point is the total contribution of all the equivalent dipoles, as shown in Fig. 4.1.

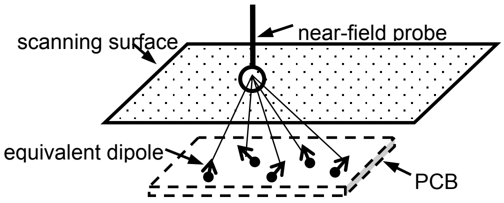

Fig. 4.1 Equivalent source identification from near-field scanning

When a PCB is backed by a ground plane, the image theory is used in the equivalent source identification, and a real sized ground plane is included in the equivalent model, together with the equivalent dipoles placed on the component side. Using this configuration, it is expected to implicitly include the effects of a finite ground plane and produce the far-field pattern in all the surrounding free space, as discussed in Section 3.4.

The position, orientation and moment of each dipole, as well as the total number of dipoles, are to be identified from near-field scans. This calls for an optimization process which searches the fitted dipoles by minimizing the objective function that is the difference between the dipole-generated field and the measured field. A large number of parameters are involved in this optimization leading to the presence of many local optima. Also, the continuity and differentiability of the objective function are not guaranteed. Traditional deterministic optimization methods [7] are therefore not appropriate. Hence the genetic algorithms are introduced for this problem because of its nature of global optimization and the capability of handling a large number of parameters.

4.3 Theory of Genetic Algorithms

Genetic algorithms are robust, stochastic and global search methods modelled on the principles and concepts of natural selection and evolution. First proposed by Holland in 1975 [8], GAs have gained wide popularities, and various alternative forms and many extensions to the basic algorithm have been developed. Here only the essentials and extensions related with this particular application are reviewed.

4.3.1 Important Terminology and Implementation Steps

The basic idea of GAs is that a set of potential solutions in a population evolve together to achieve a specific optimum. The population evolves in a probabilistic manner based on the similarity to the natural selection. GAs differ from most traditional optimization methods in two ways [9, Chapter 1]. First, they do not necessarily operate directly on the parameters being optimized but to encode them into genes instead. Second, they simultaneously optimize the entire population at once, not a single parameter at a time. Because of these natures, GAs have their unique terminology and implementation procedure, as discussed below.

Genes and Chromosomes: Generally genes are a coded representation of individual optimization parameters. A string of genes is a chromosome a specific realization of which can be decoded into parameters representing a trial solution. For example, the whole parameter space of all the equivalent dipoles is encoded into a chromosome, which consists of a number of genes representing the position, moment and orientation of each dipole. The popular encoding techniques include binary coding, real-number coding, and combination of them.

Population: A set of trial solutions in the form of chromosomes is assembled as a population. For example, one can specify 50 dipole arrays each being a trial solution so as to form a population consisting of 50 individuals. The whole population evolves by iterations and the final objective is to find the best fitted individual among the population.

Generations: The iterations of the population are generations. In every generation, a new population, called the *children*, is re-created from the original population, called the *parents*, from a probabilistic reproduction. Better fitted individuals are more likely to be copied to a subsequent generation so as to drift the whole population toward an optimal solution. The reproduction is finished by GA operators – *selection*, *crossover* and *mutation*.

Selection, Crossover and Mutation: In every generation, individuals from the parent population are selected in pairs and recombined with a probability to reproduce the child population, and better fitted individuals would be chosen with larger probability to enhance the fitness of the population. The genes of child individuals are generated by combining the genes of their parents from a probabilistic operation called crossover. Also mutation is applied with a certain probability which modifies some chromosomes of individuals at random to introduce unexplored points into the search domain and avoid premature convergence to local optima.

Fitness function: It is a function of the parameters being optimized for every individual which defines the optimization goal. In the optimization process, GAs assess an individual (a trial solution in the physical problem) is good or not by the value of its fitness function. For example, the difference between the measured near field and that generated by the equivalent dipoles can be a fitness function for a trial dipole array which must be minimized by the optimization.

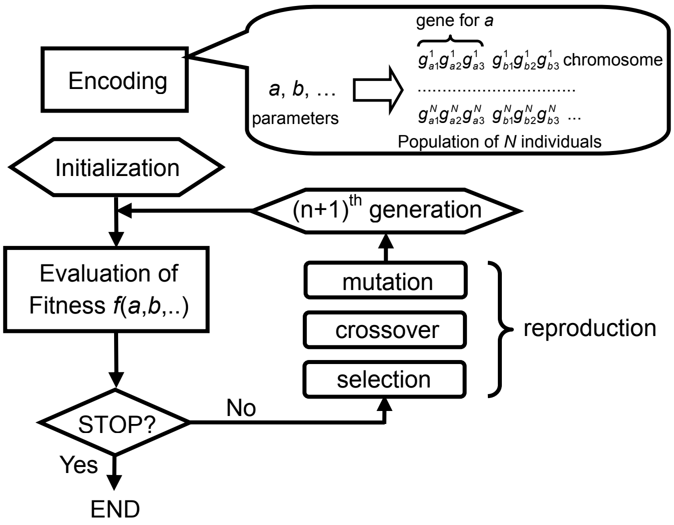

Fig. 4.2 Flowchart of GA implementation

The basic implementation procedure is illustrated in Fig. 4.2, including five major steps:

1. Encode the parameters being optimized to genes.

2. Create an initial set of chromosomes for the starting population, usually in a random manner.

3. Evaluate the value of the fitness function for every individual in the population.

4. Based on the fitness values, select the parents and reproduce the child population through the probabilistic operations.

5. Run the iterative algorithm until a good enough fitness value of an individual is achieved or other stop conditions are met (e.g. maximum generations reached).

Despite the wide application, the theory of GAs is still incomplete. At present, there is no theoretical proof of global convergence [10], and most knowledge of implementation, such as the choice of parameters and generations to run, is based on experience and experiment. Therefore it is necessary to investigate a guideline for GA implementation in this particular application.

4.3.2 Genes and Chromosomes

For a parameter space ***x*** $\{x_1, x_2, \ldots, x_N\}$ where each parameter x_i has a searching space $[x_i^{\min}, x_i^{\max}]$, the most popular representation in GAs is the binary coding [8] where M_i binary bits are assigned to the parameter x_i. This can be written as

$$\text{chromosome} = \overbrace{g_{x_1}^1 g_{x_1}^2 \ldots g_{x_1}^{M_1}}^{M_1 \text{ bits for } x_1} \overbrace{g_{x_2}^1 g_{x_2}^2 \ldots g_{x_2}^{M_2}}^{M_2 \text{ bits for } x_2} \ldots \overbrace{g_{x_N}^1 g_{x_N}^2 \ldots g_{x_N}^{M_N}}^{M_\mathrm{N} \text{ bits for } x_\mathrm{N}} \tag{4.2}$$

where $g_{x_i}^m$ can be 1 or 0. The genes are decoded to discrete real-valued parameters by

$$x_i = x_i^{\min} + \frac{x_i^{\max} - x_i^{\min}}{2^{M_i} - 1} \sum_{m=1}^{M_i} g_{x_i}^m \cdot 2^{m-1} \tag{4.3}$$

The encoding precision depends on the number of bits M_i and the searching space, given by

$$\Delta x_i = \frac{x_i^{\max} - x_i^{\min}}{2^{M_i} - 1} \tag{4.4}$$

In alternative coding forms, the gene strings $g_{x_i}^m$ are selected from an alphabet of cardinality other than binary. Especially, the real-coded GAs [11] use a single real number $g_{x_i}^m$ to represent the real-valued parameter x_i, allowing to vary the parameter continuously. However, the Schema Theorem [8], which is the most fundamental theory of GAs, predicts that a low-cardinality alphabet used for coding provides larger searching space and locates similarities between successful chromosomes. Considering this particular application, with binary coding all the possible positions of the dipoles can be located discretely on a mesh grid. Such a dipole array is more convenient to be incorporated into a full field solver. For these reasons binary coding is adopted for this application.

4.3.3 Fitness Function

The fitness function is the only connection between the physical problem and GA. It is problem dependent and probably the trickiest component in GAs. Some empirical guidelines are widely recognized. First, the value returned by the fitness function should be proportional to the “goodness” of a trial solution in order to perform a meaningful selection procedure [12]. In this application it is to find a quantity proportional to the balance between the number of dipoles and the agreement of the measured field and that generated by the equivalent dipoles. Second, the schema theorem implies that a larger population will significantly speed up the convergence therefore it is helpful to make the calculation for the fitness function faster in order to allow for the use of a larger population.

4.3.4 GA Operators

Selection. According to Darwin’s principle of “survival of the fittest” [8], the algorithm selects individuals from the parent population based on their fitness values. The most common scheme is the roulette wheel selection [12] where a parent individual is selected with a probability proportional to its fitness value:

$$p_{\text{selection}} = \frac{f\left(\text{individual}_i\right)}{\sum_i f\left(\text{individual}_i\right)} \tag{4.5}$$

Consequently, highly fit individuals receive preferred representation over unfit ones. However, roulette wheel selection only works with positive fitness values and appropriate scaling for the fitness function is required in every generation.

Another popular scheme is the tournament selection [12]. A subpopulation of N individuals is chosen at random from the parent population, and the best individual in the subpopulation is selected. This process is repeated until the required individual number is reached. Tournament selection has many advantages over roulette wheel selection. First, scaling of the fitness function is not required. Second, it has been proven that tournament selection has faster convergence and execution time [12]. For these reasons it is employed in this application.

Elitist strategy. All the selection schemes do not guarantee that the child generation is evolved toward the optimal due to the probabilistic nature of the operations. Therefore the elitist strategy [13] is introduced. A few best individuals in the parent population are directly saved and inserted to the selected individuals which will be combined to generate the child population. These elitists can be also copied to the child population. This memory is expected to accelerate the convergence as the best individual in the last generation acts as a reference for the evolution. However, too many elites will increase the risk of premature convergence to local minima. Based on the author's experience an elite proportion of 1-5% is useful.

Crossover. Crossover is a probabilistic operation of combining a pair of selected parent individuals with a probability p_{cross}. It maintains a good balance between exploiting the currently good regions and exploring new regions where better solutions may be found. For binary coding the basic operations are the one-point crossover [8] and two-point crossover [9, Chapter 2], as depicted in Fig. 4.3. In one-point crossover, a random number p between [0, 1] is first generated. If $p > p_{\text{cross}}$, a random location in the parent's chromosome is selected, dividing the chromosome into two proportions. One proportion of the chromosome is copied from parent 1 to child 1 and from parent 2 to child 2. The other proportion of the chromosome of parent 1 is placed to child 2 and from parent 2 to child 1. If $p< p_{\text{cross}}$, the entire chromosome of parent 1 is copied to child 1 and parent 2 to child 2. But a problem in one-point crossover is that the first and last bit can never appear on the same child chromosome after the cross. Hence the two-point crossover has been proposed which interprets the chromosome in circular structure, as illustrated in Fig. 4.3(b). The chromosomes to be combined are split at two locations and the central set of genes is exchanged. Empirically the crossover rate p_{cross} for a successful implementation of binary-coded GAs is between 0.6 and 0.9.

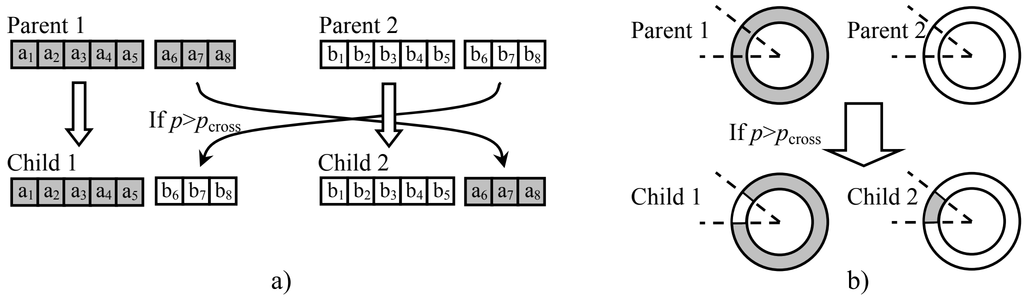

a) b)

Fig. 4.3 Action of one-point and two-point crossover between two parent chromosomes

a) one-point crossover [9, pp. 15]; b) two-point crossover [9, pp. 42]

It is clear that either one-point or two-point crossover operates on some selected genes but not on the whole chromosome. Although very efficient for optimization with few parameters, the convergence time increases with the increase of optimization parameters. One possible reason is that different parameters do not have the same evolution speed. Considering that the optimization for the equivalent dipoles must handle a great number of parameters, the uniform crossover scheme [14] is introduced in this application. For binary-coded GAs, two parent chromosomes are combined by independently swapping every bit (0s and 1s) with a probability p_{cross}, as illustrated in Fig. 4.4. By doing this all the parameters are expected to have the same evolution speed in their searching space.

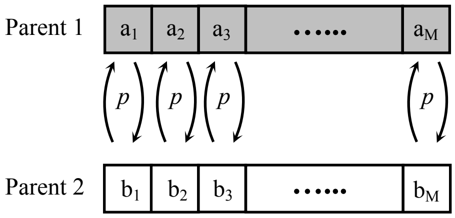

Fig. 4.4 Schematic of uniform crossover between two M-bit parent chromosomes [14]

Mutation. As far as the author is aware, there are very few improvements and alternatives for the mutation schemes. In the classical mutation scheme, if $p > p_{\mathrm{mutation}}$, a bit making up the chromosome is randomly selected and mutated. For binary-coded GAs, the bit is simply changed from 1 to 0 or 0 to 1. Usually mutation with a rate between 0.01 and 0.1 is quoted in the literature [10].

4.4 Implementing GAs in Equivalent Source Identification

4.4.1 Definition of the Optimization

The GA terminologies corresponding to this application are clarified in TABLE 4.1.

TABLE 4.1 GA terminologies for the equivalent dipole identification

GAs	The physical problem
Individual	A dipole array
Population	All the possible dipole arrays
Gene	A coded parameter of a dipole array
Chromosome	A coded vector of the whole parameter space
Fitness	The balance between fewer dipoles and better agreement of field

Encoding the parameters. The first step of GA optimization is to encode the genes of the individuals, which are the parameters of the equivalent dipoles in this application. A dipole can be described by the following set of 8 parameters:

$$\{x_i, y_i, \mathrm{Re}(Mx_i), \mathrm{Re}(My_i), \mathrm{Re}(Mz_i), \mathrm{Im}(Mx_i), \mathrm{Im}(My_i), \mathrm{Im}(Mz_i)\}$$

where

- x_i and y_i are the position of the dipole. As mentioned earlier, all the equivalent dipoles are placed in a 2D surface of the PCB component side. Hence their positions are described by two Cartesian coordinates. Also the searching space for x_i and y_i is defined within the PCB area.

- $\mathrm{Re}(Mx_i)$, $\mathrm{Re}(My_i)$, $\mathrm{Re}(Mz_i)$, $\mathrm{Im}(Mx_i)$, $\mathrm{Im}(My_i)$, $\mathrm{Im}(Mz_i)$ are the real and imaginary part of the three components of the dipole moment in the Cartesian coordinates, respectively. For the searching space, it is reasonable to use a pre-calculated range

$$-|M_0| < \mathrm{Re}(M_i) < |M_0|, \quad -|M_0| < \mathrm{Im}(M_i) < |M_0|$$

where M_0 is the moment of a single dipole generating the maximum intensity of the scanned field which can be calculated from (4.1) by setting $\overline{H}$ to the maximum value of one of the measured field components.

For binary-coded GAs, W_1 bits are assigned to x_i and y_i and W_2 bits are assigned to every moment parameter, respectively. The optimization starts with N_0 dipoles specified by the user, so an equivalent dipole array is encoded to a chromosome consisting of $N_0 \cdot (2W_1+6W_2)$ binary bits. In the initialization, the value of every parameter is generated randomly in its own searching space.

Fitness functions. The fitness function F is the target that the algorithm runs to minimize. Suppose there are Q measurement points and denote H_{0q} and H_q to be the measured field and the field generated by all the N dipoles at point q, respectively, the fitness function for the problem is defined as follows.

For both amplitude and phase data:

$$F = N^{\alpha} \cdot \sum_{j} \sum_{q=1}^{Q} \left(\left| \mathrm{Re}\left(H_{0qj}\right) - \mathrm{Re}\left(H_{qj}\right) \right| + \left| \mathrm{Im}\left(H_{0qj}\right) - \mathrm{Im}\left(H_{qj}\right) \right| \right) \tag{4.6}$$

For amplitude only data:

$$F = N^{\alpha} \cdot \sum_{j} \sum_{q=1}^{Q} \left[H_{0qj}^{2} - \left| H_{qj} \right|^{2} \right]^{2} \tag{4.7}$$

where in H_j, j corresponds to a measured field component or a vectorial combination of the components, and α is a weighting factor of the number of dipoles N.

The fitness functions to be minimized in (4.6) and (4.7) consist of two parts: the N^{α} term is the contribution of the number of dipoles and the other term determines how close the field generated by the equivalent dipoles agrees with the measured field. Obviously the fitness value depends on both the global minimum and the number of dipoles used. So the objective of this optimization is to find out the best fitted equivalence with as small number of dipoles as possible. The N^{α} term links the two objectives in the same optimization. When more than one dipole array generates the same fitted field, the one with the smallest dipole number is preferred. Although this may bring additional risk of reducing the accuracy, the method is expected to give an idea of the necessary number of dipoles for efficiently characterizing a PCB.

The variable α controls the weight between accuracy of the computation and simplicity of the equivalent array. As this number becomes smaller the fitness value depends more on the computational accuracy rather than efficiency. This variable is adjustable and problem dependent, and it effects will be discussed in Section 4.4.3. Normally the choice of α between 0.2 and 0.4 leads to a balanced solution. In addition, in order to maintain computational stability, a lower limit N_1 must be set for the number of equivalent dipoles (because if N=0, then F=0, which is meaningless). Thus in fact the method is expected to find a semi-empirical optimum of the necessary dipole number in the range of [N_1, N_0].

On the other hand, considering the global minimum terms in the fitness functions, when phase information is available the real and imaginary parts of the field are evaluated separately in (4.6). For amplitude only data, the near-field amplitude distribution is the only parameter to fit. The quadratic function in (4.7), which has been mathematically discussed in detail in [15], has advantages in avoiding the occurrence of local minima as the risk of convergence to a local minimum increases due to the lack of phase information.

4.4.2 Optimization by Mutually Competitive Evolution

The basic idea of this optimization is to set up two sub-populations with a different number of dipoles evolving and competing at the same time. The evolution takes place within each sub-population separately and is finished by the GA operations. It targets to evolve the sub-populations to better fit the measured field. Meanwhile a mutual competition between the two sub-populations takes place in every generation. The sub-population with fewer dipoles wins the competition only when its agreement to the measured field is not worse than the other sub-population. The flowchart of this optimization is illustrated in Fig. 4.5.

Initially, the whole population consisting of P individuals (dipole arrays) is divided into two sub-populations each consisting of P/2 individuals. One sub-population starts the iteration with N dipoles and the other with N-1 dipoles.

In every generation, each sub-population is evolved through the GA operations – selection, crossover and mutation. This is finished separately therefore selection and crossover are performed within each sub-population. Also after every generation there is a competition between the two sub-populations by comparing their average fitness values of all the individuals in each sub-population. Based on the competition result, if the *N*-1 dipole population outperforms the *N* dipole one (e.g. the average fitness value is smaller), individuals in the *N* dipole sub-population randomly drop 2 dipoles to form *N*-2 dipole arrays. Otherwise the evolution continues without changing the dipole number in each sub-population. The evolution and competition runs until the population with fewer dipoles can not outperform the one with more dipoles, or another stop condition is met, e.g. maximum generation reached.

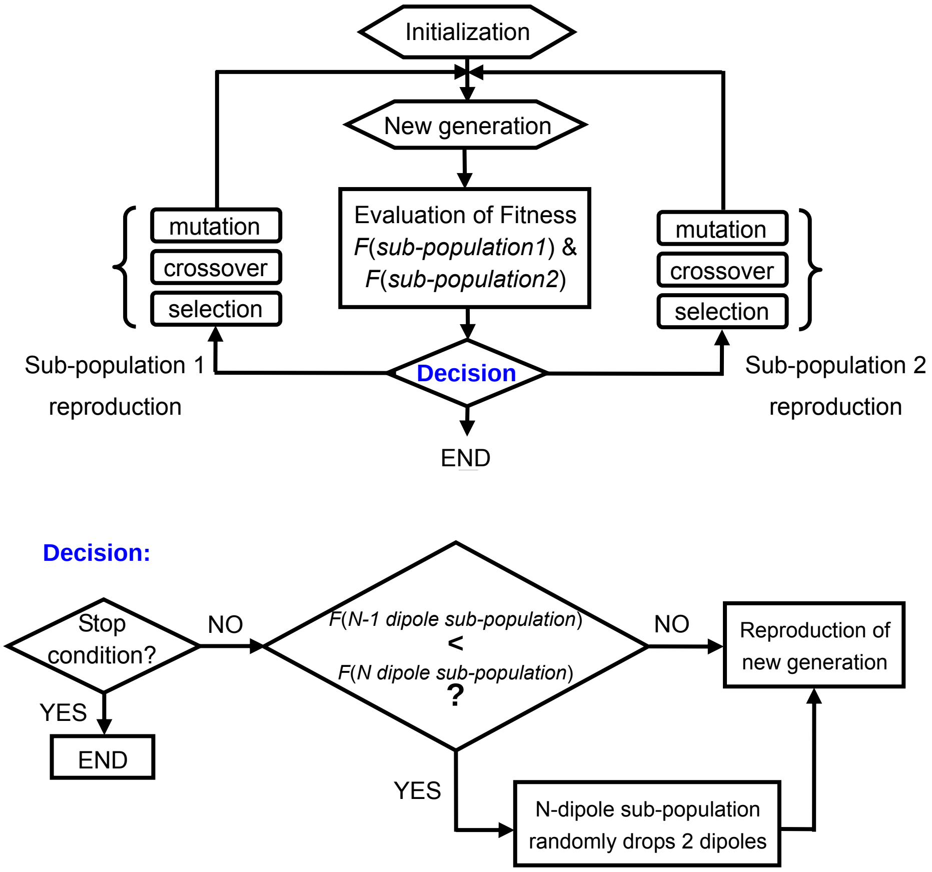

Fig. 4.5 Flowchart of the mutually competitive optimization

Here some points must be noted for the competition. First, the average of the fitness values is compared rather than the elitist. This is because the convergence of each sub-population must be guaranteed when decisions (drop dipoles or not) are to be made based on the competition result. Only when most individuals in a sub-population outperform the individuals in the other, the whole population is believed to be better fitted. Second, due to the effects of the N^{α} term in the fitness function, an array with fewer dipoles is allowed to be better fitted even though the agreement to the measured field is slightly worse than an array with more dipoles. As mentioned earlier, the parameter α controls the weight between accuracy and simplicity. Finally, the N-1 dipole sub-population starts its evolution a few generations later than the N dipole one. This aims to ensure that the decision of dropping dipoles is made in the situation that both sub-populations are in the converged stable state but not a coincidence during the random evolution process. When a sub-population drops two dipoles, its previous convergence is broken but the other sub-population is already well converged. So it must evolve to a new converged stable state to outperform the other. The convergence process is illustrated in Fig. 4.6.

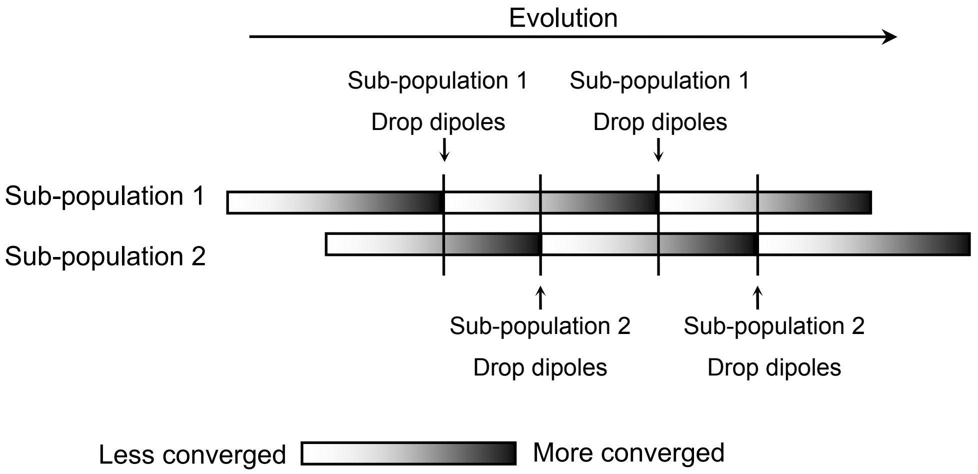

Fig. 4.6 Illustration of the convergence in the mutually competitive optimization

Results of this optimization are presented below taking the L-shaped microstrip board studied in Chapter 3 (structure shown in Fig. 3.3) as an example. According to the knowledge of the dependence on measurement parameters in Section 3.7, near-field data with “sufficient” information were used for the GA optimization where scanning resolution = 2.5mm, scanning plane size = 120×75 mm, and scanning height = 11.5 mm. The optimization started with

N_0=20 dipoles and a lower limit N_0=5 was specified. The population size was P=10000 and the weighting parameter α=0.2. The parameters of GA operations were p_{cross}=0.7, p_{mutation}=0.015, and elitist proportion=1%. Finally the competition stopped at N=7 which means that modelling with 6 dipoles could not outperform 7 dipoles. This implies that 7 is the essential number for modelling this board under these algorithm settings. The location of these dipoles is shown in Fig. 4.7 (a). It can be seen that the dipoles are distributed almost along the microstrip. It is reasonable because electromagnetic fields are actually produced from the microstrip track. This implies that an efficient way of modelling a PCB is to place the equivalent dipoles around the real radiating components if *a priori* information of the circuit structure is available.

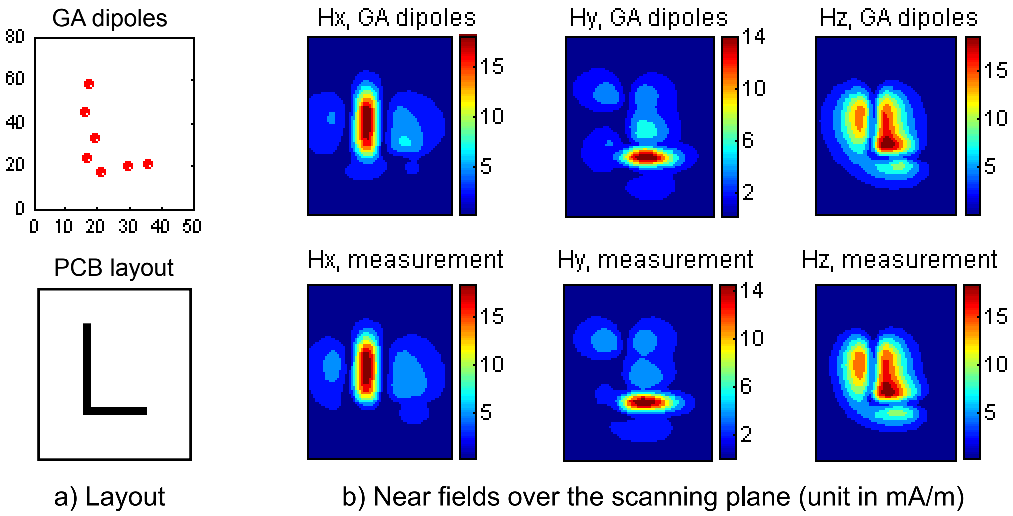

Fig. 4.7 Equivalent dipoles for the L-shaped microstrip board identified by a GA optimization

The reconstructed near field over the scanning plane and predicted far field in the E plane are presented in Fig. 4.7(b) and Fig. 4.8, respectively. Good agreement with full field simulation can be observed, showing that the equivalent dipoles identified from a GA optimization are a good representation of the PCB as an emission source.

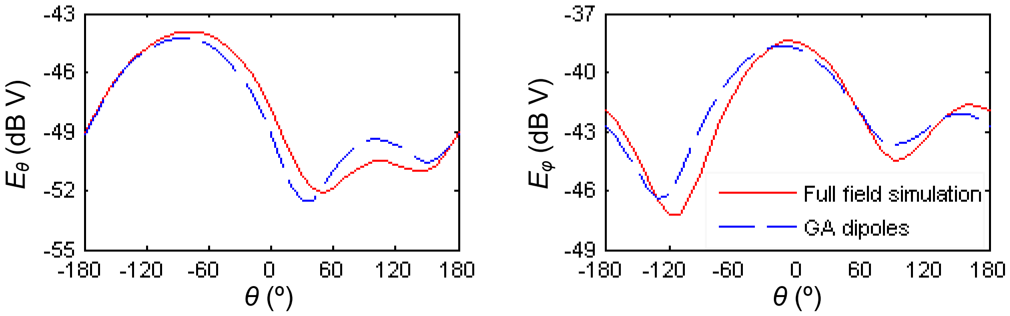

Fig. 4.8 Far field in the E plane predicted by the equivalent dipoles identified by GA

It must be recognized that there are some drawbacks in this optimization method. First, there is no rigid mechanism to ensure the global convergency of this optimization. All the techniques for the convergency discussed above are based on experience. Second, the computational costs are extremely large. The memory requirement and computational task are doubled in order to set up two sub-populations. Also the execution time is very long because whenever a sub-population drops dipoles it must evolve again to converge to another optimum and then become competitive against the other sub-population. Thus evolution within each sub-population is actually being repeated. For the example above, the running time was 20 hours on an Intel Core 2 Duo E8400 3.0 GHz computer. However, this method is able to provide the essential number and distribution of dipoles and predict the EM emissions. For these reasons, its usefulness for theoretical validations is more important than for practical applications.

4.4.3 Optimization by Self-Competitive Evolution

This optimization is called self-competitive evolution because fitting to the measured fields and searching the minimum number of dipoles are finished in the evolution of the same population. To implement this, a binary parameter γ_i is added to a dipole's parameter set which indicates whether to use this dipole. Therefore a dipole is described by 9 parameters besides the 8 parameters for position and moment as mentioned above. The whole dipole array is then encoded to a chromosome consisting of $N_0 \cdot (2W_1+6W_2+1)$ binary bits and the length of this chromosome remains the same in the optimization process. In the GA evolution, the number of dipoles updates from N_0 to N according to the value of every γ_i which is evolved by GA operations based on the fitness value. When $\gamma_i=1$, the corresponding dipole is set "active" and contributes to the total field. When $\gamma_i=0$, the corresponding dipole is set "inactive" and does not contribute to the total field. GA operations are carried out to evolve the other 8 parameters as normal no matter what value γ_i is. Due to the effects of the N^α term in the fitness function, an array with fewer dipoles is more likely to be fit even though the agreement of its field with the measured field is slightly worse. This dual-objective competition pushes the algorithm towards an optimal array generating the fitted field with as few dipoles as possible. The balance between accuracy and simplicity is controlled by the parameter α.

The effects of α is illustrated by taking the L-shaped microstrip board as an example. GA algorithms were repeatedly implemented by tuning the value of α. The starting number of dipoles N_0 and the lower limit N_1 were specified as 20 and 5 respectively. Due to the nature of random search, results may differ every time. A general result is presented in Fig. 4.9 showing the resulting number of dipoles N (dipoles with $\gamma_i=1$) and the mean squared error σ_{MSE} between the dipoles' field and measured field. A larger value of α tends to use fewer dipoles. But when α is too large ($\alpha \geq 0.5$), the balance between accuracy and simplicity is broken and the resulting number of dipoles falls to the lower limit $N_1=5$. On the other hand, when α is too small ($\alpha<0.1$), the fitness completely depends on the field agreement and the resulting number of dipoles remains at the starting number $N_0=20$. For the field agreement, obviously fewer dipoles lead to worse agreement. But when the essential number of dipoles is reached (in this example about 8), further increasing it would not significantly improve the field agreement.

This is indicated by the very slight variation of the mean squared error for *N*=8~16. Considering a balance between the two objectives – accuracy and simplicity – the value of *α* between 0.2 and 0.4 is reasonable in most cases.

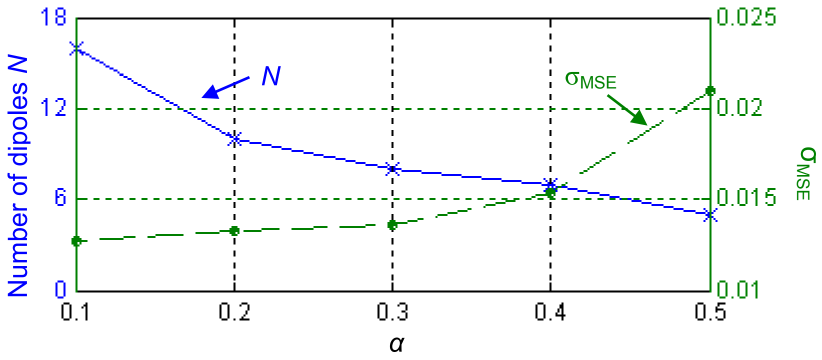

Fig. 4.9 Number of dipoles and field agreement as a function of the weight parameter *α*

The self-competitive evolution has some advantages over the mutually competitive evolution. First, the algorithm implementation is the standard GA routine. One can refer to the GA guidelines for considerations on convergency and algorithm stability. Second, as the optimization is finished within one population in one time, the computational costs are less heavy. For the case of the L-shaped board, the running time on the same computer was about 5 hours to achieve a convergence. However, compared to the inverse problem solution, the computational requirements of GA optimizations are still much heavier. The running time for the former is in the order of a few minutes and for the latter a few hours.

4.5 Results

4.5.1 Validation with Analytical Fields

The method was validated by identifying 4 dipoles which were randomly generated in a 2D area of *x*, *y*=-5~5mm with random moments and orientations. The GA optimization identified the dipoles from the analytically calculated tangential magnetic field over a 10×10mm plane at a height of 5mm above the original dipoles. The complete field information including both amplitude and phase was used in this test. The chromosome was encoded to include 8 possible dipoles in the searching space of x, y =-10~10mm. The parameters of GA operations were p_{cross}=0.7, p_{mutation}=0.014, and elitist proportion=2%. Due to the simplicity of this problem, a relatively small population size P=200 was specified, and the algorithm converged very fast, as shown in Fig. 4.10. After about 500 generations, almost all the individuals converged to the best fitted one.

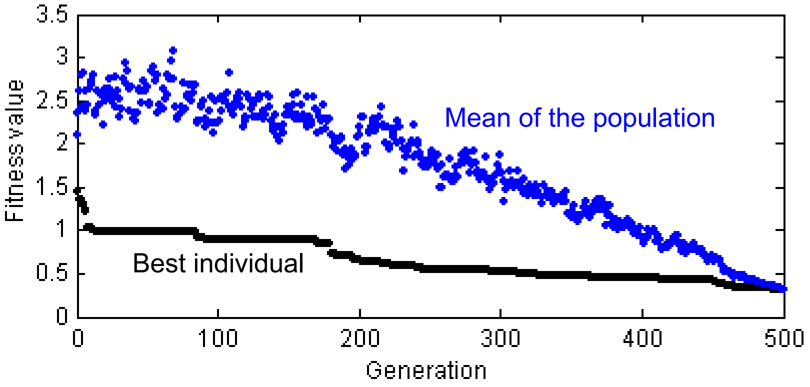

Fig. 4.10 Convergence of GA optimization for the analytical dipoles

Exactly 4 dipoles were identified after the optimization. Fig. 4.11 compares their positions with the original dipoles. In the chromosome each position parameter, x and y, was encoded with 8 binary bits. In terms of the encoding precision $20/(2^8-1)$=0.078mm, the reconstructed dipoles agree well with the original ones. The GA identified and original moments of the dipoles are presented in Fig. 4.12. Amplitude and phase of each Cartesian component M_x, M_y and M_z are shown separately, and the index n^th^ denotes the dipole in the n^th^ quadrant. A reasonable agreement with an average error of approximately 10% can be observed. This confirms that the method is useful for source diagnostics.

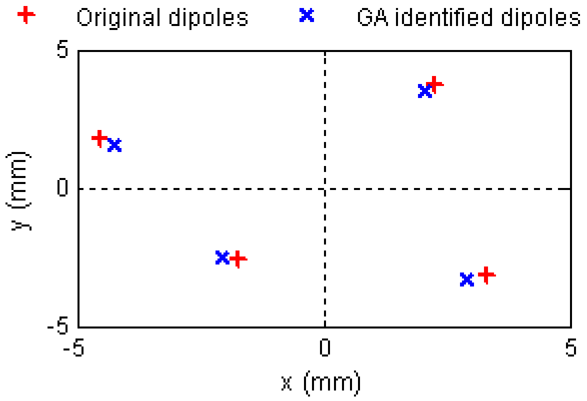

Fig. 4.11 Position of the original and GA identified dipoles

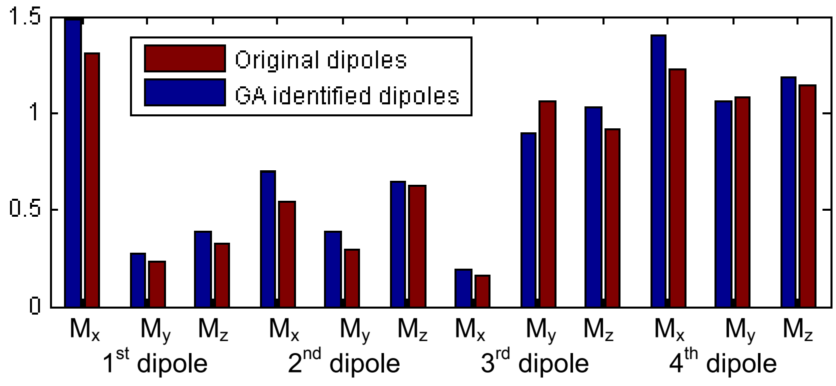

a) amplitude

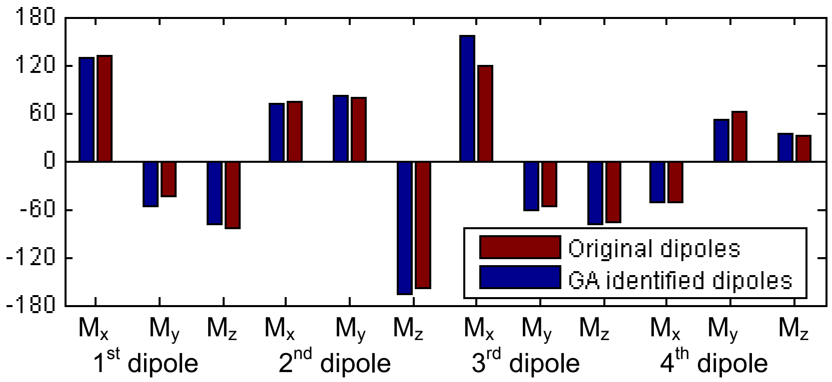

b) phase

Fig. 4.12 Amplitude and phase of the original dipoles and GA identified dipoles

The radiated field from the original source can then be predicted by the GA identified dipoles. The far-field H_θ in the E plane and H plane is shown in Fig.4.13 for illustration. As the real source naturally consists of dipoles, prediction by the equivalent dipoles has a very close agreement with the real field.

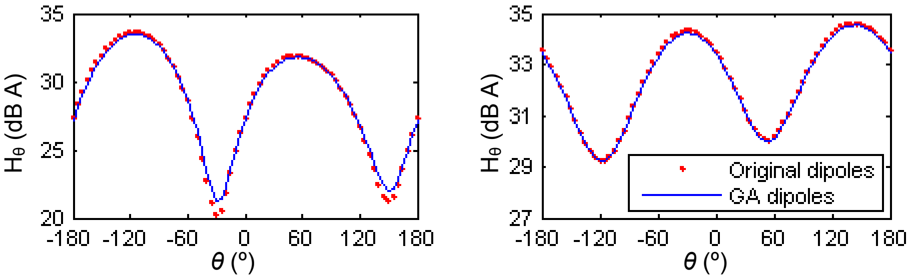

a) in the E plane (*xz* plane, φ=0) b) in the H plane (*yz* plane, φ=90°)

Fig. 4.13 Far-field patterns of the test set of dipoles

4.5.2 Application on a Digital Circuit Board

The digital circuit board, as shown in Fig. 2.32, was represented by equivalent dipoles from a GA optimization in order to illustrate a more general situation. The near-field data required for equivalent source identification were collected experimentally from near-field scanning. Both amplitude and phase of the tangential magnetic fields were measured with 2.5 mm scanning resolution over a 120×75 mm plane which was 8 mm above the PCB and centered at the PCB. The operation frequency was arbitrarily chosen at the 3rd harmonic 96 MHz.

The equivalent dipole identification by GAs was carried out with 16 possible dipoles in a 2000-individual population, and a weighting parameter α=0.2. The parameters of GA operations were p_{cross}=0.7, p_{mutation}=0.014, and elitist proportion=1%. The position parameters, x and y, were encoded with 3 binary bits for each, and the searching space was -10 to 60mm for x and 0 to 70mm for y denoting the PCB left bottom corner at (0, 0). Thus all the possible positions of the dipole were located on a mesh grid of a resolution 10mm.

After the GA optimization 11 dipoles were found to represent the PCB. The layout of the PCB and its equivalent dipole sources is shown in Fig. 4.14. As discussed in Chapter 2, the oscillator and the tracks carrying fast clock signal are the significant radiating components at this harmonic. This profile is represented by the equivalent dipoles identified by the GA optimization, as indicated by the distribution of the dipoles which is almost around the oscillator and clock signal tracks. Therefore the GA optimization not only represents the emissions from a PCB but also identifies the location of the primary source components.

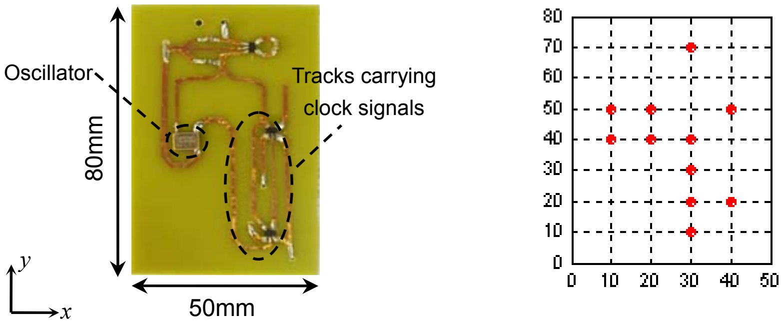

a) PCB

b) Equivalent dipoles

Fig. 4.14 Layout of the digital circuit board and it equivalent dipoles

The reconstructed near field over the scanning plane is compared with the measured field in Fig. 4.15. The inner border in the first graph sketches the size and position of the PCB. The original field is correctly represented by the dipoles identified by the GA, with a mean squared error of σ_{MSE}=4.8%. With the equivalent dipoles the electromagnetic field of this PCB at any position can be predicted. However, due to the lack of an appropriate receiver at this frequency, the measurement for far-field patterns was not able to be completed. Nevertheless, measurement of near field over a plane sized 120×75 mm and separated 30 mm from the PCB was carried out. Fig. 4.16 compares the field results obtained from measurement and dipole model prediction. A reasonable agreement can be found with a mean squared error σ_{MSE}=6.1%. Another field prediction is the evolution of the vertical electric field intensity $|E_z|$ against height, as presented in Fig. 4.17. Both measurement and simulation were carried out for the field from the centre of the PCB (x=25mm, y=40mm) upward and up to z=50mm limited by the sensitivity of the probe. The decreasing rate of the field obtained by the two methods is very close. Across the investigated height range the field intensities agree within 2 dB. Based on these results, it is confirmed that the equivalent dipole model favorably predicts the emission from the PCB.

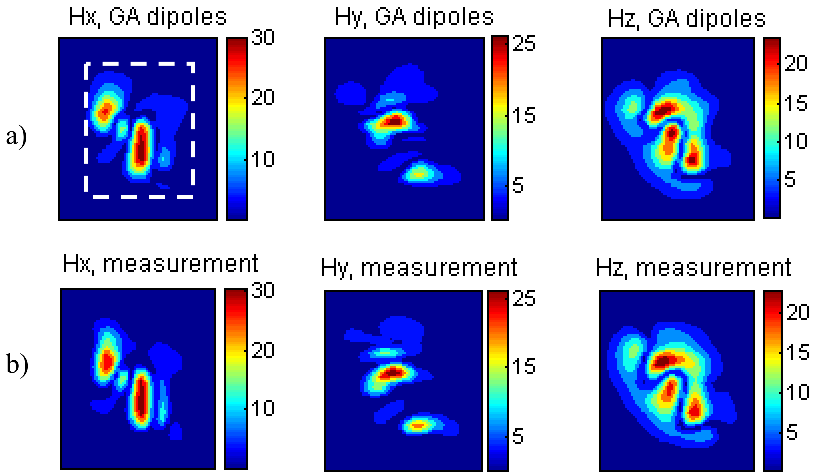

Fig. 4.15 Near field over the scanning plane from the digital circuit board (Unit in mA/m)

a) Reconstructed by the equivalent dipoles; b) measurement

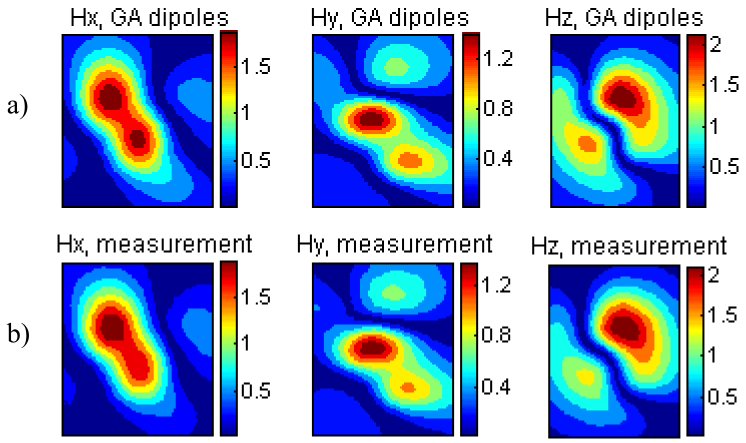

Fig. 4.16 Near field at 30mm above the digital circuit board (Unit in mA/m)

a) Prediction by the equivalent dipoles; b) measurement

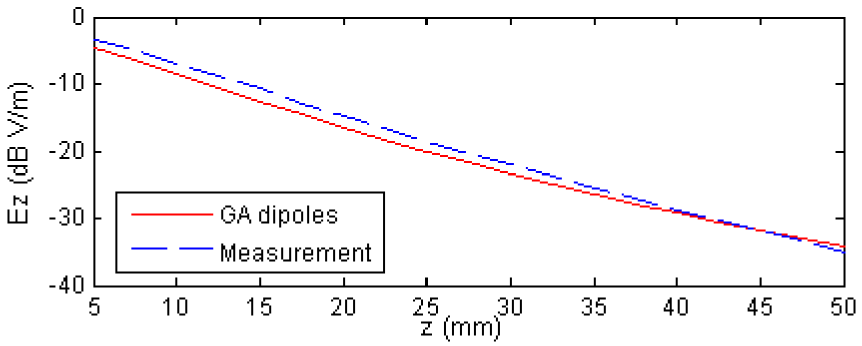

Fig. 4.17 Evolution of the vertical electric field from the centre of the PCB upward

4.5.3 Dependence on Near-Field Measurement

As theoretically there is no restriction on the type of the known near-field data to be fitted in the GA optimization, the method works with many types of information (amplitude, amplitude and phase; any component or a combination), provided that the given information is sufficient for electromagnetic characterization. The criteria for sufficiency, which were characterized as a function of the scanning parameters for the inverse solution method in Chapter 3, must be extended to consider the impact of phase and the number of field components in this case. Also considered is the usefulness of phaseless data over more than one near-field plane. This is inspired by the phase retrieval techniques where amplitude on two planes is used to retrieve the phase information [5]. When the information volume is reduced due to the lack of phase information, it can be compensated by collecting independent field data over more than one plane. To simplify the problem, the criteria for information sufficiency are studied in terms of the following pairs of situations: phase versus phaseless, H_x only versus $H_x + H_y$, 1 plane versus 2 planes. The scanning parameters used for every field plane are information sufficient according to the results in Section 3.7.

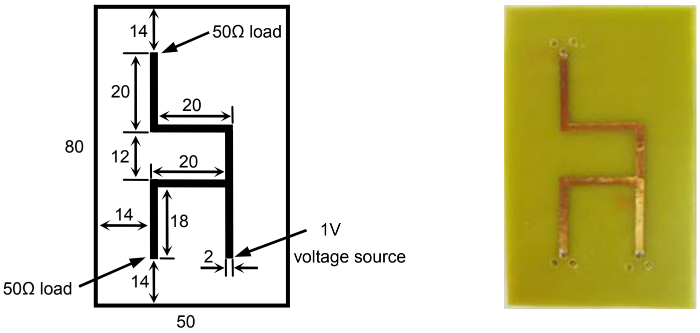

a) Schematic (unit in mm)

b) Photograph

Fig. 4.18 Top view of the test PCB with several coupled microstrips

A test PCB (dimension: 80×50×1.5mm) is introduced which has several coupled microstrips on one side and a ground plane on the other side, as shown in Fig. 4.18. The operation frequency was arbitrarily chosen at 1 GHz. The magnetic near field was collected over two planes at the height 8mm and 15mm, respectively. The size of both planes was 1.5 times of the PCB and the scanning resolution was 2.5mm. The equivalent dipoles for this board were identified following the GA optimization routine with different types of near-field data. Then the far-field pattern was predicted using every set of equivalent dipoles. The accuracy of using each type of near-field data was evaluated by comparing its predicted far field with the full field simulation. The normalized far-field component E_φ in the E plane is shown in Fig. 4.19, representing a typical result. The correlation coefficients of the patterns in each plot are listed in TABLE 4.2.

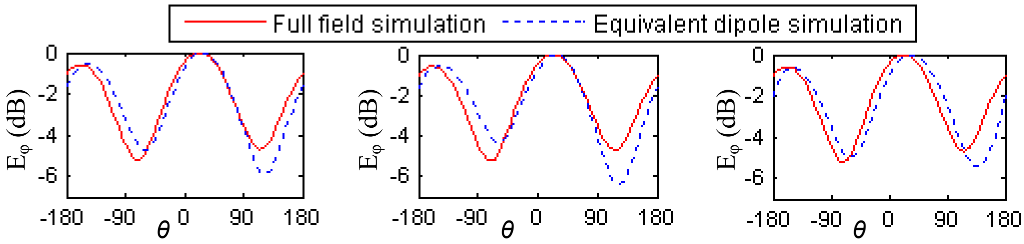

a) H_x and H_y, with phase b) H_x and H_y, phaseless, 2 planes c) H_x and H_y, phaseless, 1 plane

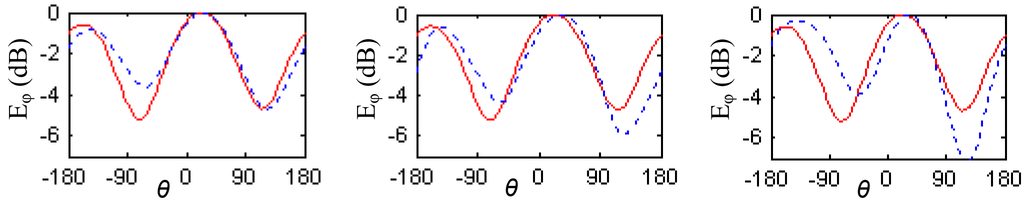

d) H_x, with phase e) H_x, phaseless, 2 planes f) H_x, phaseless, 1 plane

Fig. 4.19 Far field predicted by the equivalent dipoles identified from different types of near-field information

TABLE 4.2 Correlation coefficients of the field results in Fig. 4.19

Phase & planes Components	With phase, 1 plane	Phaseless, 2 planes	Phaseless, 1 plane
H_x and H_y	92%	88%	85%
H_x	90%	82%	73%

A quantitative assessment for the dependence on near-field information, as done in Section 3.7, is not appropriate here but only a general conclusion is considered. Generally, modelling from data with phase is more accurate even if only one field component H_x over one plane is used. When phase information is unavailable, the modelling accuracy can be improved by increasing the scanned field components and increasing the number of independent scanning planes. For the worst case with the least information (phaseless, H_x only, one plane), only an approximate far-field pattern can be predicted from the model. However, it is still useful for qualitative prediction such as pointing out hotspots and the maximum radiating direction, provided that the scanning parameters are information sufficient. All the others are accurate enough for quantitative prediction in EMC studies. Although the modelling accuracy varies, computationally the iterative generations required to achieve a convergence are almost at the same level for all the cases considered above. Therefore, with this method the near-field data required for the equivalent dipole modelling are less restricted and can be collected depending on the experimental feasibility.

4.6 Conclusions

A method for modelling equivalent sources for PCBs from near-field scans and the genetic algorithms is presented in this chapter. A PCB is modelled with an array of equivalent dipoles deduced from an optimization procedure using GAs by fitting to the measured near fields. Two optimization procedures are proposed based on the mutually competitive evolution between two subpopulations and self-competitive evolution within the whole population, respectively.

The GA optimization is introduced in the equivalent dipole identification in order to find the optimal number and layout of the equivalent dipole. The optimization not only provides a means to diagnose the location of the primary real sources but also leads to a more efficient equivalent dipole representation for the PCB. Another advantage of the method is the ability of making use of many types of near-field data, including phaseless data, therefore alleviating the demands on experimental facilities. However, due to the nature of iterative random search of GAs, the computational costs are very heavy and the running time for real PCBs is normally more than a few hours.

The method is validated with analytical fields from a simple dipole-like source and measured fields from PCBs. The favorable source identification and field prediction show that the method is suitable for EMI and EMC studies. In addition, the usefulness of several types of near-field information for GA optimization is demonstrated.

References

[1] P. Petre and T. K. Sarkar, “Planar near-field to far-field transformation using an equivalent magnetic current approach,” *IEEE Trans. Antennas Propagat.*, vol. 40, no. 11, pp. 1348-1356, Nov. 1992.

[2] T. K. Sarkar and A. Taaghol, “Near-field to near/far-field transformation for arbitrary near-Field geometry utilizing an equivalent electric current and MoM”, *IEEE Trans. Antennas Propagat.*, vol. 47, no. 3, pp. 566-573, Mar. 1999.

[3] P. A. Barrière, J. J. Laurin, and Y. Goussard, “Mapping of equivalent currents on high speed digital PCBs based on near-field measurements”, *IEEE Trans. Electromagn. Compat.*, vol. 51, no. 3, pp. 649-658, Aug. 2009.

[4] Y. Vives-Gilabert, C. Arcambal, A. Louis, F. de Daran, P. Eudeline, and B. Mazari,

"Modelling magnetic radiations of electronic circuits using near-field scanning method," *IEEE Trans. Electromagn. Compat.*, vol. 49, no. 2, pp. 391-400, 2007.

[5] R. G. Yaccarino and Y. R. Samii, "Phase-less bi-polar planar near-field measurements and diagnostics of array antennas," *IEEE Trans. Antennas Propagat.*, vol. 47, pp. 574–583, Mar. 1999.

[6] C. A. Balanis, *Advanced Engineering Electromagnetics*. New York: Wiley, 1989.

[7] R. Fletcher, *Practical Methods of Optimization*. Chichester, U.K.: Wiley Intersci., 1980.

[8] J. H. Holland, *Adaptation in Natural and Artificial Systems*. Ann Arbor, MI: Univ. Michigan, 1975.

[9] Y. Rahmat-Samii and E. Michielssen, *Electromagnetic Optimization by Genetic Algorithms*. New York: Wiley, 1999.

[10] D. S. Weile and E. Michielssen, "Genetic algorithm optimization applied to electromagnetics: a review," *IEEE Trans. Antennas Propagat.*, vol. 45, no. 3, pp. 343-353, Mar. 1997.

[11] D. E. Goldberg, "Real-coded genetic algorithms, virtual alphabets and blocking," *Complex Syst.* 5, pp. 129-167, 1991.

[12] D. E. Goldberg and K. Deb, "A comparative analysis of selection schemes used in genetic algorithms," in Foundations of Genetic Algorithms, G. J. E. Rawlins, ed. San Mateo, CA: Morgan Kaufmann, pp. 69-93, 1991.

[13] K. A. DeJong, "An analysis of the behavior of a class of genetic adaptive systems," Ph.D. dissertation, Univ. Michigan, 1975.

[14] X. Qi, and F. Palmieri, "Theoretical analysis of evolutionary algorithms with an infinite population size in continuous space - Part II: analysis of the diversification role of crossover," *IEEE Tran. Neural Networks*, vol. 5, no. 1, pp. 120-129, Jan. 1994.

[15] T. Isernia, G. Leone, and R. Pierri, "Radiation pattern evaluation from near-field intensities on planes," *IEEE Trans. Antennas Propagat.*, vol. 44, pp. 701–710, May 1996.

CHAPTER FIVE

Equivalent Dipole Modelling in Closed Environments

5.1 Introduction

High-density packaging has been widely applied to modern PCB designs. For example, a signal processing module can be completely enclosed with only the I/O ports exposed for connections. This however leads to more electromagnetic interference problems between PCBs and enclosures. It is particularly the case for large electronic systems with several PCBs enclosed in their operating environment (e.g. a conducting cabinet with apertures). Therefore the consideration of electromagnetic compatibility of PCBs must include the interactions between PCBs and enclosures.

In this chapter, the equivalent dipole model is extended to represent a PCB in closed environments. This method is attractive due to the computational simplicity and the independence of circuit information. However, the equivalent dipole models discussed in previous chapters, either found from an inverse solution or a genetic algorithm optimization, do not work in closed environments. Such an example is shown in Fig. 5.1 where both full field simulation and equivalent dipole simulation were carried out for predicting the field excited by the L-shaped microstrip board, as shown in Fig. 3.3, inside an enclosure at 4 GHz.

The geometrical configuration of the model is detailed in Fig. 5.1(a). In the full field simulation which acted as a reference for the accuracy of the equivalent model, both the board and box were modelled with a Method of Moment (MoM) based solver Concept-II 9.4 [1], while in the equivalent dipole simulation the board was replaced by the equivalent model consisting of dipoles and a ground plane derived from near-field scans in free space. It is found that the two results completely disagree. One possible reason is that the free space equivalent model only represents the electromagnetic excitations of the PCB but not the interactions between the PCB and the enclosure. Accurate models in closed environments call for an equivalent representation for both the radiating sources and interactions between PCBs and enclosures.

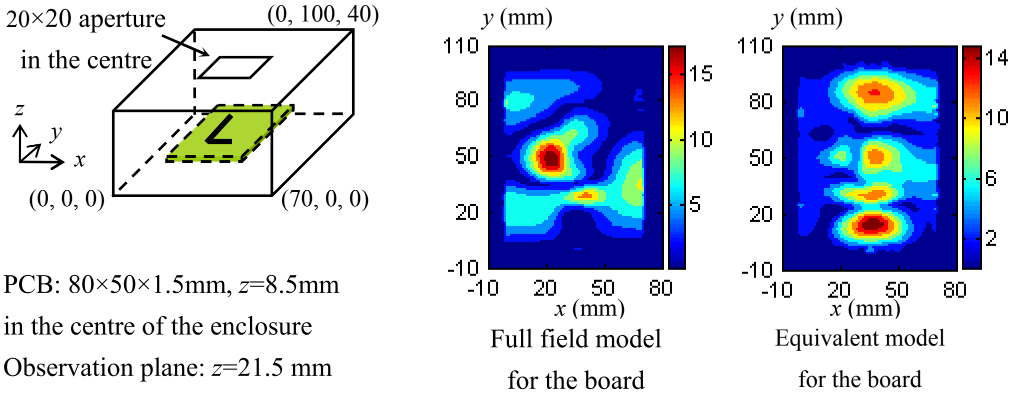

a) Configuration (length in mm)

b) H_y (mA/m) in the enclosure

Fig. 5.1 Field of the L-shaped microstrip box inside a test box obtained by modelling the board with a full field model and the free space equivalent model

To the author’s knowledge, there have been very few reports on equivalent source simulation for PCBs inside an enclosure. In [2], it is reported that the equivalent current method has considerable inaccuracies when applied to printed circuits inside an enclosure. This was attributed to the change of current distribution of the circuit due to the multiple interactions with nearby objects. But in the studies of this project, it is found that the changes in the wave propagation characteristics of an enclosure due to the physical presence of a PCB affect the radiated emissions more significantly than the change of the PCB currents in closed environments. This effect is the most important factor in characterizing the interactions between the PCB and the enclosure. Other effects caused by the multiple interactions, such as the change of current distribution, radiation loss and impedance, are much less significant and can be neglected for an approximate model. Thus the equivalent model must represent not only the excitations but also the gross physical presence of a PCB, such as its ground plane and dielectric body. For this purpose, the equivalent model is extended to explicitly include the ground plane and the PCB dielectric. This model is referred to as the dipole – dielectric – conducting plane (DDC) model, which is a general representation of a PCB, the model in free space being a special case. The equivalent dipoles can then be incorporated into a full field solver together with nearby objects, enclosures, etc. for prediction of near and far fields in both free space and closed environments.

This chapter is organized as follows. In Section 5.2, the electromagnetic characteristics of a PCB in free space and closed environments are compared in order to characterize how the multiple interactions affect the PCB in closed environments. Based on these results, the DDC model is proposed in Section 5.3, and the identification of the equivalent dipoles in this model is detailed. Then in Section 5.4, simulation and experiment results for the L-shaped microstrip board at both resonant and non-resonant frequencies are presented for a validation of the DDC model. Finally in Section 5.5 the model is applied to the typical enclosed PCB configurations and the results are compared with measurements.

5.2 Electromagnetic Characteristics of PCBs in Closed Environments

Once a PCB is mounted inside an enclosure, multiple interactions will take place, including a number of factors such as multiple reflections, induced currents, and dampening of the PCB to the cavity fields, etc. The electromagnetic characteristics of a PCB are then affected. But the equivalent models derived from near-field scans in free space do not represent these effects. Therefore, in order to establish equivalent models in closed environments, the multiple interaction effects on a PCB must be additionally modelled.

As a radiating source, the major characteristics of a PCB generally include the current distribution, radiating efficiency, impedance, and physical presence. It is difficult to model the effects of multiple interactions on all of them. In this work, it aims to establish an approximate model thus it is reasonable to only consider the significantly affected PCB characteristics. For this reason, a series of experiments and simulations were carried out to test the electromagnetic characteristics of a PCB in both free space and closed environments. The purpose of these tests was not to establish a general theory of multiple interaction effects, but to provide evidence for making assumptions for an approximate equivalent model. Thus simple configurations were treated.

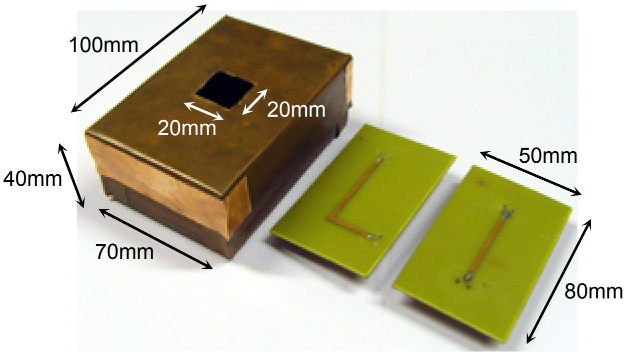

Fig. 5.2 Configuration of the test box

A test enclosure made of 1mm thick copper was introduced for the characterization which was a 100×70×40mm rectangular box with a 20×20mm square aperture in the centre of the top surface, as shown in Fig. 5.2. When a PCB was placed in the enclosure, the lid was sealed from both the inside and outside using copper tape. The resonant frequencies of a closed rectangular box are given by [3, Chapter 8]

$$f_{\mathrm{cmn}} = \frac{1}{2}\sqrt{\frac{\left(\frac{m}{a}\right)^2 + \left(\frac{n}{b}\right)^2 + \left(\frac{p}{c}\right)^2}{\mu\varepsilon}} \tag{5.1}$$

where ε and μ are the permittivity and permeability of the media, a, b, and c are the geometrical size of the box ($a \geq b \geq c$), and m, n, and p are the cavity orders (integers). The frequency allowing TE_{110} mode (m=1, n=1, p=0, and the media is air) is the cutoff frequency and for this box it is approximately 2.62 GHz.

5.2.1 Current Distribution on a PCB

The first characteristic studied is the current distribution on a PCB which is the radiating source of the whole PCB-enclosure configuration. The L-shaped microstrip board was chosen as the radiating source, and its current distributions in free space and closed environments were compared. At one end of the track the board was excited by a 1V voltage source with 50Ω impedance, and at the other end the track was terminated with a 50Ω load. The currents were obtained numerically by modelling the board with an MoM based solver Concept-II 9.4 [1], as illustrated in Fig. 5.3. For the closed environment model the board was located 8.5mm above the bottom of the test box. Identical meshes were employed for the board in both free space and the closed environment, and the current distribution on the top surface of the board was observed. In addition, a detailed observation was made along the L-shaped track where the currents were the most significant. The track was discretized with 25 segments as illustrated in Fig. 5.3(d).

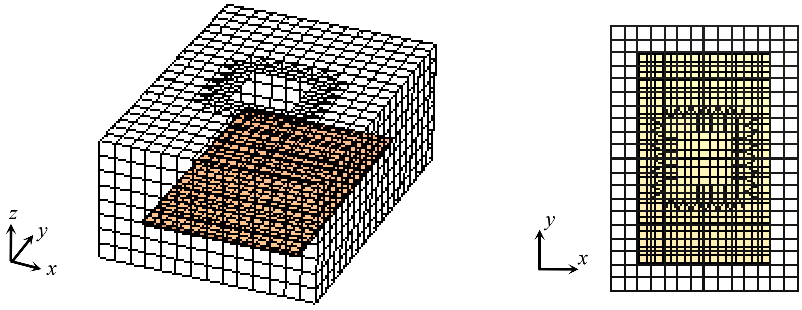

a) 3D view b) top view

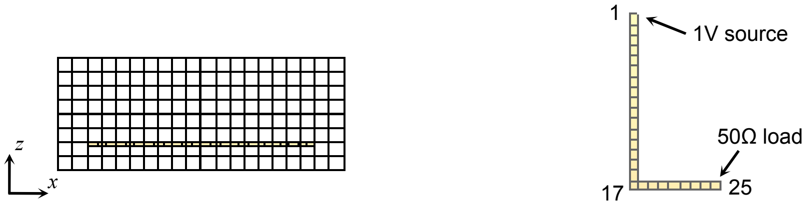

c) side view d) segment numbers of the track

Fig. 5.3 Full field model of the L-shaped microstrip board inside the test box

The current distribution at 1 GHz is displayed in Fig. 5.4, showing the whole intensity map on the top surface of the board and a detailed view along the L-shaped track. This frequency is below the cutoff thus there are only evanescent modes. It is observed that the current distribution in the closed environment is almost identical to that in free space.

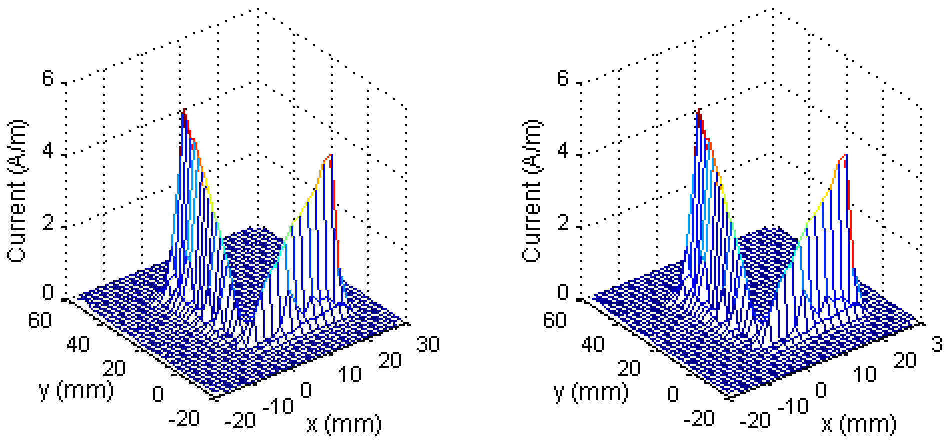

a) Full map over the top surface of the board

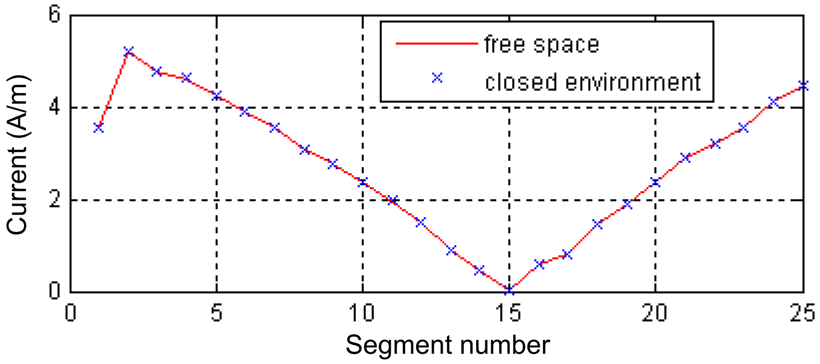

b) Observation along the track

Fig. 5.4 Current distribution on the L-shaped microstrip board in free space and in the test box at 1 GHz

The current distribution at a higher frequency 4 GHz is presented in Fig. 5.5. At this frequency both propagating modes and evanescent modes exist inside the box, and the current distribution of the PCB is slightly affected by the multiple interactions, as indicated by the minor difference of the currents along the track. However, the change of the current distribution in the closed environment is not significant (<1% at 4 GHz). For an approximate equivalent model it is safe to assume that the change is negligible. This means that the equivalent dipoles obtained from the near-field scans in free space are still able to represent the current distribution of the PCB in closed environments.

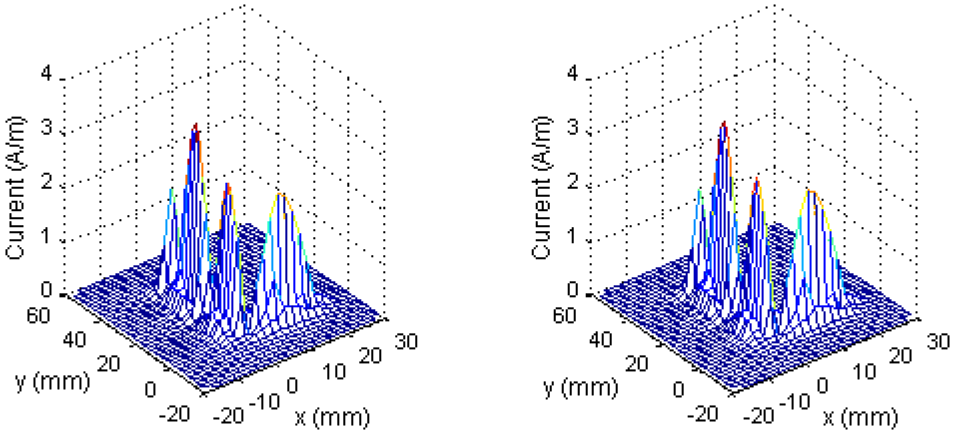

a) Full map over the top surface of the board

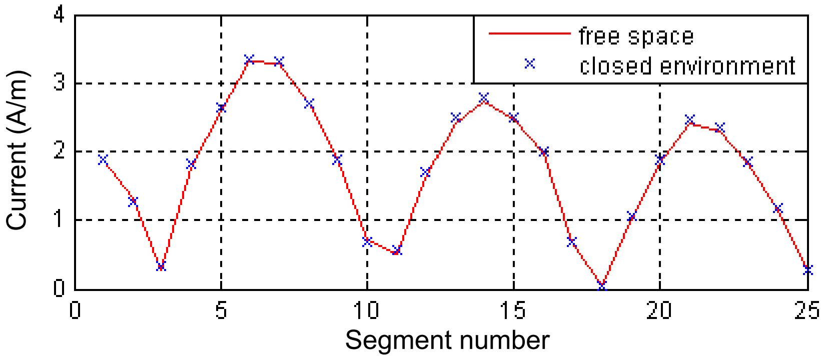

b) Observation along the track

Fig. 5.5 Current distribution on the L-shaped microstrip board in free space and in the test box at 4 GHz

5.2.2 Radiation Loss

Radiation loss is the ratio of the power radiated from a PCB divided by the power applied to the PCB. It is an indicator of the efficiency of a PCB as a radiating source. The equivalent dipoles only represent the radiated proportion of the total power. Hence, if the radiation loss is significantly changed by the multiple interactions it must be taken into account in the equivalent models.

A convenient way to characterize the radiation loss is by experimental measurement with a vector network analyzer (VNA). For the L-shaped microstrip board, denote the source end of the track as port 1 and the load end port 2 (both ends are fed to the VNA via 50Ω cables with SMA connectors), the scattering parameters S_{11} (reflected power) and S_{21} (transmitted power) were measured and the power loss can be calculated by:

$$\text{Total loss} = \text{Radiation loss} + \text{Other losses} = 1 - |S_{11}|^2 - |S_{21}|^2 \tag{5.2}$$

Although the measurement includes other losses such as losses associated with induced currents, radiation loss accounts for the major part of the total loss. Measurements were carried out in free space and in the test box independently and the results are shown in Fig. 5.6. Up to 5 GHz the radiation loss of the board in free space and the closed environment does not make a significant difference. Almost the same proportion of the power applied to the board is radiated which is readily fully included in the equivalent dipole model obtained from the near-field scans in free space.

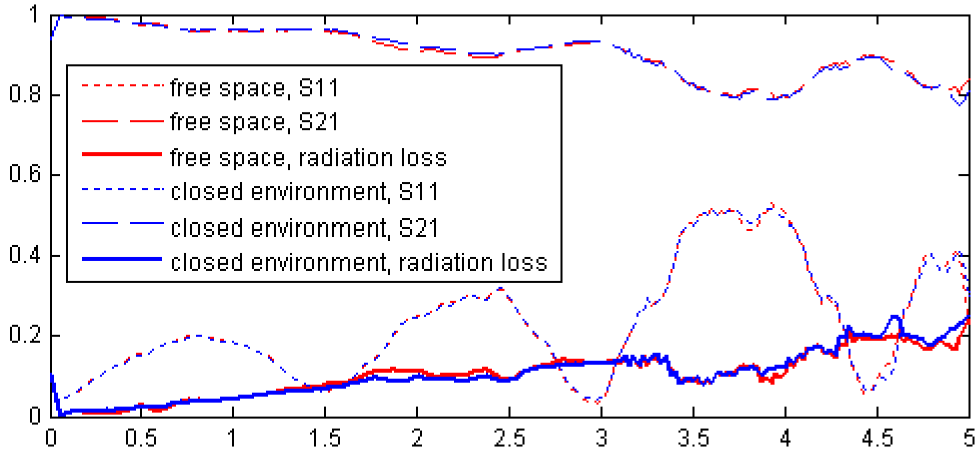

Fig. 5.6 Scattering parameters and radiation loss of the L-shaped microstrip board in free space and in the test box

5.2.3 Impedance of PCB Tracks

The characteristic impedance Z_o of PCB tracks determines the propagation of signals along the tracks. An impedance matched design can be applied for good transmission. When impedances do not match, some of the energy is reflected back. Thus, if the impedance of PCB tracks significantly changes in closed environments, the transmission of energy along the tracks will be affected, leading to a change in the radiated emissions. Here the characteristic impedance of PCB tracks in free space and closed environments is compared by experimental measurements. The sample was a 2mm wide and 40mm long track mounted on an 80×50×1.5mm FR4 substrate and backed by a ground plane, as shown in Fig. 5.2.

A convenient way of measuring the characteristic impedance is to use a time-domain reflector meter (TDR) [4]. A TDR transmits a short rise time pulse along a conductor and measures the reflected power in the time domain. As the reflected power is sensitive to impedance variations, the characteristic impedance can be obtained as a function of the track length. Measurements were carried out with the test track in both free space and in the test box. In both measurements, the track was terminated with a 50Ω load via an SMA connector. Fig. 5.7 presents the location of each component in this setup and the characteristic impedance obtained from TDR measurements. The fluctuations along the PCB track are due to the manufacturing imperfection and on average $Z_o = 59\Omega$ is found for this track. It is observed that only a very small change of the impedance occurs in the closed environment.

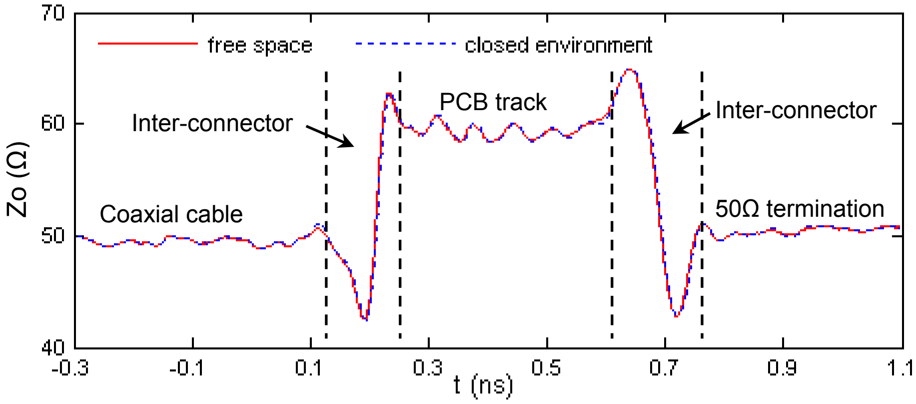

Fig. 5.7 Characteristic impedance of a 2mm wide PCB track in free space and in the test box measured with a TDR

The TDR measurements do not show the frequency dependence of Z_o. But it can be obtained indirectly from the input impedance Z_{in} measured in the frequency domain with a VNA. According to the transmission line theory [5, Chapter 2], the input impedance of a PCB track of finite length can be expressed in terms of its characteristic impedance Z_o by

$$\frac{Z_{\text{in}}}{Z_{\text{o}}} = \frac{\dfrac{T_x}{Z_{\text{o}}} + j\tan\beta l}{1 + j\dfrac{T_x}{Z_{\text{o}}}\tan\beta l} \tag{5.3}$$

where T_x is the impedance of the termination (for example, T_{50} stands for 50Ω loaded termination), β is the phase constant and l is the length of the track. The term $\tan\beta l$ can be eliminated by performing two independent measurements with different terminators. In this test, a 50Ω load T_{50} and a short terminator T_0 were used. It should be noted that normally the impedance of a short terminator is not ideal but a frequency dependent inductive value $T_0 = j\omega L$ is present which can be measured with a VNA. Then Z_o can be calculated from the two Z_{in} measurements by

$$Z_o = \sqrt{\frac{T_{50}Z_{\mathrm{in}(0)}Z_{\mathrm{in}(50)} - T_0 Z_{\mathrm{in}(0)}Z_{\mathrm{in}(50)} + T_0 T_{50} Z_{\mathrm{in}(0)} - T_0 T_{50} Z_{\mathrm{in}(50)}}{Z_{\mathrm{in}(0)} - Z_{\mathrm{in}(50)} - T_0 + T_{50}}} \tag{5.4}$$

where $Z_{in(50)}$ and $Z_{in(0)}$ are the input impedances of the track terminated with a 50Ω load and a short terminator, respectively. The calculated characteristic impedances in free space and in the test box are presented in Fig. 5.8. The values of the real part across the whole frequency horizon are very close to the TDR measured results. The imaginary part of Z_o, which can not be obtained from the TDR measurement, is nearly zero, showing that the track is approximately lossless. Again, the difference of Z_o in free space and the closed environment is very small. This suggests that closed environments do not significantly affect the impedance of PCB tracks.

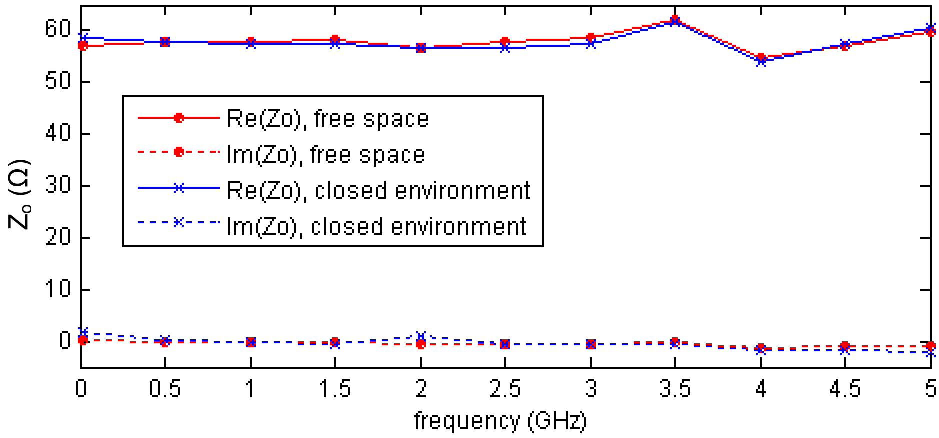

Fig. 5.8 Characteristic impedance of a 2mm wide PCB track in free space and in the test box obtained based on VNA measurements

5.2.4 Physical Presence of a PCB

The enclosure can be understood as a waveguide operating either above or below cut-off, with the PCB acting as the excitation. The presence of a PCB changes the propagation characteristics of the waveguide. This effect is illustrated in Fig. 5.9 which shows the electric field inside the test box with illuminated by a plane wave from the aperture at 4 GHz. The field was obtained by the Transmission Line Modelling (TLM) simulation [5], when the L-shaped microstrip board (not powered) was either present or not present. The field distribution and magnitude in the two cases are completely different. When the PCB is not present, a standard mode field is observed inside the enclosure. But the field distribution is significantly distorted by the presence of the PCB, indicating that the propagation of the electromagnetic wave in the enclosure is affected. It can also be seen that this effect is much more important than the other effects discussed in previous sections and can not be neglected under any approximation. In this configuration, the PCB is not powered therefore its only contribution is the physical presence. Thus the physical presence of a PCB which dampens the wave propagation characteristics is the most important factor for predicting the fields in closed environments and must be additionally modelled to accurately represent the interactions between the PCB and the enclosure.

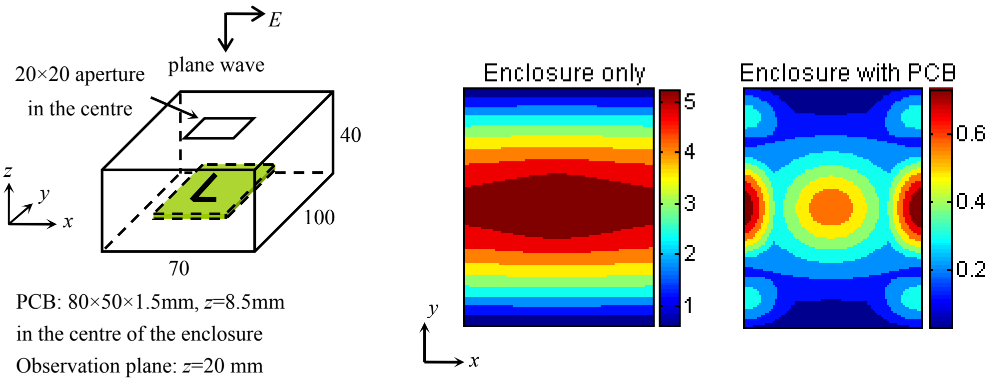

a) Configuration (length in mm)

b) E_x (V/m) in the enclosure

Fig. 5.9 Horizontal electric field inside the test box in the presence and absence of a PCB

5.3 The Dipole-Dielectric-Conducting Plane Model

Based on the results in the previous section, the physical presence of a PCB, which affects the propagation characteristics of a waveguide, is the most important effect due to the multiple interactions between the PCB and the enclosure. The change of the radiating source, such as current distribution, radiation loss and impedance, can be assumed negligible for an approximate model. Therefore it appears necessary to include the gross physical structures of the PCB in addition to modelling the equivalent sources. However, practical PCBs normally contain ground planes, dielectrics, conducting tracks and components. It is not possible to model in detailed all this complexity. An approximate representation for a PCB may be useful.

D. W. P. Thomas, *et*., *al*. [6] studied the equivalent circuits for the shielding effectiveness of an enclosure loaded with PCBs. In their approach a populated PCB (excluding the ground plane) were approximated by a slab of homogeneous dielectric and reasonable results were obtained. This representation is used in the equivalent dipole model to approximate the passive electromagnetic properties of a PCB. If the PCB has a ground plane, it is also taken into account as an essential feature of the model. The active radiating sources are still modelled with equivalent dipoles. To illustrate this approach, the dipole – dielectric – conducting plane (DDC) model is developed.

Fig. 5.10 shows the configuration of the model. The dielectric slab with a ground plane at the bottom has the same thickness h as the PCB. The dielectric material is described by the relative permittivity ε_r, assuming that the relative permeability μ_r is 1 and the effective conductivity σ is 0. This is a reasonable approximation for a vast majority of PCB substrate materials. Similar to the approximations made to the free space model, the equivalent dipoles are placed on the top surface of the substrate and in an area which is $6h \sim 10h$ smaller than the

PCB dimensions. No information of the real circuit structure is needed for building the model.

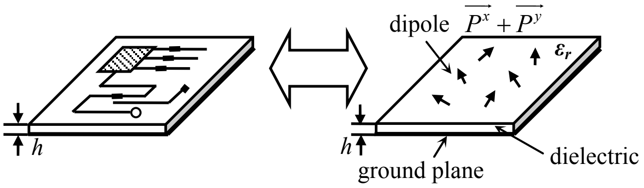

Fig. 5.10 Configuration of the Dipole-Dielectric-Conducting plane model

The equivalent sources are still identified from the solution of an inverse problem by fitting to the scanned tangential magnetic near field in free space. For the DDC model horizontal electric dipoles are used for the active excitations because the computation of their radiated near fields is simpler than that of magnetic dipoles. Each dipole is decomposed into x and y directed moment components P^x and P^y. The exact expressions of the magnetic field radiated by the dipole component are used which integrate the product of the moment with the dyadic Green's function at the air-dielectric interface to calculate the fields [7]. Suppose the origin of the coordinate system is set to be the location of the infinitesimal dipole and considering the P^x component, the tangential magnetic field can be expressed in the cylindrical coordinates as:

$$H_x\left(\rho,\phi,z\right)=\frac{P^x}{2\pi}\left(\varepsilon_r-1\right)\sin 2\phi\int_0^\infty \frac{k_\rho^3}{D_{\mathrm{TE}}D_{\mathrm{TM}}}e^{-u_0 z}\cdot\left(J_0\left(k_\rho\rho\right)-\frac{J_1\left(k_\rho\rho\right)}{k_\rho\rho}\right)dk_\rho=P^x\xi_x^x \quad (5.5)$$

$$\begin{aligned}H_y\left(\rho,\phi,z\right)=&\frac{P^x}{2\pi}\int_0^\infty J_0\left(k_\rho\rho\right)\frac{k_\rho u_0}{D_{\mathrm{TM}}}e^{-u_0 z}dk_\rho-\\&\frac{P^x}{2\pi}\left(\varepsilon_r-1\right)\sin 2\phi\int_0^\infty \frac{k_\rho^3}{D_{\mathrm{TE}}D_{\mathrm{TM}}}e^{-u_0 z}\cdot\left(\cos^2\phi J_0\left(k_\rho\rho\right)-\cos 2\phi\frac{J_1\left(k_\rho\rho\right)}{k_\rho\rho}\right)dk_\rho=P^x\xi_y^x\end{aligned} \quad (5.6)$$

where

k_p is the complex radial component of the wave number,

$u_0=jk_{z0}=\sqrt{k_\rho^2-k_0^2}$

$u=jk_z=\sqrt{k_\rho^2-\varepsilon_r k_0^2}$

and the functions D_{TE} and D_{TM} are given by

$$D_{\mathrm{TE}} = \varepsilon_r u_0 + u \tanh uh$$
$$D_{\mathrm{TM}} = u_0 + u \coth uh$$

The y-directed dipole component has similar expressions with just a coordinate transformation. It should be recognized that the computation in (5.5) and (5.6) involves extensive numerical integrations. There are many reports on the detailed derivation and efficient techniques for this integration which have been successfully applied to printed antenna calculation [7]-[9]. Here the technique described in [7, Chapter 3] which integrates along the real axis and decomposes the integration interval into three sub-intervals [0, k_0], [k_0, $k_0\sqrt{\varepsilon_r}$], and [$k_0\sqrt{\varepsilon_r}$, ∞] is used. The computational details of this integration are discussed in Appendix C and D. After numerical integration, the equations of the inverse problem finally have the form

$$\begin{aligned} \begin{bmatrix} \xi_x^x & \xi_x^y \end{bmatrix}_{m\times n} \begin{bmatrix} P^x \\ P^y \end{bmatrix}_{n\times 1} &= \begin{bmatrix} H_x \end{bmatrix}_{m\times 1} \\ \begin{bmatrix} \xi_y^x & \xi_y^y \end{bmatrix}_{m\times n} \begin{bmatrix} P^x \\ P^y \end{bmatrix}_{n\times 1} &= \begin{bmatrix} H_y \end{bmatrix}_{m\times 1} \end{aligned} \qquad (5.7)$$

where the coefficients ξ_x and ξ_y are defined in (5.5) and (5.6), m is the number of the discretely scanned field points, and n is the number of the modelled equivalent dipoles. Thus the moment of each equivalent dipole can be found from the inverse of the problem in (5.7). Once the equivalent sources in the DDC model have been determined, they can replace the PCB in a full field solver model which also includes nearby objects such as enclosures and packages. An example of modelling a PCB inside an enclosure is illustrated in Fig. 5.11. In this work all the simulations with the DDC model were performed with a MoM based solver Concept-II 9.4 [1].

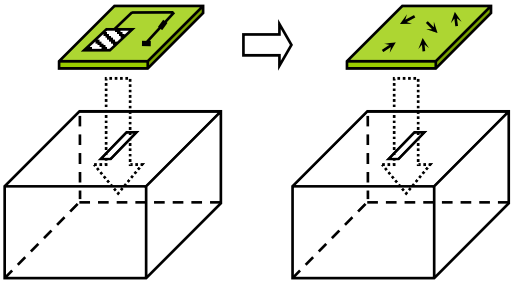

Fig. 5.11 Modelling in closed environments: equivalent DDC model and nearby objects

5.4 Validation of the Model

5.4.1 Simulation for the L-shaped Microstrip Board

In order to validate the DDC model, simulations for the configuration shown in Fig. 5.1, where the free space equivalent model did not work, were repeated with a DDC model. All the settings of the board, enclosure and observation plane were exactly the same as in Fig. 5.1. An equivalent DDC model was first derived from near-field scans in free space. Parameters of the scans were chosen according to the studies of information sufficiency in Section 3.7, as listed in TABLE 5.1. The DDC model was then incorporated into the full field model to replace the PCB. Magnetic fields over the observation plane inside the enclosure were predicted and compared with the results of directly modelling the board, as presented in Fig. 5.12.

TABLE 5.1 Parameters of the near-field scans for the L-shaped microstrip board

frequency (GHz)	4
scanning plane height (mm)	11.5 above the PCB
scanning plane size (mm)	120 × 75
scanning resolution (mm)	2.5

The white border in the first intensity map shows the area of the enclosure. With the DDC model, the predicted fields have been significantly improved than using the free space equivalent model. An approximate field distribution can be obtained, and the predicted maximum field intensities are very close to the full field modelling results.

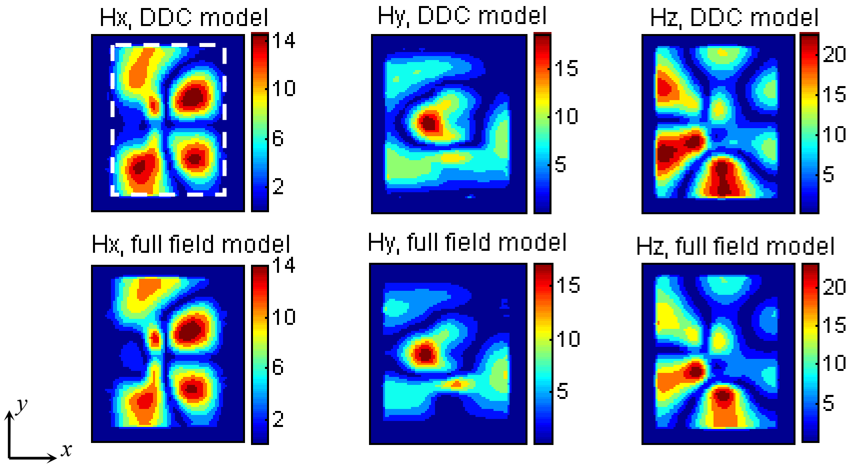

Fig. 5.12 Magnetic fields (unit in mA/m) of the L-shaped microstrip board inside the test box obtained from the equivalent DDC model and full field model

It must be pointed out that the DDC model contains a lot of simplifications and is an approximate representation of the interactions between the PCB and the enclosure. In addition, the real current distribution on a PCB slightly changes when it is placed in an enclosure. But in the DDC model, the equivalent dipoles are obtained from near-field scans in free space and these small changes are not included. This contributes additional errors to the equivalent dipole simulations. Therefore equivalent models for closed environment problems are generally less accurate than for free space problems. The mean squared error σ_{MSE} between the results of DDC model and full field model in Fig. 5.12 is 15%. However, the DDC model is still valid for approximate EMC analysis.

The computational costs of simulation with the DDC model and full field model for the above case on an Intel Core 2 Duo E8400 3.0 GHz computer are compared in TABLE 5.2. Although the DDC model is also computed with a MoM solver, the mesh of the equivalent dipole array is much coarser than that of a full field model. Therefore the equivalent DDC model dramatically reduces the memory requirement and computational time. In some complex problems benefits may be even greater because the mesh size of the DDC model does not depend on the complexity of the circuit.

TABLE 5.2 Computational costs of simulation with the DDC model and full field model

Computational costs / Model	Memory	Computational time	Time of modelling the configuration
DDC model	20 MB	10 min	5 min
Full field model	0.96 GB	1.5 h	30 min

5.4.2 Resonances of an Enclosure with a PCB Inside

When a PCB is inside an enclosure, it is of particular interest to investigate the behavior near resonant frequencies of the enclosure. With the L-shaped microstrip board fed by external RF signals, the resonant frequencies of an enclosure were found experimentally by observing the peaks of the field magnitude inside the enclosure across a wide frequency span. The study was focused on the first three resonant frequencies. Then the equivalent DDC model was established and incorporated into the full field solver together with the enclosure. Fig. 5.13 shows the configuration of the setup. The board was mounted on the bottom of a 284×204×65 mm enclosure. The vertical electric field E_z on a plane, which was 35 mm above the bottom of the enclosure, was predicted with the equivalent dipole sources and compared with 1) direct simulations which modelled the details of the board and 2) measurements which were taken along two lines defined by access slots (used to position the probe and re-sealed during measurement), as marked in the graph. Fig. 5.14 shows the full patterns of E_z given by the DDC model simulation, as well as the detailed results along the two lines. The general profiles of the results given by three different methods agree well, although the magnitude of measurements is always smaller than the simulations. This may be because the enclosure has features not included in the model, i.e. the imperfect resonance in practical measurements and effects caused by the presence of the probe.

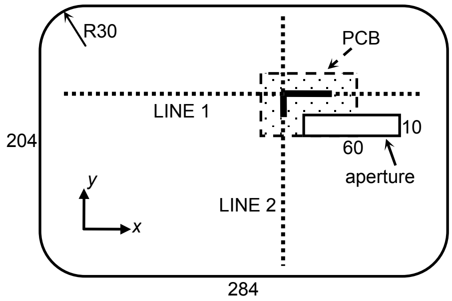

a) Top view and definition of the measurement lines

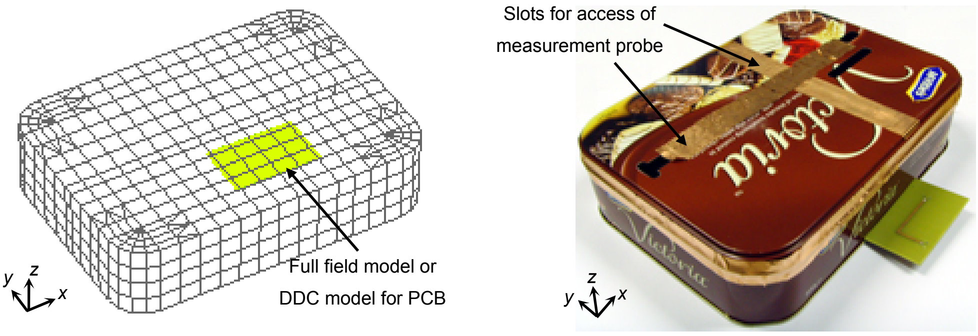

b) Model of the configuration for MoM simulations

c) Photograph of the configuration (enclosure and PCB shown separately)

Fig. 5.13 Configuration of the L-shaped microstrip board inside an enclosure for resonance simulations

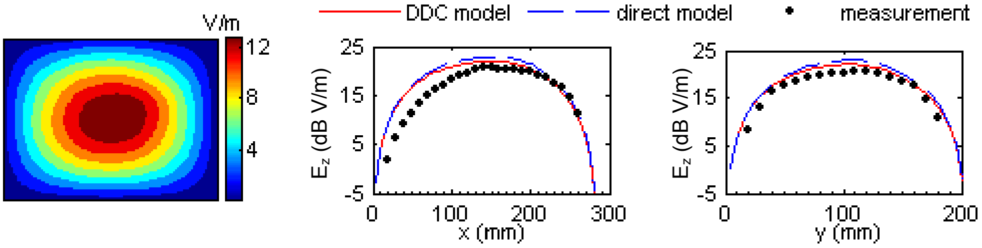

a) 1st resonant frequency 0.9 GHz

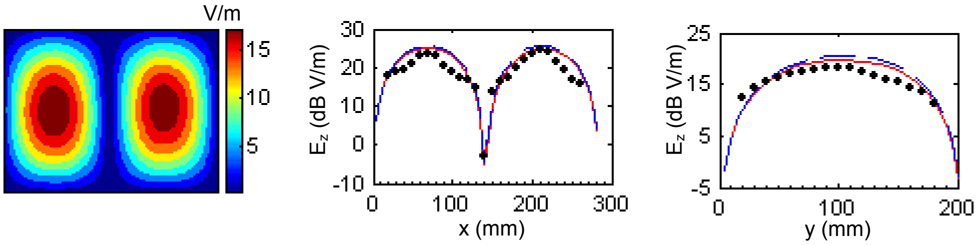

b) 2nd resonant frequency 1.29 GHz

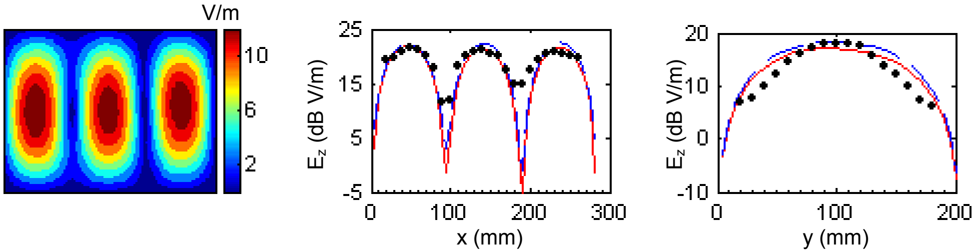

c) 3rd resonant frequency 1.74 GHz

Left column: full map predicted with the DDC model
Middle column: Comparison along observation line 1
Right column: Comparison along observation line 2

Fig. 5.14 Vertical electric field inside the enclosure near resonant frequencies

The observed resonant frequencies at 0.9 GHz, 1.29 GHz and 1.74 GHz are for the PCB loaded enclosure, not for the enclosure alone. To illustrate the resonant frequencies of the empty enclosure, the configuration of the empty enclosure illuminated by a 1V/m plane wave from the aperture was simulated across a wide frequency span, and the maximum electric field intensities over the same plane as the above configuration were plotted as a function of frequency in Fig. 5.15. The resonant frequencies are indicated by the peaks in the plots. The shift of the resonant frequencies compared to the PCB loaded enclosure is only 10 MHz because the volume of the populated PCB is much smaller than the volume of the enclosure. However, this slight shift in frequency can cause a very large variation (about 10 dB) in the resulting field intensities. Therefore the effect of the presence of the PCB on the propagation characteristics of the enclosure, which is particularly sensitive near resonant frequencies, must be taken into account for an accurate model. This confirms that modelling the dielectric and ground plane of a PCB is essential for enclosed environment simulations.

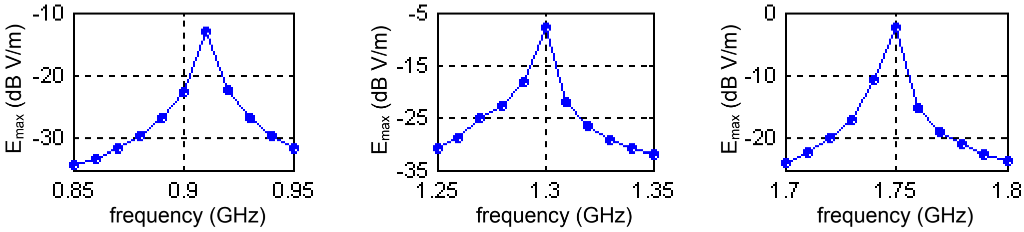

Fig. 5.15 Maximum electric field intensities of the empty enclosure illuminated by a plane wave from the aperture

5.4.3 Dependence on the Dielectric Parameters

Knowledge of the permittivity of the PCB substrate is needed when constructing the complete DDC model. The most accurate way is to measure it experimentally, but not every EMC lab has the required equipment. Normally PCB manufacturers provide general information of the substrate. For all the PCBs used in this work the substrate material is FR4 which has a typical permittivity value 4.6 [10]. In practice, the actual value may differ due to manufacturing uncertainties, constructional details, etc. It is therefore necessary to establish how accurate the value of permittivity should be for inclusion in the model. As a quantitative study, the vertical electric field along the two observation lines in the configuration shown in Fig. 5.13 at a non-resonant frequency (1 GHz) was predicted with DDC models built with different values of permittivity. The same field was then solved with a full field model for comparison where the typical permittivity value 4.6 was used. The correlation coefficients between the two simulated field results indicate the accuracy of the modelled permittivity values, as shown in Fig. 5.16. The field predicted by the DDC model is in an acceptable range provided that the modelled permittivity value is within 20% of the actual value. This implies that an accurate enough model can be built for most EMC studies as long as the general type of the dielectric substrate is known.

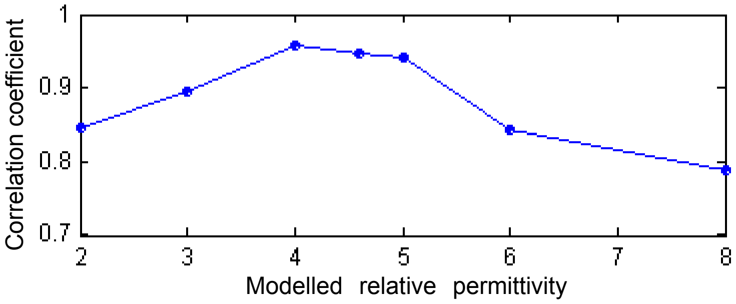

Fig. 5.16 Effects of the modelled permittivity value on the modelling accuracy

5.5 Application of the Model

The typical enclosed PCB configurations include PCBs with packaging and PCBs working in enclosed operating environments. In this section the DDC model is applied to these configurations for predicting the electromagnetic emissions both inside and outside the enclosures.

5.5.1 Packaged PCBs

The widely used PCB packaging is designed to protect PCBs from physical damages, electrostatic discharges and electromagnetic interferences. At the design stage normally only the circuit components and the layout of traces are considered. Therefore, it is useful to provide an equivalent model for a bare PCB which is able to predict the emissions from the PCB with any package designed and assembled.

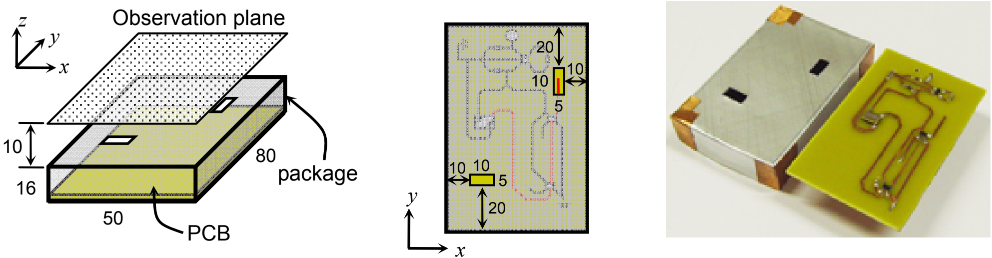

a) Overall configuration

b) Top view

c) Photograph (package and PCB shown separately)

Fig. 5.17 Configuration of the packaged digital circuit board

The equivalent DDC model was applied to the digital circuit board as shown in Fig. 5.17 (also discussed in Fig. 2.32 for near-field scans) assembled in a package. The DDC model was built for the bare PCB from near-field scans in free space at a height of 10mm above the board at 96 MHz. Then the whole board was assembled into a package with only two slots exposed – one for the access of a switch and the other for the connection of the signal output port, as shown in Fig. 5.17. The radiated magnetic field from the enclosed configuration over an 80×50mm plane at 10mm above the package was predicted using the DDC model together with a full field model for the package. The predicted field is compared with near-field measurement results in Fig. 5.18. A reasonable agreement is observed. The model generally locates the field hotspots and approximately predicts the maximum intensities with about 1 dB error. The error may be because of the approximations of the model and the imperfections of the packaging, e.g. imperfect rectangular shape and imperfect shielding.

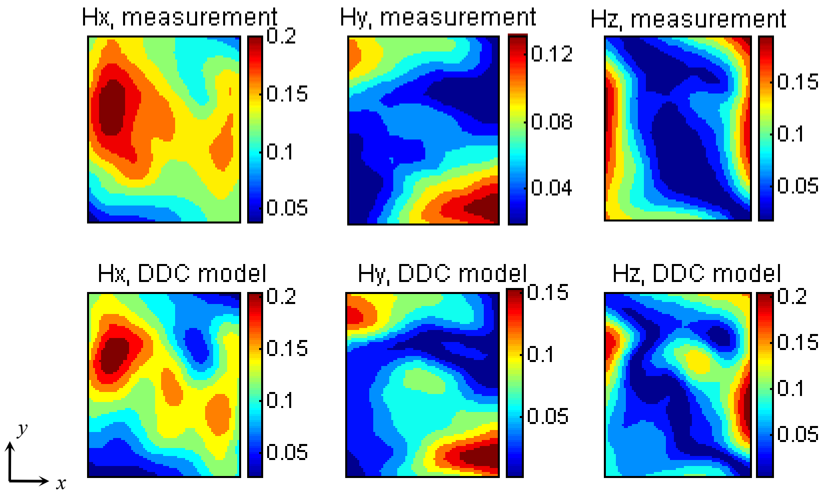

Fig. 5.18 Magnetic field (mA/m) outside the package with the digital circuit board enclosed

5.5.2 PCBs in Enclosed Operating Environments

Another typical kind of closed environment configuration is that of PCBs working in enclosed operating environments, such as in an electronic case and a conducting cabinet. It is particularly the case for large electronic systems, for example, the computer components inside a PC case. The electromagnetic emissions inside the enclosures and leaking outside the enclosure are the important factors for EMC assessments. To illustrate the application of the DDC model to these problems, the radio telemetry PCB working at 868.38 MHz, as shown in Fig. 5.19 (also discussed in Fig. 3.17 for the free space problems), was mounted in enclosed environments and equivalent model simulations were carried out. In the first step the equivalent DDC model was built for the PCB from magnetic near-field scans in free space. Then two examples with different enclosures were studied.

In the first case, the PCB was mounted in the center of the bottom surface of a diecast enclosure with a 20×20 mm aperture in the center of the top surface, as shown in Fig. 5.19. Magnetic field over a 50×50 mm plane which was outside the box and 12 mm above the aperture was predicted with the equivalent method and compared with near-field measurement results, as presented in Fig. 5.20. The equivalent DDC model accurately predicts the hotspots and the maximum field intensities with about 1 dB error.

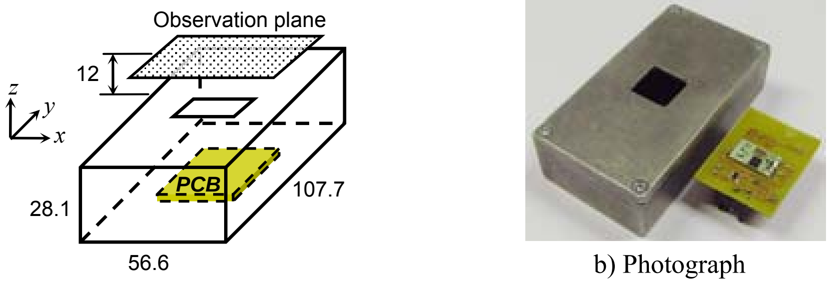

a) Geometry

b) Photograph
(enclosure and PCB shown separately)

Fig. 5.19 Configuration of the telemetry PCB in enclosure 1 (unit in mm)

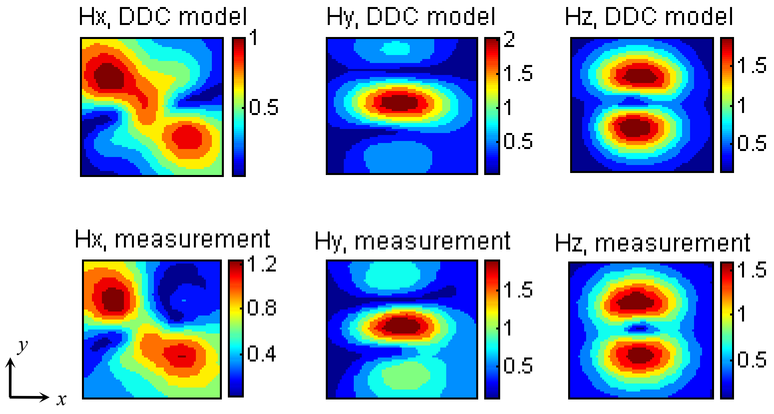

Fig. 5.20 Magnetic field (mA/m) outside the aperture of enclosure 1, 868.38 MHz

In the second case, the PCB was mounted on the bottom of a larger diecast enclosure with an aperture. Fig. 5.21 shows the geometry of this configuration. Two lines 35 mm above the PCB were marked and measurements were performed along them. Two slots were created on the lid of the enclosure in order to access the near-field probe and the slots were re-sealed at every measurement step. Limited by the measurement conditions, only the tangential magnetic field components, H_x and H_y, were measured. The same field was predicted with the DDC model and the two results are compared in Fig. 5.22. Above the measurement noise floor (approximately -70 ~ -65 dB A/m), an agreement within 3 dB can be observed. Also, as before, the presence of the measurement probe was not included in the model.

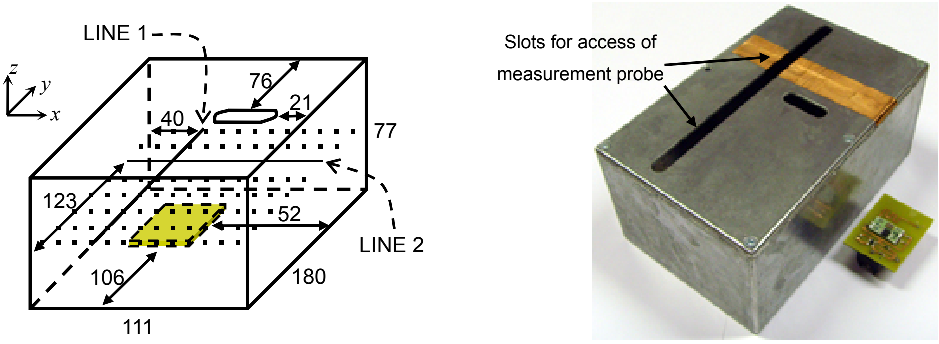

a) Geometry and observation lines

b) Photograph
(enclosure and PCB shown separately)

Fig. 5.21 Configuration of the telemetry PCB in enclosure 2 (unit in mm)

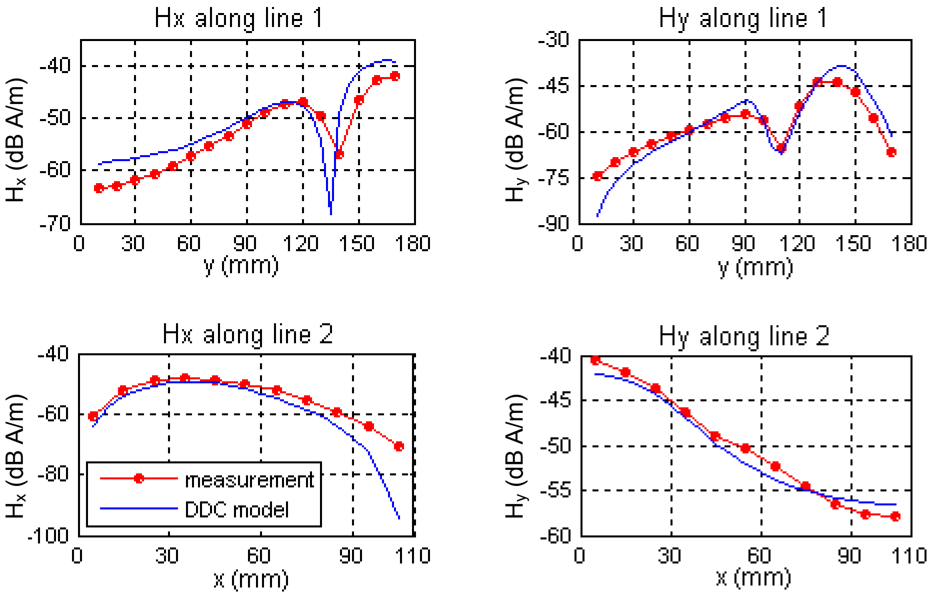

Fig. 5.22 Tangential magnetic field (dB A/m) along the two observation lines in enclosure 2

5.6 Conclusions

In this chapter, the equivalent dipole method is extended to modelling the emissions of PCBs in closed environments. The multiple interactions between PCBs and enclosures are studied and the effects on the loaded PCB are characterized. It is found that the physical presence of a

PCB which distorts the wave propagation characteristics of an enclosure is the most important factor. Therefore the Dipole-Dielectric-Conducting plane model is developed which includes both the active excitations and the passive electromagnetic properties of a PCB in order to approximately represent the multiple interactions between the PCB and the enclosure.

Validation studies of the DDC model for predicting electromagnetic emissions from PCBs, particularly near resonant frequencies show a general agreement with direct modelling results. The DDC model is applied to simulate the emissions from two typical enclosed configurations – packaged PCBs and PCBs working in enclosed operating environments. It has been shown that the inclusion of rudimentary details of ground plane and substrate in addition to the equivalent dipoles permit fairly accurate prediction of emitted fields to be made not only in free space but also in enclosures that have interactions with the PCBs inside. Moreover, simulations with the DDC model require much less computational costs than full field simulations.

Generally, the equivalent modelling method has better performance in free space than in closed environments. This may be attributed to the greater degree of approximations made to the model in enclosed environments. The real current distribution of the PCB is also assumed to be the same in free space and closed environments. This may be true in most but not all cases. In a highly populated enclosure (several PCBs in close proximity), stronger interactions may be present and the model may display a lower accuracy. A possible solution may be modelling every dipole with one more parameter – the impedance – which is a function of the conditions of a closed environment. Then the change in current distribution can be equivalently modelled by the variation of the dipole impedance. This may be a direction for further research. Nevertheless, it has been demonstrated that the proposed techniques have the potential to characterize emissions from complex structures in realistic environments reducing computational efforts significantly and making it possible to perform complete system EMC studies.

References

[1] (2010) Concept - II homepage. [Online]. Available: http://www.tet.tu-harburg.de/concept/index.en.html

[2] J. Shi, "Near-field measurement and analysis procedures for characterizing electromagnetic interference," Ph.D. dissertation, Dept. Elect. Eng., Univ. Missouri-Rolla, Rolla, MO, 2005.

[3] C. A. Balanis, *Advanced Engineering Electromagnetics*. New York: Wiley, 1989.

[4] Agilent 54753A/54754A TDR Plug-in Modules User's Guide, Agilent Technologies Inc., Santa Clara, CA, 2002.

[5] C. Christopoulos, *The Transmission Line Modelling Method*. New York: IEEE Press, 1995.

[6] D. W. P. Thomas, A. Denton, T. Konefal, T. M. Benson, C. Christopoulos, J. F. Dawson, A. C. Marvin, S. J. Portor, and P. Sewell, "Model of the electromagnetic fields inside a cuboidal enclosure populated with conducting planes or printed circuit boards", *IEEE Trans. Electromagn. Compat.*, vol. 43, no. 2, pp. 161-169, May 2001.

[7] R. Garg, P. Bhartia, I, Bahl, and A. Ittipiboon, *Microstrip Antenna Design Handbook*. Norwood, MA: Artech House, 2001.

[8] J. R. Mosig and T. K. Sarkar, "Comparison of quasi-Static and exact electromagnetic fields from a horizontal electric dipole above a lossy dielectric backed by an imperfect ground plane," *IEEE Trans. Microwave Theory Techniques*, vol. MTT-34, No. 4, April 1986, pp. 379-387.

[9] D. G. Fang, Antenna Theory and Microstrip Antennas. Boca Raton, FL: CRC Press, 2010.

[10] L. W. Ritchey, "A survey and tutorial of dielectric materials used in the manufacture of printed circuit boards," *CircuiTree Magazine*, Nov. 1999. [Online]. Available: http://www.speedingedge.com/docs/tutorial.doc

CHAPTER SIX

Conclusions and Future Work

6.1 Conclusions

This thesis is focused on a novel method for modelling the electromagnetic emissions from PCBs that fully represents the near field coupling mechanisms in a succinct manner and can accurately predict the radiated emissions in both free space and closed environments. The research work includes both measurement and modelling techniques. On the measurement side, a near-field scanning system was developed and near-field probes were characterized in order to experimentally collect the near-field information required for building equivalent models of PCB emission sources. On the modelling side, a simple and efficient emission model was developed based on near-field scanning in order to rapidly prototype a system design for emission and internal electromagnetic field strengths. Conclusions of this research work can be summarized as below.

In Chapter 2, the development of a planar near-field scanning system and the measurement methodology were presented. In the scanning system, a near-field probe was held by the positioning subsystem to scan over the interested region, and its output was recorded by connected receiving equipment and converted to amplitude and phase of the near field. The controlling software was developed to link the components of the system and provide fully automatic near-field scans with approximately 10 μm motion precision.

Two methods were described for measuring both amplitude and phase based on a vector receiver VNA and an amplitude-only receiver SA, respectively. Both methods were tested to be reliable, but the difference was that the VNA based method measured phase information directly but the SA based method measured phase indirectly from three scans by using a power combiner. In addition, a dual probe approach must be used with one probe providing the phase reference when the DUT was self-powered.

The near-field probes, either the loop H-field probe or monopole E-field probe, were designed for measuring individual field components. Performance of the probes was characterized, including sensitivity, spatial resolution, rejection ability to the unwanted field components, and disturbance to the measured fields. These characteristics showed how the probe outputs were related to the field intensities being measured. Then the conversion factors from probe outputs to field intensities were obtained by using a reference near field.

Experimental scans with a simple test board and a fast clock digital circuit board were carried out and the results were compared with full field simulations and GTEM cell emission tests. Reasonable agreement was obtained for the frequencies and distances of interest. Error analysis was also done for the near-field scanning system and it was estimated that there was a typical error bound of 0.35 dB and 5° for amplitude and phase measurement. These results confirmed that the near-field scanning system was able to experimentally provide reliable and sufficient near-field data which were required for building equivalent models of PCB emission sources.

In Chapter 3, a method to represent radiated emissions from a PCB using an equivalent dipole model deduced from magnetic near-field scans was described. In free space, a PCB was modelled with a set of equivalent dipoles placed in a matrix layout on the component surface. The PCB ground plane was also included in the model based on certain approximations in order to take into account the effects of incomplete grounding and diffraction. Based on the equivalence principle, inverse problem equations linked the equivalent dipoles to the measured near field including both amplitude and phase at discrete points over a surface. The equivalent dipoles were identified by fitting to the measured near fields from the solution to the inverse problem. The electromagnetic fields at any position could then be predicted from the equivalent dipole model.

The modelling accuracy was affected by measurement errors, condition number of the inverse problem matrix, and sufficiency of near-field information. Numerical techniques and optimization of the measurement and model parameters were investigated in order to improve the modelling accuracy. First, it was demonstrated that mathematically the regularization technique applied to the inverse problem for equivalent source identification could significantly enhanced the stability to measurement errors. Second, guidelines for setting the parameters of near-field scanning were studies which aimed to reduce the condition number of the inverse problem matrix and obtain sufficient near-field information. Generally this was achieved by setting an optimal scanning resolution and area, and by scanning as close as possible to the PCB. Third, the number of dipoles used for the model was not only a tradeoff between computational costs and modelling accuracy, but also a tradeoff between numerical stability and information sufficiency. Although effective simplification schemes of the dipole array were proposed, the initial number of dipoles for a particular model was determined empirically which was similar to setting the mesh size in a full field solver.

The method was validated experimentally with a simple test board and a practical telemetry PCB, and compared with full field simulations and measurements. The equivalent model accurately predicted the electromagnetic fields in both the near and far field in the whole free space. Low computational costs and no requirements for detailed information on PCB circuit structure were the significant advantages of the method.

In Chapter 4, an alternative method for identifying the equivalent dipoles based on near-field scans and genetic algorithms was proposed. A PCB was modelled with an array of equivalent dipoles deduced from an optimization procedure using GAs by fitting to the measured near fields. Two optimization procedures were proposed based on the mutually competitive evolution between two subpopulations and self-competitive evolution within the whole population, respectively.

The GA optimization was introduced in the equivalent dipole identification in order to find the optimal number and layout of the equivalent dipole. The optimization not only provided a means to diagnose the location of the primary real sources but also led to a more efficient equivalent dipole representation for the PCB. Another advantage of the method was the ability of making use of many types of near-field data, including phaseless data, therefore alleviating the demands on experimental facilities. However, due to the nature of iterative random search of GAs, the computational costs were much heavier than the inverse problem solution method. The method was validated with analytical fields from a simple dipole-like source and measured fields from PCBs. The favorable source identification and field prediction showed that the method was suitable for EMI and EMC studies.

In Chapter 5, the equivalent dipole method was extended to modelling the emissions of PCBs in closed environments. The multiple interactions between PCBs and enclosures were studied and the effects on the loaded PCB were characterized. It was found that the impact of the change on PCB currents and impedance was minimal, but the physical presence of a PCB which distorted the wave propagation characteristics of an enclosure was the most important factor of the multiple interactions. This facilitated the building of an approximate model for simulating the emissions in closed environments. Therefore the Dipole-Dielectric-Conducting plane (DDC) model was developed which included both the active excitations and the passive electromagnetic properties of a PCB in order to approximately represent the multiple interactions between the PCB and the enclosure.

For validation purposes, the DDC model was applied to a variety of configurations, including a simple test enclosure, configuration near resonant frequencies, a packaged practical PCB, and a practical PCB working in an enclosed operating environment. It was shown that the inclusion of rudimentary details of ground plane and substrate in addition to the equivalent dipoles permitted fairly accurate prediction of emitted fields to be made not only in free space but also in enclosures that had interactions with the PCBs inside.

Generally, the equivalent dipole modelling method had better performance in free space than in closed environments. This might be because the multiple interactions in closed environments were only approximately modelled. This might be effective in most but not all cases. In a highly populated enclosure (several PCBs in close proximity), stronger interactions might be present and the model might display a lower accuracy. Nevertheless, it has been demonstrated that the proposed techniques have the potential to characterize emissions from complex structures in realistic environments reducing computational efforts significantly and making it possible to perform complete system EMC studies.

6.2 Suggestions for Future Work

It is attractive to extend the methodology developed so far to provide a complete EMC analysis tool for complete and more complex electronic systems with multiple multilayer PCBs and interconnects [1]. This will bring current capabilities to a realistic level of complexity and include electromagnetic interactions hitherto neglected in PCB designs. A generic system is illustrated in Fig. 6.1.

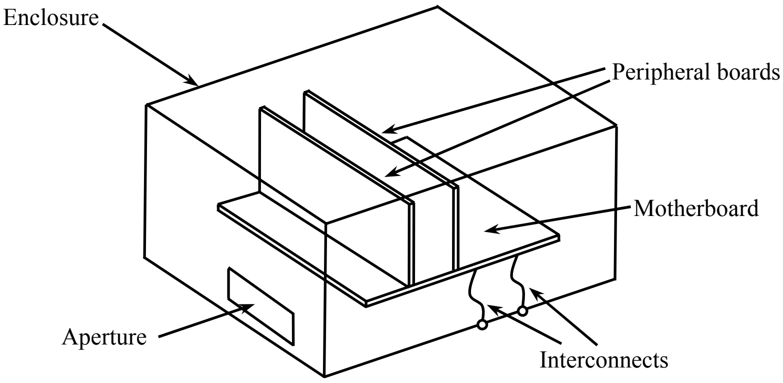

Fig. 6.1 A generic electronic system with multiple multilayer PCBs and interconnects

Further research directions may include the following issues. First, multilayer PCBs will radiate from all sides with possibly significant radiation from the edge waveguides [2]. The scanning area necessary for complete characterization of multilayer boards will have to be carefully evaluated. This may require complete scanning on all sides of the PCB including the edges.

Second, for multiple PCBs the fields will not be a linear combination of the field amplitudes from the individual radiators as the mutual coupling of the radiators needs to be taken into consideration. Also, the PCBs will have different modes of operation. Therefore, where possible the relative phase of each component PCB should be measured but each mode of operation of the PCBs may occur in a random way making it only possible to give models based on a statistical average.

Third, in more complex closed environments, there may be several highly populated PCBs in very close proximity as well as interconnects, leading to stronger interactions. Thus, the approximations made for the closed environment model should be carefully evaluated to allow for systematic and accurate characterization of these interactions. The change in the electromagnetic characteristics of PCBs, for a range of trace layouts, may be estimated from comparison with input power measurements and the measured total radiated power. The coupling to interconnects can be estimated from a TEM cell measurement [3]. By combining these approaches it is possible to develop a complete emissions characterization scheme for whole systems.

References

[1] D. W. P. Thomas, “Simplified models of emissions from electronic systems based on near field scans”, Univ. of Nottingham, EPSRC Research Proposal, Jul. 2009.

[2] H. W. Shim and T. Hubing, “A closed-form expression for estimating radiated emissions from the power planes in a populated printed circuit board”, *IEEE Trans. Electromagn. Compat.*, vol. 48, no. 1, pp. 74-81, Feb. 2006.

[3] S. Deng, T. Hubing, and D. Beetner, “Using TEM cell measurements to Estimate the maximum radiation from PCBs with attached cables due to magnetic field coupling”, *IEEE Trans. Electromagn. Compat.*, vol. 50, no. 2, pp. 419-423, May 2008.

Appendix A

Mechanical Hardware of the Positioning Subsystem in the Near-field Scanning System

The mechanical hardware of the positioning subsystem, including programmable motors, stepper drives, motorized slides and peripheral components, was commercially bought and then assembled and wired at GGIEMR. TABLE A.1 is a checklist of the commercially bought components. This section describes the mechanical structure and the most important characteristics of each component. Full specifications of all the components can be found in [1-4] most of which are available online.

TABLE A.1 Checklist of the main mechanical components

Item	Manufacturer	Model / Part No.	Quantity
Motorized slide	Velmex [1]	BiSlide	4
Programmable motor	Parker Hannifin [2]	SY872	1
Programmable motor	Parker Hannifin	SY563	2
Stepper drive	Parker Hannifin	ViX500	3
Power supply	LG motion [3]	N/A	1

Four motorized slides, which were driven by programmable motors, were used to construct the *x*-, *y*-, and *z*-axis tracks of the positioning workbench, as illustrated in Fig. A.1. The *x*-axis track was the base of the whole workbench so two parallel slides were used to provide solid construction. Axes of the two slides were center-to-center coupled to synchronize the motion. The *y*-axis slide was mounted on the *x*-axis track, and the *z*-axis slide was mounted on the *y*-axis slide. Thus the bench provided 3D positioning with 4 slides and 3 motors. Detailed structure of the slides is shown in Fig. A.2. At the “motor plate” end of each slide (except one of the two *x*-axis slides), a motor was mounted onto the plate and coupled to the axis of the slide.

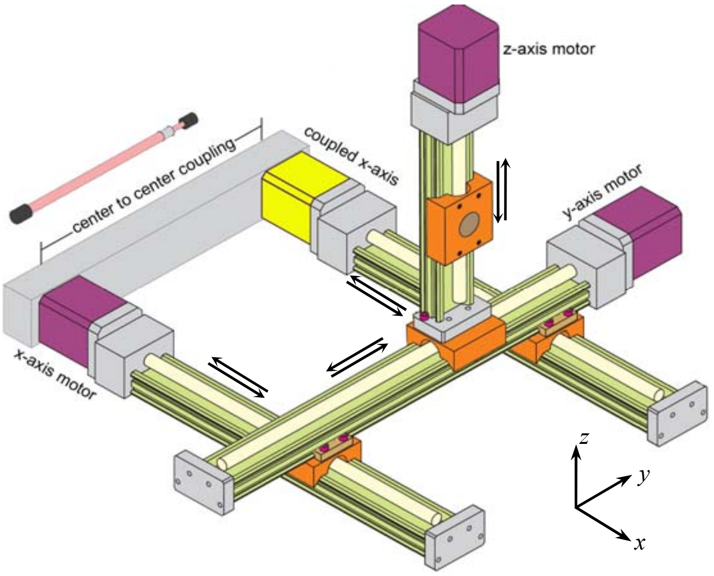

Fig. A.1 Construction of the positioning subsystem

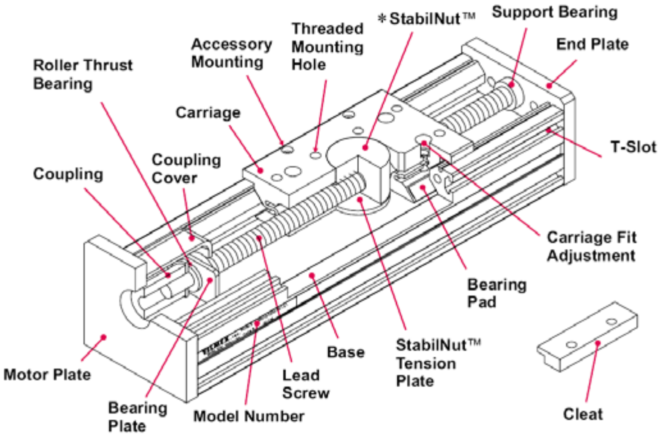

* StabilNut^{TM} is a Velmex exclusive low friction connection between the lead screw and carriage

Fig. A.2 Configuration of the slide [1]

The most important characteristics of the positioning subsystem are the load capacity and motor torque, which are shown in Fig. A.3 and Fig. A.4, respectively. Both quantities are a function of the maximum speed allowed, thus these specifications determine the motion speed of a particular scan. The *x*-axis track, which is the base of the workbench, is driven by a motor with a greater torque.

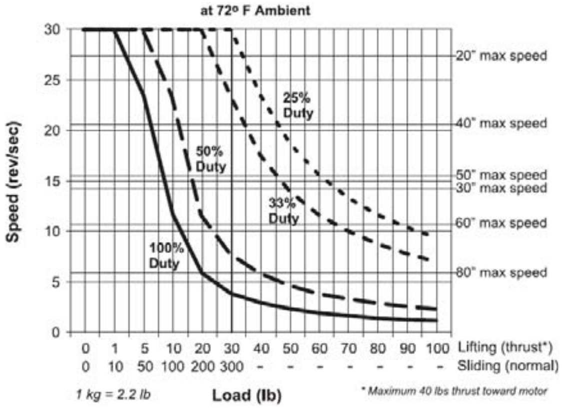

Fig. A.3 Speed-load curve of the slide [1]

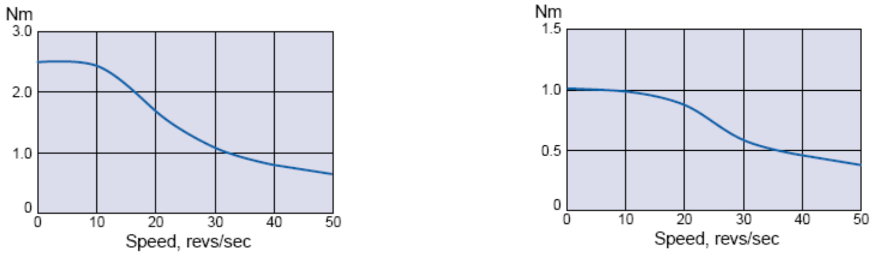

a) Motor for x-axis track

b) Motors for y- and z-axis tracks

Fig. A.4 Motor performance data [2]

Each motor is driven by a separate stepper drive. The stepper drives encode the motion algorithms received from the controlling software to motor-recognizable codes, and send them to the servo panel to drive the motors. Flowchart of the software design was presented in Section 2.3. Wiring from stepper drives to the computer, power supply, and motors was finished according to the pin layout of the stepper drive as illustrated in Fig. A.5.

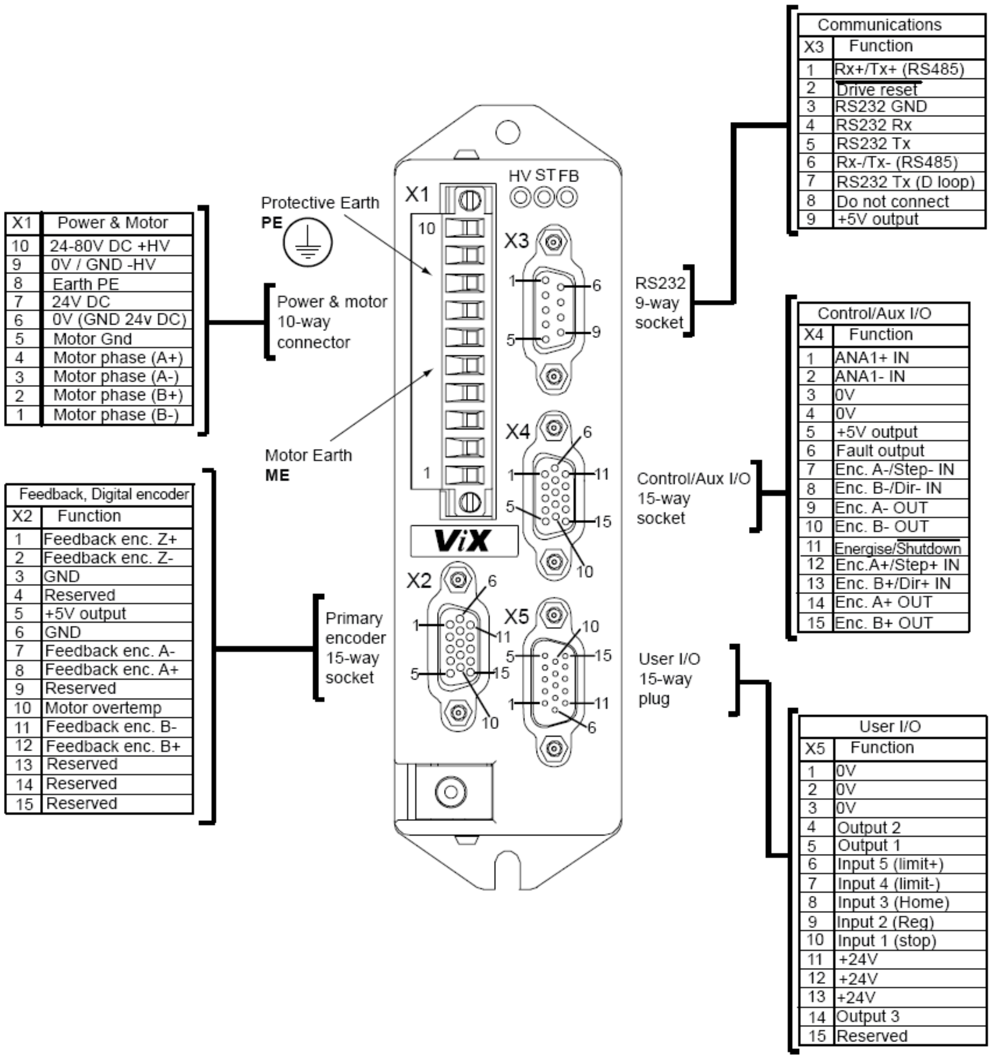

X1	Power & Motor
10	24-80V DC +HV
9	0V / GND -HV
8	Earth PE
7	24V DC
6	0V (GND 24v DC)
5	Motor Gnd
4	Motor phase (A+)
3	Motor phase (A-)
2	Motor phase (B+)
1	Motor phase (B-)

Feedback, Digital encoder

X2	Function
1	Feedback enc. Z+
2	Feedback enc. Z-
3	GND
4	Reserved
5	+5V output
6	GND
7	Feedback enc. A-
8	Feedback enc. A+
9	Reserved
10	Motor overtemp
11	Feedback enc. B-
12	Feedback enc. B+
13	Reserved
14	Reserved
15	Reserved

Communications

X3	Function
1	Rx+/Tx+ (RS485)
2	Drive reset
3	RS232 GND
4	RS232 Rx
5	RS232 Tx
6	Rx-/Tx- (RS485)
7	RS232 Tx (D loop)
8	Do not connect
9	+5V output

Control/Aux I/O

X4	Function
1	ANA1+ IN
2	ANA1- IN
3	0V
4	0V
5	+5V output
6	Fault output
7	Enc. A-/Step- IN
8	Enc. B-/Dir- IN
9	Enc. A- OUT
10	Enc. B- OUT
11	Energise/Shutdown
12	Enc.A+/Step+ IN
13	Enc. B+/Dir+ IN
14	Enc. A+ OUT
15	Enc. B+ OUT

User I/O

X5	Function
1	0V
2	0V
3	0V
4	Output 2
5	Output 1
6	Input 5 (limit+)
7	Input 4 (limit-)
8	Input 3 (Home)
9	Input 2 (Reg)
10	Input 1 (stop)
11	+24V
12	+24V
13	+24V
14	Output 3
15	Reserved

Fig. A.5 Connector pin layout of the stepper drive [4]

References

[1] (2010) *BiSlide Assemblies*, Velmex Inc., [online]. Available: http://www.velmex.com/bislide/motor_bislide.html.

[2] (2010) SY Stepper Motors Data Manual, Parker Hannifin Eletromechanical Division Europe, Offenburg, Germany, [online]. Available: http://www.parker-eme.com.

[3] (2010) LG Motion homepage. [online]. Available: http://www.lg-motion.co.uk.

[4] *ViX 250/500IM Stepper Drivers User Guide*, Parker Hannifin Eletromechanical Division Europe, Offenburg, Germany, 2004.

Appendix B

Mathematics of Regularization for Inverse Problems

Euclidean norm

The norm of a matrix is a scalar that gives some measure of the magnitude of the elements of the matrix. There are several different kinds of matrix norms. The Euclidean norm (also called Frobenius norm) of an $m \times n$ matrix A, denoted as $\|A\|_2$, is defined as the square root of the sum of the absolute squares of its elements. The MATLAB function to calculate the Euclidean norm of matrix A is

```
norm(A, ‘fro’)
```

Condition number

For a matrix A associated with of a system of linear equations $Ax=b$, the condition number Cond(A) measures the sensitivity of the solution x to the errors in b. The formal definition is

$$\text{Cond}\ (A) = \|A^{-1}\| \cdot \|A\| \tag{B.1}$$

It gives an indication of the accuracy of the results from matrix inversion and the linear equation solution. Values of cond(A) near 1 indicate a well-conditioned matrix which is less sensitive to errors in b. The MATLAB function to calculate the condition number of matrix A is

```
cond(A)
```

Complex conjugate transpose

The conjugate transpose of a matrix A consisting of complex numbers, denoted as A^T, is to transpose the matrix and reverse the sign of the complex part of each element. The MATLAB command to obtain the conjugate transpose of matrix *A* is

```
A’
```

Trace

The trace of a matrix A is the sum of the diagonal elements, denoted as tr(A) or trace(A). The MATLAB function to calculate the trace of matrix A is

```
trace(A)
```

Identity matrix

It is a kind of matrices with ones on the main diagonal and zeros elsewhere, generally denoted as *I*. These matrices have the property that *IA=A* and *AI=A* whenever the dimensions are compatible. The MATLAB function to return an $m \times n$ rectangular identity matrix is

```
eye(m,n)
```

Discrete derivative operator matrix

For an arbitrary derivation $f(x) = dF(x)/dx$, its discrete version is given by:

$$\begin{bmatrix} f(x_1) \\ \dots \\ f(x_n) \end{bmatrix} = \frac{1}{\Delta x} D \begin{bmatrix} F(x_1) \\ \dots \\ F(x_n) \end{bmatrix} \tag{B.2}$$

where *D* is the discrete derivative operator matrix.

From $f(x_1) = \frac{F(x_1)}{\Delta x}, \dots f(x_n) = \frac{F(x_n) - F(x_{n-1})}{\Delta x}$, *D* is formally given by

$$D = \begin{bmatrix} 1 & & & 0 \\ -1 & 1 & & \\ & \ddots & \ddots & \\ 0 & & -1 & 1 \end{bmatrix} \tag{B.3}$$

Appendix C

Derivation of Electromagnetic Fields of a Horizontal Electric Dipole Above a Dielectric Backed by a Ground Plane

The electromagnetic fields of a horizontal dipole above a microtrip structure can be addressed in different ways [1]. The formulae used in this research work (Chapter 5) are the exact solutions derived from the dyadic Green's function which have been extensively studied in the literature and successfully applied to microstrip antenna design. A good review can be found in [2], and the detailed theory can be found in [3]. This section summarizes the key points of the derivation procedure.

The problem

Consider an x-directed horizontal electric dipole (HED) of a moment Idx located at the air-dielectric interface of a microstrip structure with infinite transverse directions as shown in Fig.C.1. The substrate is a homogeneous isotropic dielectric of thickness h and relative permittivity ε_r. The origin of the coordinate system is chosen to be the location of the HED. The ground plane is located at $z = -h$ and is considered to be a perfectly conducting plane. The space above the ground plane is divided into two regions. Region 1 and 2 refer to the air and dielectric, respectively.

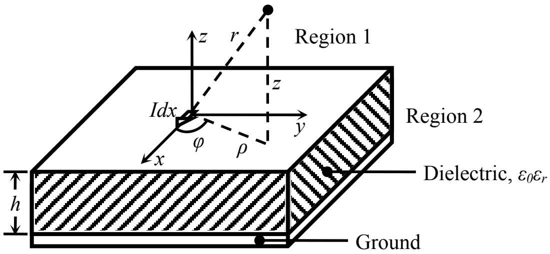

Fig. C.1 Geometry of a horizontal electric dipole over a microstrip structure [2, pp. 226]

Helmholtz equations

The MPIE (mixed potential integral equation) method [2] is used to obtain the electromagnetic field of the HED. A vector potential $\vec{A}$ and a scalar potential V are introduced to set up the integral equations for arbitrarily shaped scatterers. The electromagnetic fields can then be expressed in terms of the vector and scalar potentials as

$$\mu\vec{H} = \nabla \times \vec{A} \tag{C.1a}$$

$$\vec{E} = -j\omega\vec{A} - \nabla V \tag{C.1b}$$

The potentials are related through the Lorentz gauge condition as

$$\nabla \cdot \vec{A} + j\omega\mu\varepsilon V = 0 \tag{C.2}$$

The general solutions for potentials are obtained from the Helmholtz equations

$$\left(\nabla^2 + k^2\right)\vec{A} = 0 \tag{C.3a}$$

$$\left(\nabla^2 + k^2\right)V = 0 \tag{C.3b}$$

where $k = \omega\sqrt{\mu\varepsilon}$ is the wave number in the medium considered.

It is not possible to obtain $\vec{A}$ in a closed form if the medium is inhomogeneous such as for the layered dielectric. However, in the spectral domain it has a closed-form solution. Thus, (C.3a) is transformed to the spectral domain using the double Fourier transform in the *xy* plane defined by

$$\tilde{f}\left(k_x, k_y\right) = \frac{1}{2\pi}\int\int_{0}^{+\infty} f\left(x, y\right)\exp\left(-jk_x - jk_y\right)dxdy \tag{C.4}$$

The Fourier transformation of (C.3a) is formally given by

$$\left(\frac{d^2}{dz^2} - u_i^2\right)\tilde{\tilde{A}} = 0 \quad i = 1, 2 \tag{C.5}$$

where

$$u_i^2 = k_x^2 + k_y^2 - k_i^2 = k_\rho^2 - k_i^2$$

$$u_1^2 = u_0^2 = k_\rho^2 - k_0^2 \quad \text{for } z \geq 0 \text{ (medium 1)}$$

$$u_2^2 = u^2 = k_\rho^2 - \varepsilon_r k_0^2 \quad \text{for } -h \leq z \leq 0 \text{ (medium 2)}$$

and k_ρ is the complex radial component of the wave number, k_x, k_y, and k_z are the Cartesian components of the wave number.

Solution to (C.5) can be obtained in cylindrical coordinates. An inverse Fourier transform is then applied to the spectral domain solution in order to transform it back to the space domain. The potential function depends on k_x and k_y only through the radial spectral variable k_ρ. For functions exhibiting such dependence, the inverse Fourier transform becomes Bessel-Fourier transform, and can be written as

$$f\left(\rho\right) = \int_0^\infty J_n\left(k_\rho \rho\right)\tilde{f}\left(k_\rho\right)k_\rho dk_\rho \tag{C.6}$$

where $J_n(x)$ is the Bessel function of the first kind. Therefore, the general solution of Helmoltz equation (C.3a) in the space domain is

$$\int_0^\infty J_n\left(k_\rho \rho\right)\left[a_1 e^{jn\varphi} + a_2 e^{-jn\varphi}\right]\left[b_1 e^{jk_z z} + b_2 e^{-jk_z z}\right] dk_\rho \tag{C.7}$$

where ρ, φ, and z are the descriptions of the cylindrical coordinates.

Boundary conditions

The fields must satisfy boundary conditions at the interface and the ground plane which can be expressed as

$$\hat{z}\times\left(\vec{E}_1 - \vec{E}_2\right) = 0 \qquad \text{at the interface } z=0 \tag{C.8a}$$

$$\hat{z}\times\left(\vec{H}_1 - \vec{H}_2\right) = \vec{J}_s \qquad \text{at the interface } z=0 \tag{C.8b}$$

$$\hat{z}\times\vec{E}_2 = 0 \qquad \text{at the ground plane } z=-h \tag{C.8c}$$

$$\hat{z}\times\vec{H}_2 = \vec{J}_s \qquad \text{at the ground plane } z=-h \tag{C.8d}$$

where the indices 1 and 2 refer to air and dielectric region, respectively.

The surface current associated with the HED is given by the Dirac's Delta distribution

$$\vec{J}_s = \hat{x}\frac{\delta(\rho)}{2\pi\rho} Idx = \hat{x}\frac{Idx}{4\pi}\int_0^\infty H_0^{(2)}\left(k_\rho \rho\right) k_\rho dk_\rho \tag{C.9}$$

where the Hankel transform for $\delta(\rho)/\rho$ has been utilized.

In an inhomogeneous medium, two components of $\vec{A}$ are needed to satisfy the continuity of V at the interface. According to Sommerfeld's approach [3],

$$\vec{A} = \hat{x}A_{xx} + \hat{z}A_{zx} \tag{C.10}$$

where $A_{\alpha\beta}$ is the α component of potential due to the β-directed current, $\alpha,\beta=x,y,z$.

Introducing the field expressions (C.1) and the Lorentz gauge condition (C.2) into the boundary conditions (C.8), the boundary conditions of the vector and scalar potentials can be obtained as

$$V_1 = V_2 \quad \text{at } z=0 \tag{C.11a}$$

$$A_1 = A_2 \quad \text{at } z=0 \tag{C.11b}$$

$$\frac{\partial A_{xx1}}{\partial z} - \frac{\partial A_{xx2}}{\partial z} = -\mu J_x \quad \text{at } z=0 \tag{C.11c}$$

$$A_{xx2} = 0 \quad \text{at } z=-h \tag{C.11d}$$

$$V_2 = 0 \quad \text{at } z=-h \tag{C.11e}$$

$$\frac{\partial A_{zx2}}{\partial z} = 0 \quad \text{at } z=-h \tag{C.11f}$$

Vector and scalar potentials

Introducing the above boundary conditions (C.11) and utilizing the general expression (C.7), the vector potential components A_{xx} and A_{zx} can be obtained. By introducing the vector potential into the Lorentz gauge condition (C.2), the scalar potential V can be obtained. Both the potentials are formally expressed as

$$A_{xx} = \frac{\mu_0}{4\pi} Idx \int_0^\infty J_0\left(k_\rho \rho\right) \frac{k_\rho}{D_{\text{TE}}} e^{-u_0 z} dk_\rho \quad \text{for } z\geq 0 \tag{C.13a}$$

$$A_{xx} = \frac{\mu_0}{4\pi} Idx \int_0^\infty J_0\left(k_\rho \rho\right) \frac{k_\rho}{D_{\text{TE}}} \frac{\sinh u\left(z+h\right)}{\sinh uh} dk_\rho \quad \text{for } -h\leq z\leq 0 \tag{C.13b}$$

$$A_{zx} = -\frac{\mu_0}{4\pi} Idx\left(\varepsilon_r - 1\right)\cos\varphi \cdot \int_0^\infty J_1\left(k_\rho \rho\right) \frac{k_\rho^2 N}{D_{\text{TE}} D_{\text{TM}}} e^{-u_0 z} dk_\rho \quad \text{for } z\geq 0 \tag{C.13c}$$

$$A_{zx} = -\frac{\mu_0}{4\pi} Idx\left(\varepsilon_r - 1\right)\cos\varphi \cdot \int_0^\infty J_1\left(k_\rho \rho\right) \frac{k_\rho^2 N}{D_{\text{TE}} D_{\text{TM}}} \frac{\cosh u\left(z+h\right)}{\cosh uh} dk_\rho \quad \text{for } -h \leq z \leq 0 \tag{C.13d}$$

$$V = \frac{\cos\varphi}{4\pi j\omega\varepsilon_0} Idx \cdot \int_0^\infty J_1(k_\rho \rho) \frac{k_\rho^2 N}{D_{\mathrm{TE}} D_{\mathrm{TM}}} e^{-u_0 z} dk_\rho \quad \text{for } z \geq 0 \tag{C.13e}$$

$$V = \frac{\cos\varphi}{4\pi j\omega\varepsilon_0} Idx \cdot \int_0^\infty J_1(k_\rho \rho) \frac{k_\rho^2 N}{D_{\mathrm{TE}} D_{\mathrm{TM}}} \frac{\sinh u(z+h)}{\sinh uh} dk_\rho \quad \text{for } -h \leq z \leq 0 \tag{C.13f}$$

where

$$D_{\mathrm{TE}} = u_0 + u \coth uh$$
$$D_{\mathrm{TM}} = \varepsilon_r u_0 + u \tanh uh$$
$$N = u_0 + u \tanh uh$$

Electromagnetic fields

Introducing the potentials (C.13) into the field expressions (C.1), the derivation of electromagnetic fields is then straightforward. The tangential magnetic field components for $z \geq 0$, as used in Chapter 5, can be finally derived as

$$H_x(\rho,\varphi,z) = \frac{Idx}{2\pi}(\varepsilon_r - 1)\sin 2\varphi \int_0^\infty \frac{k_\rho^3}{D_{\mathrm{TE}} D_{\mathrm{TM}}} e^{-u_0 z} \cdot \left(J_0(k_\rho \rho) - \frac{J_1(k_\rho \rho)}{k_\rho \rho} \right) dk_\rho \tag{C.14a}$$

$$\begin{aligned} H_y(\rho,\varphi,z) &= \frac{Idx}{2\pi} \int_0^\infty J_0(k_\rho \rho) \frac{k_\rho u_0}{D_{\mathrm{TM}}} e^{-u_0 z} dk_\rho - \\ &\frac{Idx}{2\pi}(\varepsilon_r - 1)\sin 2\varphi \int_0^\infty \frac{k_\rho^3}{D_{\mathrm{TE}} D_{\mathrm{TM}}} e^{-u_0 z} \cdot \left(\cos^2\varphi J_0(k_\rho \rho) - \cos 2\varphi \frac{J_1(k_\rho \rho)}{k_\rho \rho} \right) dk_\rho \end{aligned} \tag{C.14b}$$

References

[1] J. R. Mosig and T. K. Sarkar, “Comparison of quasi-Static and exact electromagnetic fields from a horizontal electric dipole above a lossy dielectric backed by an imperfect ground plane,” *IEEE Trans. Microwave Theory Techniques*, vol. MTT-34, no. 4, pp. 379-387, Apr. 1986.

[2] R. Garg, P. Bhartia, I, Bahl, and A. Ittipiboon, *Microstrip Antenna Design Handbook*. Norwood, MA: Artech House, 2001.

[3] J. R. Mosig and F. E. Gardiol, “A dynamic radiation model for microstrip structures,” *Advances in Electronics and Electron Physics*, vol. 59, New York: Academic Press, pp. 139-237, 1982.

Appendix D

Computational Details of Scalar and Vector Potentials

For the evaluation of the fields derived in Appendix C, it is necessary to evaluate certain infinite integrals of oscillatory functions and divergent integrals as $\lambda \to \infty$. In addition, the integrands in (C.14) have a branch-point singularity at $\lambda = k_0$ and pole singularities associated with zeros of D_{TE} and D_{TM} which make the numerical integration complicated. A typical example is illustrated for the scalar potential with parameters ε_r=2.55, k_0h=0.3π, and $k_0\rho$=03 [1]. The integrand of this function is shown in Fig.D.1. The branch-point behavior can be observed at A ($\lambda = k_0$), and pole singularity at B due to the first zero of D_{TM}. The main difficulties in the numerical integration are the infinite derivatives at the branch point and the strong variation near the pole. Moreover, the function oscillates and diverges at infinity.

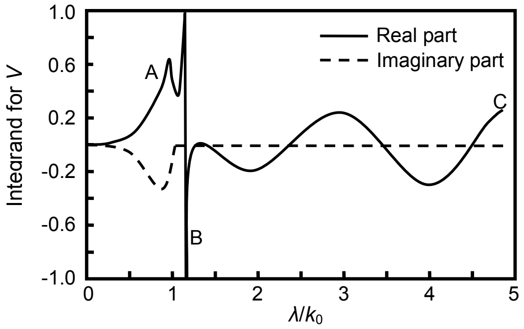

Fig. D.1 Normalized value of the integrand associated with the scalar potential [1]

Efficient numerical techniques to this integration problem have been extensively studied and a good review can be found in [2, 3]. This section gives an outline of the numerical techniques used in this research work. The integration is evaluated along the real axis, and the integration interval is decomposed into three subintervals [0, k_0], $[k_0, k_0\sqrt{\varepsilon_r}]$, and $[k_0\sqrt{\varepsilon_r}, \infty]$.

In the region [0, k_0], the infinite derivative at k_0 corresponding to the branch point is eliminated with a change of variable $\lambda = k_0 \cosh t$. The resulting smoother function can be integrated numerically.

In the region $[k_0, k_0\sqrt{\varepsilon_r}\,]$, singularity extraction techniques are used for integration because at least one singular point is known to exist. For this, the integrand is redefined as

$$f(\lambda) = \left[f(\lambda) - f_{\sin g}(\lambda) \right] + f_{\sin g}(\lambda) \tag{D.1}$$

where

$$f_{\sin g}(\lambda) = \frac{R}{\lambda - \lambda_p} \tag{D.2}$$

Here λ_p is the pole and R is the residue of $f(\lambda)$ at the pole. The first part of (D.1) is regular and can be evaluated numerically. A change of variable $\lambda = k_0 \cosh t$ can be used to eliminate the infinite derivative at k_0. Effects of these operations are shown in Fig.D.2 for the example mentioned above. For the singular part of (D.1), it is integrated analytically and is given by

$$\int_{k_0}^{k_0\sqrt{\varepsilon_r}} f_{\sin g}(\lambda)\, d\lambda = R \ln \frac{k_0\sqrt{\varepsilon_r} - \lambda_p}{\lambda_p - k_0} - j\pi R \tag{D.3}$$

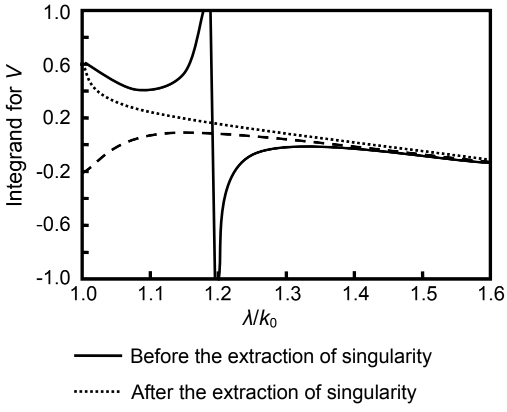

Fig. D.2 The integrand of Fig. D.1 (real part) and effects of numerical techniques [1]

In the region $[k_0\sqrt{\varepsilon_r},\infty]$, there are oscillations and function divergence. The asymptotic extraction technique is therefore used to separate the dominant term. The asymptotic value ($k_\rho \to \infty$) of the integrand, which is equal to its static value ($k_0 \to 0$), is extracted. Then the integrand can be written as

$$f(\lambda,k_0)=\left[f(\lambda,k_0)-f(\lambda,k_0=0)\right]+f(\lambda,k_0=0) \tag{D.4}$$

The first part of (D.4) shows a convergent oscillating function which can be efficiently integrated using a weighted-average algorithm [3]. Fig. D.3 shows the effect of asymptotic extraction. For the static term, it is integrated analytically and is given by

$$\int_0^\infty f(\lambda,k_0=0)\,d\lambda=\begin{cases}\dfrac{\mu_0}{4\pi r}, & \text{for the vector potential}\\[2ex] \dfrac{1}{2\pi\varepsilon_0(\varepsilon_r+1)r} & \text{for the scalar potential}\end{cases} \tag{D.5}$$

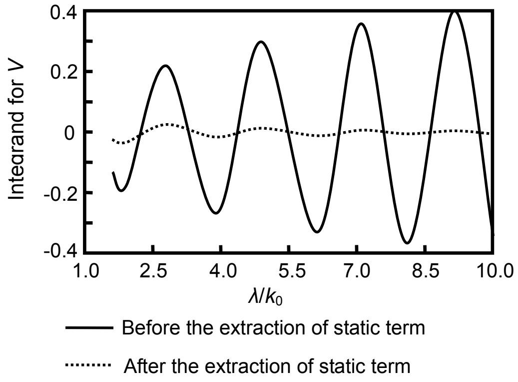

Fig. D.3 The integrand of Fig. D.1 (real part) and effect of asymptotic extraction [1]

References

[1] J. R. James and P. S. Hall, *Handbook of Microtrip Antennas*, Peter Peregrinus, London, UK, 1989.

[2] R. Garg, P. Bhartia, I, Bahl, and A. Ittipiboon, *Microstrip Antenna Design Handbook*, Norwood,

MA: Artech House, 2001.

[3] T. Itoh (Ed.), Numerical Techniques for Microwave and Millimeter-Wave Passive Structures, New York: John Wiley, 1989.